The properties and role of carbonate cementation in fault zones

Helen C P Lacey

Imperial College London

Department of Earth Science and Engineering

This thesis is submitted for the degree of Doctor of Philosophy

October 2018

Although in (many) moments this study has led to me pulling my hair out and considering giving everything up to go live self-sufficient in a forest, it did start my love affair with travel. I will never forget the first time I saw Mt Fuji emerging from the clouds and dominating the skyline in Japan, nor the sheer beauty of a star-studded galaxy in my wake swimming through the bioluminescent algae in the Bay of Islands, New Zealand. I have had so many new experiences, from spending five weeks on a swaying ship obtaining seismic data, to learning how to scuba dive after having the simple need to do something else during my write-up. It has made me much more resilient and excited for the chapters in my life to come, which, I'm happy to say, will not involve writing any.

Abstract

The interaction between fluids and rock is recognised as being highly important in the seismic cycle. Both the mechanical and chemical processes induced by fluid-rock interactions can alter various rock physical properties, which in turn has implications ranging from altering slip behaviour on faults to affecting hydrocarbon reservoir longevity. Therefore, the study of physical manifestations of fluid-rock interactions in fault zones, *specifically* the cements present, is of both societal and economic value.

Due to its reactivity with even weak acidic fluids, carbonate rocks, composed mostly of the mineral calcite ($CaCO_3$), are very susceptible to dissolution-precipitation processes. Sedimentary rocks are frequently cemented by carbonate and they are also hosts of many hydrocarbon reservoirs (50% of the world's hydrocarbon reservoirs are in carbonates). Perhaps most importantly, carbonate-bearing terrains are host to a multitude of destructive earthquakes, from the 1981 sequence in the Gulf of Corinth, to the 2008 Wenchuan earthquake in China and the numerous earthquakes in the Apennines, Italy over the last ten years (L'Aquila 2009, central Italy 2016, 2017). The effect of the interaction between carbonates and fluids on the physical properties of fault zones has been questioned in recent years, but detailed studies are few.

The focus of this study is to better constrain the properties and role of carbonate cementation in fault zones. A multidisciplinary approach is taken in this project, in which methods of isotope geochemistry, microscopy of cements in fault zones, and rock deformation experiments are combined to gain insight in the processes concerned with cementation over the course of the earthquake cycle, and the subsequent effect on rock properties. Stable and clumped carbon and oxygen isotope ratios in cement phases are determined to derive information on the fluid source, the migration of fluids, and the associated interactions with the surrounding rock. Field descriptions and microscopy (conventional, cathodoluminescence (CL), scanning electron microscopy (SEM) and transmitted electron microscopy (TEM)) permit the analysis of the textures and cement generations. Rock deformation experiments inducing field-relevant conditions in carbonate-saturated fault zones permit the characterisation of changes in rock properties.

The multidisciplinary approach used has permitted me to link together the geochemistry of cements with the alteration of fault physical properties. I have identified that textures within a fault zone fingerprint the chemical and mechanical processes which have occurred during fault

zone evolution. Such heterogeneities produced by fluid-rock interactions can influence future fracture propagation, non-optimal fault activation and enigmatic events, such as slow-slip. I have found that fault properties, including strength, permeability and fault slip behaviour are strongly dependent upon the degree of cohesion and compaction achieved within the fault zone, which in turn is dependent upon temperature, the presence of gouge, host rock type, the presence of fluid (and fluid type) and fault roughness.

This thesis documents the use of cements in studying fault zone evolution, and how the processes leading to, and characteristics induced by, cementation in fault zones exert profound changes in rock physical properties across all scales.

Declaration of originality

I am responsible for the interpretations, writing and conclusions contained within this thesis. No portion of this thesis has been submitted elsewhere for any additional qualification or in support of any other degree. References and all other contributions throughout this thesis are acknowledged as appropriate.

Helen C P Lacey

The copyright of this thesis rests with the author and is made available under a Creative Commons Attributions Non-Commercial No Derivatives licence. Researchers are free to copy, distribute or transmit the thesis on the condition that they attribute it, that they do not use it for commercial purposes and that they do not alter, transform or build upon it. For any reuse or redistribution, researchers must make clear to others the licence terms of this work.

Acknowledgements

Many thanks go to NERC, the Grantham Institute at Imperial College, the GDL Foundation, the Geologist's Association, the International Association of Sedimentologist's, EAGE, AGU, the University China Committee in London, the International Relations Office at Imperial College, the Earthquake Research Institute in Tokyo, Santander and the Engineering and Physical Sciences Partnered Access Fund, all of whom contributed funds to this project.

Exceedingly special thanks go to Yongsheng Zhou, Philip Benson, Brian Evans, Steve Smith and Cedric John, all of whom agreed to collaborate with me. Each of these people enabled significant parts of this thesis to come about. Yongsheng in particular went out of his way to accommodate me halfway across the world, and to him I am eternally grateful. I thank Ioannis Papanikolaou for showing us around field sites in Greece, Gerald Roberts for introducing us to the Psatha Fault and Claire Veillard, who never lost her patience with me asking a million questions about clumped isotope analyses.

Lei Zhang, Pete Rowley, Ulrich Mok, Chris Parmenter and Jens Najorka are sincerely thanked for invaluable help in the various rock mechanics, FIB-SEM and XRD laboratories. They all spent weeks of their time in the lab with me asking silly questions and being terrified by the big machines with lots of buttons. In addition to this, Lei continued to support me years after we carried out the initial experiments and enabled data to be produced which, due to my limited time in China and lower skill level, would have been entirely improbable by myself. Further thanks go to colleagues and teams at the China Earthquake Administration, the University of Portsmouth, Massachusetts Institute of Technology, the Nanoscale and Microscale Research Centre at the University of Nottingham and the Carbonate Research Group at Imperial College, who collectively enabled this thesis to come to fruition.

I would like to thank my supervisors for their help in this project. I have great respect for John Cosgrove and his love of fluidised breccias. As well as showing me seemingly obvious methods to correct stress values, I learnt more about formatting and grammar than I care to admit from Robert Zimmerman. Rebecca Bell adopted and rescued me in the last year of my project and kept believing in me when I had lost belief in the project. Without her, this final thesis would be a mere shell and I cannot thank her enough.

Further thanks go to all my friends and colleagues at Imperial College. Not only did some of them read and edit previous version of chapters or show me new laboratory methods, but their support, chats and humour really helped me through.

Last, but my no means least, I would like to specially mention Tom Phillips as my wonderful partner, for dealing with continuous commentary and varying mood levels, but, most importantly, being by my side throughout this PhD.

Table of contents

List of Figures 10

List of Tables 12

Chapter Summaries 13

Chapter I: Introduction 16

1.1 Historical theory of fault slip 16

1.2 Deformation processes 18

1.3 Fluid-flow in fault zones 19

1.4 Fault zone textures 21

1.5 Fluid-rock interactions enabling processes outside standard mechanical theory 25

1.6 Thesis rationale 27

1.7 Aims and objectives of this study 28

Chapter II: Methods 31

2.1 Structural analysis in the field 31

2.2 Rock deformation experiments 31

2.3 Microscopy 37

2.4 Isotope analyses 41

2.5 X-Ray diffraction (XRD) 45

2.6 Fluid inclusion analysis 46

Chapter III: Independent temperature constraints on precipitation within the core of the Zuccale Fault: investigating the deformation mechanisms of Elba's low-angle normal fault 47

3.1 Introduction 48

3.2 Geological setting 50

3.3 Methods 53

3.4 Results 55

3.5 Discussion 67

Chapter IV, Part I: Characterisation of fluid-fault interaction products: An example from the Gulf of Corinth, Greece 76

4.1.1 Introduction 76

4.1.2 Geological setting 79

4.1.3 Methods 81

4.1.4 Results 82

4.1.5 Discussion 90

4.1.6 Conclusions 95

Chapter IV, Part II: Implications of pre-existing veins upon future fracturing: An example from the Gulf of Corinth, Greece 96

4.2.1 Introduction 96

4.2.2 Methods 98

4.2.3 Results 100

4.2.3 Discussion 107

4.2.4 Conclusions 113

Chapter V: Precipitation in carbonate faults: a requirement to allow different slip behaviours?

5.1 Introduction 114

5.2 Methods 116

5.3 Results 118

5.4 Discussion 126

5.5 Conclusions 130

Chapter VI: Slow-slip events on limestone faults enabled by temperature-activated and fluid-dependent flow, cementation and compaction 131

6.1 Introduction 131

6.2 Data and Methods 133

6.3 Results 135

6.4 Discussion 146

6.5 Implications 153

6.6 Conclusions 154

Chapter VII: Discussion 155

7.1 Summary of main findings 155

7.2 To what extent do pre-existing textures inform upon the history of a fault? 156

7.3 Can heterogeneities produced by fluid-rock interactions permit fault motion at a sub/non-optimal orientation? 158

7.4 To what scale are heterogeneities produced by fluid-rock interactions important? 159

7.5 What is the relative importance of fault system parameters on fault zone characteristics? 160

7.6 How important are chemical effects of fluid-rock interactions compared to mechanical effects? 169

7.7 What is the relevance of the mechanisms exhibited in rock deformation experiments to the field? 171

7.8 Unresolved issues and suggested further work 173

Chapter VIII: Conclusions 175

Appendix A: Origins of carbonate-cemented tubes in Tenerife 208

Appendix B: Full images of limestone fault zones (Chapter VI) 229

Figures

Figure 1.1 Structural elements of a fault zone in crystalline rocks with fault core (FC) composed of the slip surface, breccia, gouges and cataclasites, and the associated damage zone (DZ) composed of fractured wall rock 20

Figure 1.2 Textural classification of fault rocks 21

Figure 1.3 a) Thin section examples of crackle breccia, mosaic breccia, and chaotic breccia from the Dent Fault Zone, NW England. b) Subdivision of fault breccias by percentage of large clasts. From Woodcock and Mort (2008) 23

Figure 1.4 The interplay between structure, mechanics and fluid-flow 24

Figure 1.5 Example of the variation of the value of σ_1 needed to cause failure, as a function of the angle β between the normal to the plane of weakness and the maximum principal stress 25

Figure 1.6 The variation of calcite solubility with temperature 28

Figure 2.1 Paterson triaxial apparatus setup at Massachusetts Institute of Technology 33

Figure 2.2 Schematic diagram of Sanchez triaxial cell at the University of Portsmouth 34

Figure 2.3 Schematic diagram of sample assembly within the servo-controlled gas medium triaxial deformation apparatus at CEA 36

Figure 2.4 Step-by-step guide for using a FIB-SEM to locate, cut, extract and thin a desired sample 40

Figure 2.5 The oxygen isotope composition of calcite precipitated at isotopic equilibrium from water of the O isotope composition shown on the *X* axis and at the temperature shown on the *Y* axis 43

Figure 2.6 Basic geometry of an X-Ray diffractor 46

Figure 2.7 Example of a fluid inclusion (within a quartz vein) 46

Figure 3.1 Geological setting of the Zuccale and Gubbio Fault's 51

Figure 3.2 (a) Geological sketch map of thrust complexes in southeastern Elba, (b) cross section from central to eastern Elba Island 53

Figure 3.3 The Zuccale Fault exposure at Punta di Zuccale 55

Figure 3.4 The foliated carbonate-rich fault core at Punta di Zuccale 56

Figure 3.5 Veins within the foliated cataclasite in the roof above the calcite ultramylonite 58

Figure 3.6 The Gubbio Fault: a classic high-angle normal fault in the Italian Apennines 59

Figure 3.7 Samples taken from the Gubbio Fault 60

Figure 3.8 Optical microscopy of the carbonate-rich samples within the Zuccale Fault core 61

Figure 3.9 XRD diffractogram from the calcite-ultramylonite layers and the calcite veins in the roof of the fault core 63

Figure 3.10 Stable isotope results from the Zuccale Fault and Gubbio Fault 64

Figure 3.11 Fluid inclusion analyses from the dolomite veins and calcite veins in the foliated cataclasite layer of the Zuccale Fault 66

Figure 3.12 Weakening processes due to placement of the Porto Azzuro pluton which enable slip 73

Figure 4.1.1 The mechanical effects of fluids 77

Figure 4.1.2 Geological setting and location Gulf of Corinth 80

Figure 4.1.3 The Psatha Fault 83

Figure 4.1.4 Field photographs from along the Psatha Fault 84

Figure 4.1.5 The three main breccias on the fault; breccia embedded within the fault scarp (FB), a thin overprinted breccia (TOB) and a massive overprinting breccia (MOB) 85

Figure 4.1.6 Thin section scans of the three main breccias within the Psatha Fault zone 86

Figure 4.1.7 Microscope images of the different crystal clusters within the breccias 89

Figure 4.1.8 Stable isotope results from the different breccias on the Psatha Fault 90

Figure 4.1.9 Progressive uplift of the Psatha Fault 94

Figure 4.2.1 Psatha Fault host rock used in experiments 99

Figure 4.2.2 Stress-strain graph from Psatha Fault host rock uniaxial experiment 100

Figure 4.2.3 Resultant fracture within the core following uniaxial deformation of Psatha Fault host rock 101

Figure 4.2.4 Scanned thin sections showing vein-fracture interactions after uniaxial deformation of Psatha Fault host rock 103

Figure 4.2.5 Micrographs of vein-fracture interactions after uniaxial deformation 104

Figure 4.2.6 Stress-strain curves following triaxial deformation of Psatha Fault host rock 106

Figure 4.2.7 Schematic cartoon showing the evolution of veins throughout subsequent deformation events 110

Figure 4.2.8 The relationships between pre-existing structures and subsequent faulting found on a field scale also exist on a much smaller scale 111

Figure 5.1 Comparative stress-strain data between C2, C4, C5 and C7 119

Figure 5.2 Permeability vs time graphs during deformation of bare-interface calcite faults 120

Figure 5.3 Comparative data of the duration and degree of stress drop following peak stress between C4, C5 and C6 122

Figure 5.4 Scanned thin sections of all deformed Carrara marble samples 123

Figure 5.5 Micrographs of bare-interface calcite fault samples deformed under a variety of conditions 124

Figure 6.1 Coefficient of friction-shear displacement plots illustrating the characteristic mechanical behaviour at each temperature for limestone samples 139

Figure 6.2 Experiments utilising gabbro host rock, chert gouge, no pore fluid pressure and multiple temperature steps 140

Figure 6.3 Variation of the (a) *a*-*b* parameter, (b) μ_{pk} and (c) μ_{pk}-μ_f with temperature 141

Figure 6.4 SEM photographs of deformed limestone gouge 143

Figure 6.5 FEG-TEM performed on limestone samples deformed 144

Figure 6.6 XRD spectra from gouges deformed at 30°C, 70°C, 130°C and 220°C 145

Figure 6.7 The solubility of calcite, the duration of the slip-weakening phases and the duration of the stress drops of the subsequent oscillations all have an inverse relationship with temperature 152

Tables

Table 3.1 Results from clumped isotope analyses of the Zuccale Fault core 65

Table 5.1 Summary of experiments performed in this study on slip on bare-interface calcite faults 117

Table 6.1 Experiments performed at the China Earthquake Administration on gouge-filled faults and key parameters obtained 138

Table 7.1 Comparison table of values of μ of fault surfaces from experiments carried out in this study 165

Chapter Summaries

Chapter I: Introduction

This chapter gives a background to the study and overview of the research problem to be addressed, including a brief overview of the frictional properties of faults, deformation processes, fluid-flow in the fault system, and the manifestations of water-rock interactions in fault zones. I also outline the aims and objectives of the study.

Chapter II: Methods

This chapter outlines the various methodologies which are used in this project, including (i) structural analysis in the field; (ii) rock deformation experiments; (iii) microscopy; optical, cathodoluminescence (CL), scanning electron microscopy (SEM; also including focussed ion beam scanning electron microscopy (FIB-SEM)) and transmitted electron microscopy (TEM), (iv) isotope analyses: stable and clumped; (v) Fluid inclusion analysis and; (vi) X-Ray Diffraction (XRD).

Chapter III: Independent temperature constraints on precipitation within the core of the Zuccale Fault: investigating the deformation mechanisms of Elba's low-angle normal fault

This chapter provides constraints on the fluid-rock interaction within the core of the Zuccale Fault, a low angle normal fault (LANF) on the Isle of Elba, Italy. The Zuccale Fault is one of high controversy, given its exceptionally low angle for a normal fault regime. This work, combining optical microscopy, SEM, XRD, fluid inclusion analysis and stable and clumped isotope analyses, constrains the textures and precipitation temperature in the fault core, providing quantitative data on fluid-rock interactions. The results indicate that a combination of mechanical changes, from the emplacement of the pluton, with chemical changes not addressed in standard Andersonian rock mechanical theory may be the reasoning behind the evolution of the Zuccale Fault and notably the distinct weakness of the fault core.

Chapter IV:

Part I: Characterisation of fluid-fault interaction products: An example from the Gulf of Corinth, Greece

Part I examines the fluid-fault interaction within the highly altered and complex Psatha Fault, Gulf of Corinth, Greece, locally associated with extensive calcite cementation. A study of the fault-related diagenetic alteration through structural and microscopic analysis combined with a stable isotope study aims to relate deformation-fluid-flow behaviour to the internal architecture of the fault zone. The results indicate that the Psatha Fault underwent deformation both above and below the water table. Carbon and oxygen stable isotope geochemistry reveal that meteoric water dominated the fluid-flow. In addition, the variation in these isotopic signals between different cements are indicative of the changing influence of water temperature and/or composition fluctuations during fault zone evolution.

Part II: Implications of pre-existing veins upon future fracturing: An example from the Gulf of Corinth, Greece

Part II explores (i) how fractures may propagate in fault rock, which has a complex deformation-fluid-flow history and (ii) how slip behaviour may alter in a heavily altered rock. In collaboration with the University of Portsmouth (UoP), cores from the heavily veined and altered Psatha Fault, Gulf of Corinth, Greece were fractured in an Instron uniaxial and a Sanchez triaxial cell. Subsequent optical microscopic analysis found that fracture propagation was characterised by reactivation within the most continuous untwinned crystalline veins optimally oriented to the stress field and cross-cut the older heavily twinned calcite crystals. This indicates that distinct, pre-existing structures can form the focus of subsequent rupture propagation where stress fields can concentrate on a microscale. Further experiments which tested the effect of healing on a pre-existing fracture illustrated that the effect of fault movement, effectively smoothing the fault was of greater importance that any interseismic precipitation.

Chapter V: Precipitation in carbonate faults: a requirement to allow different slip behaviours?

This chapter details a set of rock deformation experiments undertaken upon bare-interface calcite faults, in collaboration with Massachusetts Institute of Technology (MIT). Rock deformation experiments were undertaken in a Paterson gas medium triaxial apparatus,

followed by an optical microscopy study, to provide initial constraints on the effect of temperature and pore fluid pressure fluid type upon fault healing and sealing. The results show long duration slip-weakening is induced on a bare-interface calcite fault following healing at 150ºC in water-saturated conditions. This treatment also resulted in a shear strength increase and a dramatic reduction in permeability, even during sliding, compared to a fault saturated in non-reactive argon. Calcite faults hydrothermally treated at temperatures of 450ºC exhibited purely stick-slip behaviour. These behaviours are confirmed by optical microscopy of the experimental fault zones. These results indicate that cementation in fault zones can have a significant influence upon fault slip behaviour, fault strength and permeability.

Chapter VI: Slow-slip events on limestone faults enabled by temperature-activated and fluid-dependent flow, cementation and compaction

This chapter develops the concepts explored in Chapter VI, exploring the possibility that cementation, cohesion and compaction processes can alter the strength and sliding behaviour of a fault zone. A suite of experiments, undertaken in collaboration with the China Earthquake Administration (CEA), investigated the contribution that incremental lithification within a carbonate fault zone makes in producing an aseismic-seismic transition. The results from my hold-slide experiments on saturated limestone gouges at different temperatures suggest that, within carbonate-rich zones, slow-slip type behaviour is due to the competition between dilatant granular flow, cementation and compaction. Between 50ºC and 130ºC, long-duration instabilities (up to 33 sec) are accompanied by incremental grain aggregation. Above this temperature, stick-slip type behaviour is observed, alongside increasing strength with increasing temperature. Such changes attributed to thermally-driven cementation and compaction leading to lithification of sediment could have significant implications for SSEs in the field.

Chapter VII: **Discussion**

In this chapter, the main findings of this research are summarised, and the implications discussed. The original questions posed in Chapter I are answered. Possible routes for further work are discussed, following the insight gained in this work, in another project or with additional funding.

Chapter VIII: **Conclusions**

The key conclusions from this work are summarised.

Chapter I: Introduction

1.1 Historical theory of fault slip

A fault is a planar fracture accumulating displacement of two adjacent blocks of crust sliding past one another (Fossen, 2010; Price and Cosgrove, 1990). Over multiple cycles of deformation and displacement along the fault, the blocks themselves become deformed. Drilling and field studies have revealed that many faults contain a principal slip zone, PSZ, within the fault zone which is only a few mm wide (Sibson, 1986b, 2003), in which the bulk of the deformation is localised. The fault core, which is a few to tens of metres wide, accommodates more distributed deformation (Sibson, 1977); see Fig. 1.1. With such thin, localised, and persistent weaknesses in the crust, tectonic loading localises on these faults, which accommodate the strain. Faults accumulate this tectonic loading as elastic energy, and when the external applied stress exceeds the shear strength of the fault, the stored energy will be released, and the fault will move.

An understanding of the frictional processes along faults is fundamental for understanding earthquakes. The strength of the contact between the two blocks, i.e., the strength of the fault, defines how much stress can build up before an earthquake will occur. This can be defined by the coefficient of sliding friction, μ, the ratio of shear to normal stress acting on the plane:

$$\mu = \tau/\sigma_n \tag{1.1}$$

This parameter was first defined by da Vinci and Amontons (but also see Scholz (2002)). Typical coefficients of sliding friction lie in the range 0.6–0.85 (Byerlee, 1978), hereafter known as the 'Byerlee range'. This law is obeyed to first degree; however, laboratory experiments demonstrate that μ tends to decrease with elevated normal stresses, and is thus better defined by a Coulomb-Mohr expression:

$$\tau = S_0 + \mu\sigma_n \tag{1.2}$$

where S_0 is the cohesion of the fault surface, or of the gouge filled fault (Paterson and Wong, 2005). This is the criterion for slippage along a plane of weakness and is described in detail by the Jaeger's Plane-of-Weakness model (JPW) (Jaeger, 1960).

In the field, there will also be a pore fluid pressure acting on the pore walls. Therefore the key parameter is actually the effective normal stress (Hubbert and Rubey, 1959; Nur and Byerlee, 1971), which is defined as:

$$\sigma_n^{eff} = \sigma_n - P_f \tag{1.3}$$

Combined, this gives:

$$\tau = S_0 + \mu(\sigma_n - P_f) \tag{1.4}$$

The interseismic period, the period of time between seismic events, allows the fault strength to increase due to further cohesive strengthening with time. This time-dependent nature of friction is described by a rate-and state-variable friction law (Dieterich, 1972, 1978; Ruina, 1983); static friction, μ_s, is found to increase logarithmically with the hold time, t (Dieterich, 1972). In the immediate build-up to an earthquake, i.e., the pre-seismic period, wherein slip accelerates and an instability is created, the dynamic friction coefficient, μ_d, is dependent on sliding velocity. When the sliding velocity increases, μ_d increases, which is represented by the parameter a (Scholz, 1998). Subsequent to this instantaneous increase in μ_d, friction evolves to a steady state over a slip distance D_c, represented by the parameter b (Dieterich, 1979; Ruina, 1983; Scholz, 1998). The difference between these parameters, (a-b), defines whether the fault is stable or unstable. If (a-b) < 0, the fault is velocity-weakening, i.e., unstable, and will exhibit earthquake stick-slip type behaviour (Brace and Byerlee, 1966; Scholz, 1998). If (a-b) > 0, the fault is velocity-strengthening and will show stable sliding, creeping behaviour (Scholz, 1998). Thus, the coefficient of dynamic friction is as follows:

$$\mu_d = \mu_* + aln\left(\frac{v}{v_*}\right) + bln(\frac{v_*\theta}{D_c}) \tag{1.5}$$

where $\mu*$ is the steady-state slip coefficient of friction at reference velocity v*, θ is a state variable with dimensions of time, a and b are the dimensionless empirical parameters, and D_c is the critical slip distance.

If an earthquake were to occur in a velocity-weakening area of the crust, but then propagate into a velocity-strengthening area, the stress would increase, and the propagation would be slowed or even stopped (Scholz, 1998). The frictional properties of a fault can depend on a number of properties, including temperature (Blanpied et al., 1991; Blanpied et al., 1998; Blanpied et al., 1995; Karner et al., 1997; Shimamoto, 1986; Stesky, 1978; Stesky et al., 1974), the presence of fluids (Blanpied et al., 1995; Brace, 1972; He et al., 2007; Karner et al., 1997;

Moore and Lockner, 2004; Morrow et al., 2000; Olsen et al., 1998) and the roughness of the fault surface (Barton, 1976; Byerlee, 1967; Fang and Dunham, 2013; Harbord et al., 2017). Thus, the evolution of a fault's frictional behaviour over the course of the seismic cycle defines the way that a fault will behave in the next cycle.

1.2 Deformation processes

Subduction zone earthquakes typically nucleate between depths of 10-40 km (Hyndman et al., 1997), and continental earthquakes between 5-15 km (Scholz, 1988). The upper 15 km of the crust typically exhibits velocity-weakening behaviour, where there is low temperature and confining pressure (Marone and Scholz, 1988). Deformation mechanisms within the velocity-weakening regime including grain fracture, grain rotation, and grain boundary sliding (Sibson, 1977; Sibson, 1986b), which make up the overall progressive fracturing and comminution of existing fault rock, i.e., cataclasis (Blenkinsop, 1991; Engelder, 1974).

Brittle-type mechanisms can only occur where there is limited pore space, and where deformation cannot be distributed, i.e., in lithified rock (Aydin, 1978; Fossen, 2010; Sibson, 1977). In fact, where sediments are not lithified in the very top of the crust, grains can accommodate grain boundary sliding and thus behave plastically on a mesoscale, i.e., moving as a function of shear localisation and density changes (Frye and Marone, 2002) rather than grain fracture or crushing. This sliding of grains is referred to as granular flow, and it exhibits the aforementioned stable, velocity-strengthening type behaviour (Hatano, 2007; Marone et al., 1990). The lower limit of seismogenesis corresponds to a transition from velocity-weakening to velocity-strengthening behaviour (Marone and Saffer, 2007) with the increase of temperature with depth inducing the onset of crystal plasticity (Chen et al., 2013; Scholz, 1998; Tse and Rice, 1986).

Clearly, the manner in which a fault zone deforms varies according to numerous factors. As well as the apparently distinct regions of velocity-weakening and velocity-strengthening behaviours, there are more intricate mechanisms at play. For example, in wider, more mature fault zones, cataclastic flow can occur: a moderate type of cataclasis where crushed grains flow during shearing, leading to ductile-like structures at the mesoscale (Fossen, 2010). Such a process is one example of how, over time, deformation mechanisms within fault zones can change, as previous deformation imparts new structure and changes rock properties. Also, in addition to the typical 'mechanical' deformation mechanisms in fault zones, there are numerous chemical deformation mechanisms at play, especially in reactive rocks such as carbonates. A

notable mechanism is pressure solution, a deformation mechanism that involves dissolution of minerals at grain-to-grain contacts into an aqueous pore fluid in areas of relatively high stress and deposition in regions of relatively low stress (Rutter, 1976, 1983; Weyl, 1959). This deformation is much less localised than that which is achieved by fracturing (Sibson, 2003).

There are also a number of further processes and complexities. For example, all of the aforementioned processes refer to the time periods on either side of the co-seismic moment. Notably, however, at the moment of energy release, the processes can be quite different; frictional values remain in the Byerlee range (0.6-0.85) until slip rates approach seismic slip rates (~1 m/s), at which point a dramatic decrease in frictional sliding coefficient occurs, to values of nearing zero, known as dynamic weakening, due to mechanical and thermally-activated chemical reactions on the fault at such high speeds (Di Toro et al., 2004; Han et al., 2007; Hirose and Bystricky, 2007). Furthermore, the coefficient of friction between fault surfaces is often determined to be within Byerlee's range, regardless of fault texture and composition (Numelin et al., 2007). However, some clay minerals have been found to have a coefficient of sliding friction of ~0.2 (Morrow et al., 2000), and exhibit velocity-strengthening rather than velocity-weakening behaviour (Saffer et al., 2001; Schleicher et al., 2010, 2012). Variations in the coefficient of friction can also be induced by fault roughness (Barton, 1976; Byerlee, 1978), and recent experiments have shown that changing fault roughness may also alter how the fault slips (Harbord et al., 2017). These additional examples of how multiple factors can significantly alter the frictional behaviour of a fault, along with the changes induced by temperature and the presence of fluids, illustrate that the frictional behaviour of faults is a complex issue.

1.3 Fluid-flow in fault zones

The process of brittle failure in the crust is generally viewed as a mechanical system; there is a critical stress to overcome, at which point sliding will occur on a pre-existing fault. This idea is consistent with the mechanical role of fluids in the earthquake system; the presence of water 'enriching' the elastic rebound model (Sornette, 1999). The dilatancy/fluid-diffusion model for shallow earthquakes describes a dilatational response of the crust to the rising tectonic shear stress preceding the earthquake, accompanied by the opening of extension fractures and a fluid pressure decrease (Sibson et al., 1975; Sibson, 1981; Stuart, 1974). This fracturing and dilation increases the porosity and permeability in the fault zone, permitting a slow migration of fluid from the surrounding crust due to the gradient flux, increasing the pore fluid pressure, P_P,

effectively reducing the stress equally in all directions, and thus facilitating further rock fracturing (Hausegger et al., 2010). This effect is graphically illustrated by Mohr's Circle and failure envelopes in the presence of pore fluid pressure, and in additional detail by Sibson et al. (1975), Sornette (1999), and Streit & Hillis (2004). As well as water flowing into fractures produced in a fault zone prior to rupture and increasing the pore fluid pressure (a mechanical process), the final failure is propagated not only by the mechanical process of shear stress overcoming frictional resistance, but also by chemically activated subcritical crack growth processes, inclusive of stress corrosion and dissolution (Sornette, 1999). As detailed previously, when the shear stress is greater than the frictional resistance of the fault, slip occurs. Following an earthquake, the fault surface can act as a passageway for fluid-flow, with fractures and irregularities serving as channels for the flow (Sibson et al., 1975). Sibson et al. (1975) suggest that faulting associated with shallow earthquakes acts as a pumping mechanism, redistributing fluids within the crust. During the interseismic period, the frictional fault strength will increase over time whilst in static contact, i.e., increasing the cohesive strength of the fault (Sibson, 2002) but the presence of fluids in the fault zone can lead to sealing and healing of cracks (Atkinson, 1984), which can further increase the frictional fault strength (Sibson, 1992). Flow outwards can then be prevented by a seal of mineral precipitation (Blanpied et al., 1992; Byerlee, 1993; Faulkner and Rutter, 2001). Such reactions between minerals and fluids have been identified as being relevant to the earthquake system (Brace, 1972), but they are not included in standard rock mechanical theory. Their relevance, comparative to mechanical effects, needs futher investigation.

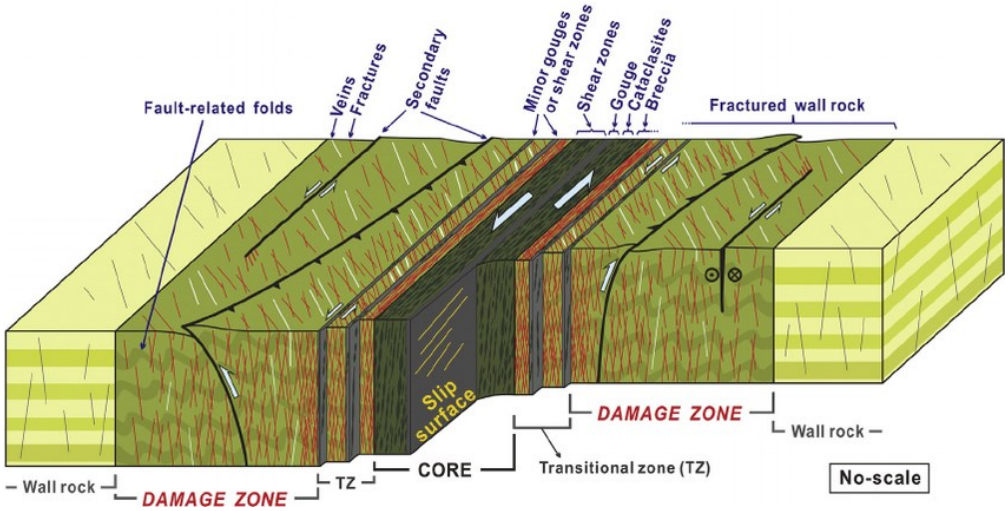
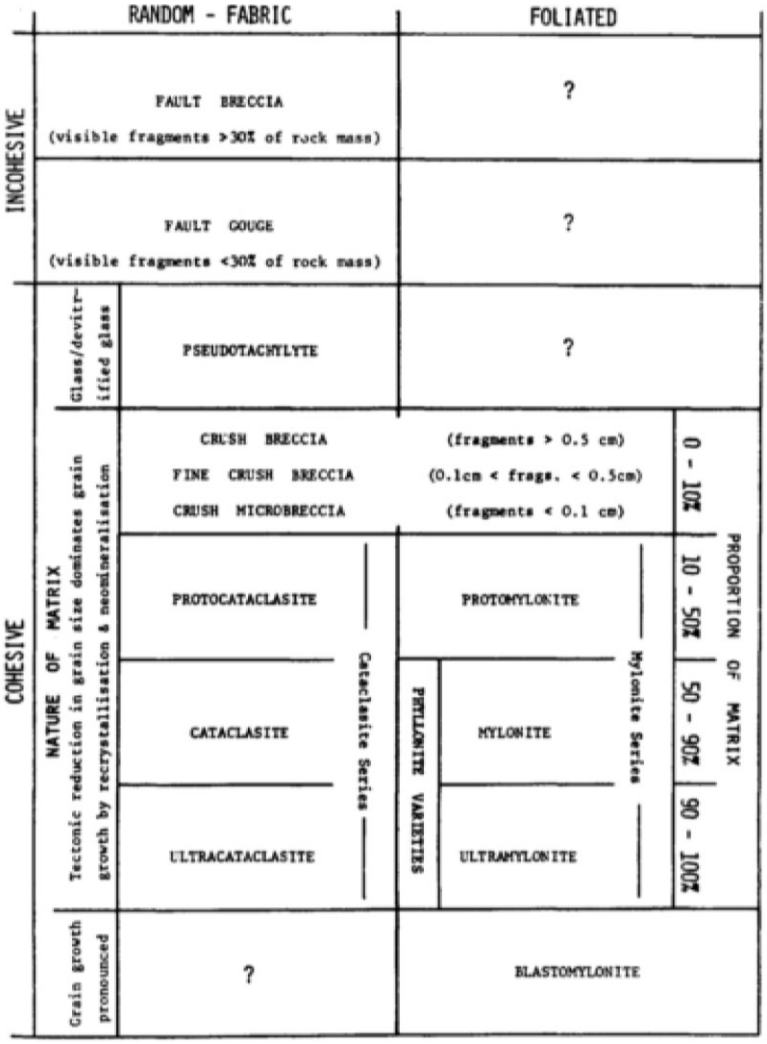


Figure 1.1 Structural elements of a fault zone in crystalline rocks with fault core (FC) composed of the slip surface, breccia, gouges, and cataclasites, and the associated damage zone (DZ) composed of fractured wall rock (from Choi et al. (2016))



		non-foliated	foliated
>30% large clasts >2 mm	75-100% large clasts (>2 mm)	fault breccia: crackle breccia	
	60-75% large clasts (>2 mm)	fault breccia: mosaic breccia	
	30-60% large clasts (>2 mm)	fault breccia: chaotic breccia	
<30% large clasts >2 mm	incohesive[1]	**fault gouge**	
	cohesive: glass or devitrified glass	**pseudotachylyte**	
	cohesive: 0-50% matrix (<0.1 mm)	**protocataclasite**	**protomylonite**
	cohesive: 50-90% matrix (<0.1 mm)	**(meso)cataclasite**	**(meso)mylonite**
	cohesive: 90-100% matrix (<0.1 mm)	**ultracataclasite**	**ultramylonite**
	cohesive: pronounced grain growth		**blastomylonite**[2]

[1] incohesive at present outcrop

[2] some blastomylonites have >30% large porphyroclasts

Figure 1.2 Textural classification of fault rocks (from Sibson (1977)) and fault rock classification from Woodcock & Mort (2008).

1.4 Fault zone textures

Characteristic fault rocks and textures are formed in areas of high strains by progressive fracturing and comminution of existing rock (Engelder, 1974). Early fracturing is overprinted by the formation of gouge and breccias after the fragmented fault zone is infiltrated by fluids, permitting precipitation of minerals such as calcite, and cementing the rock (the dilatational strain in the fault zone permits breccia formation (Woodcock and Mort, 2008)). The structural elements of a fault zone are shown in Fig. 1.1. A cataclasite is, generally speaking, a non-foliated cohesive fault rock (see Fig. 1.2). Within the top 4 km of the crust, breccias, gouges and veins are common, illustrative of the brittle regime. Veins are also common features within a fault zone, whereby minerals carried by an aqueous solution are deposited through

precipitation, often quickly during deformation by precipitation of minerals within incipient fractures or progressively in open spaces. Sibson (1977) defined a conceptual model of a major fault zone, and the features associated with it (Fig. 1.2). Breccias are rock textures consisting of angular rock fragments from pre-existing rock that are bounded by cement or fine-grained matrix. Fault breccias occur on faults with increasing dilation through three mechanical processes: (i) attritional wear (frictional wear and grain cataclasis associated with major shear separation); (ii) distributed crushing (microcracking and microfaulting over a broad area to produce a structureless microbreccia), and; (iii) implosion brecciation (when cavities open during rapid slip allowing wall rock to infill the cavity, often due to increased pore fluid pressures which leads to extensive vein networks) (Sibson, 1986a). In Woodcock and Mort (2008), fault breccia is defined as having at least 30% of its volume being clasts larger than 2 mm in diameter and can be further subdivided into the crackle-mosaic-chaotic breccia spectrum approximately corresponding to large (>2 mm) clast percentages of 75% and 60% (Fig. 1.3). Fault gouges, however, are incohesive rocks composed <30% of large clasts (>2mm in size) and may be non-foliated (random-fabric orientation) or foliated (Woodcock and Mort, 2008). Breccia and gouge are overall differentiated by grain size distribution and width within the fault zone; the grain-size distribution is governed by a power law (Storti et al., 2003) (the fracturing process of the grains controlled by contact geometry (Aydin, 1978)) and their width within fault zones has a relationship with comminution of fault rocks (Billi, 2005), which in turn is dependent upon the amount of fault displacement (Amitrano and Schmittbuhl, 2002). The fault rocks progressively change across a fault zone (Fig. 1.1).

The formation of breccias and gouges is progressive, and leads to permeability differences across the fault core, due to changes in porosity and particle size distribution that characterise the different evolutionary stages (Hickman et al., 1995; Parry, 1998; Storti et al., 2003). Fluid flow through fault breccias often induces cementation (Woodcock and Mort, 2008). Over time, fault zones are characterised by cemented breccias, which show several periods of displacement on the fault; cycles of fracturing and crushing followed by cementation, healing processes and mineralisation (Sibson et al., 1975). Thus, breccias can alter the permeability of a fault zone: some studies believe that they can act as fluid barriers, altering the concentrations of fluid pressure within a fault zone (decrease permeability and porosity due to the high degree of comminution which inhibits flow (e.g., Tămaș and Milėsi, 2002)), some argue that they act to increase permeability (e.g., Voorn et al., 2015), and some argue for transient permeability (Melosh et al., 2016; Woodcock et al., 2007), which is more in keeping with the constant

evolution of fault zones. Clearly, the presence of cements can affect fault zone properties, but the discrepancies between different studies as to how their presence affects fault system properties highlights a gap in knowledge. In addition, the original rock properties are continuously modified through fluid-rock interactions, which then influences the fluid-flow and deformation mechanisms in the next seismic cycle (Fig 1.4). Thus, a detailed study of cemented features should provide constrains upon the history of a fault. In a sense, fault zone rocks can be thought of as low-to medium-grade metamorphic rocks (Faulkner et al., 2010).

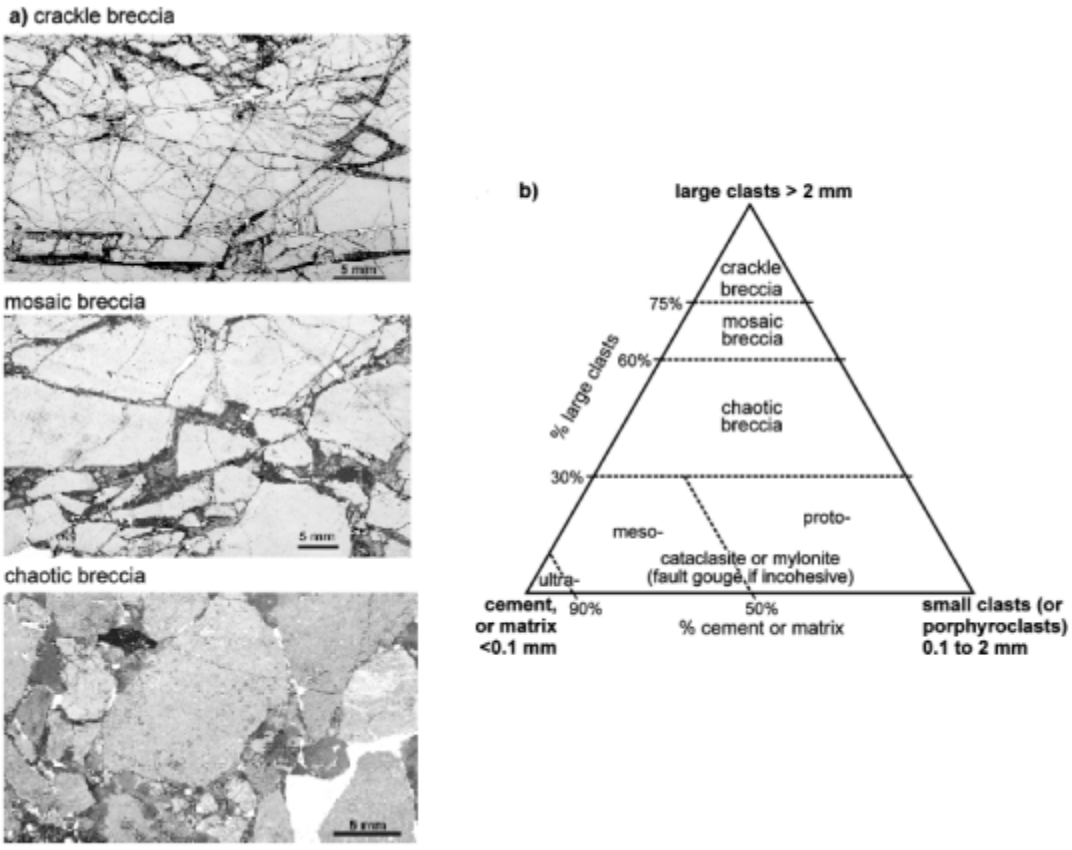


Figure 1.3 a) Thin section examples of crackle breccia, mosaic breccia, and chaotic breccia from the Dent Fault Zone, NW England. b) Subdivision of fault breccias by percentage of large clasts. From Woodcock and Mort (2008).

Cementation textures in a fault zone can also be produced by processes that are not directly linked to the movement of the fault. Numerous processes can be responsible for cementation within fault zones, from the pressure solution associated with fault movement, to karstification (Ford and Williams, 1989) and cementation via biological means. All of these processes can induce permeability, porosity, and strength alterations to a fault or sedimentary interval

(Archie, 1950; Schön, 2015), which in turn will have implications for reservoir characteristics and deformation in the next seismic cycle. Understanding the processes of feature formation is important in order to further understand the complex fluid-rock interactions on faults, and how these interactions influence the earthquake cycle and fault zone evolution. Furthermore, such features (breccias, gouges, veins and fractures) also exist on multiple scales. Precipitation can occur on a grain scale (via pressure solution but can also form extensive vein networks at the fault scale. Studies have shown that such pre-existing architecture can characterise fault reactivation and influence subsequent faulting patterns (Phillips et al., 2016). However, aside from studies showing the interplays between pre-existing fluid-rock interaction features at their relative scale (e.g. veins against other veins; see Virgo et al., 2013) how smaller scale may influence macroscale propagation appears less investigated. Knowing how smaller scale pre-existing structures may influence macroscale fracturing is essential to understand possible future rupture properties and fault zone evolution.

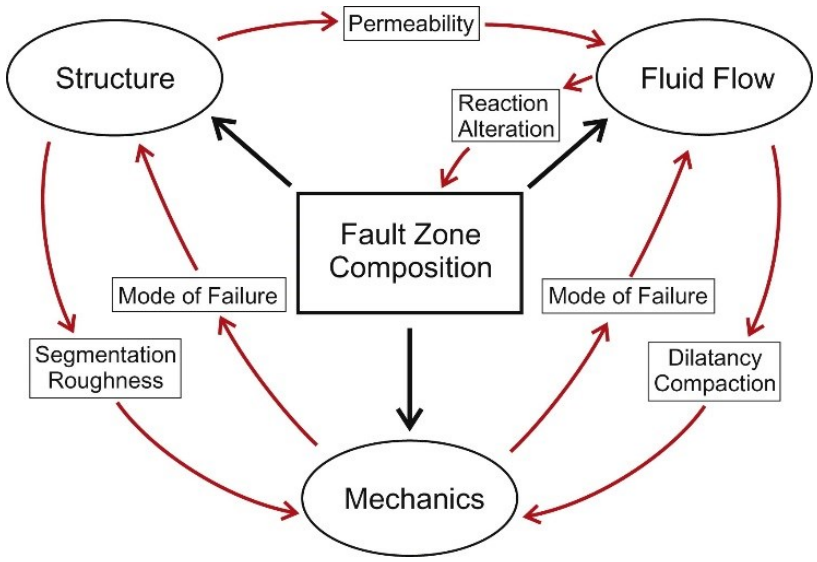


Figure 1.4 The interplay between structure, mechanics and fluid-flow (Faulkner et al., 2010).

An example of the variation of the value of σ_1 needed to cause failure along a pre-existing weakness within a rock mass is shown in Fig. 1.5. The value of σ_1 required to cause failure tends to infinity as $\beta \rightarrow \pi/2$ or $\beta \rightarrow \tan{-1}\ \mu_w = \varphi_w$ (where φ_w is the angle of internal friction of the weakness). The minimum value of σ_1 that failure will occur at is given by:

$$\sigma_1^{min} = \sigma_3 + 2(S_w + \mu_w\sigma_3)([1 + \mu_w^2)^{\frac{1}{2}} + \mu_w \quad (1.6)$$

If the planes of weakness are oriented from the direction of maximum principal stress by a different angle (other than β_w), failure can still occur at a value of σ_1 greater than σ_1^{min}. Failure can also occur on a plane other than the pre-existing planes of weakness (usually a *fault*), as long as the Coulomb failure criterion (1.2) is satisfied.

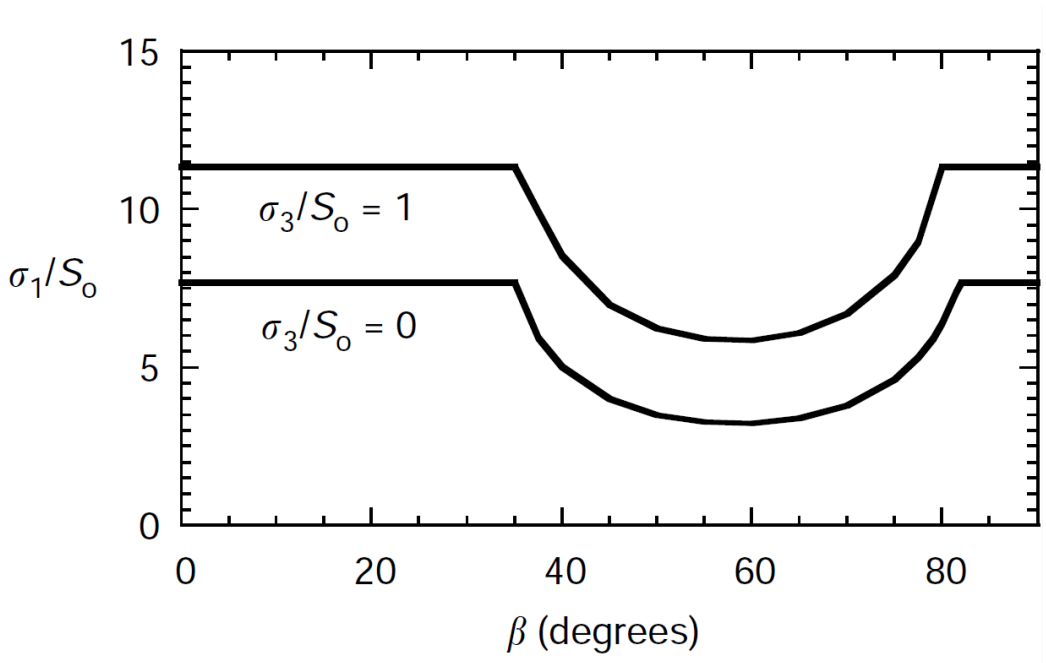


Figure 1.5 Example of the variation of the value of σ_1 needed to cause failure, as a function of the angle β between the normal to the plane of weakness and the maximum principal stress. This example is for the case $\mu_w = 0.5$, $\mu_0 = 0.7$, $S_0 = 2S_w$ (from Jaeger et al. (2009)).

1.5 Fluid-rock interactions enabling processes outside standard mechanical theory

Standard Andersonian rock mechanical theory (Anderson, 1905), which discusses the fundamental relations between the three basic fault types and the orientation of the causative stress tensor relative to the Earth's surface, suggests that normal faults should not form at dips

< ~50◦, and, if rotated to below 30°, failure should then occur by formation of new higher-angle normal faults. However, there are many examples of low-angle normal faults (LANFs) worldwide (Collettini and Barchi, 2002; Haines et al., 2010; Hayman et al., 2003; Numelin et al., 2007; Wernicke, 1995), and thus the conditions which enable their existence need to be investigated. Notably, the impact of fluid-rock interactions on rock physical properties (i.e., chemical interactions) lie outside standard Andersonian rock mechanical theory and thus how they may enable LANFs should be investigated. An increased pore fluid pressure reduces the effective stress upon a fault and permits slip at a lower stress. However, if chemical processes associated with fluid-rock interactions were to create a scenario where the fault surface has a very low coefficient of friction of far below standard Byerlee values, slip could be enabled at a non-optimal angle (e.g., Numelin et al., 2007). This could also highlight the relative importance of chemical processes vs mechanical in a fault zone.

In a similar manner, the discovery of SSEs (slow slip earthquakes) in 1996 (Linde et al., 1996) are a conundrum. These transient slip events involve displacement on a fault that occurs over hours to months rather than seconds (Linde et al., 1996; Saffer and Wallace, 2015). The range of fault slip behaviour ranges from stick-slip type fault slip (velocity-weakening; see section 1.1), associated with destructive earthquakes, to aseismic creep (velocity-strengthening), the motion along faults without generating seismic waves (Ide et al., 2007; Linde et al., 1996; Peng and Gomberg, 2010). Slow-slip lies inbetween these two end members of fault slip. Unfortunately, the physical conditions that enable this spectrum of fault slip behaviour are still poorly understood. Initially, different temperature regimes were suggested to account for these variations in fault slip behaviour (Blanpied et al., 1995); however the discovery of SSEs at various subduction margins that do not share a common temperature window led to the role of temperature being largely discounted (Saffer and Wallace, 2015). Other hypotheses put forward to explain the variations in fault slip behaviours focus on the role of fluid pressure (Kodaira et al., 2004), and, although there is evidence for overpressured fluids where SSEs have been found (Bell et al., 2010), their precise role has not been quantified. The existence of SSEs demonstrates a need to investigate possible mechanisms that may allow such variations in fault slip behaviour. As chemical processes within fault zones are not included in standard Andersonian rock mechanical theory (Axen and Karner, 2004), their effects may contribute to the generation of such enigmatic events. Given the range of fault system parameters (e.g., temperature, pore fluid) which have previously been suggested to account for

controlling fault slip behaviour (Blanpied et al., 1995; Kodaira et al., 2004), different parameters should be investigated in a controlled setting.

1.6 Thesis rationale

The basic concepts of fault friction and the features produced in fault zones are well known. However, the formation mechanisms, and the manner in which the processes of cementation and associated features affect the physical rock properties as the fault zone continues to evolve, remain poorly understood. Understanding these processes has seemed to be essentially a characterisation issue (e.g., Woodcock et al., 2006), until recently. The debate on the mechanisms permitting enigmatic field events, such as slip on LANFs, and SSEs, as well as recent studies highlighting complex interactions with pre-existing structures over various scales (Shaw, 2005), has highlighted the importance of determining how fluids have interacted with the rock mass over various timescales. Chemical alteration in fault zones requires more attention, in order to better understand fault zone history, evolution, and fluid-flow.

Carbonate-bearing faults are important structures for fluid distribution in the brittle upper crust, because calcite is a highly reactive compound at ambient conditions, with even slightly acidic fluids, and so flaws and fractures can be easily exploited. This reactivity leads to fractures frequently being cemented by carbonate. The fractures in carbonate rocks commonly control much or all of the permeability (Sibson, 1996), and so any changes in permeability should characterise the cementation present. The ability of sedimentary rocks to serve as reservoirs is significantly affected by how the carbonate cements affect the porosity and permeability (Jackson, 2012). In addition, the solubility of calcite in water (Fig. 1.6) varies inversely with temperature (and little with pressure), which is the opposite to that of the majority of compounds (Stumm and Morgan, 1981). Carbonates are also important because they host a large fraction of the world's hydrocarbon reservoirs, and they are also platforms to many seismically active areas; for example, the Lazio-Abruzzo carbonate platform was host to the L'Aquila 2009 earthquake (Anzidei et al., 2009). Overall, their study is an ideal tool to investigate cement formation mechanisms and how the processes of cementation and the features produced may affect fault zone properties.

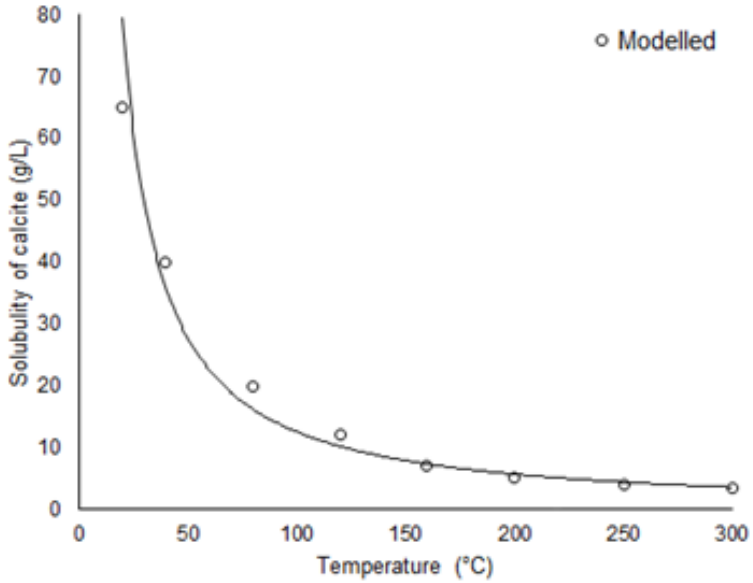


Figure 1.6 The variation of calcite solubility with temperature (modelled using Geochemists workbench)

1.7 Aims and objectives of this study

The aim of this research is to (i) utilise the physical manifestations of fluid-flow fro fault zones, in the form of carbonate cementation, in order to constrain fluid-rock interactions over time, and (ii) to discover the effect of these interactions on rock physical properties by replicating the processes in the laboratory. Understanding the interplay between fluids and fractures, both chemically and mechanically, and the influence on fault zone strength, permeability, and overall structural evolution, is fundamental to understanding fault zone properties and slip behaviour, as well as reservoir longevity.

Due to the complexity of the fluid-fracturing system, a multidisciplinary approach of structural analysis, microscopy (optical, cathodoluminescence, SEM and TEM), stable and clumped isotope analyses, and rock deformation experiments, are combined to investigate the processes at hand. A multi-disciplinary study on features cemented by carbonate helps to discriminate formation mechanisms and understand the changes in rock physical properties.

1.7.1 Aims

In this work, I aim to:

1. Characterise the features produced by the interaction between fluids and fractures in shallow seismogenic fault zones, with a focus on carbonate faults;
2. Characterise the microstructures, deformation mechanisms, and fluid-flow processes within carbonate cements in shallow seismogenic fault zones;
3. Characterise the microstructures, deformation mechanisms and fluid-flow processes within experimental faults, deformed under a range of conditions;
4. Extrapolate the mechanical behaviour and microstructural processes of experimental faults to natural fault zones.

By addressing these aims I seek to answer the following questions:

1. To what extent do pre-existing textures inform upon the history of a fault?
2. Can heterogeneities produced by fluid-rock interactions permit fault motion at a sub-optimal orientation?
3. To what scale (nano to basin) are heterogeneities produced by fluid-rock interactions important?
4. How important are fault system parameters (e.g., temperature, pore fluid, lithology) in controlling fault zone properties (e.g., strength, permeability, how a fault will slip)?
5. How important are chemical effects of fluid-rock interactions important compared to mechanical effects?
6. What is the relevance of the mechanisms exhibited in rock deformation experiments to the field?

1.7.2 Objectives

1. Conduct field studies of two faults hosting carbonate cementation features in order to address Aim 1:
    - The Zuccale Fault (Chapter III) is a low-angle normal fault on the Isle of Elba, Italy, which contains cataclastic rocks, carbonate gouge, and calcite vein fillings. The results will be compared to a typically oriented (~60^{o}) normal fault in the same extensional regime, the Gubbio Fault in the Northern Apennines of Italy.
    - The Psatha Fault (Chapter IV Part I) in the Gulf of Corinth is a fault segment kinematically linked to the Skinos fault in the South Alkyonides fault system. This

fault is superbly exposed along the coastline and can be walked along strike. The fault zone is formed of Jurassic and Cretaceous limestone host rock and Pliocene and Quaternary sediments, and hosts various breccias, fault gouge, and calcite veins.

2. Conduct isotopic analysis and microstructural analyses on carbonate cements from the aforementioned field areas, to address Aim 2.
3. Perform sub-seismic rate triaxial hold-slide rock deformation experiments and subsequent microstructural analysis. This includes (i) producing new textures in the timescale of an experiment and (ii) testing rock with pre-existing heterogeneities. This seeks to address Aim 3. The material to be used includes:
    - Calcite standard Carrara marble (i) (Chapter V)
    - Homogeneous Scaglia Bianca limestone gouge, obtained from a quarry in the Apennines (i) (Chapter VI)
    - Calcite veined host rock from the Psatha fault, Gulf of Corinth (ii) (Chapter IV Part II)
4. Using the microstructures from field study samples and the experimental studies to make conclusions about the frictional behaviour and physical properties of cement-rich fault zones to address Aim 4.

Details of the field and laboratory methods used are presented in Chapter II.

Chapter II: Methods

2.1 Structural analysis in the field

Fieldwork is at the heart of this study, with fault zones characterised during fieldwork and samples collected for further microscopic and geochemical analysis, as well as rock deformation experiments. The morphology, dimensions, and spatial distribution of textures and structures on and adjacent to exposed fault planes were described and recorded in photographs. Any cross-cutting relationships between fractures and veins were recorded in order to be able to make sense of the fluid-fracturing cycle in the fault zone through time. Analyses on the clasts within the cements, inclusive of composition, orientation, size, and distribution, were studied to help constrain the formation mechanism.

2.2 Rock deformation experiments

Rock deformation experiments were utilised to recreate idealised fault zone conditions, inclusive of confining pressure, pore fluid pressure, pore fluid type, host rock type, etc., to test hypotheses on rock physical properties.

Four rock deformation machines have been used in the duration of this PhD project: the Paterson gas-medium triaxial apparatus at the Massachusetts Institute of Technology (MIT), the Instron uniaxial and the Sanchez triaxial cell at the University of Portsmouth (UoP), and an argon gas-medium triaxial apparatus at the China Earthquake Administration (CEA). Different machines have been used due to the different collaborations during this four-year study, machine availability at the collaborative institutions, and the specific requirements of the experiments to suit the aims (see section 1.7.1, Chapters IV Part I, V & VI).

2.2.1 Paterson gas-medium triaxial apparatus at MIT

The carbonate core samples were drilled as 10-mm-diameter cylinders (20 mm length) and then a saw-cut was inserted at 35° using a low-speed diamond saw to produce two blocks. A hole of 0.5 mm diameter, to allow pore fluid to infiltrate the fault zone, was drilled into one block (Fig. 2.1).

The sample assembly consisted of split alumina spacers at either end, permitting pore fluid to permeate into the sample and fault (Fig. 2.1). Ceramic and zirconia spacers were placed on either side of the alumina spacers, which minimises the heat dissipation from the sample. The samples and spacers were encased in a 0.3 mm thick copper jacket, wrapped in cotton sheets

to insulate the sample. Iron tubing encasing the sample assembly isolated the pore fluid from the confining medium (argon).

The experiments were undertaken in a Paterson triaxial apparatus (Fig. 2.1). The Paterson triaxial apparatus is an internally heated, servo-controlled deformation apparatus, as detailed by Karner et al. (1997). All pressures, sample temperatures, and piston displacements are acquired digitally and monitored electrically. The machine comprises a main pressure vessel, a hydraulic ram for applying axial pressure, and a two-zone wire-wound furnace (Fig. 2.1). Confining pressure is produced in a Haskell intensifier, and maintained within ±3 MPa by air-driven Haskell boosters. Pore-fluid pressure is generated and maintained by a HIP-brand pressure generator to within ±2 MPa and controlled using pressure transducers. Axial pressure is produced using a servo-controlled hydraulic piston, the displacement of which is measured by a direct-current displacement transducer, and the load measured by an external load cell. Within the main vessel, the jacketed sample and spacers are encased by the heating furnace (Fig. 2.1), which is controlled to ±2°C by a thermocouple at the sample top, keeping the temperature within the sample at the desired temperature, ±5°C. Unlike the CEA vessel (see section 2.2.4 & 2.2.5), piston-seal friction here is assumed to be insignificant due to the use of a constant displacement rate.

Permeability was measured periodically, using the oscillation technique, to track the evolution and influence of any compaction and precipitation. This tracking of permeability involves imposing an oscillating (sinusoidal) pore fluid pressure of magnitude 0.3 MPa at the upstream end of the sample and monitoring the response at the downstream end for differences in phase and amplitude. As the optimum frequency of oscillation, and the ratio of downstream to upstream pore fluid pressures, are dependent upon the size of the sample and the magnitude of the hydraulic diffusivity, the measurable range is limited to ~microDarcys (10^{-19} m^2) (Karner et al., 1997). At the end of each experiment, the samples remain held within their copper jackets, so the final textures are preserved. The samples were immediately preserved in Epoxy resin, then vertically cut to intersect the fault zone and thin sectioned. Microscopic analysis was carried out on each sample to assess any microstructural changes.

Unlike the other experimental setups used in this study, this apparatus allows different pore fluids to be used (e.g., water, argon) and permeability measured (using the oscillation technique).

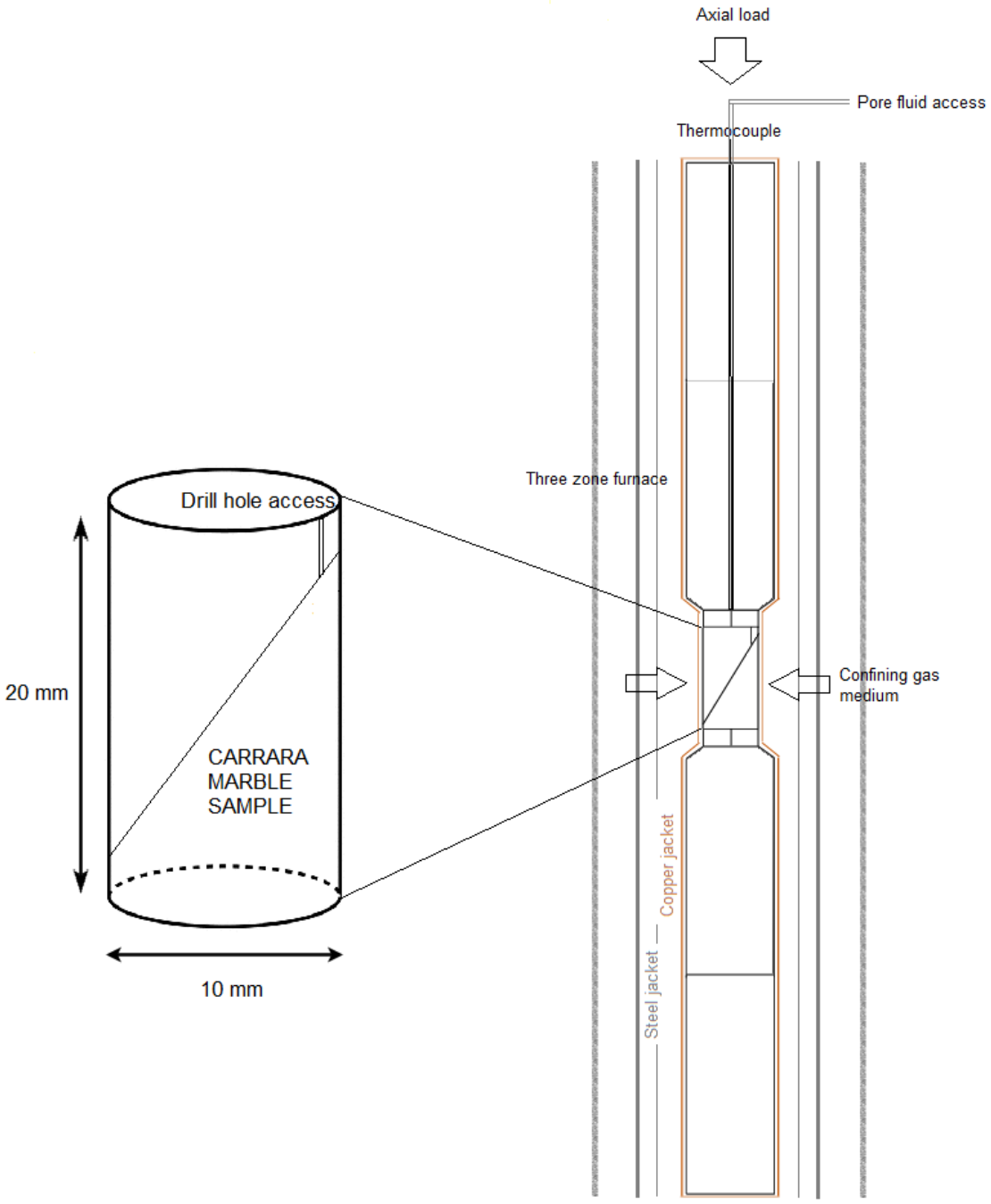


Figure 2.1 Paterson triaxial apparatus setup at Massachusetts Institute of Technology.

2.2.2 Instron uniaxial cell at University of Portsmouth

The carbonate core samples were drilled as 40-mm-diameter cylinders (100 mm length) using a diamond-tipped drill.

The sample was placed into a thin plastic jacket, to contain the sample following rupture, then placed under an Instron 60 tonne uniaxial press. This apparatus used was a 600 kN uniaxial

loading frame equipped with ancillary pressure systems to provide confining pressure via a simple Hoek-type cell which logs force and strain digitally. This apparatus does not confine the sample or input pore fluid but solely uses axial pressure (P_A) and tests sample strength under the simplest conditions.

2.2.3 Sanchez triaxial cell at University of Portsmouth

As for the uniaxial experiment, the carbonate core samples were drilled as 40-mm-diameter cylinders (100 mm length) using a diamond-tipped drill.

The sample was placed into an engineered rubber jacket which slots into the pressure chamber (Fig. 2.2). The Sanchez triaxial cell consists of an oil-medium pressure chamber with two servo-controlled pumps (Fazio, 2017). These pumps independently generate confining and axial pressure and are electronically synchronised to provide an isotropic stress field. Two more servo-controlled pumps supply pore fluid pressure to either end of the sample, and the use of electronically-operated values permits a hydraulic gradient to be set. Axial pressure is provided using a hydraulically driven piston. Unlike the apparatuses at MIT and CEA, which use copper jackets, this setup utilises a rubber jacket, which permits a fracture to form within an originally intact core without rupturing the jacket.

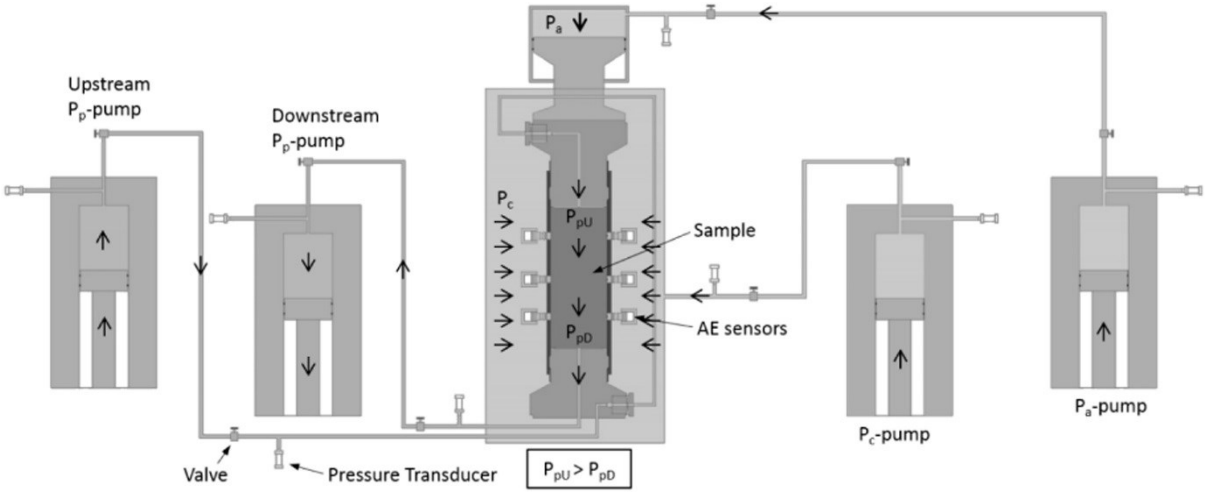


Figure 2.2 Schematic diagram of Sanchez triaxial cell at the University of Portsmouth (from Gehne and Benson (2017)). P_{pU} is pore fluid pressure upstream, P_{pD} is pore fluid pressure downstream P_P is pore fluid pressure, P_C is confining pressure and P_A is axial pressure.

2.2.4 Servo-controlled gas medium triaxial deformation apparatus at CEA

The carbonate core samples were drilled as 20-mm-diameter cylinders (40 mm length), after which a saw-cut was inserted at 35° using a low-speed diamond saw to produce two limestone blocks. A hole for pore fluid pressure was drilled into one half. Carbonate 'gouge' was produced from the host rock, by crushing, grinding, and sieving rock material through 200-mesh sieve (74 μm). The simulated gouge was inserted between the saw-cut surfaces, by first being prepared as a paste with deionized water in a 4:1 ratio, then spread on the saw-cut surface of the upper driving block and subsequently sandwiched by the lower block. Copper netting, inserted into the pore fluid hole, stops gouge from re-entering the hole but still permits effective communication between the external pore fluid pressure system and the drill hole.

The sample assembly (Fig. 2.3), consisting of the assembled saw-cut sample with gouge inserted, tungsten-carbide spacers, alumina pistons, and steel end-pieces, was placed within a copper tube with thickness of 0.35 mm. Double O-ring seals are set within slots in the steel end-pieces, within the copper tube at both ends of the sample assembly, which isolates the sample from the pressurised gas medium.

The apparatus used was a servo-controlled triaxial testing machine, made up of a gas medium pressure vessel, as detailed by He et al. (2006). A servo-controlled intensifier controls the confining pressure (P_C) to within 0.5 MPa, which is generated by pressure boosters. Temperature is applied using a two-zone internal furnace and controlled using a Yamatake-Honeywell DCP30 controller. The pore fluid pressure is held to within 0.5 MPa using a servo-controlled intensifier. Both confining and pore fluid pressures are initially raised to half of their final set values, then once the required temperature was met (raised at a rate of 5ºC/min), P_C and P_P were subsequently raised to account for the pressure increase associated with higher temperature. When the defined pressure and temperature conditions were reached, the sample was held to establish equilibrium at the set conditions. The displacement rate is then applied. Axial pressure is applied using a servo-controlled hydraulic ram. Axial displacement is measured using an LVDT attached to the hydraulic loading ram. The maximum displacement is limited by the displacement available in the apparatus (4 mm).

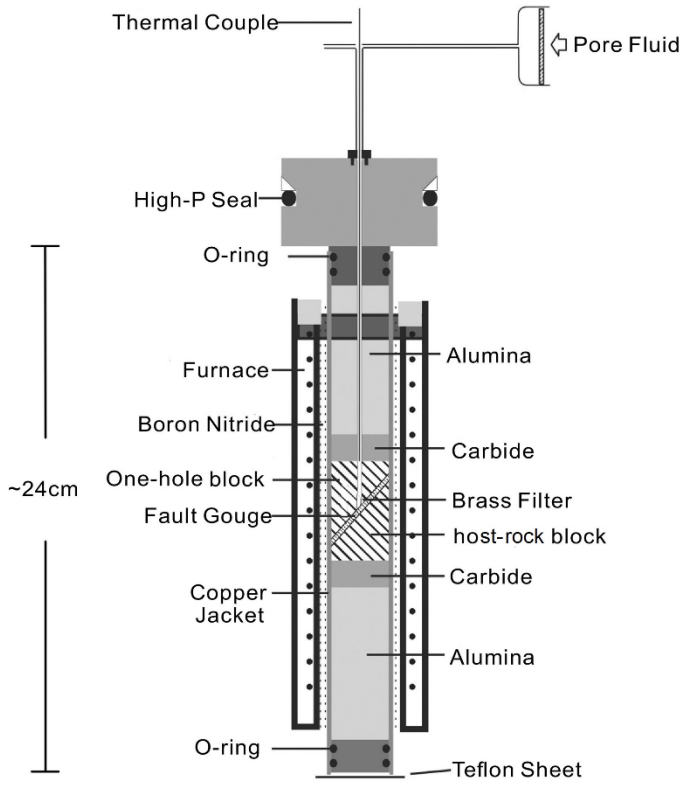


Figure 2.3 Schematic diagram of sample assembly within the servo-controlled gas medium triaxial deformation apparatus at CEA (adapted from Zhang et al. (2017)).

Following deformation, the samples were preserved in LR white resin, a hydrophilic acrylic resin of exceptionally low viscosity (comparable to that of water), which permits relatively easy permeation of the rock overnight in a vacuum to preserve the deformation structures. The samples were then cut in half lengthways using a low-speed diamond saw to expose the fault zone. Thin section production, or SEM analysis, could then be undertaken.

2.2.5 Data corrections

A number of corrections had to be made to the data. Data were corrected automatically at MIT and UoP, but at CEA these corrections had to be done manually. The first correction is completed at the beginning of each experiment, to account for the seal friction, which acts between the bronze seal ring and the piston. After the desired confining pressure and temperature conditions are reached, seal friction was measured by moving the piston up and down (up to, but not in contact with, the sample) and a ratio between seal friction (in dimension of stress) and confining pressure was obtained (He et al., 2006).

Following the experiments, corrections had to be made to the raw, output data. As sample slip along the fault results in decreasing contact area between the two saw-cut blocks, the raw axial stress needed to be corrected to account for this change in area:

$$\sigma_{1c} = \frac{\sigma_{10}}{1-\frac{2}{\pi}\left[\arcsin\frac{\Delta L \tan\phi}{2r}\sqrt{1-\left(\frac{\Delta L \tan\phi}{2r}\right)^2}\right]} \quad (2.1)$$

where σ_{10} is the measured apparent axial stress, σ_{1c} is the corrected axial stress as a function of slip ΔL resolved in the axial direction, and ϕ is the angle of fault to sample axis (He et al., 2006).

As the axial stress had changed, the corrected value of axial stress had to be combined with the confining pressure (σ_3) to obtain the shear stress (τ_{1st}):

$$\tau_{1st} = \frac{\sigma_{1c} - \sigma_3}{2}\sin(2\phi) \quad (2.2)$$

The data are then subsequently corrected for the shear resistance of the jacket. He et al. (2006) calibrated this for copper jackets. The coefficient of friction between steel and Teflon was tested in a standard friction testing system up to 300°C, and the shear resistance of copper was measured with steel sample pieces sandwiched with 1-mm-thick Teflon slice, at temperatures up to 420°C. The linear approximation of shear resistance resulted in a maximum error of +/- 0.005 in the absolute value of coefficient of friction, with little effect on relative changes such as rate dependence.

2.3 Microscopy

Thin sections were produced from samples collected from the field or following rock deformation experiments. Undertaking microscopic analysis of host rock, breccias, and cements within fault zones allows one to characterise the different products, distinguish the different deformation mechanisms, and identify different cement generations (Gribble, 1993). The technique of cathodoluminescence microscopy utilises the differences in the colour of diagenetic phases and luminescence intensity due to chemical composition differences (Götze, 2012; Marshall and Mariano, 1988).

The original samples were cut to billet size (25 × 40 × 150 mm) using a diamond-tipped rock saw in the rock preparation laboratory at Imperial College, and then sent to Miekinia laboratories to be made into thin sections. The optical and cathodoluminesence microscopy

was undertaken using a Zeiss Axioscope 40 and a CITL mk5 cold cathodoluminescence stage, mounted on a Nikon 50i microscope with a Nikon digital camera.

2.3.1 Electron microscopy

2.3.1.1 Scanning electron microscopy (SEM)

SEM analysis permits an investigation of the microstructures and properties of a material down to the microscale, or even hundreds of nanometres scale. A fine electron beam, produced by a cathode ray tube (CRT) is used to scan a sample's surface. This leads to elastic and inelastic scattering of electrons and electromagnetic radiation variations (Goldstein et al., 2017). Next, a mass of secondary signals can be detected, including secondary electrons, backscattered electrons, cathodoluminescence or X-rays. As the primary electron beam scans across the sample, the intensity of the secondary signal changes depending on the morphology of the surface and chemistry of the sample.

Initial SEM analyses were undertaken with the Fuel Cell Group at Imperial College London, utilising a Hitachi Tabletop Microscope TM3030. Detailed SEM analyses were undertaken at the University of Beijing using a Hitachi S-5500 FEG (Field Emission Gun) SEM, which also utilised an In-lens detector. An In-lens secondary electron detector is sensitive to low energy electrons (energy less than 40 eV) and are easily attracted by the electrostatic field, providing high surface sensitivity.

Samples are cut to the size of the sample mount (~10 × 10 mm), then coated in either carbon (whereby a carbon source in the form of a rod is mounted in a vacuum system between two high-current electrical terminals, heated to an evaporation temperature producing a fine stream of carbon which is deposited onto the samples) or gold (using splutter coating, which involves bombarding a gold source with gas ions, eroding this target material and causing subsequent omni-directional deposition of the sputtered atoms forming coatings on the sample surface). The sample is then attached to the mount with carbon dots or metallic tape and inserted into the SEM apparatus.

2.3.1.2 Focussed ion beam scanning electron microscopy (FIB-SEM)

FIB-SEM couples traditional SEM with a focused ion beam that can be used for materials processing and sample preparation, e.g., sectioning an area of interest for TEM analysis (Langford and Clinton, 2004). This technique permitted me to select areas of localised strain (of ~10 μm width) within experimental samples, cut out these areas using the focussed ion beam, and undertake TEM analysis of nanometre scale.

Following the preparation of rock billets from field and experimental samples in the rock preparation laboratories at Imperial College London, FIB-SEM imaging was undertaken at the Nanoscale and Microscale Research Centre (NMRC) at the University of Nottingham using a FEI Quanta200 3D DualBeam FIB-SEM.

The preparation of a sample using a FIB-SEM is shown in Fig. 2.4. The steps required to use a FIB-SEM are as follows:
(a) The area of interest is located on the sample;
(b) Using the focussed ion beam (FIB), the front and back of the area of interest are removed;
(c) The sample is rotated, one side and the base of the sample are removed. One half of the other side of the sample is removed, and a needle placed next to the sample;
(d) Platinum is then deposited across the top of the needle and the sample edge to bond them together. The bottom side of the sample is then cut free using the FIB. The sample is then lifted and placed next to the grid;
(e) Platinum deposition is used to attach the grid to the sample. The sample is then cut away from the needle using the FIB;
(f) The sample is rotated and, using a low current FIB, thinned to optical transparency, so that the TEM can be utilised.

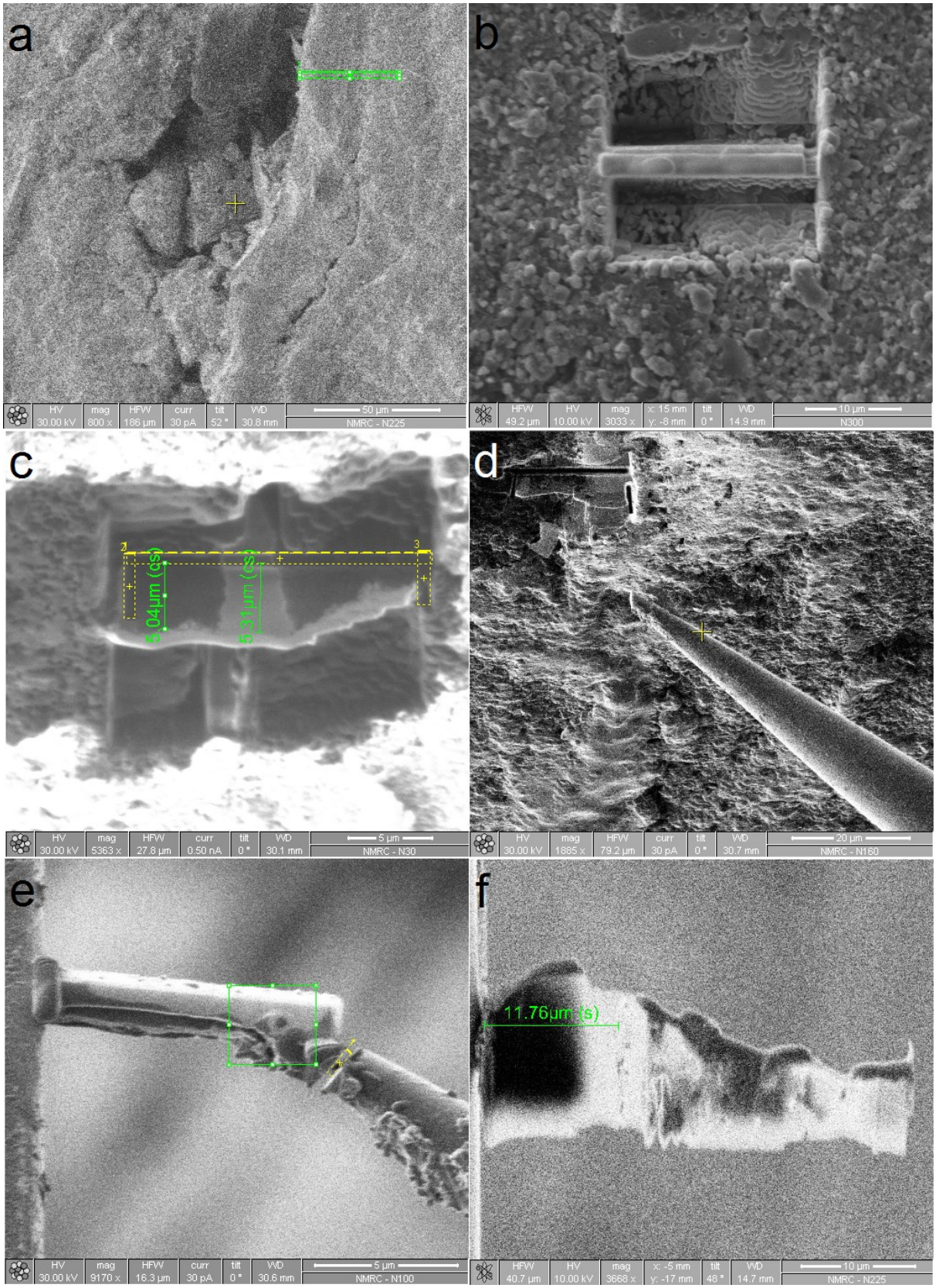


Figure 2.4 Step-by-step guide to using a FIB-SEM to locate, cut, extract and thin a desired sample. See text in section 2.3.1.2 for descriptions of each step.

2.3.1.3 Transmission electron microscopy (TEM)

Following preparation of samples using FIB-SEM, transmission electron microscopy (TEM) can be undertaken on the micrometre-scale samples produced.

TEM is an electron microscopy technique used to achieve spatial resolutions down to sub-nm scale. By monitoring what happens to the electron beam passing through the sample, nanostructural characterisation can be performed. This analysis was undertaken using a JEOL 2100+ TEM machine at NMRC.

2.4 Isotope analyses

2.4.1 Stable isotope analyses

Analysis of stable carbon and oxygen isotopes is one method of acquiring information about fluid-rock interactions and identifying the type of fluids involved in dissolution and precipitation processes in fault zones. The ratio of $^{13}C/^{12}C$ can be used to identify the carbon source (Stahl, 1977). For example, a ^{13}C-depleted nature suggests that the source of the carbon is related to organic complex evolution (Labaume et al., 2001), and slight differences in $\delta^{13}C$ compositions can be indicative of a fairly open system (Hausegger et al., 2010), as is a decrease in $\delta^{18}O$ values (Marquer and Burkhard, 1992). The $^{18}O/^{16}O$ ratio is dependent on precipitation temperature and the oxygen isotope composition of the precipitation fluid, permitting water movement to be tracked (Clark and Fritz, 1997). A range of $^{18}O/^{16}O$ ratios indicates that precipitation has taken place over a range of temperatures and/or $\delta^{18}O$-water values (Labaume et al., 2001), and low $\delta^{18}O$ values in respect to the host rock indicate precipitation from higher temperature fluids, or fluids with lower $\delta^{18}O$ composition (Hausegger et al., 2010) which may be due to the water's salinity, freshwater input and local evaporation. For example, rainwater is ^{16}O-enriched due to the preferential evaporation of the lighter ^{16}O from seawater. However, identification of the actual source, and/or contributors from mixed sources is often quite difficult and open to interpretation, as source compositions typically vary over a fair range or even overlap (see Fig. 2.5). Uncertainties can also result from sample preparation (extraction, weighting) and uncertainties arising from the instrumental analysis (conversion to gas, separation).

100 µg of cement is initially drilled from samples obtained during fieldwork using a dental drill at Imperial College. Depending upon where the analysis was undertaken, the samples were either reacted with 100% phosphoric acid at 60ºC using a Gasbench connected to a ThermoFinnigan MAT 253 mass spectrometer (at Durham University), or were reacted with

100% phosphoric acid at 70°C using a Gasbench II connected to a ThermoFisher Delta V Plus mass spectrometer (University of Erlangen-Nuremberg). The carbon dioxide produced during the reaction was analysed using a mass spectrometer. The different temperatures used at the different laboratories is simply a matter of laboratory protocol. However, the higher the temperature used for the reaction, the faster the analysis, as more ^{16}O goes to the gas, thus becoming more negative as the temperature of the reaction increases. The fractionation factor, α, for calcite, decreases by 0.12 per mil (‰) per 1°C increase; therefore, this effect must be corrected for. Oxygen isotope values are corrected using the phosphoric acid fractionation factors given by Kim et al. (2007) and Rosenbaum and Sheppard (1986). The ratios are then reported per mil (‰) relative to V-PDB (Vienna Pee Dee Belemnite) standard by assigning a $\delta^{13}C$ value of +1.95‰ and a $\delta^{18}O$ value of -2.20‰ to NBS19 (Friedman et al., 1982).

The $\delta^{18}O$ of a solid phase (e.g., calcite (cc), dolomite (dc)) is usually reported in PDB (heavy standard) while the $\delta^{18}O$ of liquid phase (e.g., seawater, rainwater, generally the precipitating fluid) is usually reported in S-MOW (Vienna Standard Mean Ocean Water, light standard). The interconversion equations are as follows (Friedman and O'Neil, 1977):

For calcite and dolomite:

$$\delta^{18}O^{CC}_{SMOW} = 1.03091(\delta^{18}O^{CC}_{VPDB}) + 30.91 \quad (2.3)$$

If we know the $\delta^{18}O$ value of the precipitating fluid, the temperature of precipitation can also be calculated, and vice versa (Friedman and O'Neil, 1977); see Fig. 2.5 for a graphical representation of the relationship between temperature, the $\delta^{18}O$ value of the precipitating fluid and the $\delta^{18}O$ value of calcite.

In calcite:

$$T\ (^oC) = \sqrt{\frac{2780000}{2.89+(1000\ \ln(\frac{\delta^{18}O^{CC}_{SMOW}+1000}{\delta^{18}O^{liquid}_{SMOW}+1000})}} - 273.15 \quad (2.4)$$

In dolomite:

$$T\ (^oC) = \sqrt{\frac{3200000}{3.3+(1000\ \ln(\frac{\delta^{18}O^{CC}_{SMOW}+1000}{\delta^{18}O^{liquid}_{SMOW}+1000})}} - 273.15 \quad (2.5)$$

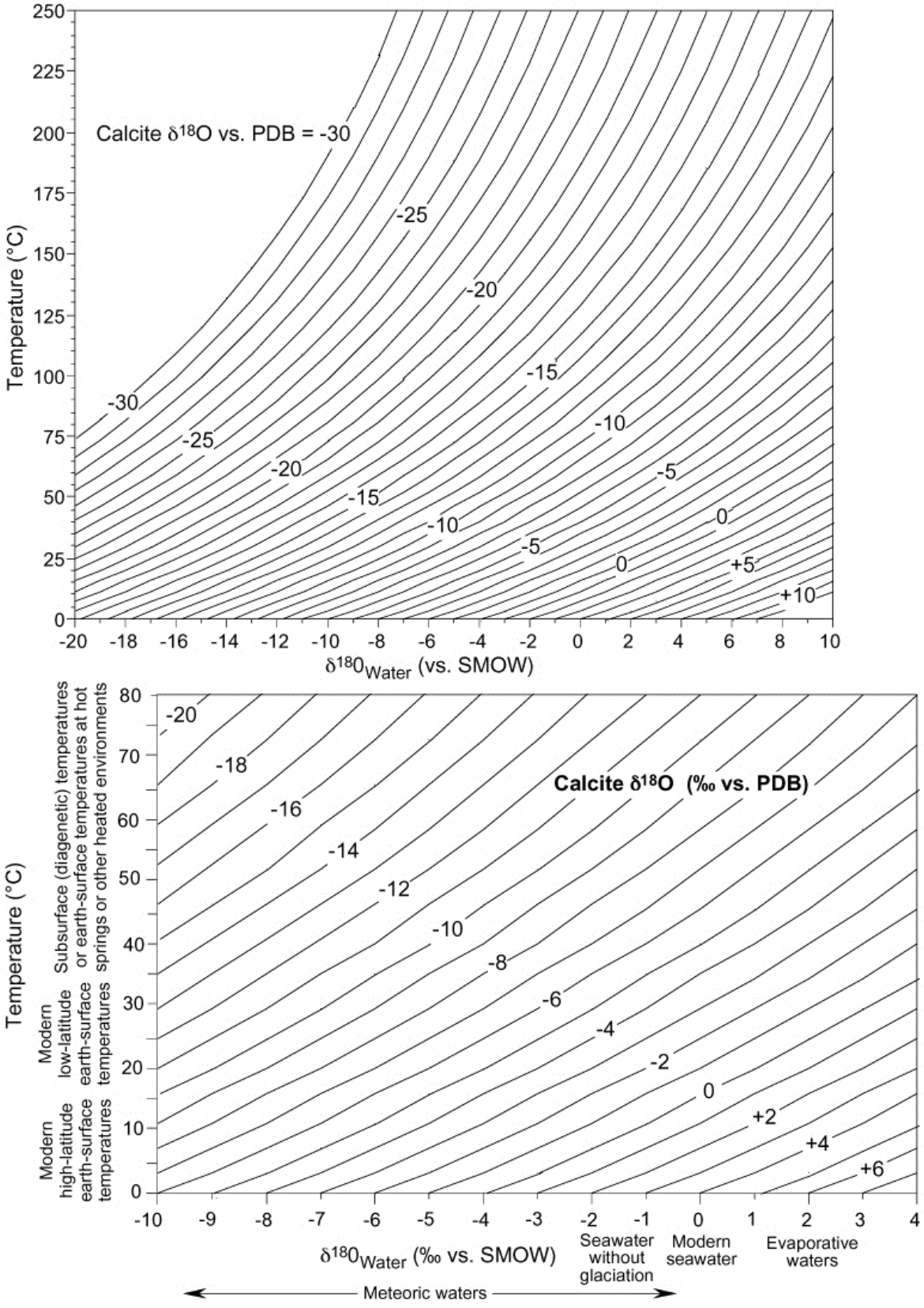


Figure 2.5 The oxygen isotope composition of calcite precipitated at isotopic equilibrium from water of the O isotope composition shown on the *X* axis and at the temperature shown on the *Y* axis (from Friedman and O'Neil, 1977).

2.4.2 Clumped isotope analyses

When temperature data are not available for the $\delta^{18}O$ value of the precipitating fluid, clumped isotope analysis may be used to constrain the formation temperature. From stable isotope analysis alone, it is not possible to know whether the fluid composition or the temperature is altering the oxygen isotope signature. This information can be obtained from fluid inclusions, if available (Friedman and O'Neil, 1977). Another technique is clumped isotope analysis, as this method requires no assumptions about the $\delta^{18}O$ of waters from which carbonates grew, by using the temperature dependence of the clumping of ^{13}C and ^{18}O into bonds within the carbonate mineral lattice (Eiler, 2007; John et al., 2012). When carbonates are reacted with phosphoric acid, they produce CO_2 in isotopic equilibrium with the original carbonate, but with a constant offset linked to acid temperature. By measuring an isotopologue (molecules of similar chemical composition but different isotopic composition) of CO_2 gas with a mass of 47, i.e., where the two 'heavy' rare isotopes (^{13}C and ^{18}O) are substituted in the CO_2 molecule, this gives the amount of 'clumping' of the heavy isotopes in the crystal lattice of the carbonate (Eiler, 2007; Lea, 2014). The amount of clumping at a known temperature can be determined using the laws of thermodynamics: heavy isotopes tend to 'clump' with each other, increasing the proportions of multiply substituted isotopologues, as temperature decreases (Eiler, 2007; Affek, 2012).

The use of clumped isotope analysis permits the isotopic signature of carbon and oxygen in the cements to be obtained, as in stable conventional isotope analysis, but also allows the cement formation temperature and the $\delta^{18}O$ of the fluid to be constrained, and thus differentiate whether the fluid source is of meteoric origin, or from much deeper sources. This is possible because $\delta^{18}O$ and $\delta^{13}C$ are measured simultaneously to $\Delta47$ in the same sample. As $\Delta47$ is independent of fluid $\delta^{18}O$ composition and thus only reflects temperature, both the $\delta^{18}O$ composition of the fluid can be reconstructed. However, this method required 10× more material than is required for stable isotope analysis, and needs uncontaminated samples, long analytical runs, and extensive replication (Ghosh et al., 2006). The requirement for more material is due to the low relative quantity of ^{13}C-^{18}O bonds (the temperature dependence of $\Delta47$ is only 0.0033‰/°C at temperatures below 50°C (Kele et al., 2015)). Furthermore, as the number of ^{13}C-^{18}O bonds decreases with increasing temperature (the preferential 'clumping' of heavy isotopes at lower temperature i.e. the ordering of isotopes within a crystal structure, is counter-balanced by the effects of entropy), the associated error increases with increasing temperature. This error margin can be reduced by greater replication.

Similar to stable isotope analysis, samples were powdered and subsequently reacted with phosphoric acid to extract CO_2. The extracted CO_2 is then purified to remove any contaminant gases. This purified CO_2 is then analysed in a MAT 253 mass spectrometer to obtain $\delta^{13}C$, $\delta^{18}O$, and $\Delta 47$ (abundances of mass-47 CO_2) value. Standardisation was obtained by analysing standards ET2 (chalk from Germany) and ETh3 (Carrara marble). These standards are run every three days in the laboratory, and the error is the standard deviation over a month.

2.5 X-Ray diffraction (XRD)

XRD is used to identify phases within a sample. When X-Rays are fired at a sample, they diffract into specific directions (see Fig. 2.6). Constructive interference of these diffracted X-ray beams occurs and a `Bragg reflection´ will be picked up by a detector scanning at this angle (Warren, 1969). The positions of these reflections define the inter-layer spacings of atoms in the crystal structure. The peak intensities define where particular atoms lie in the structure, or how much of a phase is present in a sample (Warren, 1969).

XRD analysis was undertaken at the Natural History Museum using an Enraf-Nonius Powder Diffraction Systems 120. The system uses an INEL 120º curved position sensitive detector (PSD), which allows rapid data acquisition. As for isotope analyses, carbonate samples were powdered using a dental drill at Imperial College. The powder was then ground using a pestle and mortar, placed onto a thin plastic film with a drop of ethanol, covered with a second thin plastic film, and sealed with plastic rings. This mount was then inserted into the detector. The XRD measurement data was subsequently analysed using PANalytical software.

The X-ray diffraction pattern is distinct for each different phase. First, PANalytical can be used to determine the background before conducting a search for peaks. All intensity above the background curve determined by the software is considered in determining the phases present in the sample. If the data contains broad peaks, then the Peak Base Width should be increased to take these into account. If several phases are present in the sample, the phases need to be crystalline enough, and, from the intensity counts of the main lines of both of the phases, their relative percentages can be determined. Several estimations of the Peak Base Width should be conducted to make an estimation of the relative phases. If several estimations yield significantly different results, additional methods to determine the absolute relationship composition should be employed. If the sample has a dominant carbonate component, by running a preliminary clumped isotope measurement on the sample, the reduced proportion of

the carbonate can be estimated which can then be matched to the most likely output given by the PANalytical software.

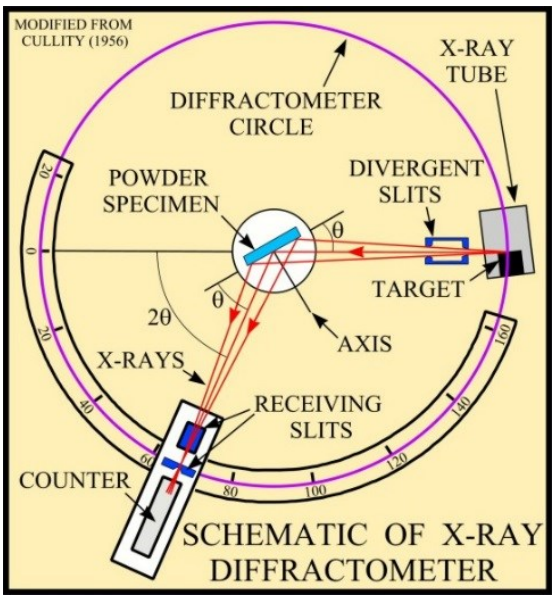


Figure 2.6 Basic geometry of an X-Ray diffractor. From Poppe et al. (2001), modified from Cullity and Stock (1956).

2.6 Fluid inclusion analysis

When a crystal grows in the presence of a fluid phase, some of the fluid may be trapped as imperfections in the growing crystal, forming fluid inclusions (Samson et al., 2003). Thus, these inclusions preserve the temperature, pressure, and fluid composition associated with the formation of the host mineral and rock. The study of fluid inclusions is performed utilising a microscope with an attached heating and cooling stage, which allows microthermometry to be performed on the inclusions. The fluid inclusion data discussed in this thesis were generously provided by Stephen Smith, University of Otago, who undertook the analysis with Alessandra Costanza, NUI Galway.

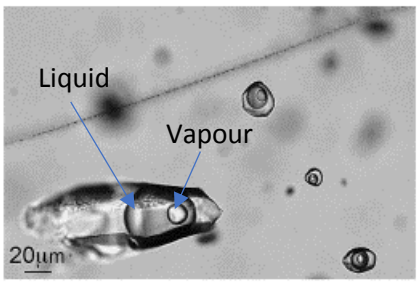


Figure 2.7 Example of a fluid inclusion within a quartz vein. Adapted from Frezzotti et al. (2012).

Chapter III: Independent temperature constraints on precipitation within the core of the Zuccale Fault: investigating the deformation mechanisms of Elba's low-angle normal fault

The Zuccale Fault, a low-angle normal fault (LANF), which lies above an ancient pluton on the Isle of Elba off the coast of Italy, has caused much scientific controversy. Standard Andersonian faulting theory suggests that normal faults should not form at dips < ~50◦, and, if rotated to below 30º, failure should then occur by formation of new higher-angle normal faults. Although the possibility that the Zuccale Fault is a reactivated reverse fault has been discredited through various regional and local structural analyses, it is possible that slip at such a low angle was enabled by conditions that significantly reduced the coefficient of sliding friction. By constraining the conditions of precipitation within the fault core, I have studied what processes may have enabled fault slip at < 30º. Here I present a multi-disciplinary study including clumped isotope thermometry, stable isotope analyses, fluid inclusion analyses, and XRD on carbonate from the Zuccale Fault to study these processes, alongside stable isotope analysis on carbonate from a typical high-angle normal fault within the Italian Apennines. These techniques permit the discrimination of the role of hot aqueous fluids in enabling slip. Samples from the two faults include foliated calcite, carbonate cements and vein fillings. The clumped isotope results indicate the presence of pore fluid temperatures of ~450ºC within the foliated calcite in the Zuccale Fault core, rapidly decreasing in temperature away from the contact with the cataclasite above (> 200ºC over < 20 cm). The results indicate that high temperatures and pressures associated with hydrothermal fluids, dissolution processes, the presence of weak minerals and associated intense foliation may have enabled normal slip to occur on this non-optimally oriented fault. The temperature constraints also support the possibility that magmatic intrusions, due to emplacement of the pluton, enabled alternating high-and-low temperatures and changing fluid sources. This may have permitted alternating formation of breccia through cataclasis (lower temperature) with the production of fine-grained foliated fault gouge (higher temperature), which also accommodated pervasive fluid-flow. This work has significant implications for the origin, evolution, and existence of the Zuccale Fault, for LANFs as seismically active structures, as well as the role of fluid-rock interactions in enabling processes, which lie outside standard faulting theory.

3.1 Introduction

The existence of active LANFs (dip < 30°) presents a conundrum in Earth sciences. Traditional frictional fault theory predicts that for typical Byerlee values of rock internal friction (~0.6-0.85), normal faults should not form at dips < ~50° and should lock up at no less than 40° (Sibson, 1985). However, examples of LANFs (LANFs) have been increasingly documented worldwide (Collettini and Barchi, 2002; Haines et al., 2010; Hayman et al., 2003; Numelin et al., 2007; Wernicke, 1995) and thus the settings and conditions that enable their existence need to be investigated. There are two main hypotheses as to why these LANFs exist: (i) reorientation of originally high-angle normal faults (Proffett Jr, 1977; Wernicke and Axen, 1988) or (ii) conditions which permit normal fault movement at a dramatic departure from standard Andersonian theory (e.g., Westaway, 1999). If other structural data indicates that reorientation is not the case (e.g., cross-cutting relationships with other structures), conditions which could make activation of the LANF the path of least resistance for stress distribution must be considered.

It is possible that fluids could play a role in permitting normal fault slip at a non-optimal orientation. The influence of fluids upon the mechanical strength of faults is well known (Blanpied et al., 1998; Faulkner et al., 2010; Faulkner and Rutter, 2001; Hickman et al., 1995; Sibson, 1981, 1994, 2000; Tenthorey et al., 2003) and it has been suggested that fault slip could occur at a lower angle if high fluid pressures are generated within the fault zone (e.g., Axen, 1992). Notably, the impact of fluid-rock interactions on rock physical properties (i.e., chemical interactions) lie outside standard Andersonian rock mechanical theory. The fabrics and textures produced by such interactions in turn may govern the subsequent properties of faults (Collettini et al., 2009; Evans and Chester, 1995; Goddard and Evans, 1995; Knipe et al., 1992; Mancktelow and Pennacchioni, 2005; Wintsch et al., 1995). If such processes were to create a scenario where the fault surface has a very low coefficient of friction of far below standard Byerlee values, slip could be enabled at a non-optimal angle (e.g., Numelin et al., 2007). Pressure solution processes enabled by an influx of fluids, in conjunction with high pore fluid pressures, could facilitate slip along pre-existing frictionally weak planes (Fagereng et al., 2010). Materials within a fault zone, which have a particularly low coefficient of friction may also permit slip at a non-optimal angle (such as shale; see Ambrose et al. (2014)). The presence of fluids in rocks generally favours ductile-type behaviour, as do higher temperatures (Fossen, 2010; Rutter, 1986). Notably, slip on LANFs does not result in large earthquakes, but rather in a combination of aseismic creep and small ruptures (Chiaraluce et al., 2007; Collettini and

Barchi, 2002; Collettini and Holdsworth, 2004), which supports a lack of significant frictional 'brittle' fault reactivation. However, the large displacements associated with LANFs worldwide (Hayman et al., 2003; John and Foster, 1993; Jolivet et al., 2010; Lister and Davis, 1989) and microseismic activity (Chiaraluce et al., 2007; Rietbrock et al., 1996) indicate that these non-optimally oriented normal faults do accommodate extension, and thus should not be neglected when thinking about seismic hazard assessment. Therefore, constraining the processes that could lead to non-optimal fault motion is essential for understanding earthquake processes. Knowing both the temperature at which precipitation occurred within a fault zone, and information on the fluid composition, may allow a constraint upon the origin of the fluids (and thus what external factors may have been at play), what fluid-rock interactions have been enabled (temperature is a key variable here), and thus ultimately what processes may have enabled activation of an LANF. Notably, along the Zuccale Fault, Collettini and Holdsworth (2004) favour a feedback process involving a pervasive cataclasis increasing fault zone permeability, promoting influx of CO2-rich hydrous fluids, which in turn triggers low-grade alteration and the onset of stress-induced dissolution–precipitation processes leading to shear localization and the formation of a narrow foliated fault core dominated by fine-grained hydrous mineral phases. Clearly, constraining the source, temperature and role of fluids and fluid-rock interactions is key in this instance.

However, obtaining definitive quantitative data on the temperature of the fluids from which cements precipitated within natural fault zones, their source and subsequent interactions, can be difficult. Stable isotope studies allow us to constrain a coupled temperature/fluid source signature responsible for cementation in fault zones and vein infill (e.g., Losh, 1997; Pili et al., 2002; McCaig et al., 1995, amongst others). But, the $^{18}O/^{16}O$ ratio is dependent on both the temperature of precipitation and the oxygen isotope composition of the precipitating fluid (Clark and Fritz, 1997). A range of $\delta^{18}O$ values can indicate that precipitation has taken place over a range of temperatures and/or $\delta^{18}O$-water values (Labaume et al., 2001) and low $\delta^{18}O$ values indicate precipitation from higher temperature fluids and/or fluids with lower $\delta^{18}O$ composition (Hausegger et al., 2010). This poses a problem for the purpose of this study, because absolute determination of temperature is required in order to determine the potential role of fluid/temperature interactions within the fault zone. To overcome this problem, the clumped isotope thermometry can be used. Clumped isotope measurements independently constrain the temperature and the ^{13}C and ^{13}O isotopic composition of carbonate, thus also

constraining the equilibrium isotopic composition of the fluid (Eiler, 2007; John et al., 2012); see section 2.4 for further details.

The aim of this study is to present new temperature constraints on the fault zone of a controversial LANF by utilising structural and textural analysis, stable isotope analyses, clumped isotope analyses, fluid inclusion analysis and X-Ray Diffraction (XRD) data. Combined with previous structural analysis, notably by Collettini and Holdsworth (2004), Smith et al. (2011a), Collettini et al. (2006), Smith et al. (2007), Smith et al. (2008) and Smith et al. (2011b), this will allow me to shed light on the cementation conditions within the Zuccale Fault zone, consider possible deformation-fluid interactions, and thus potential mechanisms for activity on such a weak, non-optimally oriented fault. This dataset is compared to stable isotope analyses from the 'classic' high-angled normal Gubbio Fault, which lies in the same extensional regime, in order to help discriminate the processes that may have enabled slip at such a low angle on the Zuccale Fault.

3.2 Geological setting

Fig. 3.1 shows the present day geological setting of the Italian Apennines. Since the Cretaceous, the Italian Apennines has experienced two phases of eastward migrating deformation (Elter et al., 1975; Scrocca et al., 2005). Shortening from the Cretaceous, due to collision between the Adria microplate and the Corsica-Sardinia block of the European plate, resulted in the development of the NW-SE striking Gubbio anticline (De Paola et al., 2006) (Fig. 3.1). This was followed by extension from the middle Miocene resulting in the opening of the northern Tyrrhenian sea, forming extensional basins bounded by normal faults trending NNW-SSE (Boncio and Lavecchia, 2000). The rollback of the Ionian-Adriatic subduction zone is believed to be responsible for the east migration of post-collisional extension (Doglioni, 1991; Royden et al., 1987). Magmatic activity is thought to be related to the development of extensional basins, starting in eastern Corsico (15-13.5 Ma), followed by Montecristo, Monte Capanne (Elba Island) and Vercelli plutons (7.3-6.2 Ma) (Peccerillo and Panza, 1999; Serri et al., 1993). The region is characterised by a high flux of non-volcanic CO_2, over a third of which is derived from the mantle (Chiodini and Cioni, 1989; Minissale, 2004; Minissale et al., 2000). These fluids cause significant fluid overpressures (~85% lithostatic) on active faults in the region, notably the active Altotiberina Fault (Chiodini and Cioni, 1989). The Gubbio Fault, which is antithetic to the Altotiberina Fault (Mirabella et al., 2005) (Fig. 3.2) is an active, typically oriented high-angle (~60^o dip) normal fault in the Northern Apennines of Italy, which

borders a Quaternary basin and pertains to the active fault alignment of the Umbria Fault System (Barchi, 2002; Mirabella et al., 2004). The intersection of the Gubbio and the Altotiberina faults is an earthquake source region, hosting medium-sized seismic events including an M_w 5.6 event in 1984 (Ciaccio et al., 2006; Haessler et al., 1988).

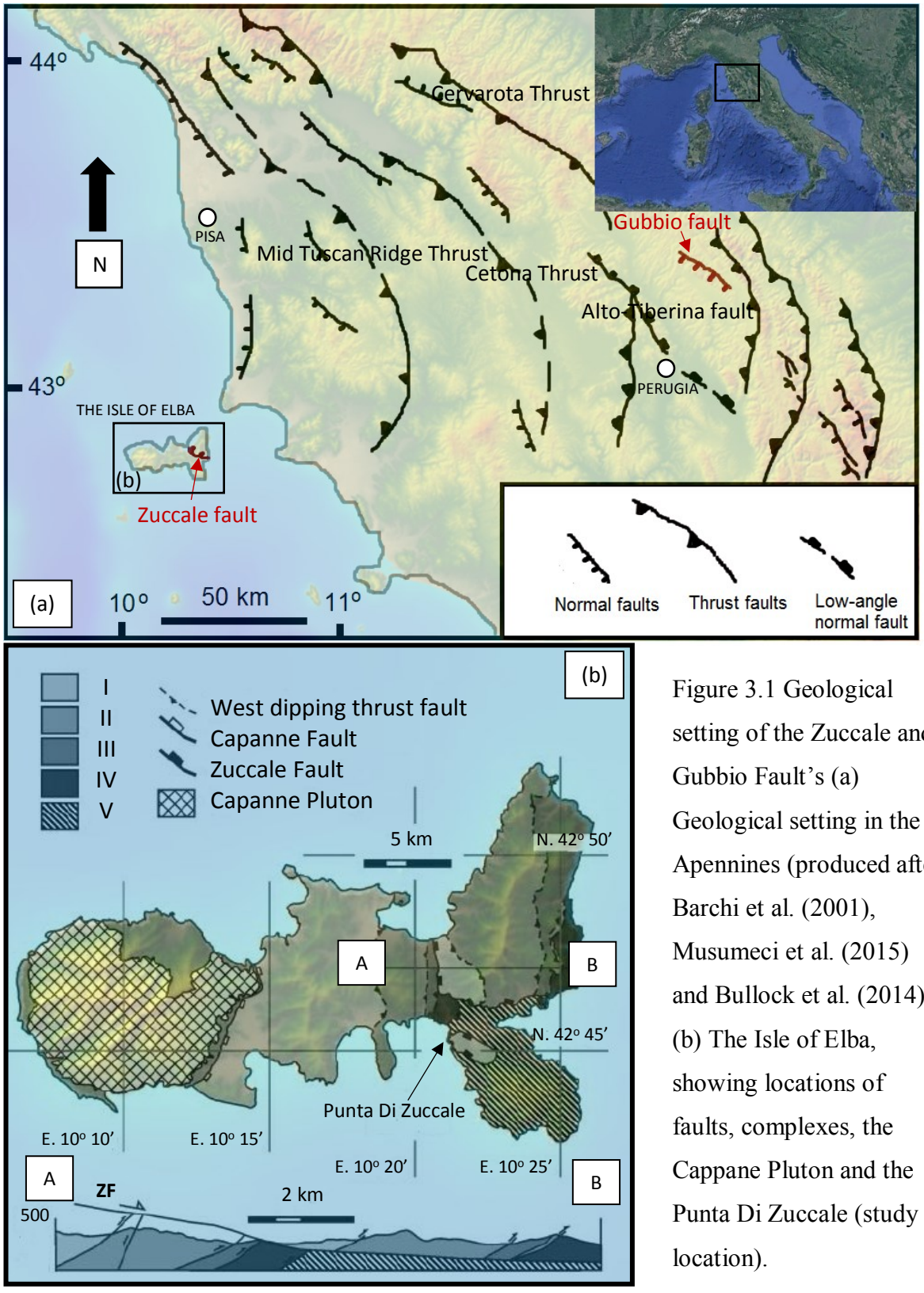


Figure 3.1 Geological setting of the Zuccale and Gubbio Fault's (a) Geological setting in the Apennines (produced after Barchi et al. (2001), Musumeci et al. (2015) and Bullock et al. (2014)), (b) The Isle of Elba, showing locations of faults, complexes, the Cappane Pluton and the Punta Di Zuccale (study location).

The Isle of Elba, in the northern Tyrrhenian Sea (Fig. 3.1), documents the Cretaceous-early Miocene compression and the later middle Miocene-early Pliocene post-orogenic extension (Bortolotti et al., 2007). Elba is split into different tectonic complexes (Complexes I-V, Fig. 3.1b), which form a moderately west-dipping stack of thrust sheets formed during the late Cretaceous early Miocene Apennine orogeny. Continued regional uplift of the area has exhumed older inactive LANFs (~late Miocene to early Pliocene (Smith et al., 2011a)), including the Zuccale Fault on Elba (Fig. 3.1b & 3.3). It cross-cuts the Complexes I-V (Fig. 3.1b) with a displacement of *c*. 6 km (Keller et al., 1994; Keller and Pialli, 1990).

The thrust complexes on Elba were intruded by upper crustal igneous bodies, associated with hydrothermal fluid systems ~8.5-5.9 Ma (Dini et al., 2002; Gagnevin et al., 2004; Maineri et al., 2003; Rossetti et al., 2007; Taylor and Turi, 1976) and at least two plutons during regional extension. Previously, structural analysis has implied that the Capanne Pluton intrusion (Fig. 3.1b) was accommodated by motion along the low-angle Capanne shear zone (Bouillin et al., 1993; Dini et al., 2002). Previous works have indicated that the intrusion of the Porto Azzurro pluton (Fig. 3.2), which intruded beneath Elba *c.* 5.9 Ma, occurred at the same time as motion along the Zuccale Fault (Smith et al., 2011a). It has been suggested that the Zuccale Fault has an overall dome shape, which may be reflective of the shape of the rising Porto Azzuro pluton (Smith et al., 2011a; see Fig. 3.2). The emplacement and uplift of the Monte Capanne and Porto Azzurro plutons is believed to have caused thermometamorphism and motion along a number of low-angle faults, including the Central Elba fault (Maineri et al., 2003; Westerman et al., 2004) and the Zuccale Fault (Daniel and Jolivet, 1995). Based on ages obtained by extensional basins in the east (Pascucci et al., 1999), as well as displaced granitic intrusions (Dini et al., 2002), the majority of displacement along the Zuccale Fault is believed to have occurred between ~8 Ma and ~4 Ma. Although emplacement of the pluton and some subsidiary faulting has affected the geometry of the Zuccale Fault, there are several indications that it was active at a low angle. Firstly, there is a group of high-angle normal footwall faults, which were active at the same time as the Zuccale Fault (Collettini and Holdsworth, 2004). The orientation of these faults limits the amount of dip rotation which the Zuccale fault could have experienced to ~5^{o}; if the Zuccale Fault was originally optimally oriented (~60^{o} dip) then these high-angle normal footwall faults would become LANFs (Smith et al., 2007). Secondly, there are thrust faults in the hanging wall of the Zuccale Fault that have standard Andersonian geometries (Collettini and Holdsworth, 2004). Finally, the Zuccale Fault zone can be traced down to 15

km depth (on seismic reflection data), and it appears to dip relatively uniformly at 15° east (Keller and Coward, 1996).

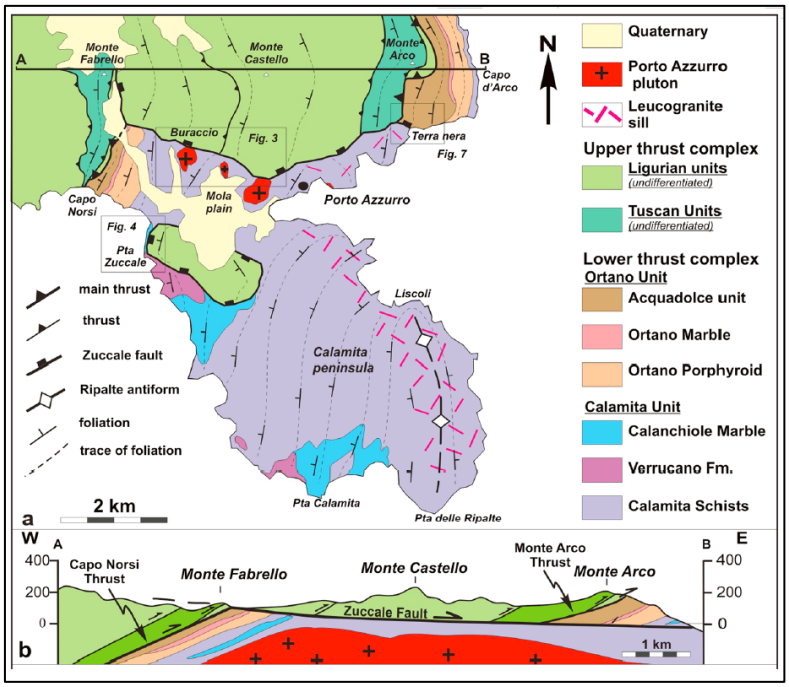


Figure 3.2 (a) Geological sketch map of thrust complexes in southeastern Elba, (b) cross section from central to eastern Elba Island. Edited from Musumeci et al. (2015).

The footwall of the Zuccale Fault (Fig. 3.2) is composed of phyllites, quartzites, and quartz-mica schists of Palaeozoic age metamorphic basement (Bortolotti et al., 2007; Garfagnoli et al., 2005), forming part of Complex I (Fig. 3.1b). The intrusion of the Porto Azzurro pluton overprinted the basement fabrics with muscovite, biotite, K-feldspar, andalusite, and cordierite porphyroblasts (Bortolotti et al., 2007). Breccias capping the footwall are 'chaotic' (following Woodcock and Mort (2008)) and are derived from quartzites locally capping Complex I, or from quartz-mica schists that dominate Complex I. The hanging wall is composed of a Cretaceous turbidite sequence; sandstones, marls, and mudstones, forming Complex V (Smith et al., 2011b).

3.3 Methods

Samples were collected from the core of the Zuccale Fault from the Punta Di Zuccale exposure (Fig. 3.1b & 3.3) and the Gubbio Fault (Fig. 3.5). Samples from the Zuccale Fault included specimens from the three coloured (orange, green and white) carbonate-rich layers within the fault core (Fig. 3.4) and the calcite veins stratigraphically above these carbonate-rich layers

(Fig. 3.5). The 'fault core' refers to the shear zone and surrounding gouges and breccias but does not include the adjacent fractured wall rock (Caine et al., 1996; Choi et al., 2016; Faulkner et al., 2003). Samples from the Gubbio Fault included breccia cements close to the fault contact, and pure calcite veins, which occupied fracture planes within the breccias (Fig. 3.6).

Thin sections were prepared for optical microscopy and samples were powdered for X-Ray Diffraction (XRD), and stable and clumped isotope microscopy. Stable isotope analyses were performed at both the Northern Centre for Isotopic and Elemental Tracing at Durham University and at the University of Erlangen-Nuremberg; carbonate powders of 100 μg were reacted with 100% phosphoric acid, and the CO_2 produced was analysed by a mass spectrometer. All values are reported in per mil relative to V-PDB. Standardisation was obtained by analysing standards NBS-18 and NBS-19 (Friedman et al., 1982); see section 2.4 for further details.

Given the expense of clumped isotope analysis, and the lack of fluid inclusions in the foliated fault core, clumped isotope analysis was only undertaken on two layers of the carbonate-rich parts of the fault core (Fig. 3.4) and the large calcite veins stratigraphically above (Fig. 3.5).

Samples were taken from these locations due to the certainty of obtaining pure, unbuffered samples (i.e., not touching and/or mixed with the host rock which could alter the isotopic signature) and the quantity of material available (a larger quantity of material is required for clumped isotope analysis; see section 2.4). The dolomite veins present proved too small to be able to get sufficient, unbuffered material for clumped isotope analysis. Fluid inclusions were only found in the thin (< 2 mm wide) dolomite veins, and in the larger calcite veins. Data from fluid inclusion analysis, which was undertaken at NUI Galway, supplements the clumped isotope data. Clumped isotope analysis was undertaken in collaboration with the Carbonate Research Group at Imperial College London. Samples of 1 gram were powdered and subsequently reacted with phosphoric acid to extract CO_2. The extracted CO_2 is then purified to remove any contaminant gases. This purified CO_2 is then analysed in a MAT 253 mass spectrometer to obtain $\delta^{13}C$, $\delta^{18}O$, $\Delta 47$ (abundances of mass-47 CO_2) value and thus the temperature of precipitation (see section 2.4 for more detail).

3.4 Results

3.4.1 The Zuccale Fault

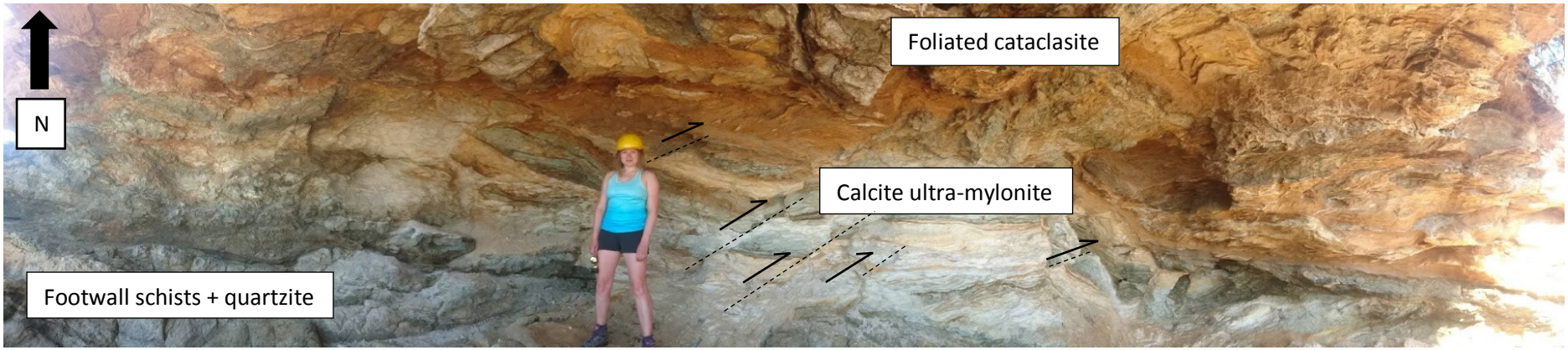


Figure 3.3 The Zuccale fault exposure at Punta di Zuccale (Fig. 3.1b). Stable isotope analysis was undertaken on the calcite-ultramylonite (white/green/orange layer, Fig. 3.4), the foliated cataclasite (orange veined layer above the calcite-ultramylonite), and both the smaller dolomite veins (Fig. 3.4) and larger calcite veins (Fig. 3.5) cross-cutting the foliated cataclasite.

The Zuccale Fault core is dominated by an intensely foliated orange, white and green carbonate-rich unit (Fig. 3.4), which has previously been termed a 'calcite-ultramylonite' (Smith et al., 2011b). This unit varies between 0-5 m thick and is cross-cut by a number of typically oriented discontinuous faults (Fig. 3.3).

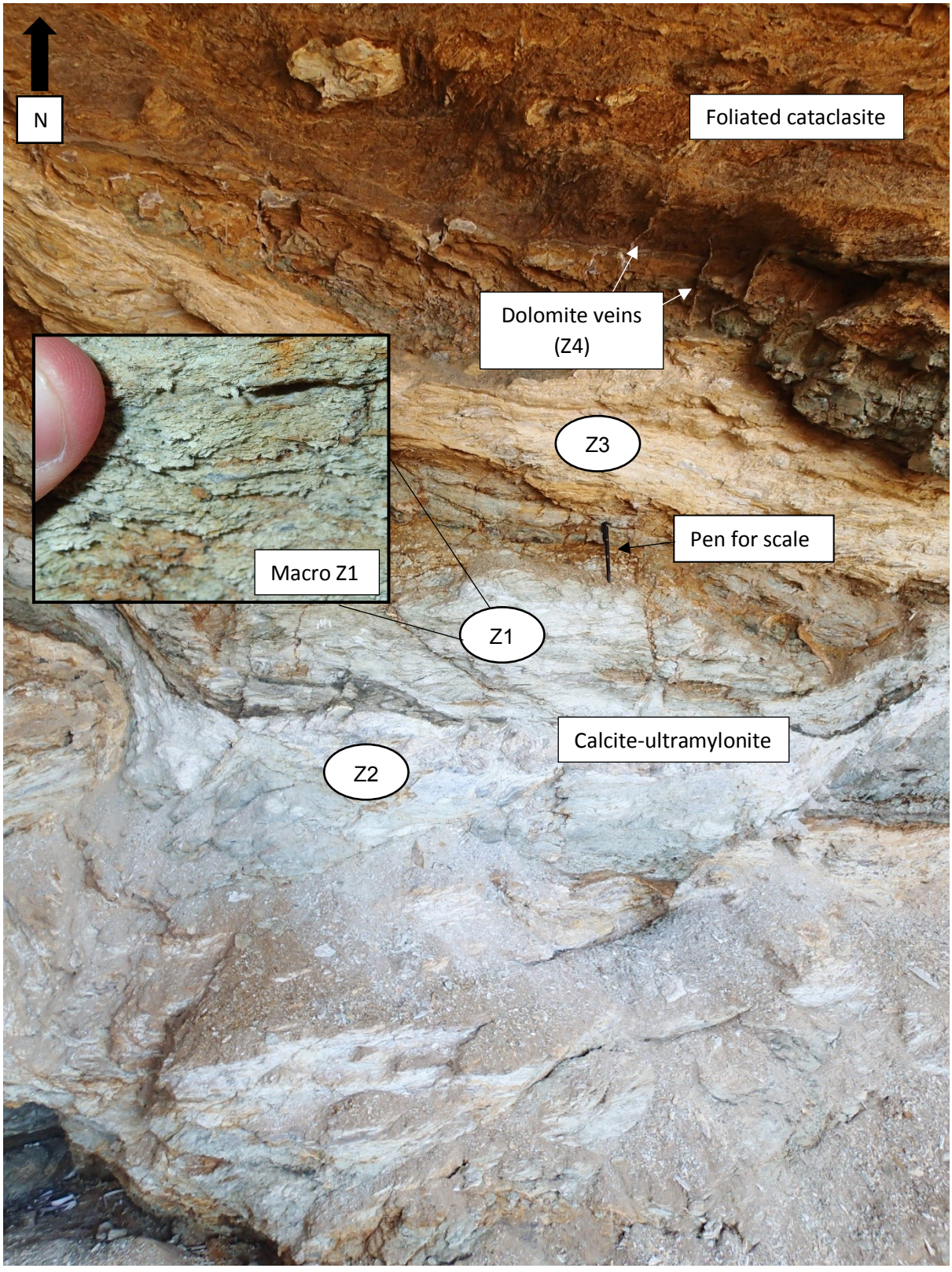


Figure 3.4 The foliated carbonate-rich fault core at Punta di Zuccale. Distinct layers were identified within the foliated fault core and labelled as Z1, Z2, and Z3. The areas where samples were taken for clumped isotope analysis are shown in circles. The zoomed in region, the macro image of Z1, shows the intense aligned foliation within these layers.

Fig. 3.4 shows the 'calcite-ultramylonite' within the Zuccale Fault core. There appear to be three distinct layers within the calcite-ultramylonite; a greenish intensely foliated pulverised layer (Z1), a white foliated layer (Z2), and an orange foliated pulverised layer (Z3). Z3 appears to be just embedded within strata above. Calcite matrix grains are oriented to the direction of the main foliation; the average (mean) long-axis orientation lies parallel. The foliation lies parallel to the direction of shear, as shown by the macro image of Z1 (Fig. 3.4).

The layer stratigraphically above the calcite-ultramylonite has been termed 'foliated cataclasite' (Smith et al., 2011b). This foliated cataclasite also hosts thin (1-3 mm wide) dolomite veins (Z4), which cross-cut at ~60^{o} (Fig. 3.3). Calcite also occupies fractures within the foliated cataclasite, although these veins (Z5) lie specifically in the roof above the core within the foliated cataclasite, cross-cutting the strata (Fig. 3.6).



Figure 3.5 Veins within the foliated cataclasite in the roof above the calcite-ultramylonite (Z1-Z3; Fig. 3.4). This foliated cataclasite layer also contains the smaller (mm-scale) dolomite veins, as reported by Smith et al. (2011a) and shown in Fig. 3.4. The larger (cm-scale) calcite veins cross-cut all other structures.

3.4.2 The Gubbio Fault

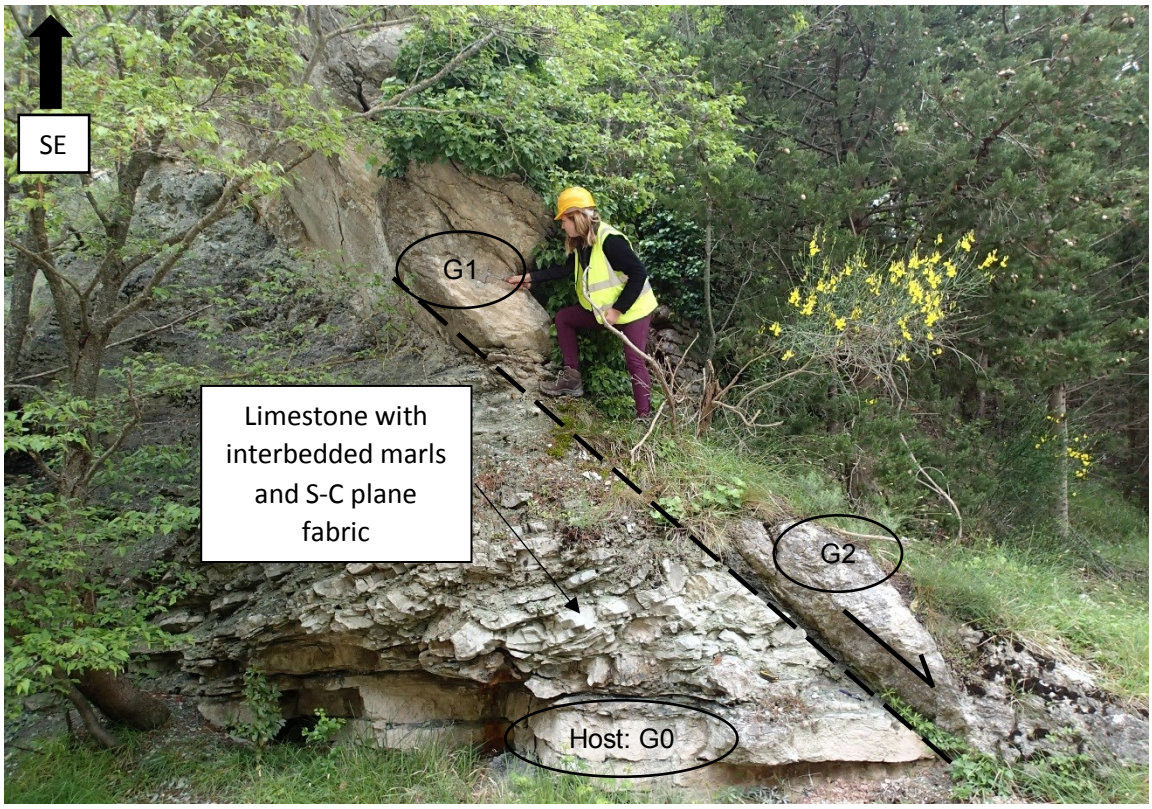


Figure 3.6 The Gubbio Fault: a classic high-angle normal fault (average dips of ~60-70° to the SW at the surface) in the Italian Apennines. Calcite samples (G1 and G2) were taken from veins and breccias (Fig. 3.7), as well as host limestone. G0 is the relatively undeformed host rock.

The Gubbio Fault (Fig. 3.6) is a typically oriented normal fault, made up of limestones and interbedded marls. The fault contact is characterised by fractures sets and breccias (Fig. 3.7). The breccias contain limestone clasts, from angular to sub-rounded, and are hosted by a crystalline calcite cement, ranging from mosaic type to b type breccia; see Woodcock and Mort (2008). The composition of the breccia varies, with some areas containing a very high proportion of crystalline cement (up to 70%), although it is difficult to discriminate between calcite clasts and pure cement (Fig. 3.7). There were no standalone cross-cutting veins, but rather veins occupying fractures (up to ~2 cm wide) within the breccias themselves and are made up of mm-cm scale calcite crystals (Fig. 3.7). The marl-rich domains exhibited pervasive foliations, containing phyllosilicate-rich pressure-solution seams. The host rock is a micritic limestone and hosts a pervasive S-C plane fabric and pressure solution seams.

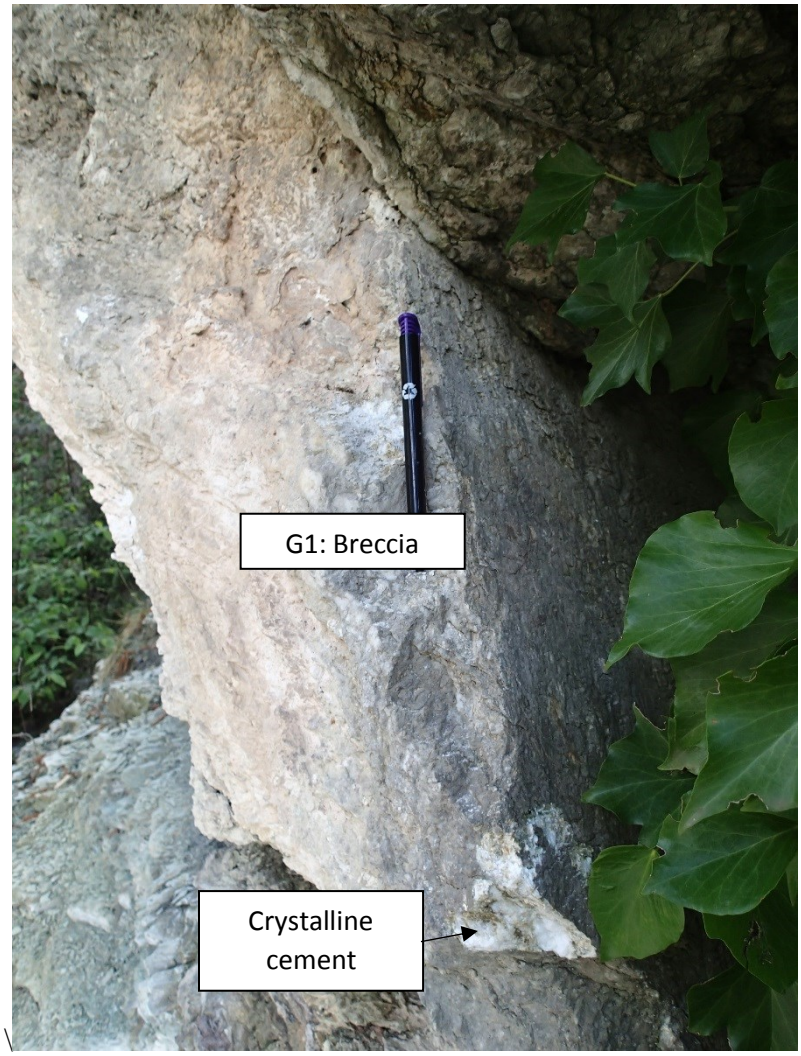




Figure 3.7 Samples taken from the Gubbio Fault.

3.4.3 Microscopy of the Zuccale Fault core: calcite-ultramylonite (Z1-Z3) and calcite veins (Z5) in the foliated cataclasite

The Zuccale Fault core is dominated by three carbonate-rich units all making up a calcite-ultramylonite; a foliated green unit (Z1), white (Z2) and orange (Z3), as shown in Fig. 3.4. Above this calcite-ultramylonite lies a foliated cataclasite, which is cross-cut by calcite and dolomite veins (Z5) (Fig. 3.5). Fig. 3.8 shows the results from optical microscopy undertaken on these samples.

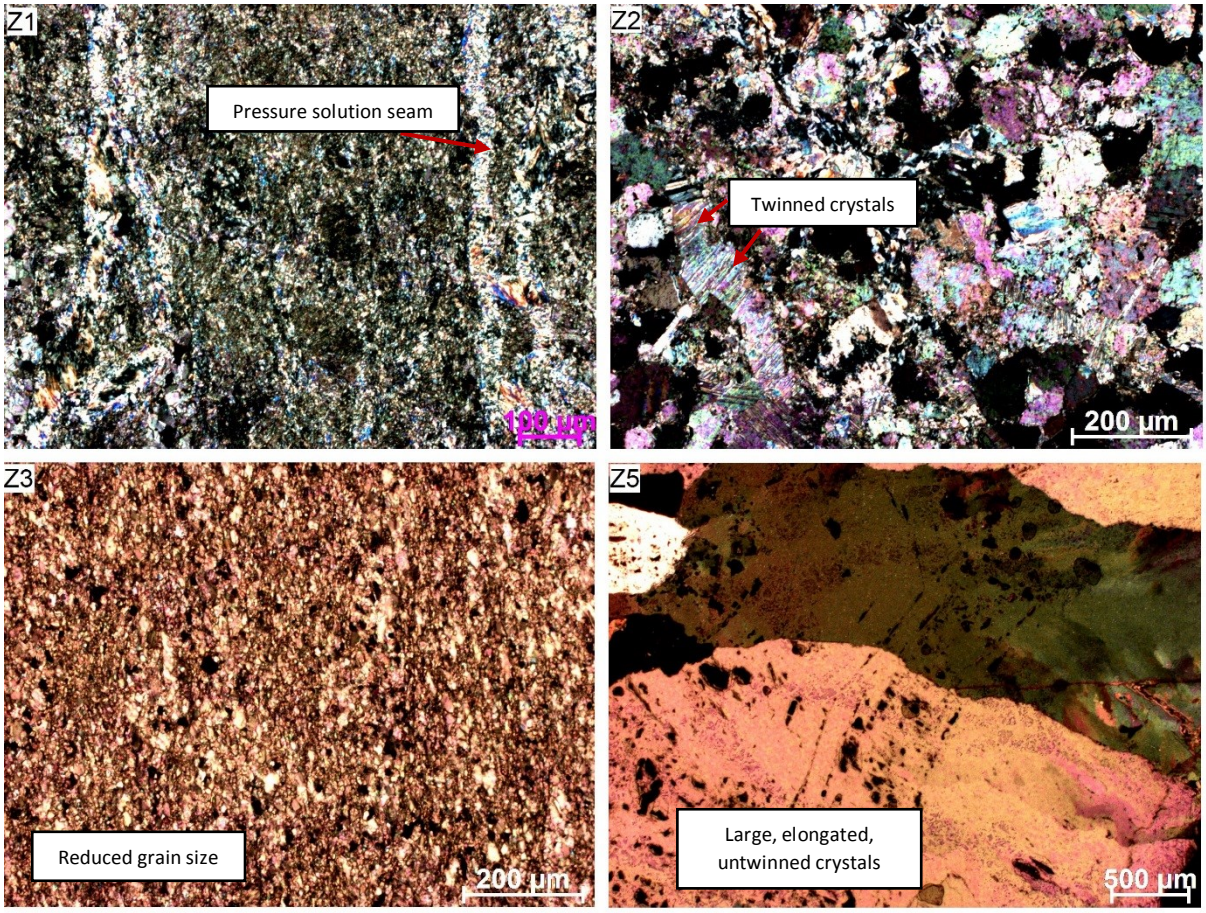


Figure 3.8 Optical microscopy of the carbonate-rich samples within the Zuccale Fault core. See Fig. 3.4 and 3.5 for sample locations.

Z1 (Fig. 3.4) contains pressure solution seams and greatly reduced grain size: all < 10 µm but a substantial portion < 5 µm (Fig. 3.8). Z1 has the smallest overall grain size, although Z3 (just above Z1, embedded just within the foliated cataclasite (Fig. 3.4)), is also distinctly small (< 10 µm). Pressure solution seams are prevalent within Z1 but are not observed within Z3 (Fig. 3.8). Z2 has distinctly larger grains than Z1 and Z3 (~100 µm), and twinning is evident in the

majority of the calcite crystals. The crystals within Z5, which make up the calcite veins in the roof of the fault core, cross-cutting the foliated cataclasite, are substantially larger than any within the calcite-ultramylonite; 1000's of μm across and of elongate-blocky morphology (Fig. 3.8). There is no evidence of deformation in the Z5 crystals, such as twinning.

3.4.4 XRD

The peaks in the XRD diffractogram define where particular atoms lie in the structure, or how much of a phase is present in a sample (Warren, 1969). By using PANalytical software, analysing the samples against the standard minerology database, it can be seen that Z1, Z2, Z3 and Z5 all contain the characteristic Bragg's peaks of calcite (Fig. 3.8). Z1 and Z2 also contain ~27.6% and 28.9% talc respectively, as shown by the additional peaks between 0-30^{o} (2θ) (Fig. 3.9; see Chapter II Methods for how these percentages were found). As shown by the difference in scale on the *y*-axis, Z5 is the 'purest' calcite sample, with the sharpest, most intense peaks, which match the standard diffractogram for calcite (Fig. 3.9).

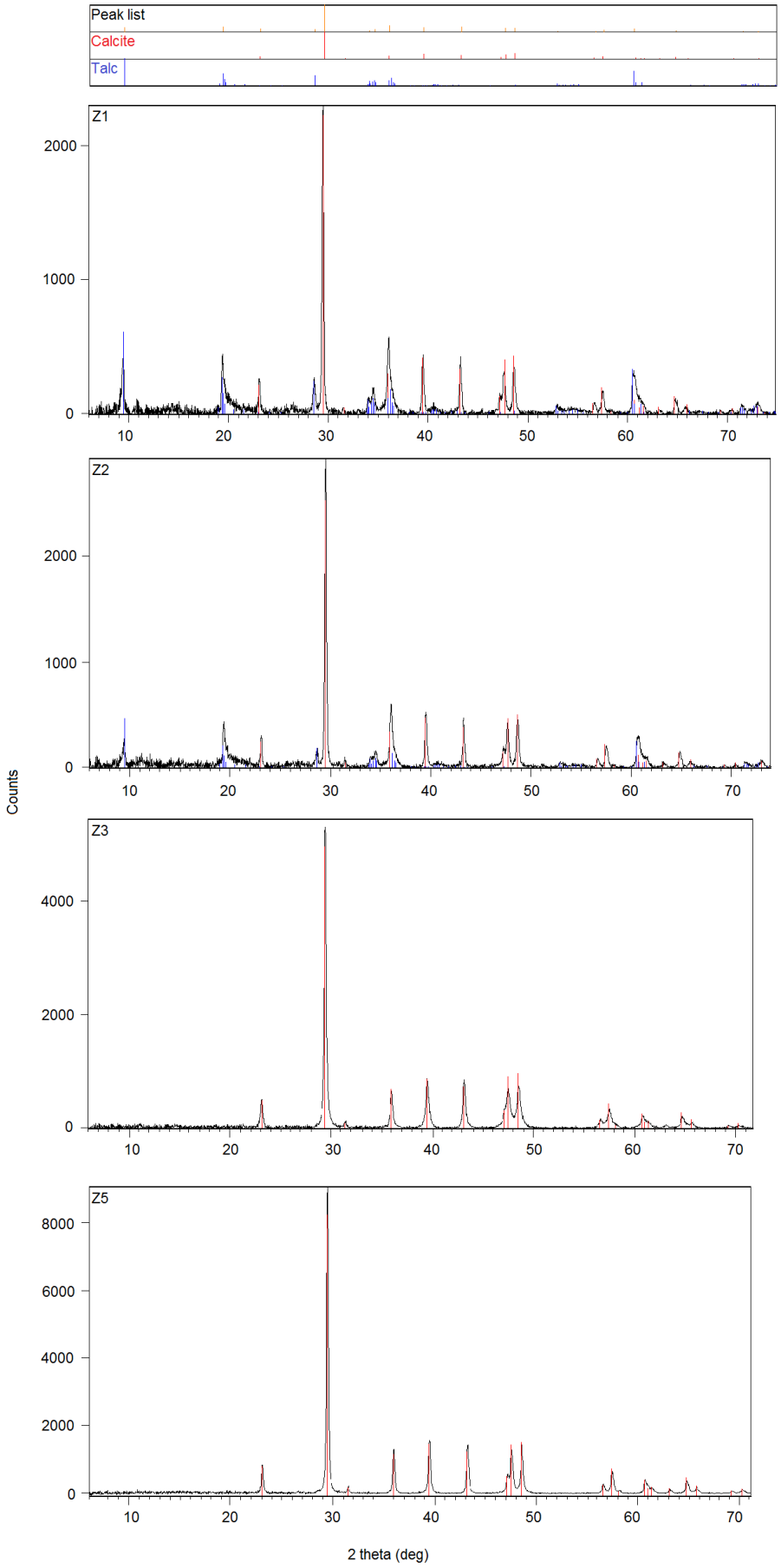


Figure 3.9 XRD diffractogram from the calcite-ultramylonite layers (Z1-Z3) and the calcite veins (Z5) in the roof of the fault core (within the foliated cataclasite).

3.4.5 Stable isotopes

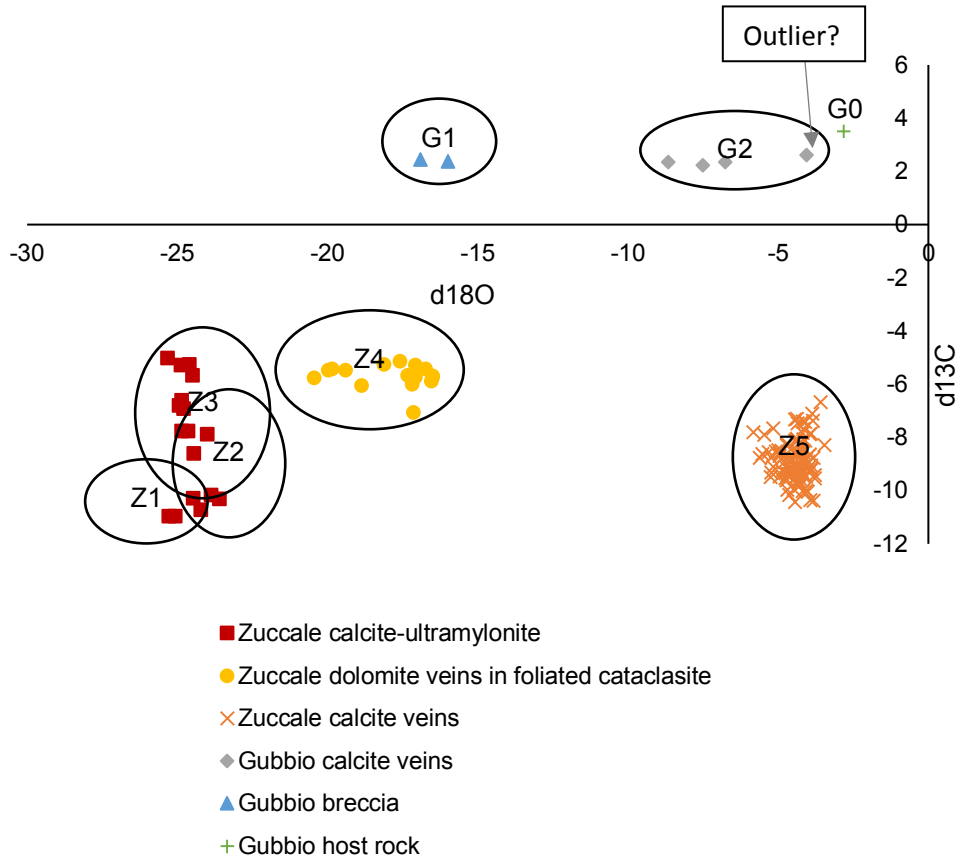


Figure 3.10 Stable isotope results from the Zuccale Fault and Gubbio Fault. All values are reported relative to V-PDB (Vienna Pee Dee Belemnite standard; see section 2.4).

There are distinct differences in the stable isotope data between the two faults. There is a limited change in the $\delta^{13}C$ values within the breccia cement or the calcite crystals in veins within the Gubbio Fault zone (+/-0.19‰) (blue triangles and grey diamonds in Fig. 3.10), whereas there is a large range of $\delta^{13}C$ values across the calcite veins and especially within the calcite ultra-mylonite (+/-2.97‰; red squares in Fig. 3.10) within the Zuccale Fault core. The $\delta^{13}C$ values of all samples taken from the Zuccale Fault core (mean -8.06‰; red squares, yellow circles and orange crosses) are far depleted compared to the values obtained for the Gubbio samples (mean 2.54‰; blue triangles and grey diamonds). Notably, however, the carbonate samples across both faults have a vast range of $\delta^{18}O$ values, and all appear to fall into distinct groups according to the sample type and location. The isotope values obtained from the Zuccale Fault fall into distinct categories according to where the sample was obtained in the fault zone, whether it was from the pervasively foliated calcite-ultramylonite (Z1-Z3; Fig. 3.4), the

dolomite veins (Fig. 3.4) or the larger calcite veins (Z5; Fig. 3.5). The $\delta^{18}O$ values from cements and veins across the Gubbio Fault also fall into groups depending on whether they were from a breccia cement sample (blue triangles, Fig. 3.10), pure calcite crystals in a vein (grey diamonds, Fig. 3.10), or the host rock (green cross, Fig. 3.10), although the latter two groups are slightly less distinct than the groupings for carbonate from the Zuccale Fault (Fig. 3.10) (there is one potential outlier; Fig. 3.10). There are no samples from the Gubbio Fault (blue triangles, grey diamonds) which are as depleted in $\delta^{18}O$ as those found on the Zuccale Fault (red squares and yellow circles).

3.4.6 Qualitative constraints on temperature: clumped isotopes and fluid inclusions

3.4.6.1 Clumped isotope analysis

Table 3.1 Results from clumped isotope analyses of the Zuccale Fault core. The values obtained for $\delta^{13}C$ V-PDB and $\delta^{18}O$ V-PDB correspond well with the values independently obtained from solely stable isotope analyses (Fig. 3.10).

Name	Type	Mass Spec	$\delta^{13}C$ V-PDB	$\delta^{18}O$ V-PDB	Δ47	Average T˚C	T interval ± 1 SE		T interval ±95%	
Z1	Calcite-mylonite	Pinta	-10.67	-23.75	0.318					
Z1	Calcite-mylonite	Pinta	-10.71	-23.78	0.306	**451**	399	518	177	∞
Z1	Calcite-mylonite	Pinta	-10.64	-23.72	0.33					
Z2	Calcite-mylonite	Pinta	-10.2	-22.99	0.395					
Z2	Calcite-mylonite	Pinta	-10.14	-22.89	0.399	**234**	228	241	166	350
Z2	Calcite-mylonite	Pinta	-10.26	-23.09	0.391					
Z5	Calcite vein	Pinta	-8.88	-4.27	0.73	**10**	-6	29	-19	52

Table 3.1 shows the clumped isotope results from the calcite-ultramylonite layers within the Zuccale Fault core (Z1, Z2) and the calcite veins (Z5) which cross-cut the foliated cataclasite. These samples were selected due to their notable differences in grain size and textures (see Fig. 3.4 and 3.5 for their location within the fault core and Fig. 3.8 for the microscopic images). By utilising the independent parameter Δ47, which is obtained from clumped isotope thermometry, the temperature of precipitation independent of the fluid source composition can be obtained (see section 2.4 for further details). The data shows that the layer, which has distinctly reduced grain size within the calcite ultramylonite in the Zuccale Fault core, Z1 (Fig. 3.8), was subject to high temperatures at the time of calcite precipitation (~451°C). The adjacent, stratigraphically lower layer, Z2, (Fig. 3.4) which contained significantly larger (~100 μm) calcite crystals (Fig. 3.8) was subject to a precipitation temperature of ~234°C. The clumped isotope data obtained for Z5 indicated that the calcite veins precipitated in much lower temperature conditions, as indicated by the maximum precipitation temperature of 29°C yielded by clumped isotope thermometry (Table 3.1).

3.4.6.2 Fluid inclusion analysis

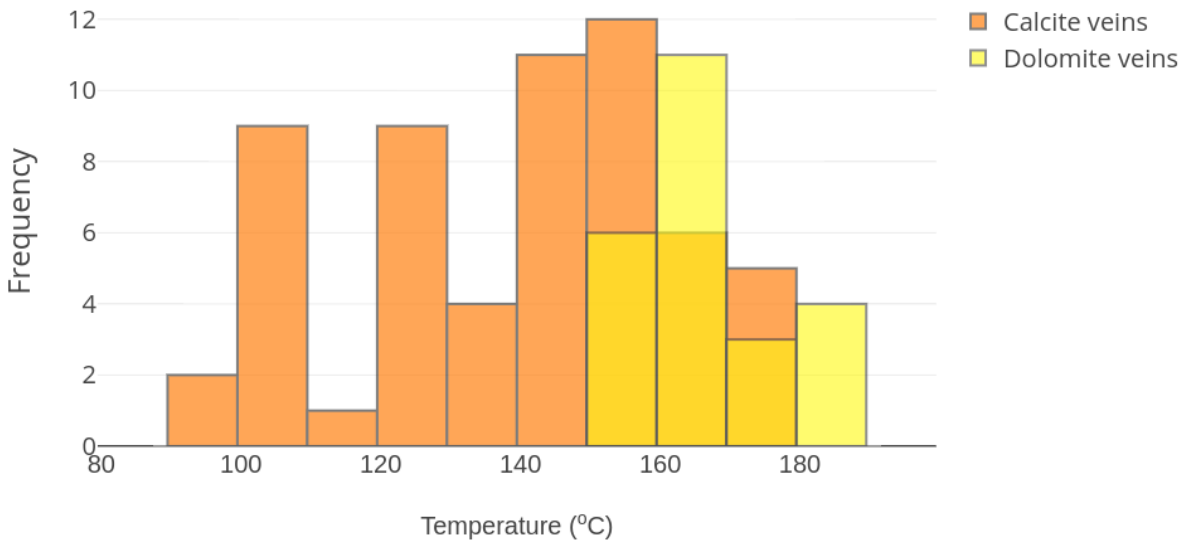


Figure 3.11 Fluid inclusion analyses from the dolomite veins and calcite veins in the foliated cataclasite layer of the Zuccale Fault.

The largest and smallest fluid inclusions within the calcite veins (Z5) were 124.1 μm and 2.7 μm in diameter respectively, with an average of 27.8 μm. The largest and smallest fluid inclusions within the dolomite veins were 10.1 μm and 2.9 μm in diameter respectively, with an average of 7.1 μm. The temperature indicated by analysis of fluid inclusions within the dolomite veins (Z4) averaged at 165.7ºC over a relatively small range (+/-16.6ºC) compared to that of the calcite veins (Z5; +/-42.8ºC) (Fig. 3.11). Perhaps most importantly, the average temperature obtained by fluid inclusion analysis (137.7ºC) within the calcite veins (Z5) is distinctly different to that obtained by clumped isotope analysis (Table 3.1), by +127.7ºC.

3.5 Discussion

The study of the different components of the Zuccale Fault core utilising a multi-disciplinary approach has shed light on the conditions and fluid sources which may have permitted slip at a non-optimal angle. This includes a study of the textures in the fault core (Fig. 3.8), their crystallography and content (Fig. 3.9) combined with constraints on the fluid source (stable isotope results, Fig. 3.10) and constraints on temperatures achieved within the pervasively foliated calcite-ultramylonite and foliated cataclasite (Table 3.1 and Fig. 3.11).

3.5.1 The role and formation of the calcite veins

The cross-cutting relationships of the larger calcite veins in the foliated cataclasite in the Zuccale Fault core (Fig. 3.5), the size of the crystals and the lack of deformation (i.e., twinning) within the crystals (Fig. 3.8) indicates that these veins occurred post-deformation. The clumped isotope results also support a low-temperature (max 29ºC) origin (Table 3.1). Furthermore, the $\delta^{18}O$ values for these larger calcite veins are comparable to all but one of the pure calcite veins from the Gubbio Fault (Fig. 3.10). Notably, the outlier of the Gubbio Fault vein signatures (Fig. 3.10), which exhibited the least depleted $\delta^{18}O$ signature aside from the Gubbio host rock, was difficult to extract without touching the surrounding limestone clasts (Fig. 3.7). Given its median value between the host rock isotope signature and the other calcite veins, I suggest that this particular sample has been buffered by the host rock signature from the surrounding limestone clasts during analysis, yielding a $\delta^{18}O$ signature closer to that of the host rock.

In the Gubbio samples, the breccia cements had depleted $\delta^{18}O$ values comparable to the $\delta^{18}O$ values of the dolomite veins in the foliated cataclasite in the Zuccale fault zone (Fig. 3.10). Given that brittle deformation processes are likely to be the dominant deformation mechanism which led to the formation of these samples (cataclasis, hydrofracturing), precipitation temperature should be 150-200°C (Blenkinsop and Rutter, 1986; Smith et al., 2011a). The fluid

inclusion data (Fig. 3.11) is in strong agreement with this, yielding an average temperature of 165.7ºC.

Based on the overall stable isotope groupings between the breccia cements and the veins from the Gubbio Fault (Fig. 3.10), it appears as if the more depleted breccia cements reflect the conditions associated with cataclasis, whereas the veins are due to the subsequent infill of fractures produced during deformation. However, the value for the precipitation temperature obtained for the Zuccale calcite veins from fluid inclusion analysis (Fig. 3.11) does not correlate with the temperature obtained from clumped isotope analysis (Table 3.1), yielding a value of 137.7ºC compared to the clumped isotope upper limit of 29ºC. A large error resulting from the rate of heating used during fluid inclusion analysis may have led to shifted values (Harker, 1971). Another possibility is that the inclusions are secondary inclusions, and rather are evidence of subsequent precipitation of higher temperature fluids, but this is also unlikely given the previously constrained deformation history obtained from structural relationships and regional evidence (Collettini and Holdsworth, 2004; Smith et al., 2008; Smith et al., 2011a; Smith et al., 2011b). Notably, however, the size of the inclusions available were, at maximum, a tenth of the size of fluid inclusions required for accurate fluid inclusion analysis (Lazar and Holland, 1988). This is quite typical of fluid inclusions within carbonates; they are generally quite small and therefore it is more difficult to produce meaningful results from them; however, given their abundance within the veins, it was important to at least attempt to gain some qualitative information from them. Furthermore, the distinct different groupings between the dolomite veins and calcite veins in the stable isotope analysis (Fig. 3.10) should yield a much larger temperature difference than what is observed in the fluid inclusion analysis (Fig. 3.11). However, given the extreme discrepancy between the fluid inclusion and clumped isotope analyses, repeated analysis using both these methods on new samples should be undertaken to try to obtain the correct temperature for these calcite veins. Furthermore, this discrepancy puts the precipitation temperature obtained for the dolomite veins into question, although the temperature obtained does support brittle deformation, and correlates well with the temperature that the Gubbio breccia samples would have been formed at, assuming cataclasis.

Assuming that the clumped isotope analysis has yielded correct limits for the precipitation temperature of the larger calcite veins in the foliated cataclasite within the Zuccale Fault, the precipitating fluid for these veins would have a $\delta^{18}O$ signature of -2‰ to -4‰ (see section 2.4), which is slightly more depleted that the dolomite veins precipitating fluid. This may reflect a shift in the isotopic values for the fluid source, especially since the larger calcite veins are

believed to be more recent, and thus may be reflective in a change in fluid isotopic signature over time. If it is purely reflective of a slightly different fluid source, or a mix of fluids, given current isotopic compositions of rainwater averaging -4.7‰ (Liotta et al., 2008), this signature could reflect a more meteoric input, but likely with an input of seawater (closer to 0‰). The $\delta^{13}C$ values are distinctly lower than those of the dolomite veins (Fig. 3.10), however, which suggests a different carbon source. They are also wider ranging values, which may indicate an organic carbon source. The mudstones of Complex V would be a realistic carbon source for these calcite veins. Given that this Complex forms part of the hanging wall and footwall, and is extensively fractured, fluid-rock interactions would have occurred relatively easily in this setting. Overall it makes sense that the calcite veins are a post-deformational stage, whereby the calcite has precipitated within pre-existing fractures. This supposition is supported by the lack of evidence of any deformation within the veins and both the stable and clumped isotope results. This would also exclude any contribution from any other fluids in these larger, post-deformational calcite veins. Again, the offset of the fluid inclusion analysis warrants further investigation, but the temperature values obtained from this method does not correlate with any other evidence.

3.5.2 Different fluids circulating within the Zuccale and Gubbio Faults

The stable isotope data (Fig. 3.10) shows distinct groupings and relationships between the $\delta^{13}C$ and $\delta^{18}O$ values, depending on the sample location in the Zuccale Fault core. Notably, the calcite ultramylonite and dolomite veins are highly depleted in $\delta^{18}O$ in comparison to the calcite veins in the fault core roof (Z5). Given that $\delta^{18}O$ depends on both temperature and fluid source, these different carbonates within the same core have either precipitated from different fluids or at distinctly different temperatures. The distinct depletion in $\delta^{13}C$ and greater depletion of $\delta^{18}O$ values from the Zuccale Fault samples in comparison to the Gubbio Fault samples indicates a distinctly different carbon source and higher temperature fluids/a different fluid source operating within the two faults (Fig. 3.10). However, the clumped isotope analysis indicates that the high depletion in $\delta^{18}O$ in the calcite-ultramylonite is due to distinctly higher temperatures of 451°C in the centre of the fault core, which drops to 234°C in adjacent strata ($\leq$ 25 cm away, see Fig. 3.4). The greater range and significant depletion in $\delta^{13}C$ values from the Zuccale Fault samples compared to the Gubbio Fault samples (Fig. 3.10) may indicate a range of carbon sources, and/or be reflective of interaction with rising pluton on Elba which would have had a very different carbon source to that of the Gubbio Fault.

As previously noted, the Zuccale Fault has an overall dome shape, reflective of the shape of the rising Porto Azzuro pluton, which was supposedly rising whilst the Zuccale Fault was active (Smith et al., 2011a). Other plutons on Elba grew by horizontal expansion followed by vertical inflation (Cruden and McCaffrey, 2001). If this were the case for Porto Azurro, this would indeed allow the Zuccale Fault to take on a dome shape. It is reported that (i) the margins of the Porto Azzuro pluton on the north, south and west sides of Monte Calamite on Elba are associated with north-, south- and west-dipping portions of the Zuccale Fault, (ii) surface outcrops of the pluton coincide with an elevated fault surface, (iii) regional-scale variations in the fault shape correlate with the super-imposed pluton position and (iv) the 'doming' of the fault has exposed Complex I schists near Monte Calamite (Smith et al., 2011a).

Previous studies concluded that the Porto Azzurro pluton had an extensive meteoric-hydrothermal fluid system (Taylor and Turi, 1976). Assuming that the fluid inclusion analysis (Fig. 3.11) for the dolomite veins has some grounding and by utilising the stable isotope data (Fig. 3.10), from standard calculations (see section 2.4 and Friedman and O'Neil (1977)) the precipitating fluid would have had a $\delta^{18}O$ signature of ~2‰ to -4‰, which is reflective of seawater or meteoric fluids. This would suggest that the veins precipitated from hot fluid sourced from seawater or meteoric fluids, or mixed. A reasonable source would be the Porto Azzurro pluton meteoric-hydrothermal system. The $\delta^{13}C$ signature in these dolomite veins correlates well with the $\delta^{13}C$ signature of -6‰ for mantle derived CO_2, which has been found to be present in groundwater springs along the present-day Tyrrhenian coast of Italy (Chiodini and Cioni, 1989; Minissale, 2004; Minissale et al., 2000). There is evidence that sub-horizontal footwall faults, approximately parallel to the Zuccale fault, may have been active during igneous sheet intrusions related to the pluton (Smith et al., 2011a); these intrusions may be the source of the carbon.

The calcite-ultramylonite also has a much more depleted $\delta^{18}O$ signature, which is indicative of higher temperature and/or a different fluid source (Fig. 3.10). Assuming that the clumped isotope results (Table 3.1) have yielded a correct indication of the temperature within these calcite ultramylonite layers, a fluid source isotopic signature can be obtained without making any assumptions on temperature (see section 2.4 for more information). I would therefore expect a fluid source isotopic signature of ~4‰ to -2‰ from standard calculations (Friedman and O'Neil, 1977; see Fig. 2.5 and Equation 2.4), representing a positive shift from the dolomite veins fluid source. This enriched $\delta^{18}O$ signature for the fluid from which the calcite-ultramylonite layers suggests greater interaction with degassing igneous bodies (notably,

feldspar megacrysts from the Porto Azzurro pluton yielded a $\delta^{18}O$ signature of ~5‰ (Taylor and Turi, 1976) which supports this shift). The wider range of $\delta^{13}C$ signatures may also indicate interaction with a greater range of country rocks. The different isotopic signature of the dolomite veins and calcite veins supports previous works (Smith et al., 2011a) that further exhumation was associated with a switch from dolomite to calcite as the principal syn-tectonic fault cement i.e. a change in fluid source.

3.5.3 Weakening mechanisms within the Zuccale Fault core

In order for slip to occur on such a non-optimally oriented fault, there must be intense weakening mechanisms that make slip on an LANF more favourable than simply creating a new fault. The clumped isotope results (Table 3.1), XRD (Fig. 3.9), field observations (Fig. 3.4) and microscopic analysis (Fig. 3.8) in particular suggest possible explanations.

Within the calcite-ultramylonite in the Zuccale Fault core, clumped isotope analysis (Table 3.1) has yielded a 217°C temperature difference between adjacent layers. Structurally, Z1, which has an estimated precipitation temperature of ~451°C, is effectively 'capped' by the foliated cataclasite above. It is possible that the higher temperature observed in Z1 may be due to intense frictional heating associated with fault movement, focussed in a very thin layer (the principal slip zone (PSZ)), which decreases exponentially away. A high temperature could also pulverise carbonate in the fault core, as observed (Fig. 3.4). However, it must be noted that the clumped isotope results (Table 3.1) are not well constrained, even with multiple analyses, and thus this layer may in fact have yielded a similar precipitation temperature to the adjacent strata. From the data obtained however, the possibility that there is a concentration of particularly high-temperature fluids within the fault core needs to be explored.

The distinctly higher temperature in Z1 compared to adjacent layer Z2 may reflect a distinct concentration of hot CO_2-rich fluids in this layer, trapped against the above strata, which exponentially decreases away from this contact. The effective trapping of hot fluids from intrusions related to pluton emplacement within this relatively thin layer of strata may start to explain how the non-optimally oriented fault underwent slip. Several researchers have suggested that deeply derived CO_2-bearing fluids have played a role in the nucleation of crustal earthquakes in central Italy (Chiaraluce et al., 2007; Collettini and Barchi, 2002; Miller et al., 2004), but in this setting, a combination of factors may have yielded slip at a low angle. Distinctly higher temperature fluids (> 450°C) within carbonate may also indicate more ductile deformation mechanisms, such as thermal softening, 'frictional–viscous' creep and grain-size

sensitive deformation mechanisms. Furthermore, pressure and strain association with emplacement of the pluton may have yielded intense foliation in the strata, like that observed (Fig. 3.4). Such intense foliation is indicative of significant differential pressure or shear. Recent experimental work has shown that, in foliated rock, foliations with orientations of 0-30^{o} produce initial failure at low shear stress (Ikari et al., 2015). The fabric acts to produce a form of lubrication, enabling slip at lower shear stress. Furthermore, it has been shown that samples with well-developed foliation are extremely weak compared to their powdered equivalents (Collettini et al., 2009).

There is also a reasonable percentage of talc within layers Z1 and Z2 (Fig. 3.9; up to 28.9%). Talc is a distinctly weak mineral, has a coefficient of friction of ~0.3, does not adhere to Byerlee friction rules, and is even weaker in the presence of fluids (Behnsen and Faulkner, 2012; Ellis, 2014; Horn and Deere, 1962; Moore and Lockner, 2008; Rutter et al., 2009). Hydrothermally generated talc, which has penetrated the fault zone, may have also distinctly reduced the coefficient of the fault.

Ultimately, the influx of hydrothermal fluids may have created a self-perpetuating positive feedback effect, which enabled slip at a non-optimal angle (see Fig. 3.12). First of all, pressure and strain association with pluton emplacement may weaken the above strata. An influx of hot fluids may have enabled mechanisms such as pressure solution in carbonate, leading to pressure solution seams and grain size reduction (Fig. 3.8), both of which are observed in Z1. An influx of hot fluids may also have introduced hydrothermally generated minerals, such as talc, which has a distinctly low coefficient of friction, thus would have significantly reduced the coefficient of sliding friction. Furthermore, strain accompanying reactions leading to the production of hydrothermally generated minerals may have induced the new minerals in a preferred orientation, thus yielding foliation in the affected strata, which was observed (Fig. 3.4). This may also be a result of strain from emplacement of the pluton. The concentration of hot fluids within a relatively small region may generate large fluid overpressure, which, from a purely mechanical perspective, would exacerbate the likelihood of slip. Increased strain due to enlargement of the pluton, or initial slip, dominated by strain and thermal softening and grain-size sensitive deformation mechanisms during the high-pressure hydrothermal conditions may have oriented the foliation parallel to the shear stress. The combination of these mechanisms would have led to a distinct anisotropy in strength and frictional properties between the host rock and the Zuccale Fault core (see Fig 3.12). Fundamentally, this interpretation agrees with the works of Collettini and Holdsworth (2004) and Smith et al. (2011a).

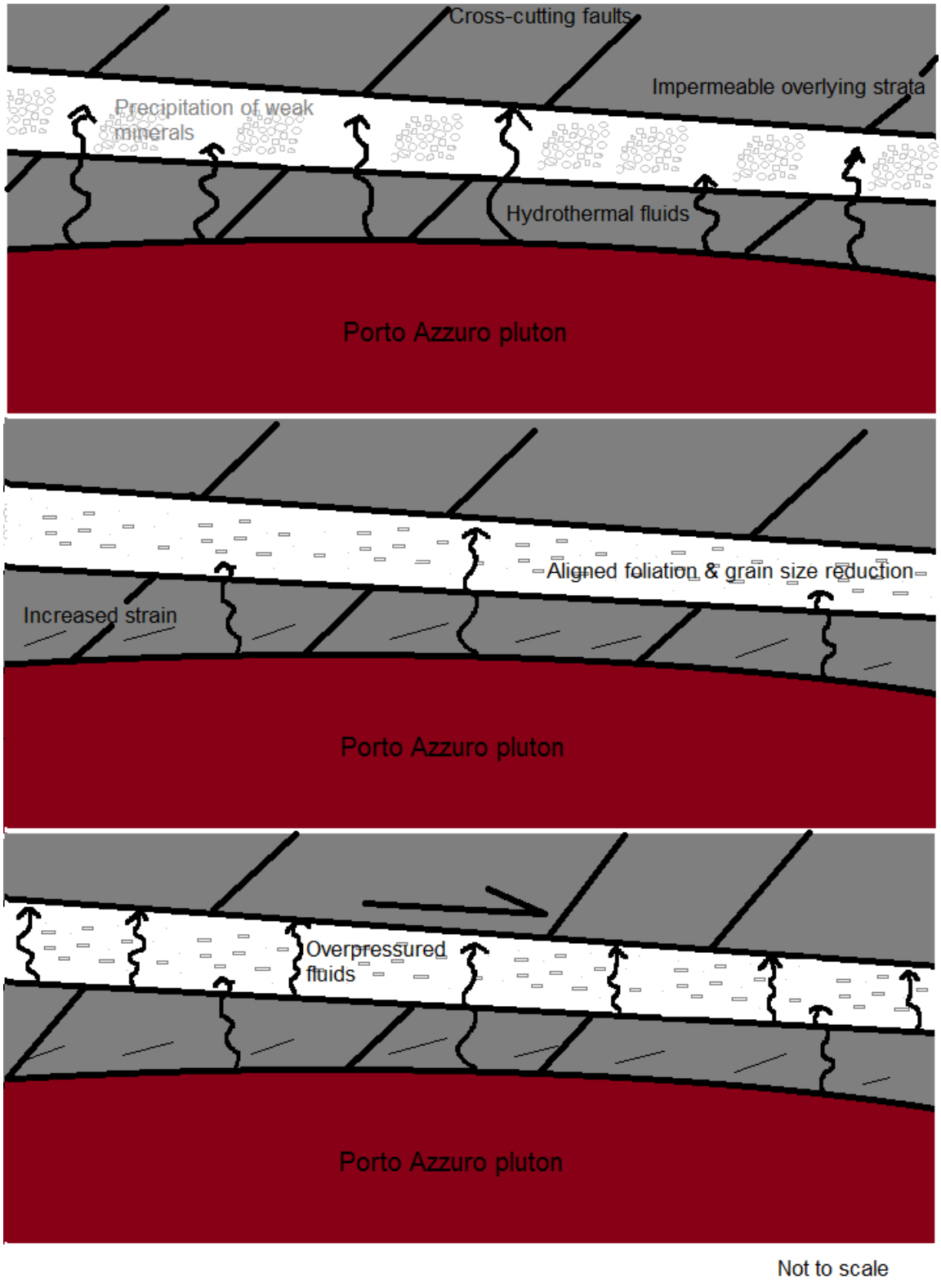


Figure 3.12 Weakening processes due to placement of the Porto Azzuro pluton which enable slip. Emplacement of the Porto Azzuro pluton weakens the crust directly above. Subsequently, the release of hydrothermal fluids provides an influx of weak minerals and fluids into the fault zone, leading to dissolution. Increased strain from pluton emplacement/ the combination of reaction and deformation inducing talc leads to preferred mineral orientation. Increased pressure increases the pressure of the pore fluid, which is trapped against the above strata. A combination of these aforementioned weakening methods (weak minerology, foliation and high pore fluid pressure) could enable slip on a sub optimally oriented fault.

Along with being the fluid source for precipitating fluids during deformation, the transient, repetitive nature of intrusions could have caused large temperature fluctuations (Lister and Baldwin, 1993). It has previously been shown that if a pre-existing weakness exists at a non-optimal angle for reactivation, the rock will form a new fracture at the optimum angle, cross-cutting the pre-existing weakness (Mitchell et al., 2011). However, these experiments do not consider the presence of weak minerals, excessively localised pore fluid pressure, nor the distinct effect of intense, optimally oriented foliation. The work of Ambrose et al. (2014) showed that, within highly laminated shales, weaknesses where $\beta < 10^{o}$ are cross-cut, and weaknesses where $\beta > 45^{o}$ are followed (where the angle, β, is the angle between the plane of weakness and the maximum principal stress; see Fig. 1.5). However, when planes of weakness are oriented between β=10-45^{o}, the failure surface follows an irregular path that jumps between the weak plane and the matrix. In this case, the discontinuous weak planes must provide an alternative path of least resistance, resulting in strength lower than the shale matrix strength. This mixed-failure mode due to competition between the matrix and the weak planes causes an uneven distribution of high stresses, resulting in shale failure at lower strength than the JPW model prediction (Ambrose et al., 2014, also see Chapter I). This data may also indicate that rather than repetitive intrusions on the Zuccale Fault, the smaller cross-cutting faults may in fact represent the failure surface jumping between the very weak carbonate-rich fault core and the production of more optimally oriented faults. During times of higher temperatures and greater CO_2-rich fluid influx, hydrothermal fluids which generated high overpressure could have been concentrated in a thin layer within the fault core and permitted slip. During cooler periods, cataclasis may have dominated, producing the high-angle east dipping faults (Fig. 3.3). The mixed fluid source during a cooler period may be a result of a lower quantity of hydrothermal fluids being available, due to reduced intrusion activity or/and associated fracturing during cataclasis, permitting a greater influx of meteoric fluids/seawater. Collettini and Holdsworth (2004) appear to favour a phase of pervasive cataclasis followed by weakening processes permitting 'frictional–viscous' creep as opposed to the failure surface jumping between the very weak carbonate-rich fault core and the production of more optimally oriented faults.

I conclude that the initial formation of the weakness that was to become the Zuccale Fault was due to the rising pluton beneath, resulting in intense foliation and intensely concentrated hydrothermal fluids, and precipitation of talc, which permitted slip at a non-optimal angle (Fig. 3.12). A suggested positive feedback loop of (i) initial concentration of mantle-bearing fluids

(during progressive exhumation due to pluton emplacement) (ii) thermal softening, high fluid pressure, intense foliation, presence of weak minerals, grain-size sensitive deformation mechanisms and flow, indicates that chemical changes, which are not addressed in standard Andersonian rock mechanical theory (Axen and Karner, 2004), may be exceptionally important in the weakening of, and general evolution of, faults. Notably, when hydrothermal fluids are not present to intensify foliation, input weak minerals, generate excess fluid pressures and enable strain softening and grain-size sensitive deformation mechanisms, cataclasis will dominate and produce optimally oriented, cross-cutting faults (Fig. 3.3). Rock deformation experiments which test whether locally high pore fluid pressures within foliations containing talc at high temperatures can generate slip at low angles, as opposed to producing a new optimally oriented fracture, should be performed, effectively combining previous experimental works of Collettini et al. (2009), Ambrose et al. (2014), Ikari et al. (2015), and Mitchell et al. (2011).

The weakening mechanisms identified during this study may have wide applications to other examples of LANFs worldwide, and their role in strain distribution. In the case of the Zuccale Fault, there are numerous mechanisms that may act to produce a distinctly weak zone, which is easier to redistribute stress along, rather than creating a new optimally oriented fault. Given the extreme combination of factors that are operating here (high pore fluid pressure, hot fluids, dissolution processes, weak minerals and intense foliation) I suggest that LANFs may only occur within specific boundary conditions. This illustrates that chemical reactions, enabled by the presence of hot fluids, may be exceptionally important in controlling fault frictional properties, which are not explained by standard Andersonian rock mechanical theory. The role of hot fluids enabling fault weakening appears to be of importance in permitting the existence of LANFs, especially related to the overpressures and thermal softening induced (Ando, 1979; Crittenden et al., 1980; Parsons and Thompson, 1993). Notably, hot silica-saturated fluids probably ascend along most detachments (Axen, 1992). Where such activity is not apparent, evidence of weak minerology, fabrics or indeed the possibility of fault rotation should be investigated. Such conditions suggest, however, that LANFs are unlikely to accommodate significant brittle faulting.

Chapter IV, Part I: Characterisation of fluid-fault interaction products: An example from the Gulf of Corinth, Greece

Fluid-fault interactions within fault zones are complex, with fault rock being continuously modified by co-seismic fluid circulation and subsequent precipitation within fractures. The uplifted, exhumed, and Holocene-active Psatha Fault in the Gulf of Corinth, which contains extensive calcite cementation, enables such fluid-fault interactions and fault evolution to be studied. In Part I of this work, I have studied the products of fluid-rock interactions within this fault zone, inclusive of breccias and veins utilising field studies, optical and cathodoluminescent microscopy and stable isotope analyses. Part II of this study utilises rock deformation experiments on the Psatha Fault rock hosting pre-existing veins to assess how pre-existing textures may influence future fracture propagation and slip. The results from Part I indicate that the Psatha Fault underwent deformation both above and below the water table, followed by precipitation from purely meteoric fluids within fractured rock. Carbon and oxygen stable isotope geochemistry reveal that meteoric water dominated the fluid-flow both above and below the water table. In addition, the variation in the isotopic signals between different cements are indicative of changing water temperature and/or composition fluctuations during fault zone evolution. This supports an interpretation of progressive uplift of the fault across the water table and constrains the possible timing of deformations events during uplift.

4.1.1 Introduction

The process of brittle failure in the crust is viewed as a mechanical system; there is a critical stress to overcome, at which point fracturing or slip on a pre-existing fault will occur. This standard Andersonian mechanical theory assumes that the host rock, that comprises the fault zone is made up of homogeneous material. However, fault zones are considerably more complex than are envisaged in such an idealised model. They typically contain structures imparted by previous seismic events, which introduce heterogeneities over all scales. Many of these structures are produced due to the interactions between fluids and rock in the fault zone (fractures, gouges, breccias, veins; see Sibson, 1977 and Sibson, 1986a). Mechanically, as per Mohr theory (Fig. 4.1.1), the presence of fluids within a fault zone reduces the effective stress acting on a fault and hence brings the fault closer to failure (Beeler et al., 2000; Price, 1966; Sibson, 1977; Sornette, 1999; Streit and Hillis, 2004).

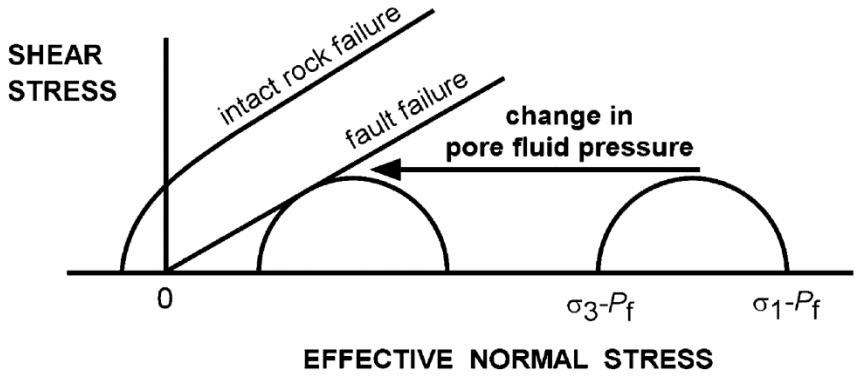


Figure 4.1.1 The mechanical effects of fluids (from Streit and Hillis (2004)).

The standard dilatancy/fluid-diffusion model for shallow earthquakes describes a dilatational response of the crust to the rising tectonic shear stress preceding earthquakes, accompanied by the opening of extension fractures and a fluid pressure decrease (Sibson, 1981). This gradient flux permits a slow migration of fluid from the surrounding crust to the focus of the subsequent earthquake, which allows the fluid pressure to rise again, i.e., the processes of deformation and fracturing increase the permeability of the fault zone and permits inflow of fluids (Hausegger et al., 2010). This coupled deformation-fluid-flow preceding an earthquake is indicated by changes in the P-wave to S-wave velocity ratio (i.e., a decrease during initial fracturing and increase during water influx) (Scholz et al., 1973). Such changes have been identified in foreshock sequences preceding large seismic events, notably four days preceding the mainshock in the case of the 1975 Haicheng earthquake (Jones et al., 1982). Although the mechanical effects of fluids are clearly important, the chemical reactions between minerals and fluids have also been identified as being significant to the earthquake system (Brace, 1972). In addition to water infilling fractures prior to rupture and causing pore fluid pressure increase, rupture also propagates due to chemically activated subcritical crack growth processes, inclusive of stress corrosion and dissolution (Sornette, 1999). Following a seismic event, not only does a fault zone act as a passageway for fluid-flow, with fractures and irregularities serving as channels (Sibson et al., 1975), the presence of fluids will lead to significant sealing and healing of cracks in the duration of the seismic cycle (Atkinson, 1984), whereby flow outwards is prevented by a seal of mineral precipitation (Blanpied et al., 1992; Byerlee, 1993; Faulkner and Rutter, 2001). These interactions between fracturing and fluids produce characteristic features in a fault zone. The structures, fabrics and textures produced are characterised in accordance with many variables, including the initial fault zone characteristics

(porosity, permeability, strength), the geological setting and fluid migratory paths and content which may have permeated the fault zone (Eichhubl et al., 2009; Knipe et al., 1997). Early fracturing is overprinted by the formation of fissure fills, including gouges, breccias and veins through localised slip, which characterises the fault core (see Fig. 1.1). These processes of fracturing and infilling are progressive, and lead to permeability differences across the fault core, which characterise the different evolutionary stages (Storti et al., 2003). The term 'fault-rock recycling' (Wibberley and Shipton, 2010) is associated with the permeability and structural changes in a fault zone due to fluid-rock interactions. During a fault zone's evolution, the original rock properties are continuously modified, which then influences the fluid-flow processes and deformation mechanisms in the next seismic cycle (Caine et al., 1996; Hickman et al., 1995; Parry, 1998). With the need to predict the integrity and evolution of hydrocarbon reservoirs, and to develop further understanding into earthquake processes, the manner in which fault-fluid interactions may influence fault zone evolution is receiving more attention.

Calcite is a common vein-filling mineral in many rock types, as well as an important rock-forming mineral in sedimentary environments. In general, the lithologies that host a fault zone are important when considering the role of fluids in the earthquake cycle (Pili et al., 2002), but carbonates are particularly interesting because they are highly reactive with even slightly acidic fluids, such as rainwater. Particularly in faults, where rocks are pre-fractured, fluids can easily follow pre-existing flaws and fractures and exploit them further as flow paths. Carbonate-bearing faults are important structures for fluid distribution in the brittle upper crust as, where such fractures exist in carbonate rocks, they commonly control much or all of the permeability (Sibson, 1996). Infilled fractures, veins, and pressure solution seams are all characteristic features in carbonate faults (e.g., Bullock et al., 2014; Conybeare and Shaw, 2000; de Graaf et al., 2017; Delle Piane et al., 2017; Fondriest, 2014; Kurz et al., 2007; Michie et al., 2014). Thus, well-exposed carbonate normal faults present a natural laboratory to study evidence of historical fracturing-fluid-flow processes.

In this study, I combine structural field observations, microscopic analyses (conventional and cathodoluminescence) and stable isotope data to study the pre-existing features within a carbonate normal fault exhumed from seismogenic depths to assess the evolution of deformation-fluid-flow features in a fault zone. The Psatha Fault, in the Gulf of Corinth, Greece, shows evidence of numerous fluid-rock interactions such as calcite veins as well as overprinted cements, and thus is an excellent natural laboratory to study these features, constrain their formation, and consider how they may have affected the fault's evolution.

4.1.2 Geological setting

The Gulf of Corinth forms a tectonic boundary between extending terrains of northern and central Greece and the uplifting Peloponnese land mass (Frostick and Steel, 1993). The area is a rapidly extending continental rift (5-15 mm/yr), which has been undergoing crustal extension since the late Miocene (Bell et al., 2011; McKenzie, 1972; Roberts and Jackson, 1991). The Hellenic subduction zone accommodates overall convergence between the Eurasian and African plates (Taymaz et al., 2007). Extension at the present-day occurs in a *c.* N-S direction in the area creating the marine basins of the Gulf of Corinth (Billiris et al., 1991; Clément et al., 2004; Morewood and Roberts, 2002; Roberts and Ganas, 2000). Active extension occurs in the overriding plate of the Hellenic Subduction zone. Deformation here is focussed along WNW-ESE trending normal faults (Frostick and Steel, 1993). A number of these faults have experienced recent ruptures; the Skinos and Pisia Faults (Fig. 4.1.2) caused M_S 6.4-6.7 earthquakes in 1981 (Jackson et al., 1982).

A number of previous works have studied Corinth Rift normal faults, regarding their role in earthquake hazard (e.g., Jackson et al., 1982), for paleoseismicity studies (Collier et al., 1998), rifting studies (Bell et al., 2009; Duffy et al., 2015; Ghisetti and Vezzani, 2005; Taylor et al., 2011) and, most relevant for this study, the role of fluids in the evolution of some of these faults (Bussolotto et al., 2015). From studying the Vela, Doumena, Heliki, and Psathopyrgos Faults (Fig. 4.1.2) which lie on the Corinth rift southern margin, using a combination of microscopy, stable isotopes and fluid inclusion analyses, Bussolotto et al. (2015) concluded that the cements within these fault zones precipitated from meteoric fluids. Precipitation from meteoric fluids was also indicated by a study on helium isotopic ratios of fossil fluids trapped in calcite, which lacked a mantle-He signal in the Corinth rift fluids, suggesting that the fault system is rooted in the upper crust (Pik and Marty, 2009). Bussolotto et al. (2015) also suggested that the process of brecciation within these fault zones allowed mechanical weakening of the faults, which favoured further deformation. The Psatha Fault Zone, a major fault on the south side of the Gulf of Alkyonides in Psatha Bay has been studied structurally (Leeder et al., 1991b; Roberts and Gawthorpe, 1995) but no detailed geochemical analysis has been undertaken to study fluid-fault interactions on the fault and their relationship to how the fault may have evolved.

The Psatha Fault is a segment linked to the Skinos Fault in the South Alkyonides fault system, within the area of active extension (Fig. 4.1.2). It was mapped 1.5 km offshore (Leeder et al., 2002) as the Holocene-active western continuation of a 7.7 km long onshore scarp (Morewood and Roberts, 2002). The base of the footwall, in a region where the Psatha Fault runs offshore, is cut by an uplifted marine solution notch. This marine solution notch has been used by Leeder et al. (1991b) to estimate a minimum footwall uplift rate of 0.3 mm a^{-1} since *c.* 7 ka, when the local Holocene marine highstand abutted the fault scarp. The Psatha Fault is formed of Mesozoic limestone and hosts various breccias, fault gouges, veins and slickensides (Holdsworth and Turner, 2002). Its particularly well-exposed fault planes and textures are indicative of multiple episodes of fluid-flow processes, which allow the study of coupled deformation and fluid-flow.

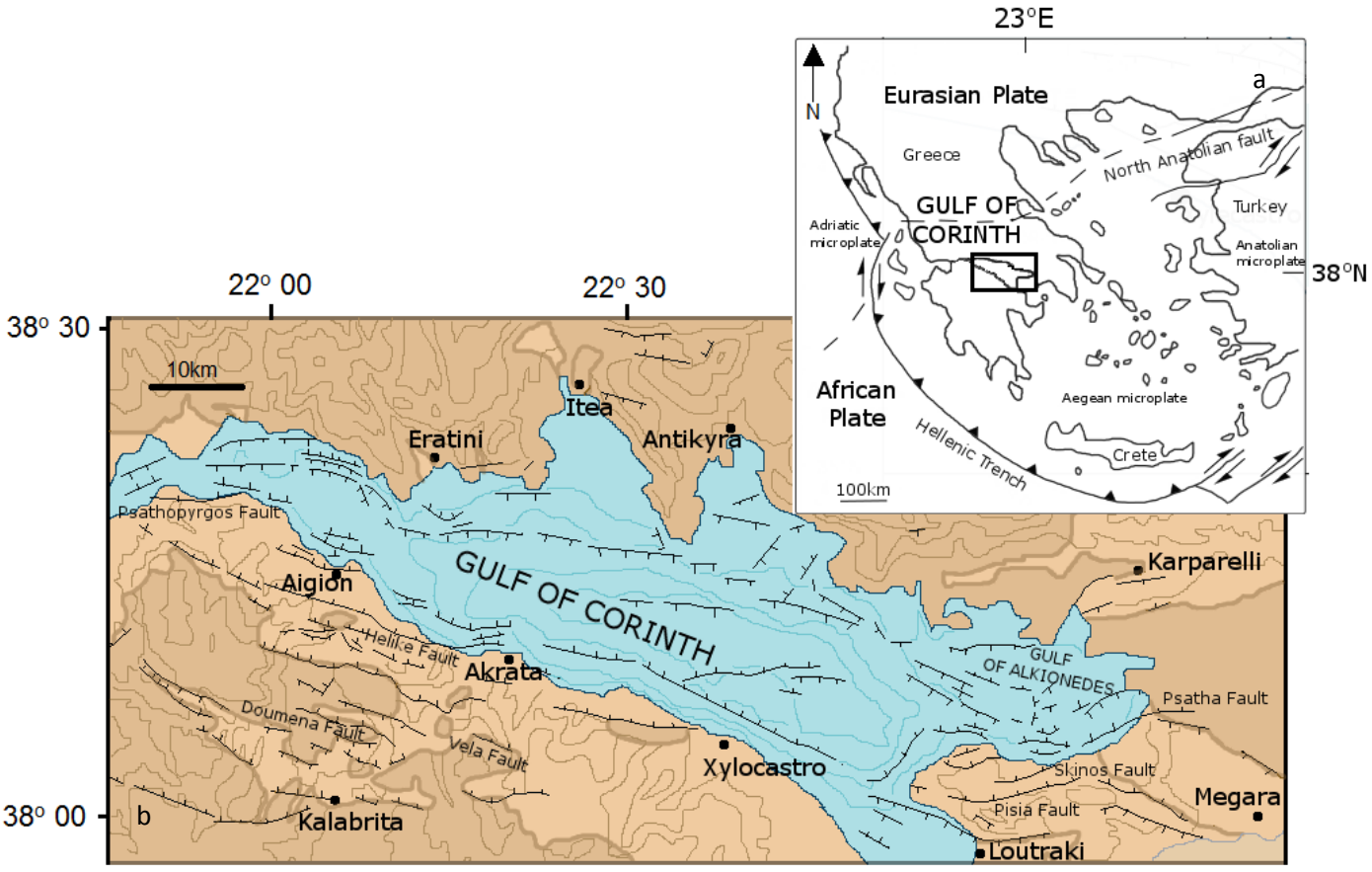


Figure 4.1.2 Geological setting and location Gulf of Corinth (a) Location of the Gulf of Corinth (b) Location of the faults on the southern margin of the Gulf of Corinth. The Psatha Fault is located at 38° 5'47'N 23°12'32'E. Figure adapted from Moretti et al. (2003) and Gobo et al. (2014).

4.1.3 Methods

4.1.3.1 Fieldwork, descriptions and structural analysis

I conducted a field study of the Psatha Fault across its exposed onshore length (Fig. 4.1.4a). The morphology of the textures and structures on and adjacent to exposed fault planes were described and recorded in sketches and photographs, with a focus on the first ~50 m away from the hanging wall contact (from N53.4, E 51.8, Fig. 4.1.4b). Thin sections were produced from samples collected from the field and were analysed utilising conventional and cathodoluminescence microscopy. Undertaking microscopic analysis of cements and veins within the host rock and breccias permits a characterisation of the different cement products, allow me to distinguish the different deformation mechanisms and identify different cement generations. The technique of cathodoluminescence microscopy utilises the differences in the luminescent colour of diagenetic phases and luminescence intensity due to chemical composition differences (see section 2.3). Statistical analyses of shape, size, and distribution of crystals was undertaken using ImageJ, the free cross-platform image analysis tool developed by the US National Institute of Health. If twinning was present in the calcite crystals, the number of twins/mm was used to estimate how much differential stress the crystals had been subject to, using the equation by Rowe and Rutter (1990):

$$\sigma_D = -52.0 + 171.1 \log D \qquad (4.1.1)$$

where D is the twin density, and σ_D is the differential stress in MPa.

4.1.3.2 Stable isotope analysis

Analysis of stable carbon and oxygen isotopes can provide information about the fluid-rock interaction and allow identification of the type of fluids involved in dissolution and precipitation processes in fault zones. Determining the source of the fluids, from which the cements in the fault zone precipitated out of, constrains the possible fluid paths, the permeability of the fault zone and the connectivity in the crust, the distribution mechanism of the fluid, and the duration of fluid migration. Carbon and oxygen isotope ratios have often been used for analysis of carbonate cements in fault zones (e.g., Hausegger et al., 2010; Labaume et al., 2001). The ratio of $^{13}C/^{12}C$ can be used to identify the carbon source and the $^{18}O/^{16}O$ ratio, dependent on precipitation temperature and the oxygen isotope composition of the precipitation fluid, gives an indication of the fluid source and conditions of precipitation (Clark and Fritz, 1997). A range of $^{18}O/^{16}O$ ratios indicates that precipitation took place over a range of

temperatures and $\delta^{18}O$-water values (Labaume et al., 2001). Low $\delta^{18}O$ values in respect to the host rock indicate precipitation from higher temperature fluids, or fluids with lower $\delta^{18}O$ composition (Hausegger et al., 2010).

An aliquot of 100µg of cement was drilled from samples obtained during fieldwork using a dental drill at Imperial College. This cement is subsequently reacted with phosphoric acid at 70ºC in an automated Kiel carbonate device (see section 2.4). The carbon dioxide produced during this process is then analysed in a MAT 253 mass spectrometer (see section 2.4). The ratios are corrected for temperature effects (see section 2.4) and then reported per mil relative to the V-PDB (Vienna Pee Dee Belemnite) standard by assigning a $\delta^{13}C$ value of +1.95‰ and a $\delta^{18}O$ value of -2.20‰ to NBS19 (Friedman et al., 1982).

In order to characterise the fluid source, I have obtained the composition of the present-day groundwater, taken from a notch spring at the Psatha Fault, from Brasier (2007).

4.1.4 Results

The position of the Psatha Fault and locations of all the photographs in this section are shown in Fig. 4.1.3.

4.1.4.1 Characterisation of calcite veins and cements on the Psatha Fault scarp

The Psatha Fault is superbly exposed along the coastline and can be walked along strike for ~1.5 km (Fig. 4.1.4a).

The fault zone forms an impressive scarp ~200 m high. The marine solution notch observed by Leeder et al. (1991b) is clearly visible at the base of the fault footwall (Fig. 4.1.4c). There is also an uplifted wave cut platform visible at low-tide, just offshore in the Alkyonides Gulf (Fig. 4.1.4d). The fault zone hosts an abundance of calcite cements, which occur as veins and breccias along slip surfaces. Regular fracture networks (Fig. 4.1.5a) are overprinted and infilled by matrix-supported breccias (Fig. 4.1.5b, c), cut by fractures filled with calcite crystals (Fig. 4.1.5a, c).

Clasts within the breccias are made up of the host limestone (Fig. 4.1.5c), although there are some smaller clasts within breccia extending out from the fault, which may be composed of indurated fault gouge (Fig. 4.1.4e). There are at least three distinct breccias on the Psatha Fault: one embedded within the fault, and two overprinting breccias (Fig. 4.1.5 & 4.1.6). There are distinct differences between these three breccias; the fault embedded breccia (FB) shows a comparatively small variation in clast size with no clasts larger than 1 cm^2 (Fig. 4.1.5c), the

thin overprinted breccia (TOB) shows a larger clast size variation, but the vast majority have an area < 0.6 cm^2 (Fig. 4.1.5e), and the massive overprinting breccias (MOB) (extending 0.5-1 m out from the fault surface, Fig. 4.1.5d) have an exceptionally large clast size variation, up to 8.5 cm^2. MOB clasts are predominantly made up of reworked FB and TOB (Fig. 4.1.5c). Within the host rock and amongst the breccias are various cross-cutting veins (Fig. 4.1.5a, c), which are predominantly simple dilatational fractures. The veins show tapering, but commonly abut other infilled fractures (Fig. 4.1.6a).

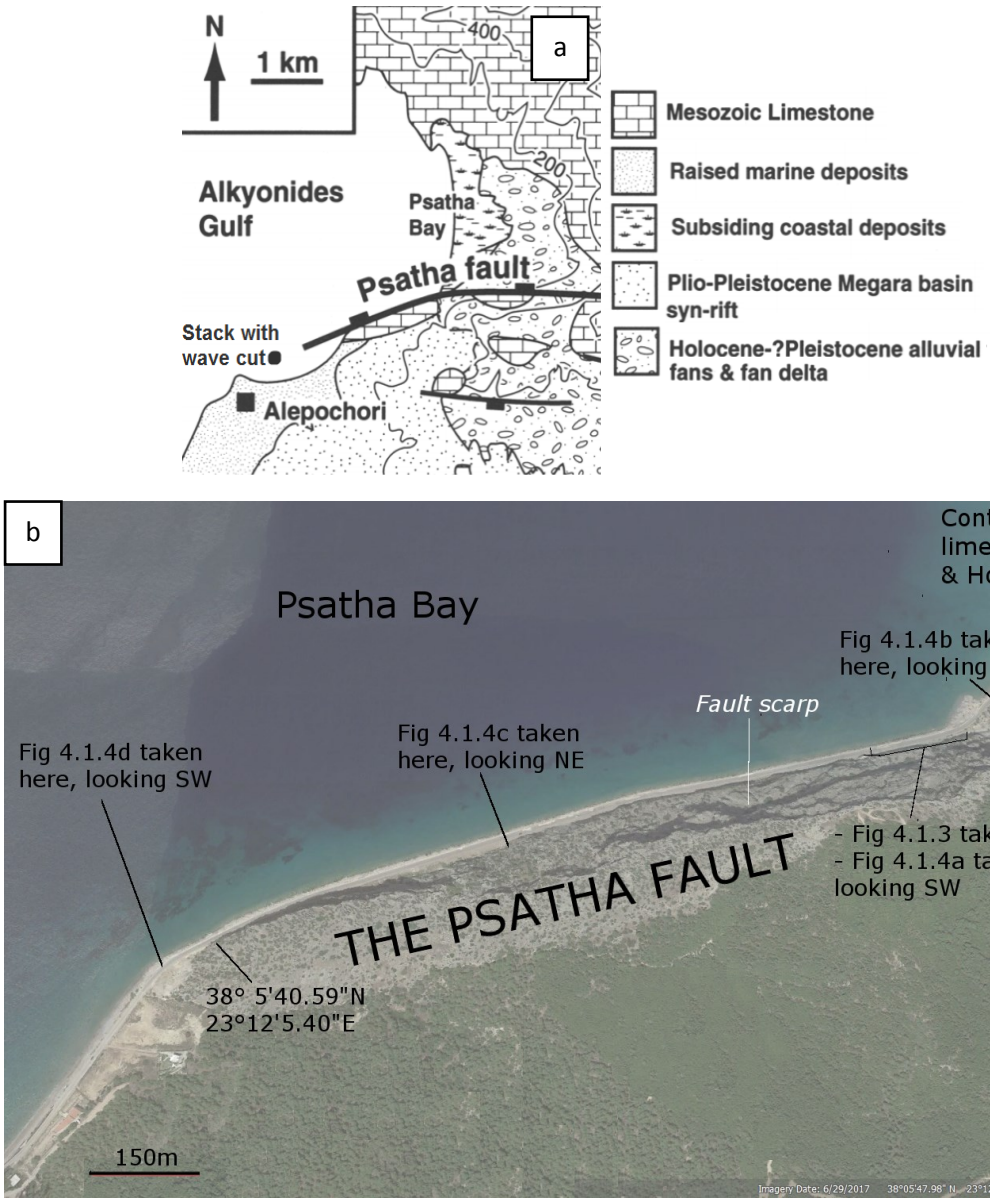


Figure 4.1.3 The Psatha Fault. (a) The position of the fault relative to the positions of other deposits (modified from Roberts and Gawthorpe (1995)) (b) Photograph locations along the Psatha Fault, Gulf of Corinth, Greece. Background image from Google Earth Pro. Psatha Bay, Greece. 38° 5'47'N 23°12'32'E Eye alt 1.5 km. SIO, NOAA, U.S. Navy, NGA, GEBCO.

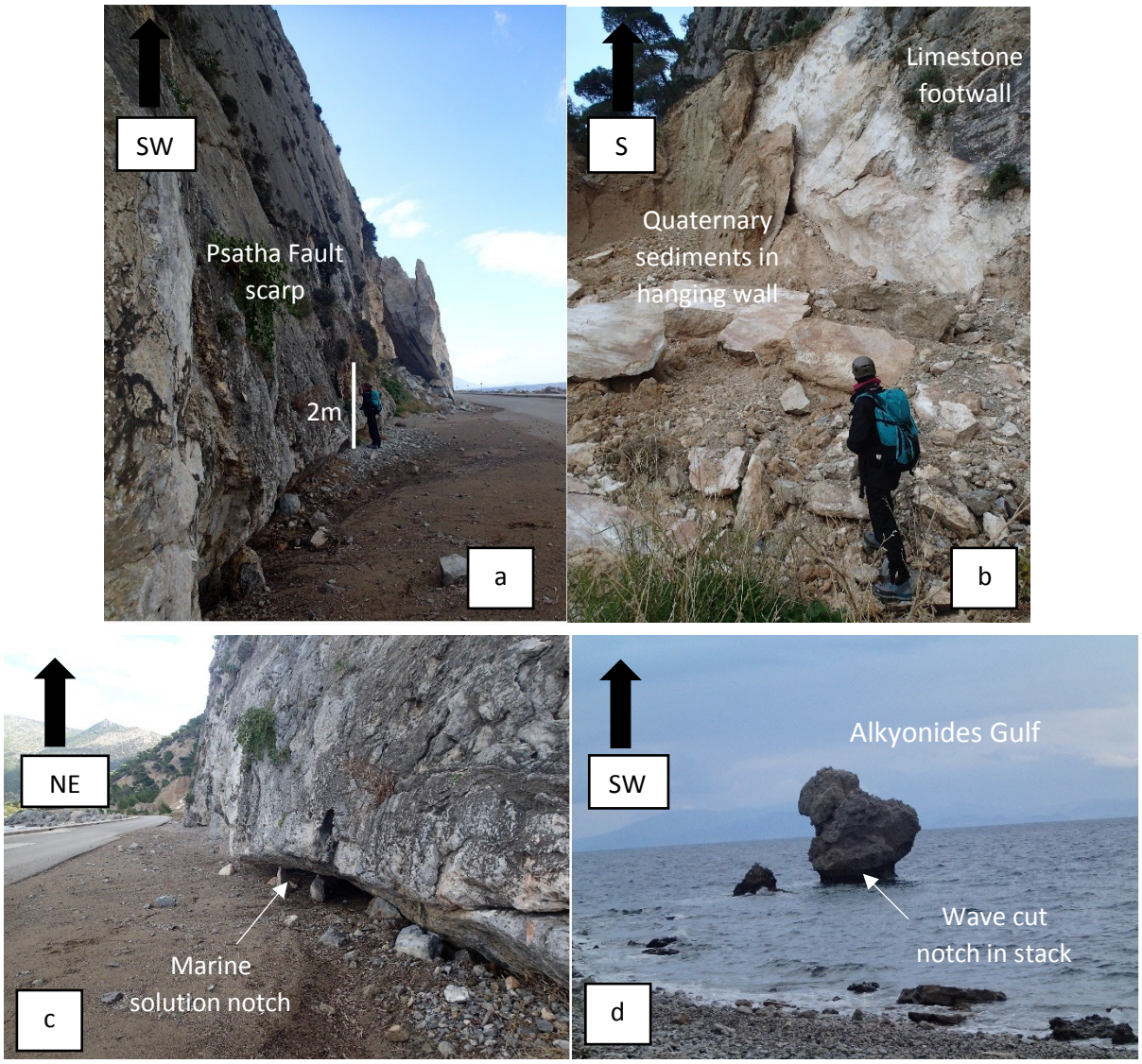


Figure 4.1.4 Field photographs from along the Psatha Fault. (a) The well-exposed Psatha Fault scarp can be walked along strike (b) The contact between the limestone footfall and the Quaternary sediments in the hanging wall (c) Marine solution notch and (d) wave cut notch offshore in the footwall of the Psatha Fault (Fig. 4.1.3a).

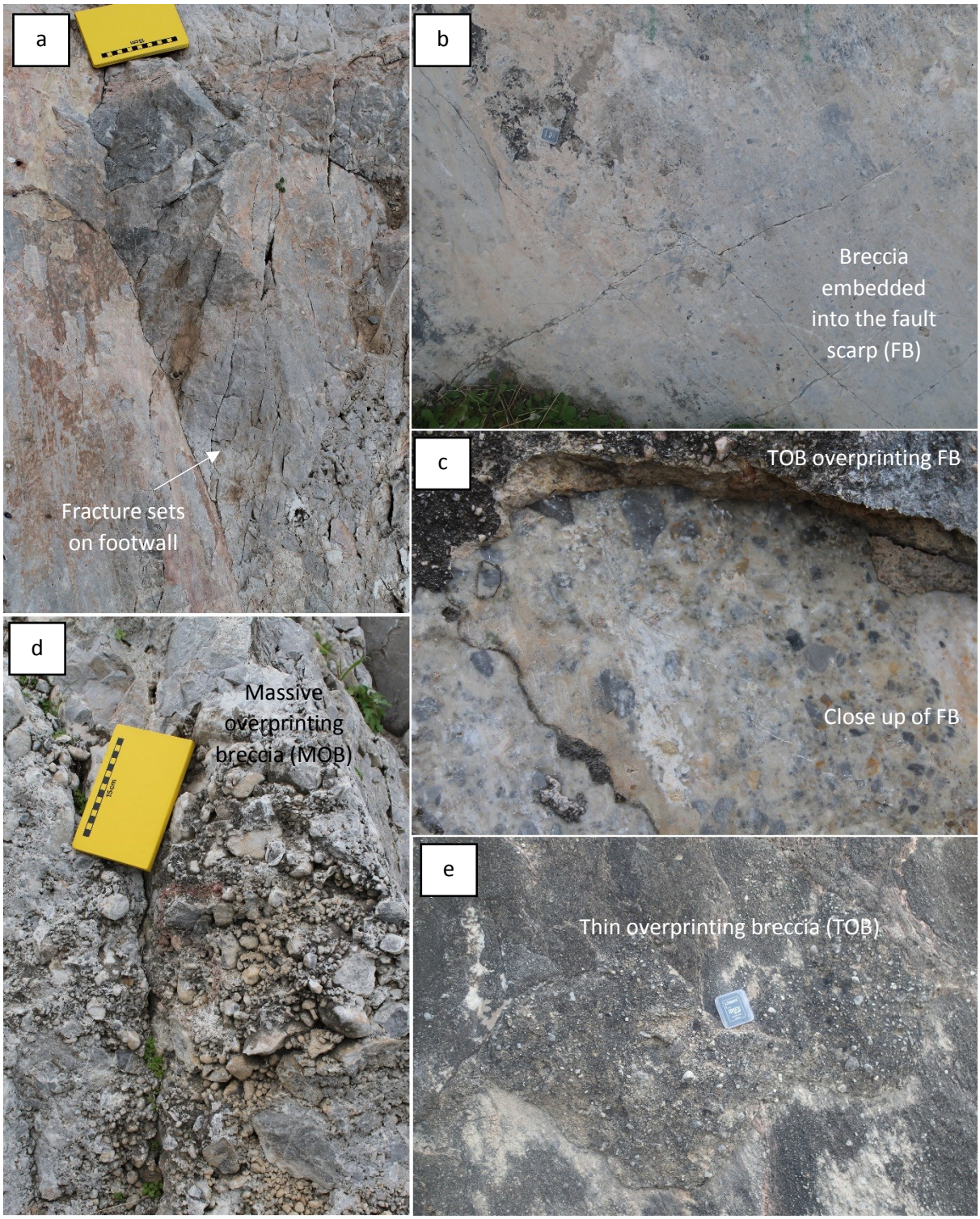


Figure 4.1.5 The three main breccias on the fault; breccia embedded within the fault scarp (FB, b & c), a thin overprinted breccia (TOB, c & e) and a massive overprinting breccia (MOB, d). The fault also hosts many fracture sets (a).

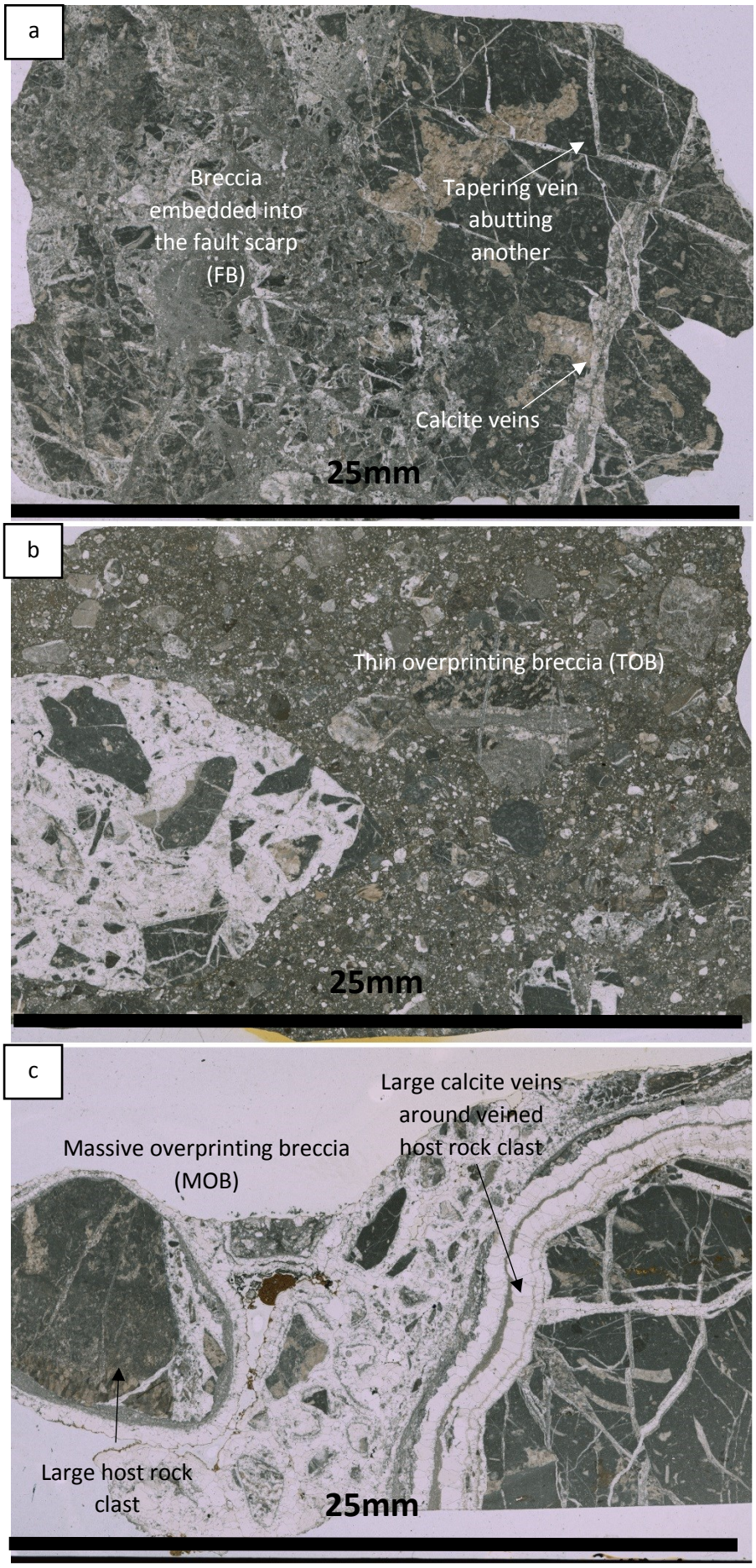


Figure 4.1.6 Thin section scans of the three main breccias within the Psatha Fault zone. (a) breccia embedded within the fault scarp (FB), (b) thin overprinted breccia (TOB) and (c) a massive overprinting breccia (MOB). MOB typically hosts clasts of reworked FB and TOB.

4.1.4.2 Microscopy

There are large variations in the crystal size and shapes within the calcite veins, depending on their location in the fault zone. The crystals group by size and amount of twinning; large untwinned crystals are grouped together, as are moderately twinned and heavily twinned crystals. Three groups of veins can be distinguished, based on the amounts of twinning, cross-cutting relationships and cathodoluminescence colour (Fig. 4.1.7). Cathodoluminescence observations revealed differences in luminescence between the different veins, indicating differences in the initial trace element composition in the fluid and/or to changes in redox conditions at the site of precipitation (Meyers, 1974).

Fig. 4.1.7a is taken from TOB in contact with FB. Heavily twinned crystals are overprinted by silt and crystals within a silty matrix. Small veins are evident crossing the heavily twinned crystals. The heavily twinned veins (> 10 twins per crystals) are dull in luminescence (FB) and are abutted or overprinted by veins with 2-4 twins per crystal (Fig. 4.1.7ai), which show orange-zoned cathodoluminescence (Fig. 4.1.7aii). Brown coloured silts are also preserved between clasts and exhibit some luminescence (Fig. 4.1.7aii). Pressure solution seams are evident, which contains crystals of similar size throughout (Fig. 4.1.7aii). Fig. 4.1.7b is taken from the TOB. In this sample, the crystals only show a couple of twins, or are untwinned. There is also crystal zoning within the moderately twinned veins seen under cathodoluminescence; most of this breccia shows orange cathodoluminescence, apart from the overprinted untwinned crystals. Fig. 4.1.7c is taken from the MOB, which contains reworked TOB and FB (see Fig. 4.1.5). In this sample, the crystals show a variety of twinning, depending upon their precise location. Large, elongated, untwinned crystals overprint the other twinned veins. There is one heavily twinned vein, and another moderately twinned vein. In the heavily twinned crystals, the crystal sizes show symmetrical variation, from large crystals in the centres of fractures, to smaller euhedral crystals lining the fracture edge (Fig. 4.1.7ci), which is typical of drusy fabrics (Scholle and Ulmer-Scholle, 2003). The crystals vary in size from 50 μm^2 to 0.025 mm^2. The moderately twinned crystals are relatively spherical, with approximately equal *x* and *y* axes. These are both overprinted by non-twinned crystalline veins and clusters (Fig. 4.1.7ci), which are dull in luminescence (Fig. 4.1.7cii). There is also brown silt in this sample, which contains luminescent crystals (Fig. 4.1.7cii). The luminescence also highlights that these crystals are relatively spherical. The untwinned crystalline veins are always the greatest distance from the fault scarp surface out of all the breccias analysed and frequently surround clasts of host rock (e.g., Fig. 4.1.6c). These veins have a much greater variation of crystal sizes, from 50 μm^2 to

0.60 mm^2 within the same fracture. The large (2D area 0.6 mm^2 to 0.01 mm^2) elongated crystals (crystal length 2-3 times crystal width) are in the centre of these infilled fractures, directly in contact with small, spherical crystals of area ~50 μm^2 (Fig. 4.1.7ci). These infilled calcite fractures are ~1 mm wide.

The peak differential stress was estimated using Equation 4.1.1, developed by Rowe and Rutter (1990). The moderately twinned veins have twin densities between 11-24 twins/mm, hence the peak differential stress is ~154.0 +/- 30.1 MPa. The heavily twinned veins (FB) have a variety of twin densities, from 48-117 twins/mm, yielding a peak differential stress is ~268.9 +/- 33.2 MPa.

4.1.4.3 Stable isotope results

The $\delta^{18}O$ values from the Psatha Fault host rock range from 2.0‰ to 2.5‰ V-PDB and $\delta^{13}C$ values from -2.1‰ to -0.9‰ V-PDB (Fig. 4.1.8). Both the $\delta^{18}O$ and $\delta^{13}C$ signatures from the calcite cements are far more depleted in comparison to the host rock. $\delta^{18}O$ values in the cements within all of the breccias range from -7.4‰ to -6.3‰ and the $\delta^{13}C$ values from -6.5‰ to -3.5‰. The cements between the clasts of the breccia that extend from the fault surface (MOB) are 0.4‰ more depleted in $\delta^{18}O$ than the mean $\delta^{18}O$ signature of the cements within the less varied breccias (FB and TOB). The cements from MOB are also 0.8‰ more depleted in $\delta^{13}C$ than the mean $\delta^{13}C$ signature of the cements within the less varied breccias (FB and TOB). The $\delta^{18}O$ values for cements in MOB range from -6.8‰ to -7.2‰ V-PDB and in TOB from -6.3‰ to -6.9‰ V-PDB. The $\delta^{18}O$ signatures of the cements from FB lie within a very small range, from -6.7‰ to -6.8‰ V-PDB. There is the greatest variation in the $\delta^{13}C$ signature from cements within TOB, which range from -3.6‰ to -5.8‰ V-PDB, a smaller variation from FB, which range from -5.0‰ to -5.6‰ V-PDB and the least variation in MOB, from -5.7‰ to -6.2‰ V-PDB.

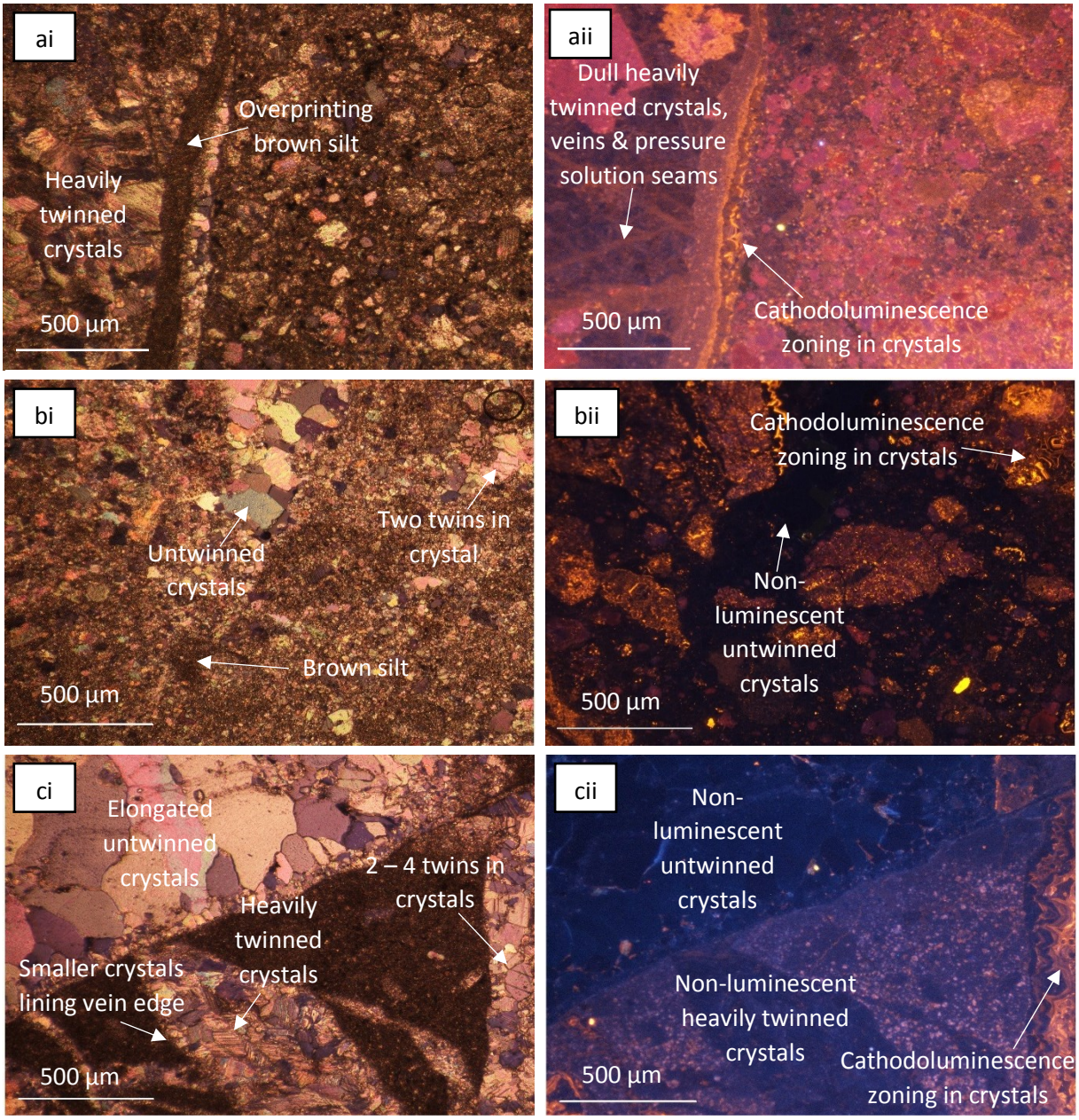


Figure 4.1.7 Microscope images of the different crystal clusters within the breccias. (ai) is taken from TOB in contact with FB. (aii) Cathodoluminescent image of (ai). (bi) is taken from the TOB. (bii) Cathodoluminescent image of (bi). (ci) is taken from the MOB, which contains reworked TOB and FB (Fig. 4.1.5). (cii) Cathodoluminescent image of (ci).

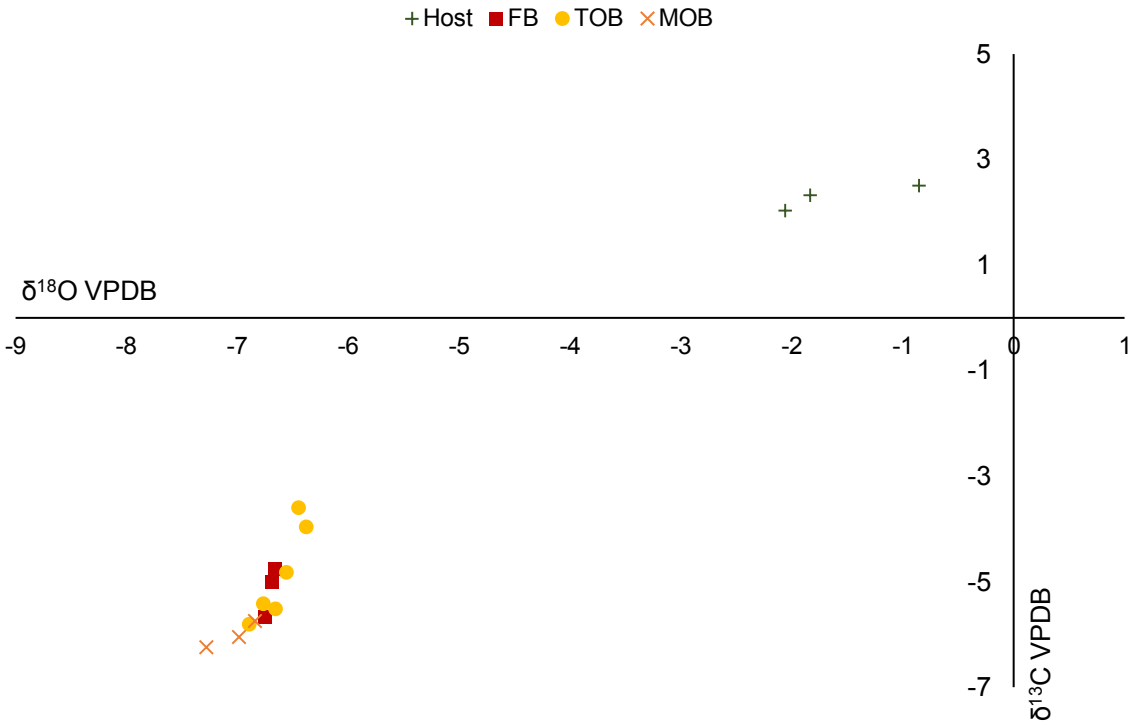


Figure 4.1.8 Stable isotope results from the different breccias on the Psatha Fault.

4.1.5 Discussion

The range of features within the fault zone reflects a complex deformation-fluid-flow history. The variety of breccias, presence of pressure solution seams and veins (Fig. 4.1.5, 4.1.6 & 4.1.7) indicate that dissolution-precipitation processes have influenced the evolution of the Psatha Fault. Fluid-assisted healing processes appear to be dominant. The protolith lithology is clearly influenced by the multiple phases of precipitation. Notably, such matrix-supported carbonate breccias and gouge identified are common on active normal faults in the Gulf of Corinth (Roberts et al., 1993).

4.1.5.1 Fault Breccia (FB)

The breccia embedded within the fault plane, FB, with its smaller, more spherical clasts, is identified as fault breccia, formed by localised brittle deformation. Fracturing attributed to the production of this fault breccia (as seen in Fig. 4.1.5a) likely induced focussed fluid-flow and subsequent crystallisation and cementation, as also noted by Bussolotto et al. (2015).

Subsequent deformation would have led to heavy twinning of calcite crystals, which are seen within veins across FB, as well as in reworked clasts within MOB (Fig. 4.1.6c & 4.1.7cii).

The minor shift in isotopic signature between MOB and FB (Fig. 4.1.8) may indicate a slight change in water composition over time, and the correlation between $\delta^{18}O$ and $\delta^{13}C$ could indicate a development from a closed system with fluid-rock equilibrium during brecciation to a more open one with influx of meteoric water (Benedicto et al., 2008). This supports the work of Bussolotto et al. (2015), who inferred that the fluid system in the Gulf of Corinth was predominantly shallow, and how 'open' or 'closed' it was depended on depth. The low $\delta^{13}C$ values have a positive correlation with the $\delta^{18}O$ values, which may be indicative of progressively greater involvement of soil-derived carbon (likely near-surface soil breakdown). The classic drusy cement fabrics seen in the heavily twinned veins, i.e., larger crystals in the centres of fractures to smaller euhedral, crystals lining the edges of fractures, is indicative of cementation below the water table in the phreatic zone within fractures completely filled with water (Guilbert and Park, 1986; Tucker and Wright, 1990). Similar phreatic cements have been described from nearby active normal fault zones (Roberts and Stewart, 1994; Roberts et al., 1993) e.g., the nearby active South Alkyonides Fault, which ruptured at the surface during the 1981 Gulf of Corinth earthquakes. The cross-cut infilled fractures found in the host rock and reworked clasts (Fig. 4.1.6) may suggest dilatant fracturing followed by rapid fluid-flow and crystallisation, which alternated with lower strain rate dissolution and cementation processes (Knipe, 1989). This is consistent with ongoing uplift of the footwall during its slip history, whereby fracturing and cementation below the water table gave way to fracturing and cementation above the water table through time.

4.1.5.2 Thin Overprinted Breccia (TOB)

The brown-coloured material (Fig. 4.1.7ai), which forms a dominant component of TOB, appears to be characteristic of vadose silts (Tucker and Wright, 1990). It has been suggested by Leeder et al. (2005) that this material was beach material cemented onto the fault surface by low-Mg calcite. This material also contains luminescent crystals (Fig. 4.1.7bii). The orange luminescence of this material indicates Mg incorporation and diagenetic growth. The crystal zoning seen in the veins under cathodoluminescence (Fig. 4.1.7bii, cii) is consistent with a pulsed fluid influx (Budd et al., 2013; Ioannou et al., 2004). A mechanism for inputting short-lived and easily diluted pulses of water could be attributed to seismic pumping (Sibson et al., 1975; Sibson et al., 1988). Temperature fluctuations associated with seismic pumping could be investigated if the oxygen isotopic signatures of individual cement zones could be sampled and measured to show fluctuations in pore water temperatures. It could also be due to tidal activity, inputting slightly Mg-rich fluids (although this should be reflected by a less depleted $\delta^{18}O$

signature, indicative of seawater input) or in fact, storm gravels rapidly deposited and cemented onto the fault surface, which could also explain the wider range of isotopic signatures due to the mixing fluid composition, a fluctuating water table, input of seawater, or small temperature variation for the pore waters (Prezbindowski, 1985). Some crystals within the brown silty material may have been formed from suspended particles within the fluid, which subsequently settled in the pore space (Grover Jr and Read, 1983). The slightly elevated $\delta^{13}C$ signature of two of the TOB cement samples (Fig. 4.1.8), which distinctly lie apart from the other data, may have been slightly buffered by host rock clasts. Ultimately, the presence of this material, cemented upon the fault surface at the most ~10.5m above mean sea level, indicate cementation and uplift across the water table during deformation, which is supported by the presence of the marine solution notch at the base of the fault and the uplifted wave-cut notch just offshore from the fault (Fig. 4.1.4).

4.1.5.3 Massive Overprinted Breccia (MOB) and veins

The vein sets, overprinted by larger crystals with no twinning (MOB), indicate that multiple sequences of diagenesis and deformation have occurred, but no significant activity has occurred since the precipitation of the untwinned veins associated with the MOB. The large untwinned crystalline veins in the MOB show a slightly more depleted signature in both $\delta^{18}O$ and $\delta^{13}C$ (Fig. 4.1.8). Given that they also overprint all other vein generation, and the breccia they form within embedded clasts are made up of the other breccias and host rock, I suggest that these veins form part of an overlying 'karstic breccia', formed by precipitation from meteoric fluids in pre-existing fractures and between clasts of host rock and pieces of fallen breccias. The composition of the present-day groundwater, taken from a notch spring at the Psatha Fault is at near equilibrium or slightly oversaturated with respect to calcium (as well as sodium, magnesium and potassium) (Brasier, 2007). The current isotopic composition of precipitation in Greece has a mean of -6‰ V-SMOW (Argiriou and Lykoudis, 2006), indicating that $\delta^{18}O$ values of calcite should range be ~-7‰ V-PDB, assuming an average temperature of 20^{o}C. This corresponds well with the MOB veins. Given this signature, and the lack of twinning, it is highly likely that these veins precipitated late in the evolution of the fault zone as a result of more recent circulation of purely meteoric fluids. The fractures they filled, however, may be much older and were simply open enough to allow advection as compared to previous fractures that could have been filled by a diffusion process. The crystals would have precipitated above the water table due to the downward percolation of rain water, similar to those reported on other active fault planes in the region (Roberts and Stewart, 1994).

The differential stresses (moderately twinned veins (TOB) peak differential stress is ~154.0 +/- 30.1 MPa, heavily twinned veins (FB) peak differential stress is ~268.9 +/- 33.2 MPa, using Equation 4.1.1, developed by Rowe and Rutter (1990)) inferred from the different amount of twinning within the different veins support multiple cycles of deformation and diagenesis. The older calcite cement generations are heavily twinned, and the newest, overprinting cements may not have experienced any deformation at all. This indicates there has been no significant activity on the fault since the formation of the MOB, although it does not certify that the fault is no longer active.

4.1.5.4 Fault zone evolution

I infer that precipitation following a first deformation event occurs in the phreatic zone to produce FB (Fig. 4.1.9). Unfortunately the actual depth of faulting is not well-constrained, and it is unknown whether uplift of the features produced in the phreatic zone were uplifted gradually or as a result of several large magnitude earthquakes. Given the decree of twinning corresponding to ~268.9 MPa, plus the preservation of this breccia, it is assuming that deformation occurred and then there was a long period of upift without deformation. Given the uplift rate of 0.3 mm a^{-1} approximated by Leeder et al. (1991b) is is still a reasonable estimate even within error of a number of earthquakes, and assuming that these veins are embedded into the visible ~25 m of fault scarp above, then they would be at most 83 ka old. This correlates well with an estimation of maximum age 110 ka as given by Leeder et al. (1991a). Following uplift and further deformation, which imparts heavy twinning into the phreatic veins, a further phase of deformation and uplift occurred (Fig. 4.1.9), producing veins which cross-cut the pre-existing phreatic veins and breccias which overprint the fault surface. Again, assuming a continuous uplift rate of 0.3 mm a^{-1}, and given that this material is at a maximum of 10.5 m above ground level, then this breccia is at most 35 ka old. Continued uplift and deformation imparts twinning within both the phreatic and overprinting veins. Eventually, precipitation of meteoric fluids within pre-existing fractures, which are easily exploited by slightly acidic rainwater, occurs on top of and around clasts of host rock, FB and TOB. This likely would have occurred whilst these fractures were uplifted to, and existed at, the surface (Fig. 4.1.9), over the last ~7 ka.

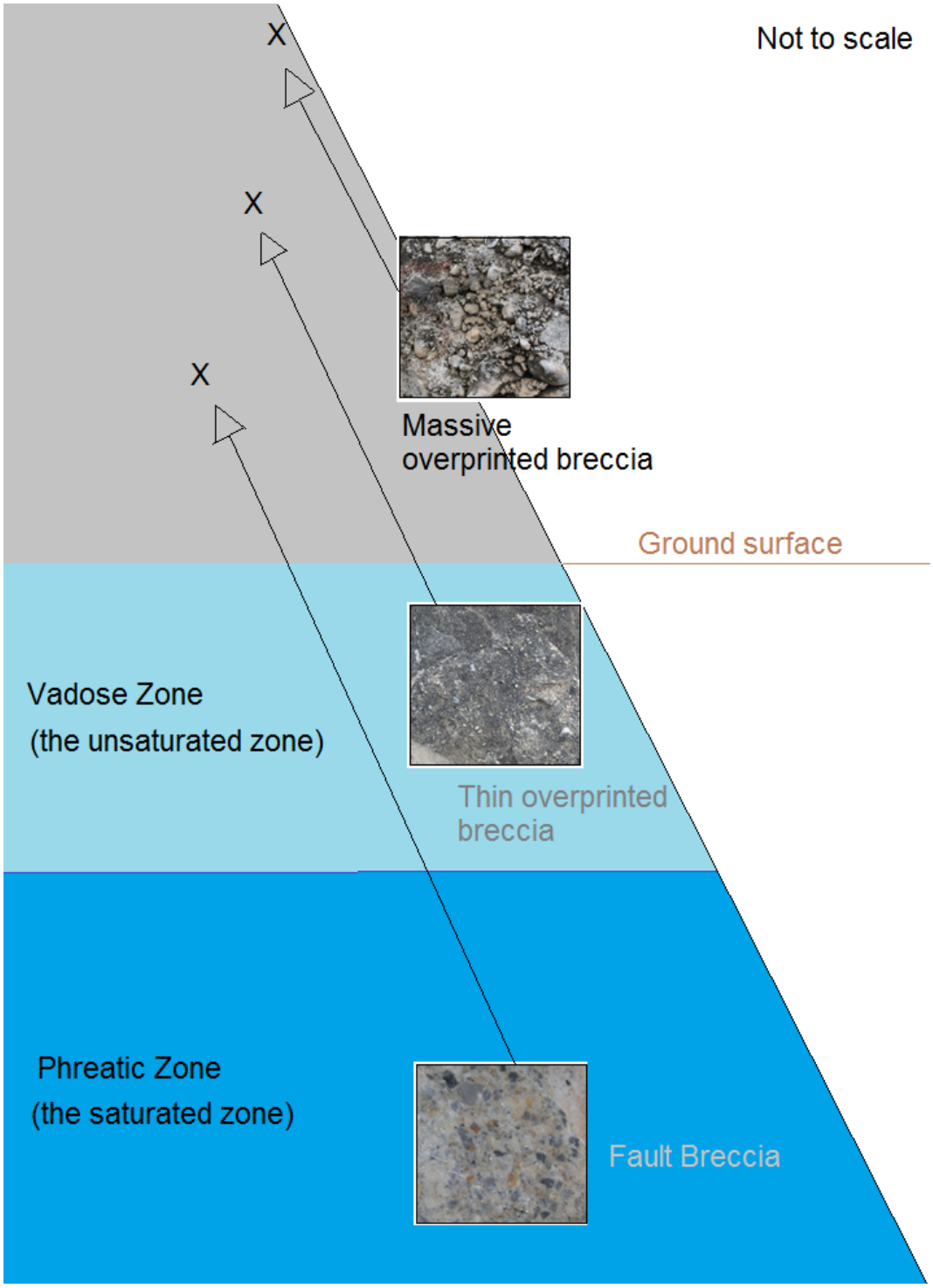


Figure 4.1.9 Progressive uplift of the Psatha Fault. The fault breccia would have formed by dilatational processes within the phreatic zone, from depths corresponding to a differential stress of ~268.9 MPa. Following uplift but no further deformation (preserving FB), gravels have been cemented onto the fault surface in the vadose zone and undergone further deformation. Finally, above current ground level, cementation around clasts from FB and TOB are cemented by meteoric fluids within fractures and atop the fault surface.

The results indicate that the cements are predominantly the result of precipitation from an upper crustal fluid system, affected by multiple episodes of fault slip. This enforces the conclusions of Bussolotto et al. (2015), who suggested that all calcite cements within normal fault zones in the Gulf of Corinth are the result of precipitation from meteoric fluids in either a closed or open circulation system, depending on depth. This work also corroborates the helium isotopic ratio study by Pik and Marty (2009), who suggest that the fault system in the Gulf of Corinth is rooted in the upper crust.

The present study has shown that outcrop studies of normal fault zones in the Gulf of Corinth provide important information on the connectivity of the fluid system, as well as details on the interplay between fluid-flow, deformation, and uplift on the Psatha Fault. This study details how using water-rock interaction features can significantly constrain fault zone evolution, which has implications for seismic hazard as well as how faults within hydrocarbon reservoirs may evolve over time. Further work should consider how such features may influence fracturing and fault slip in the future (Chapter IV Part II).

4.1.6 Conclusions

The Psatha Fault underwent early faulting below the water table, as evidenced by phreatic textures. Later faulting uplifted these textures across the water table. Further cementation occurred as a result of a pulsed fluid influx, likely tidal or storm activity, cementing imbricated silty layers onto the fault scarp. Fractures were later infilled, overprinting existing textures with larger calcite crystals precipitated from meteoric waters, reflecting the current isotopic signature of the rainwater in the region, and which have not yet been subject to deformation. The study of features produced by fluid-rock interactions has allowed the time sequence of deformation relative to uplift during the evolution of the Psatha Fault to be constrained and has indicated that the fault has not been active since the precipitation of the calcite veins which cement the MOB.

Chapter IV, Part II: Implications of pre-existing veins upon future fracturing: An example from the Gulf of Corinth, Greece

Fault zones are characterised by the results of numerous fluid-rock interactions. The structures produced by these fluid-rock interactions can exert a significant influence over the evolution of a fault zone and its subsequent rupture. However, when trying to gain more information on how a fault may fail in the future, rock deformation experiments typically use homogenous idealised samples, whereas earthquakes generally occur on pre-existing faults, which have a variety of heterogeneous properties. This study utilises rock deformation experiments on fault rock with pre-existing veins to assess how features produced by fluid-rock interactions may influence future fracture propagation and slip. This work supplements my characterisation of the deformation-fluid-flow features on the Psatha Fault (Chapter IV, Part I): investigating how rupture in the future may propagate in this already altered, overprinted fault zone. I use triaxial compression tests on cores of the heavily veined fault rock to investigate how rupture may propagate in the future in rock containing pre-existing heterogeneities (veins, breccia cements and gouges). The results from this study are twofold; (i) the key parameter for whether a fracture will be deflected by a vein is the contrast in strength between the host rock and the heterogeneity. Heavily-twinned crystals are cross-cut and the fracture continues along the ideal path in accordance with the stress orientation, whereas undeformed, continuous veins provide a propagation pathway and can deflect fractures to propagate within them; (ii) following the creation of a newly formed rough fracture, granular flow enabled by the production of broken-up material from fracturing initially dominates subsequent slip. However, cohesive strengthening mechanisms achieved by holding the sample at elevated temperature and pressure in the presence of water, as well as smoothing of the fault during slip, can enable a transition to stick-slip behaviour. This study has implications for the influence of pre-existing deformation-fluid-flow features upon future fracture propagation generally, as well as for the Psatha Fault, and the relative importance of cohesive mechanisms in fault zones in controlling slip.

4.2.1 Introduction

Healing and sealing features on faults, including veins and breccias, may alter a variety of rock physical properties, including porosity, permeability, and strength. Fault-controlled diagenesis, leading to the production of structures and textures that form fault seals, are highly influenced by fluid chemistry and the stress field (Eichhubl et al., 2009). Pre-existing discontinuities in

rocks, including natural fractures and bedding planes, act as planes of weakness which can divert fracture propagation (Jaeger et al., 2009, Ambrose et al., 2014, Lee et al., 2015). Some modelling studies have shown that interplays between pre-existing fluid-rock interaction features (such as veins, breccias and gouges) are complex, including deflection and refraction between older-younger vein interfaces, simple overprinting, as well as termination and bifurcation of a younger vein against an older vein (Virgo et al., 2013). Furthermore, it has been indicated that such interactions are not only relevant on a microscopic scale, but also on a field scale (Shaw, 2005). From small-scale fracturing to fault movement and rupture dynamics all the way up to the motion of the tectonic plates (Bercovici and Ricard, 2014), pre-existing architecture can characterise fault reactivation and influence subsequent faulting patterns at all scales (Phillips et al., 2016). This 'pre-existing architecture' refers to veins, breccia cements and gouges, which have been imparted over time from various fluid-rock interactions, as well as fractures and foliations. Such structures exist from the micro and grain scale (small cemented fractures), up to outcrop-scale fault and fracture networks (Duffy et al., 2015; Kirkpatrick et al., 2013; Whipp et al., 2014), and even up to the scale of orogenic belts (Bird et al., 2015; Bladon et al., 2015; Daly et al., 1989; Paton and Underhill, 2004). Following a study on shear zones at different scales in rocks with pre-existing penetrative foliations, Carreras (2001) suggested that shear zone formation is associated with strong strain partitioning at all scales. Given that macroscopic fracturing processes can be thought of as a culmination of smaller scale fracturing (Brantut et al., 2013), understanding the microscopic physics of deformation is critical to the study of macroscale geological processes (Fossen, 2010; Karato, 2012). Furthermore, knowing how pre-existing structures influence the manner in which fractures may propagate in a fault zone is essential to understand possible future rupture properties, how a reservoir may evolve, and even whether a site may be suitable for carbon sequestration.

Prior to the 1990's, the majority of experiments simulating faulting were done in dry conditions and at room temperature (e.g., Dieterich, 1972; Shimamoto and Logan, 1984), which is not representative of faulting conditions in the crust, despite the mechanical role of fluids being identified as early as 1966 (Byerlee, 1966). More recently, rock deformation studies have been used to attempt to study aspects of the fluid-fracturing system, in particular the change in strength of a rock following fracturing and induced cementation via hydrothermal alteration in quartz (e.g., Fredrich and Evans, 1992; Kanagawa et al., 2000; Karner et al., 1997; Nakatani and Scholz, 2004; Olsen et al., 1998). Such experiments are conducted on the basis of fault

destabilisation due to increased pore fluid pressures, followed by the healing of fractured rock in the interseismic period. Tenthorey et al. (2003) found that there are two competing effects in the healing process; increased cohesion of gouge acts to strengthen, but the creation of low permeability horizons acts to weaken, as it can permit elevated pore fluid pressures within the fault zone. Although such controlled experiments are essential to understand fundamental processes, they are frequently undertaken on rock types that are not host to areas prone to seismic hazards, but are rather 'standard' rock types that are easily obtainable, such as the Fontainebleau sandstone from the Ile de France region around Paris, as used by Tenthorey et al. (2003), and quarry grade gabbro, as used by He et al. (2006). There have, however, been some studies undertaken on actual fault gouge. Giger et al. (2008) and Haines et al. (2010) undertook experiments on fault gouge from the Whipple Mountains Detachment, the Panamint range-front detachment, and the Waterman Hills Detachment Fault (WHDF) in the Calico Mountains, southern California. Much more recent work has looked at the frictional properties of carbonate gouge from fault zones (e.g., Verberne et al., 2010). Such studies are fundamentally informative and provide specific information on the frictional properties of the gouge but are not representative of heterogeneous fault properties as such. The relationship between fluid-rock interaction structures and subsequent rupture is still not well constrained in natural, highly-altered material simply because most rock physics experiments are carried out on unaltered, homogenous samples to explore a specific property in as controlled a medium as possible.

To gain insight into how future rupture could propagate within altered fault zones, deformation tests on Psatha Fault host rock, which contains pre-existing cementation features (Chapter IV Part I), permits an insight into the influence of existing textures on further fracture propagation.

4.2.2 Methods

In this study, I performed two types of rock deformation experiments. Cores from Psatha Fault host rock (Fig. 4.2.1) were deformed in either the Instron 60 tonne uniaxial press or the Sanchez triaxial cell at the University of Portsmouth (see section 2.2 for further details on these apparatus). The first type of experiment, the uniaxial press, simply loaded the rock core to failure, at a deformation rate of 0.6 μm/s, producing an optimally oriented ~30^{o} fracture. Then, the core was preserved in resin, and thin-sectioned at 15 mm intervals to look at how the fractures have propagated in accordance with the pre-existing textures at the microscale in an idealised stress regime. The second type of experiment loaded the core to failure at a confining

pressure (P_C) of 25 MPa, pore fluid pressure (P_P) of 10 MPa and T = 200°C, in a triaxial setup. These pressures were selected to be appropriate for a shallow earthquake epicentre depth (~5 km) and the elevated temperature was used to increase the rate of any fluid-rock interactions. Then, the sample was held stable for 24 hrs (under the same conditions), after which the sample was loaded again and forced to slide along its newly formed fault plane. The sample was then held for a further 24 hrs (under the same conditions), reloaded and slid again. The second experiment sought to investigate what effect pressure and temperature have on the sample strength, what fault slip behaviour is induced following fracturing and what slip behaviour is induced following hold periods at elevated temperature and pressure.



Figure 4.2.1 Psatha Fault host rock used in experiments. (a) The block of Psatha Fault host rock from which the experimental samples were cored (b) Scanned thin section of Psatha Fault host rock. The rock contains a mixture of heavily twinned veins (~20 twins per crystal), moderately twinned veins (up to 4 twins per crystal) and veins containing crystals with no evidence of deformation.

4.2.3 Results

In this section, I first show data from Experiment 1 (loading the core to failure in the uniaxial press): the stress-strain curve and macro and microscopic images of the fracture created and how it has interacted with pre-existing veins. I then show the stress-strain data from Experiment 2 (loading the core to failure in the triaxial press at elevated temperature and pressure in the presence of a pore fluid, reloaded 24 and 48 hrs later).

4.2.3.1 Experiment 1

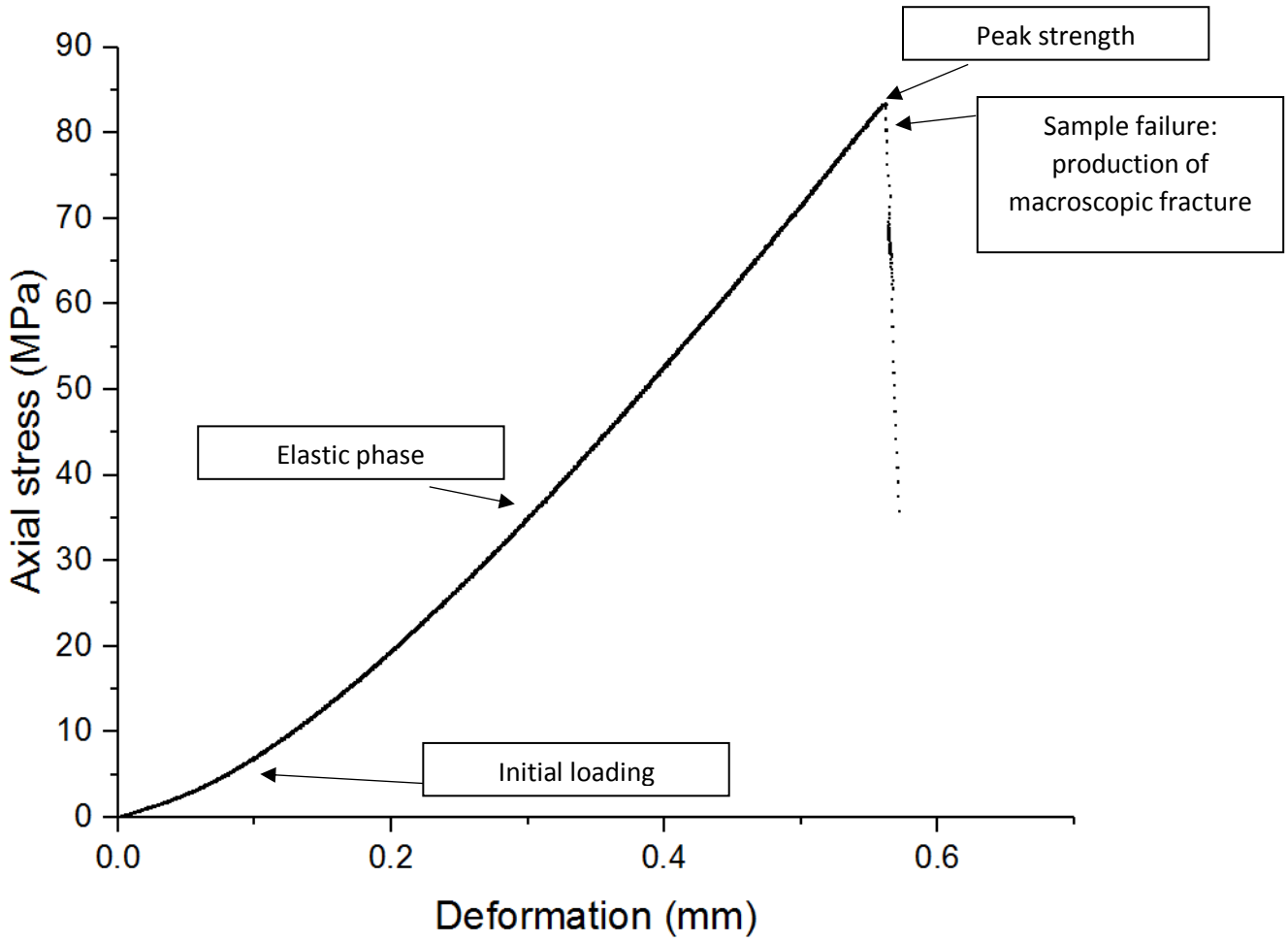


Figure 4.2.2 Stress-strain graph from Psatha Fault host rock uniaxial experiment. The stress-strain curve is very typical. There is no plastic yield, indicating the brittle nature of the rock.

The 100 × 40 mm Psatha Fault host rock sample was loaded to failure in a uniaxial setup (see section 2.2). The experiment yielded a characteristic stress-strain curve (Fig. 4.2.2; see original paper by Byerlee (1978) for a detailed explanation on classic force-displacement curves). A

phase of initial loading was followed by a linear relationship between stress and strain, from ~25.0 MPa (i.e., where elastic energy is stored in the rock) (Fig. 4.2.2). There was no discernible inelastic phase (i.e., where no more energy can be stored in the rock and further stress is accommodated by fracturing); instead, following reaching sample peak strength at 83.4 MPa (Fig. 4.2.2), failure occurred in the formation of a ~30° fracture (Fig. 4.2.3).

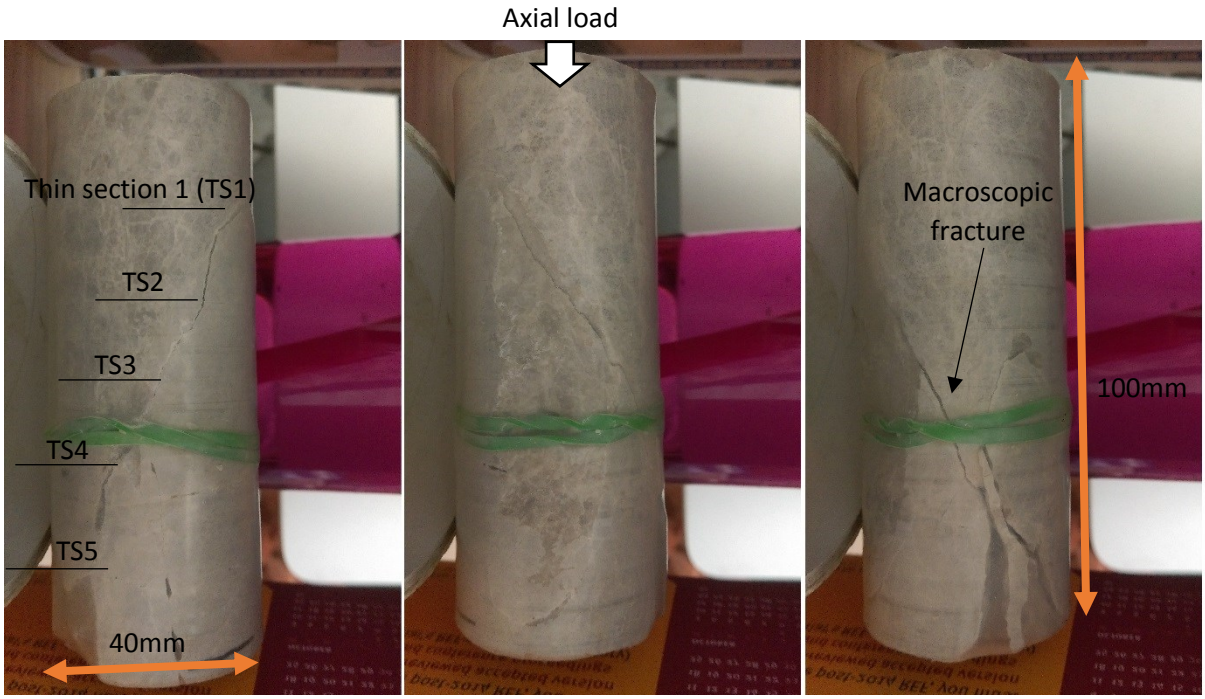


Figure 4.2.3 Resultant fracture within the core following uniaxial deformation of Psatha Fault host rock. The lines show where each thin section was taken from, at 15 mm intervals down the fractured region of the core.

Within the Psatha Fault host rock, there exists a variety of veins at various orientations (see surface of fault core in Fig. 4.2.3), indicating a complex deformation-fluid-flow history (see Chapter IV Part I). Microscopy enabled me to study the interaction between the formation of the fracture (Fig. 4.2.2) and these pre-existing veins. I was unable to conduct a detailed vein density profile of the core preceding the experiment because (i) if done by microscopy, this would involve cutting the core needed for the experiment and (ii) micro-CT scanning could not distinguish the veins in comparison to the host rock (an attempt was made but it was unsuccessful due to the lack of strong density contrast between the veins and the surrounding host rock). However, following preservation in resin and the production of thin sections, I was

able to see the orientation and positions of original veins within the core (Fig. 4.2.4) and identify several key patterns between the veins and the newly formed fracture (Fig. 4.2.4 & 4.2.5). It was also evident that idiomorphic, untwinned veins dominated the top of the core, and there were solely twinned veins from ~30 mm down. This correlates with the deformation history discussed in Chapter IV Part I; precipitation within later fractures which overlay older, deformed veins, has not yet experienced deformation.

The fracture formed (Fig. 4.2.3) is a typically optimally (~30^{o}) oriented fracture, according to standard Andersonian rock mechanical theory. The fracture propagated from the upper point in the core and progressed downwards, becoming more chaotic as it propagated to the base of the core, as can be seen in Fig. 4.2.3; the width of the deformation zone increases from a single thin fracture to a network of anastomosing fractures. The key patterns identified between the pre-existing veins and the newly formed fracture are as follows: (i) the initial fracture propagates around the crystals within the most continuous well-defined veins made up of large untwinned crystals (see Fig. 4.1.5b & 4.1.6ci, Chapter IV Part I), if consistent with the ideal ~30^{o} fracture propagation pathway (Fig. 4.2.5a); (ii) if a large, untwinned vein is slightly sub-optimally oriented (< ~10^{o} from optimal β; see 3.5.3 and Fig. 1.5) to the ideal fracture propagation pathway, the fracture will divert slightly to propagate within it (Fig. 4.2.4a); (iii) if a large, untwinned vein are non-optimally oriented (> ~30^{o}) from the ideal fracture propagation pathway, the fracture will cross-cut it (Fig. 4.2.4b); (iv) heavily twinned crystals appear to be cross-cut regardless of their orientation to the optimal fracture propagation pathway (Fig. 4.2.5c) and (v) the most chaotic part of the fracturing (in the centre of the core) does not appear to interact with the calcite crystals (Fig. 4.2.4c & 4.2.5d) in any specific manner. I assume that the small defined fractures which follow the untwinned veins, mainly found towards the top of the core, are where the main fracture propagates from, and the chaotic fracturing in the centre is a result of complete formation of the macroscopic fracture (Fig. 4.2.3). I also assume that the smaller, secondary fractures (Fig. 4.2.5e) nucleate independently during compression, and subsequently merge into the main fracture as the stress finally concentrates, rather than initiating from the major fracture during final rupture, as is typical in these types of experiments (Lockner et al., 1991; Main and Meredith, 1991). Although the new fractures look relatively independent on Fig. 4.2.4 and 4.2.5, they ultimately are part of the same macroscopic fracture, which propagated throughout the core; although they may have been influenced on a local scale, they are still defined by the optimal fault propagation orientation as per standard Andersonian rock mechanical theory.

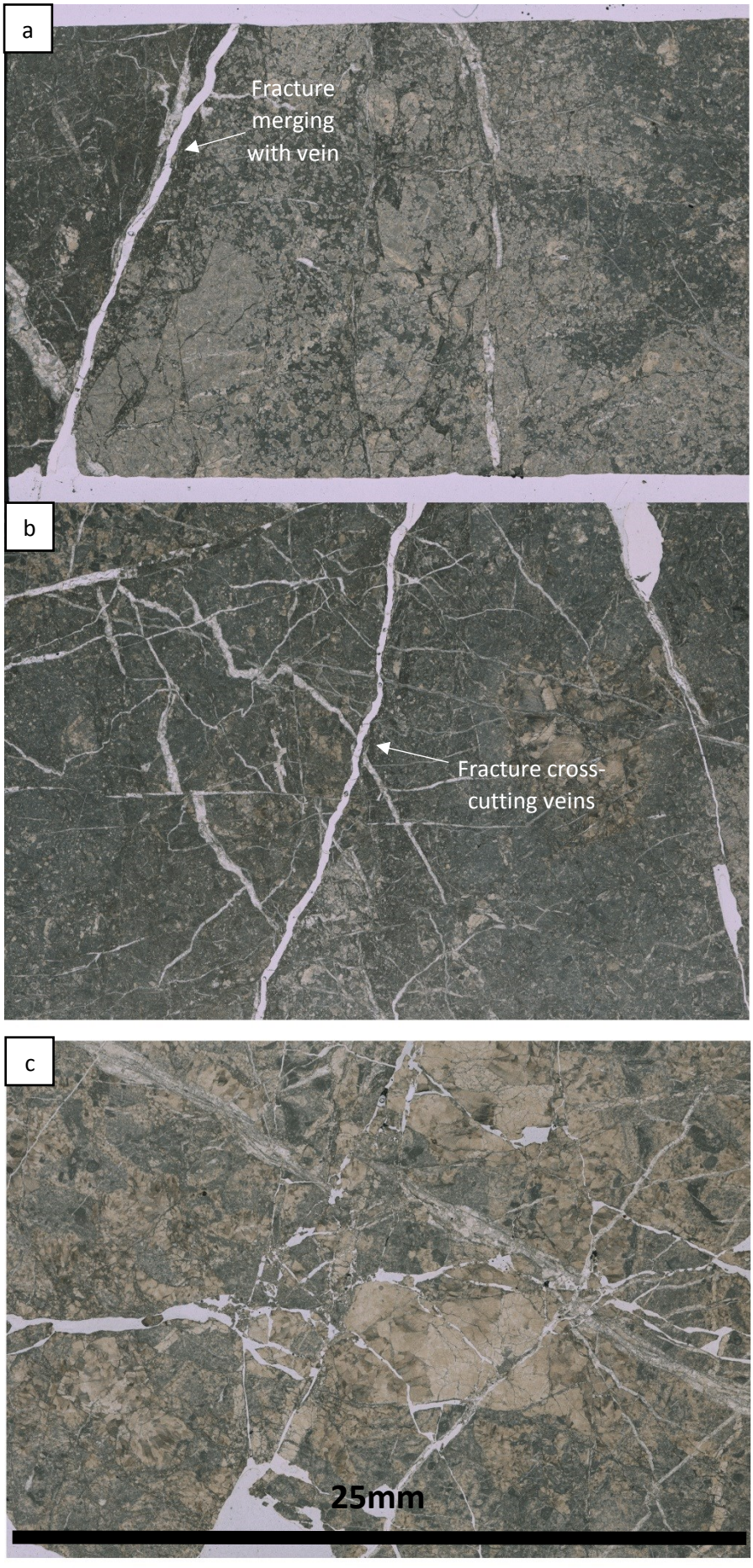


Figure 4.2.4 Scanned thin sections showing vein-fractures interactions after uniaxial deformation of Psatha Fault host rock. (a) shows a fracture starting in the host rock, then diverting to meet with a reasonably well-oriented defined pre-existing vein (TS1, see Fig. 4.2.3); (b) shows a fracture cross-cutting all the veins, as they are sub-optimally oriented to the propagation direction of the fracture (TS3, see Fig. 4.2.3); (c) chaotic fracturing (TS5, see Fig. 4.2.3).

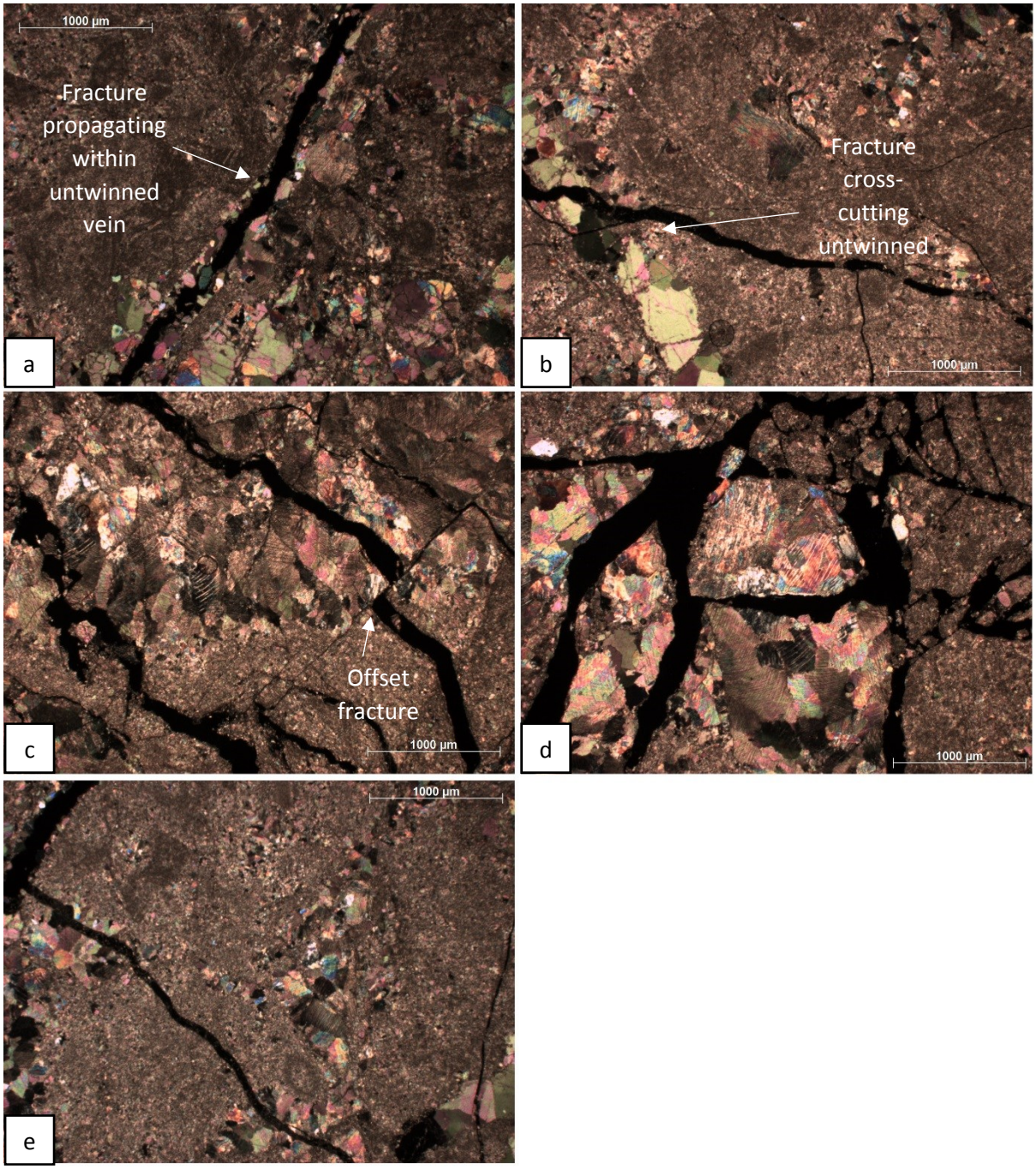


Figure 4.2.5 Micrographs of vein-fracture interactions following uniaxial deformation. (a) the fracture propagating through a well-defined, optimally oriented, untwinned vein (TS1); (b) the fracture propagating across a well-defined, sub-optimally oriented, untwinned vein (TS2); (c) the fracture propagating across twinned calcite crystals and subsequently faulted (TS4); (d) chaotic fracturing across twinned fracturing (TS5) and; (e) a smaller fracture propagating across the host rock and joining up with a fracture propagating through a vein (TS3).

4.2.3.2 Experiment 2

This experiment in a triaxial setup tested the effect of the presence of fluids, confining pressure, and temperature on initial sample strength, followed by considering how holding the sample in these conditions may alter subsequent slip. Like the uniaxial experiments, a characteristic stress-strain curve was produced (Fig. 4.2.6). The elastic loading phase lasted up to 230 MPa, followed by a slight deviation from linearity (Fig. 4.2.6a). Inelastic loading followed, up to peak axial stress at 251 MPa (top of the experimental curve, Fig. 4.2.6a). This peak stress was following by a very short period of strain softening (stress decreasing slighting with increased strain), illustrated by the small curve over at the top of the peak followed by a large stress drop (150.1 MPa) as the initial fracture was created (Fig. 4.2.6a). The sample then took more strain, from 0.9 mm onwards, but slid stably (as shown by a lack of oscillations but increasing strain, Fig. 4.2.6a) and underwent overall slip hardening (resistance increasing with increased strain, as shown by the slight positive gradient) up to 1.8 mm, when the experiment was paused. Following 24 hrs held at the set conditions (P_C = 25 MPa, P_P = 10 MPa, T = 200ºC), the sample was reloaded and, this time the sample reached peak stress at 104.7 MPa, before undergoing a period of slip-weakening (i.e., the newly formed fault is weakening during the early portion of its slip at a faster rate than the release of stress driving the fault motion (Dieterich, 1978; Jaeger et al., 2009) (Fig. 4.2.6b). The sample was then held to conserve strain in the apparatus for the next day. Following another 24 hrs held at the set conditions (P_C = 25 MPa, P_P = 10 MPa, T = 200ºC), the sample was reloaded and, following reaching peak stress at 94.7 MPa, the sample underwent small oscillatory stick-slip type behaviour (Fig. 4.2.6c). Upon retrieval of the sample, although the sample could not be extracted for preservation (removal from the reusable jacket would have led to the newly fractured rock falling apart), pieces of angular rock and smaller ground up pieces came out of the jacket, indicating that granular material had been formed in the fault zone following fracturing.

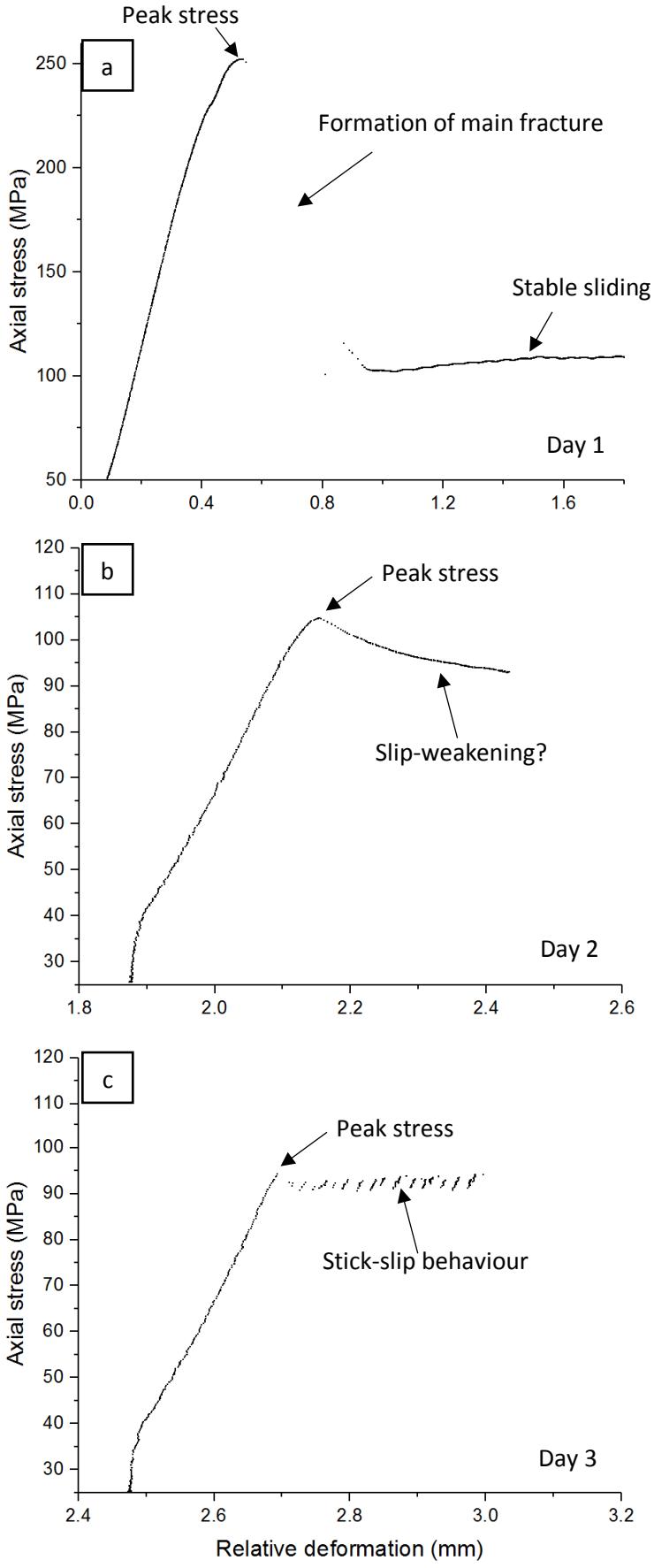


Figure 4.2.6 Stress-strain curves following triaxial deformation of Psatha Fault host rock (at P_C = 25 MPa, P_P = 10 MPa, T = 200ºC): (a) stress-strain curve of initial fracture formation; (b) stress-strain curve following reloading after 24 hours held at P_C = 25 MPa, P_P = 10 MPa ; (c) stress-strain curve following reloading after 48 hours held at P_C = 25 MPa, P_P = 10 MPa.

4.2.3 Discussion

These rock deformation experiments have shed light on future fracture propagation in heavily altered fault zones, where there are numerous cross-cutting veins (Experiment 1). They have also shown how further fluid-rock interactions can affect slip behaviour within a newly formed fault (Experiment 2).

4.2.3.1 Experiment 1

In the uniaxial experiment (Experiment 1), there was no strain-softening phase preceding the formation of the fracture (Fig. 4.2.2), indicating that the Psatha Fault rock is extremely brittle.

Fracture propagation is characterised by an expanding zone of deformation, as the initial fracture propagates from the top of the core downwards. There is reactivation within the largest, most continuous, idiomorphic, untwinned crystalline veins optimally oriented to fracture propagation pathways (Fig. 4.2.5a), as determined by standard Andersonian rock mechanical theory (see Jaeger et al. (2009)). Fractures deviate a little to propagate within slightly sub-optimally oriented veins (< ~10^{o} from the optimal fracture propagation pathway; see Fig 1.5) (Fig. 4.2.4a) but will cross-cut non-optimally oriented veins (> ~30^{o} from optimal fracture propagation direction (optimal β; see 3.5.3 and Fig. 1.5), see Fig. 4.2.5b) and will cross-cut broken, heavily twinned calcite crystals (Fig. 4.2.4c). This indicates that distinct, pre-existing structures can affect subsequent rupture propagation. This has been suggested by modelling studies (e.g., Virgo et al., 2013) but has only very recently been investigated by experiments (e.g., Ambrose et al., 2014, Everall and Sanislav, 2018). However, if previous fracture infills are not optimally oriented (possibly due to stress field changes in the field, or chaotic fracturing), cross-cutting will occur and initiate a complex evolution (Fig. 4.2.5d). Such fracture propagation within, or across, existing planes of weakness is in accordance with the JPW model (see Chapter I). Although the formation of the start of the fracture i.e., from the top of the core, may be relatively predictable, (simply following untwinned, continuous veins), the complex fracture patterns produced during the propagation of fracturing downward and formation of the new macroscale fracture (Fig. 4.2.3) show no clear correlation with pre-existing structures (Fig. 4.2.4c & 4.2.5d). However, if crystals were to subsequently precipitate within these complex fractures and lie in the optimal fracture propagation pathway (according to standard Andersonian rock mechanical theory), it is likely that the fracture would propagate within the most favourably oriented newly formed untwinned vein.

The localisation of fracturing within the untwinned veins indicates that the veins are weaker than the host rock. This is indicative that controlled fracture propagation, i.e., in the stress build up phase, may be dominated by an 'exploitative' (Phillips et al., 2016) relationship between the host rock and the pre-existing structures, i.e., fracturing exploiting pre-existing weaknesses. This indicates that, where optimally oriented continuous veins already exist, fault zone evolution would involve fracturing, refracturing along zones of pre-existing weaknesses, enhancing permeability and strength contrasts. However, in regions of the core where the dominant veins and crystals clusters were of highly twinned crystals, fractures propagated chaotically (Fig. 4.2.5d). This could be due to one of two mechanisms, or a combination of two. Firstly, this could be due to there being no discernible strength difference between the highly twinned crystalline cement and the host matrix. Ambrose et al. (2014) defined a strength anisotropy ratio (SAR) in accordance with the JPW model, defined as the ratio of the maximum strength for intact rock failure at $\beta = 0^{o}$ to the minimum strength that corresponds to the weak plane failure at angle β_{min}:

$$SAR = \left(\frac{S_0 \cos \phi_0}{S_w \cos \phi_w}\right) \left(\frac{1-sin\phi_w}{1-\sin \phi_0}\right) \quad (4.2.1)$$

where ϕ_0 is the internal angle of friction of the host rock and ϕ_w is the internal angle of friction of the weakness (in this case, the vein).

In the case of the highly twinned crystalline cement and the host matrix, the SAR would likely be close to 1. Even if fracturing initially propagated within one of these crystals, the multiple lines of weakness will constantly redirect the propagating fracture in a comparable way to how the host matrix would. This leads to a very complex, chaotic damage zone whereby the newly propagating fractures cut and modified existing deformation-fluid-flow structures, as there is no clear, discernible path/weakness for the fractures to follow. Secondly, there were no idiomorphic, untwinned crystalline veins at this depth within the fault core (below TS3). This may be because such veins are only present at the surface of the host rock and within overprinted breccias (see Chapter IV Part I). It is thus possible that fracturing may have been less chaotic if such strength contrasts and obvious fracture propagation pathways existed deeper within the host rock. However, the present complex vein relationships in the host rock that are seen indicate that any idealised situations observed, such as propagation within untwinned continuous veins, may only exist for a short time.

I propose the following sequence of events (Fig. 4.2.7):

1. Precipitation occurs within a newly formed fracture, which propagated in an ideal orientation (according to standard Andersonian rock mechanical theory).
2. A subsequent deformation event leads to (i) the main fracture propagating through the centre of the crystals, as long as the stress applied by the next deformation event is greater than the stength of the new, untwinned crystals and is optimally oriented. This would restart the sequence of events. However, a subsequent deformation event may result in (ii) twinning of the crystals, due to the crystals being stronger than the applied stress and/or being non-optimally oriented, or (iii) deviation of a fracture into the vein, due to slightly sub-optimal orientation (but still $< 30^{o}$ between the plane of weakness and the maximum principal stress). This could also occur due to chaotic fracturing.
3. Further fracturing may initially focus in the weaker crystal pathway (which has a low SAR ratio (see Ambrose et al. (2014)), but, due to twinning, the fracture gets deflected and deviates into the surrounding host rock.
4. Following multiple deformation events where twinning, fracture deflection, chaotic fracturing and overprinting have occurred may eventually reduce the strength contrast between the crystals and the host rock to ~1.
5. In the next deformation event, a new fracture will cross-cut across this effectively homogeneous rock (mechanically, in regard to the SAR ratio), cross-cutting any previous infills.
6. This newly formed fracture will form an optimal site for exploitation of slightly acidic fluids and crystal formation. The sequence repeats again.

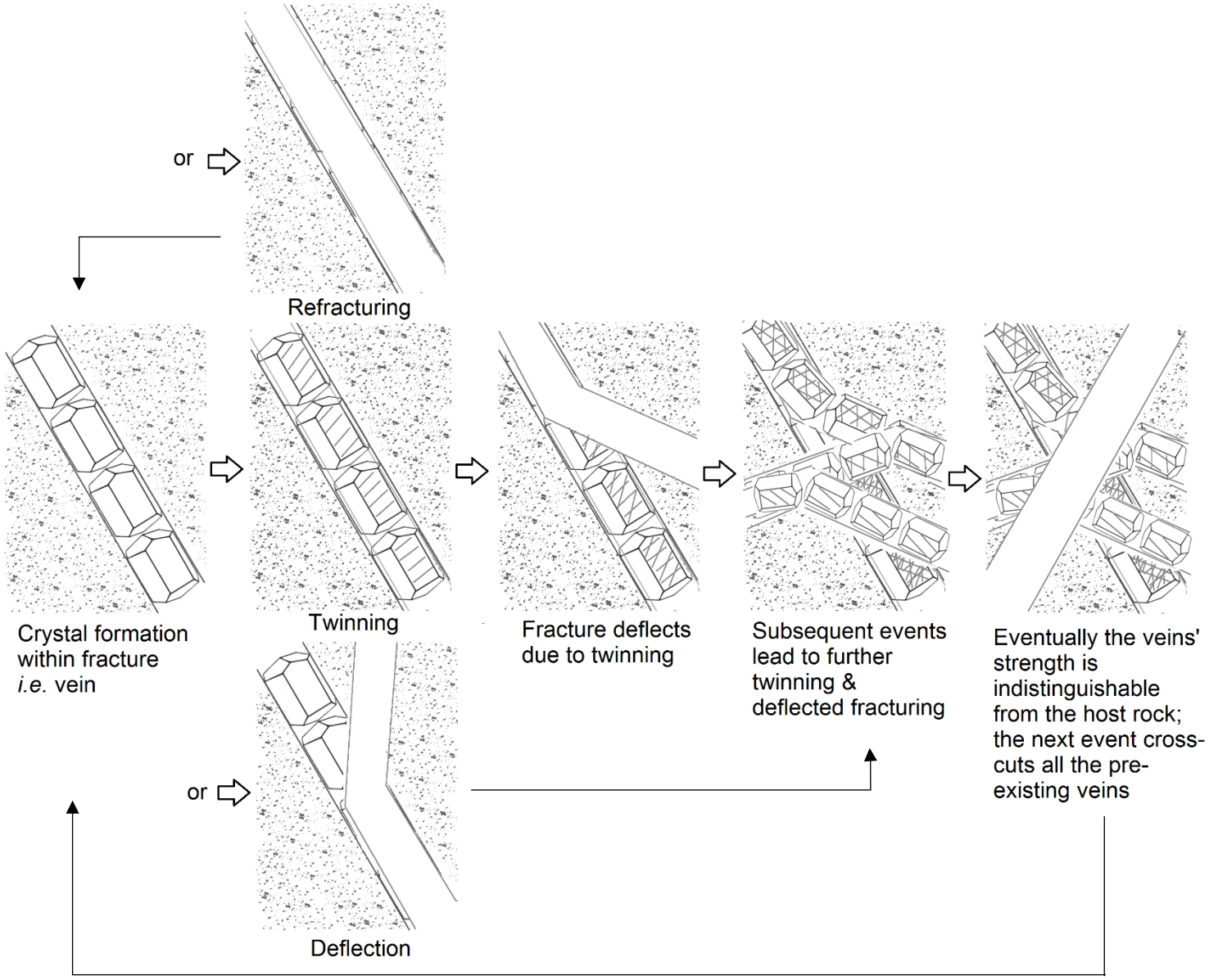


Figure 4.2.7 Schematic cartoon showing the evolution of veins throughout subsequent deformation events (as depicted by arrows). The potential evolution pathways shown are dependent upon (i) magnitude of deformation, (ii) orientation of prevailing stress field relative to pre-existing veins, (iii) degree of existing twinning within veins i.e., the strength contrast between the host rock and pre-existing features.

This process is an example of 'fault-rock recycling' (Wibberley and Shipton, 2010). Notably, however, although the newly precipitated veins must be weaker overall (otherwise the fracture would not propagate within them over the surrounding matrix), precipitation should lead to inherent strengthening i.e. the crystals themselves should be stronger. If this were not the case, a protolith would simply become progressively weaker over only a few deformation cycles and disintegrate. The intrinsic weakness lies in the incohesive nature of the veins i.e. the crystal contacts are incohesive as they have not been subjected to intense compaction processes. As the vein is less cohesive than the surrounding matrix, a propagating fracture can exploit the weak crystal-to-crystal contacts, which provide a relatively continuous propagation pathway. This is evident in Fig. 4.2.5a: there are no broken crystals but rather whole crystals separated from the rest of the vein and whole crystals left at the vein edges. The new fracture can thus propagate around the crystals rather than fracturing through them, demonstrating the inherent weakness and incohesive nature of the crystal boundaries as well as the strength of the crystals themselves.

The macroscopic fracture ultimately formed at its optimal angle of ~30° following an external applied stress being greater than the strength of the host rock. On a microscale, this main fracture has propagated according to the relationship between the weaknesses within the host rock to the applied stress (Fig. 4.2.5). On a field scale, Phillips et al. (2016) inferred three main interactions between pre-existing structures and subsequent faulting; (i) faulting can exploit pre-existing weaknesses; (ii) faults can initiate independently but subsequently inherit their orientation and merge with the pre-existing weakness; or (iii) faulting can initiate independently and cross-cut these pre-existing heterogeneities. My experiments have shown that such interactions also exist on a much smaller scale (Fig. 4.2.8).

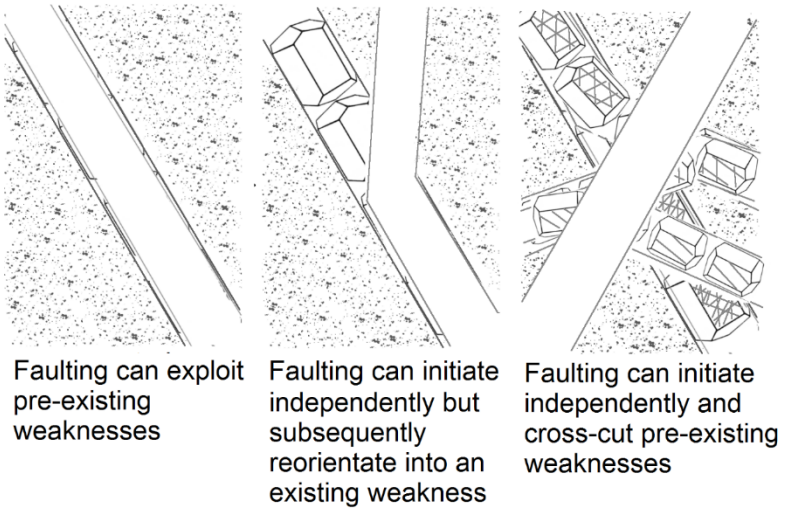


Figure 4.2.8 The relationships between pre-existing structures and subsequent faulting found on a field scale (Phillips et al., 2016) also exist on a much smaller scale.

4.2.3.2 Experiment 2

Although the formation of the new main fracture has relationships with the pre-exisiting veins, as shown in Experiment 1, the processes which occur during fracture formation clearly have an influence on subsequent slip behaviour, as shown by Experiment 2. Experiment 2 sheds light on how newly formed fault rock, which is then subjected to cohesive processes, may induce changes in fault slip behaviour. Like Experiment 1, it is clear that the Psatha Fault rock is extremely brittle, given that the strain-softening phase is extremely short (< 0.1 mm), and likely only permitted due to the use of a confining pressure and the hold of the rubber jacket (Fig. 4.2.6a).

There appears to be a change in the mechanism controlling fault slip with time. Following the formation of the initial fracture, the stable sliding behaviour observed is likely due to the formation of new fault rock material, i.e., broken pieces of the fault rock rolling over one another, which allows aseismic-type slip. This is a mechanism known as granular flow (Savage, 1984). In addition, the newly formed fracture is particularly rough. The roughness of this newly formed fault is uncontrolled (because it was produced in the experiment rather than input at the beginning as a saw-cut and sanded to a particular roughness), and thus it is difficult to quantify its effect. In addition, I note that relationships with the veins at smaller scale (deflection, merging) may alter fault roughness at the fault scale. Harbord et al. (2017) and Brace and Kohlstedt (1980) have indicated that increasing normal stress upon asperities has a stabilising influence. Following a 24 hr hold, a period of slip-weakening occurs, indicating that a degree of cohesion has been achieved within the fault zone. The two mechanisms for this could be (i) static friction increase due to the contact between the two fault surfaces for a relatively long period (Beeler et al., 1994; Dieterich, 1972; Kato et al., 1992; Marone, 1998), or (ii) precipitation achieved through the pore fluid deriving carbonate from the fracture surface and re-precipitating it within the fault zone (Atkinson, 1984), or a combination of both. Following another 24 hr hold, the fault immediately undergoes stick-slip type instabilities subsequent to loading.

I suggest a combination of mechanisms, cohesion from either static contact or/and precipitation combined with a subsequent 'smoothing' of the fault following further deformation (see the results of Harbord et al. (2017) on the relative role of rough vs smooth faults) has enabled a change from stable sliding to stick-slip type behaviour. Where there was no cohesion in the fault zone, following the formation of the main fracture, granular flow of the newly formed

fault material dominated further strain. However, following a hold period in pressurised, elevated temperature conditions, incomplete cohesion and compaction in the fault zone led to slip-weakening. Following the cohesive resistance dying out during slip-weakening, further smoothing of the fault enabled subsequent stick-slip behaviour. Unfortunately, due to the setup of the apparatus whereby the jacket is used for multiple experiments and thus cannot be preserved with the sample inside, I was unable to extract the core intact, and was thus unable to conduct subsequent microscopic analyses to determine what textures had been created in the fault zone, and determine exclusively what cohesive processes (simple static hold, or precipitation) have occurred. As with the formation of the main fracture being thought of as a culmination of small-scale fractures (Brantut et al., 2013), as is evidenced by Fig. 4.2.4 & 4.2.5, the mechanisms controlling the cohesion, e.g., grain scale diffusive processes, would be occurring on a microscale. Further experiments are needed to understand (i) the possible role that any fluid-rock interactions may have had on the subsequent slip behaviour, (ii) the possible role that temperature may have had on the subsequent slip behaviour, (iii) whether simply fault-on-fault interaction with fluid, with no gouge present, can enable an aseismic-seismic transition, and (iv) the relative important of gouge. Such experiments need to be accompanied by detailed microscopy down to the μm scale.

4.2.4 Conclusions

My experiments have shown that the fluid-fracturing cycle may exert a significant control upon future fault rupture properties. In some case, pre-existing fluid-flow structures such as veins can alter the direction or define the path of fracture propagation. Newly formed features, subject to cohesive processes, can alter fault slip behaviour. The importance of scaling has been discussed; at the microscale, heterogeneities have an influence over propagation pathways, but ultimately, they merge to form an optimally oriented fracture at the macroscale. Initial data has been provided on how subsequent cohesive processes within new fractures may in turn alter the frictional properties of the fault. Further experiments and/or modelling is needed to quantify the cohesive effect that fluid-rock interactions may have on fault slip behaviours, whereby fluid in supplied to a reactive gouge layer in a pre-existing fault at a variety of temperature/pressure conditions.

Chapter V: Precipitation in carbonate faults: a requirement to allow different slip behaviours?

Like destructive earthquakes, slow-slip events (SSEs) involve slip on a fault. However, during an SSE, the fault slips so slowly that seismic waves are not incited, and there is no shaking. These SSEs occur at a range of depths in the Earth's crust: 'shallow' SSEs occur at depths equivalent to temperatures up to ~200°C, and deep SSEs at depths equivalent to temperatures between 350°C and 450°C (although precise temperature windows are slightly different in different geographical locations (the Hikurangi margin, Nankai margin, Costa Rica, northern Japan). Slip-weakening, whereby a fault weakens during the early portion of its slip at a faster rate than the release of tectonic stress driving the fault motion, has been suggested to be of importance in generating SSEs, as has elevated pore fluid pressures. Until recently, experimental work on the frictional properties of faults has focused on silicate rock types, even though carbonates host both SSEs and destructive earthquakes. In this work, I report on laboratory observations, which show that long-duration slip-weakening is induced at 150°C on water-saturated bare-interface calcite faults. Deformation in this setup also results in a carbonate-saturated fault zone, an increase in shear strength, and a dramatic reduction in permeability, even during slip, compared to a fault saturated with non-reactive argon. Calcite faults hydrothermally treated at temperatures of 450°C did not exhibit slip-weakening, but rather stick-slip behaviour following reaching peak strength. These results have implications for the role of cohesive processes in the presence of reactive fluids on the sliding properties of bare-interface carbonate faults and fault zone evolution.

5.1 Introduction

Until recently, studies on the frictional properties of faults have focussed on silicate rock types (e.g., Blanpied et al., 1995; Chester and Higgs, 1992; Smith and Evans, 1984). However, carbonate platforms have hosted significant destructive earthquakes; for example: the 2009 L'Aquila earthquake occurred in the Lazio–Abruzzo carbonate platform (Anzidei et al., 2009), the 1981 sequence of earthquakes in the Gulf of Corinth propagated along limestone-hosted faults (Jackson et al., 1982), and the 2008 Wenchuan earthquake occurred on the Longmenshan Fault composed of limestone (Chen, 2015). Carbonates have also hosted regions demonstrating SSEs, notably along the Costa Rica margin (Kimura et al., 1997), and in the Italian Apennines (Amoruso et al., 2002; Borghi et al., 2016; Crescentini et al., 1999). Therefore, studying the

rheological properties of faults in carbonate rocks is required in order to understand more about earthquake processes in regions where carbonate lithologies dominate.

Although the process of brittle failure in the crust is viewed as a mechanical process, in which there is a critical stress to overcome, at which point fracturing or slip on a pre-existing fault occurs, fluids can also exert a significant influence upon deformational processes within the Earth's crust (see Chapter III). The presence of mineral-saturated fluids in a fault zone can lead to processes such as mineral precipitation, strengthening faults (Atkinson, 1984), decreasing their permeability, and increasing their stability, through increases in contact area and packing density (Angevine et al., 1982; Niemeijer et al., 2008; Renard et al., 2004). Fluid-rock interactions can increase the intrinsic strength of the sliding contacts, far above that achieved by simple Dieterich-type healing (strength gained from sole fault rock on fault rock contact over an extended period of time; see Niemeijer et al. (2008)).

Tectonically active regions dominated by carbonate lithologies frequently host faults which contain fractures cemented by phases of calcium carbonate, derived from either minerals transported by fluid-flow into the fault zone (Lee et al., 1996; Oliver, 1996; Sibson et al., 1975) or from reactions between the fluid and the fault zone (Egeberg and Saigal, 1991), which may act to strengthen and/or alter fault slip behaviour (see Chapters III and IV). The influence of cementation through the processes of pressure solution and precipitation on carbonate faults has also been proposed as a possible mechanism for shallow (< 10 km deep) SSEs (Bauer et al., 2014; Ikari et al., 2013b), as has elevated pore fluid pressure (Kitajima and Saffer, 2012; Kodaira et al., 2004; Saffer et al., 2000). SSEs are transient slip events, which involve displacement on a fault occuring over periods of hours to weeks to months, rather than seconds (Linde et al., 1996; Saffer and Wallace, 2015). Displacement during an SSE is usually significantly less than that of an earthquake (on the order of mm, e.g., Nakata et al. (2017)), although in some cases the fault can undergo as much displacement as during a magnitude 6-7 earthquake (e.g., 15 cm along the subduction interface beneath Guerrero, Mexico over six months (Frank et al., 2018)). The conditions that may permit an SSE to nucleate, as opposed to a larger stick-slip type earthquake, are not well understood (Saffer and Wallace, 2015). Previous experimental work on fault healing and sealing under hydrothermal conditions has focussed on characterising the properties of silicate rock types (e.g., Blanpied et al., 1995; Chester and Higgs, 1992; Smith and Evans, 1984), but interest in the complex fault behaviour in carbonates has accelerated recently (Chen et al., 2015, Kurzawski et al., 2016; Verberne et al., 2010). Notably, these experiments have focussed on the frictional properties of fault gouge

at fault interfaces; however, many natural faults have relatively narrow slip zones (at least in areas where destructive earthquakes occur; a slow-slip fault has not been directly sampled as of yet), and bare-interface sliding frequently occurs (Bauer et al., 2014; Collettini et al., 2014; De Paola et al., 2011; Sulem and Famin, 2009).

This work aims to investigate the nucleation conditions on bare-interface carbonate faults that may be required to initiate different slip behaviours. Specifically, the role of different fluids (water: reactive, and argon: inert) at different temperatures is investigated, and the implications of these conditions for any subsequent frictional instabilities is discussed.

5.2 Methods

Seven experiments were performed, and the parameters involved in each experiment, C1 to C7, are shown in Table 5.1. Cores of quarry standard Carrara marble (10 × 25 mm) were cored, a fault saw cut, and a hole drilled from the top of the core to the fault surface for pore fluid insertion (see section 2.2 for further details). Two fluids were used in these experiments: water and argon. Water is used as a geologically relevant reactive pore fluid, whereas argon is used as a comparatively inert fluid. Pore fluid pressure conditions for either pore fluid are identical (see Table 5.1). Each experiment (Table 5.1) consisted of (1) raising the confining pressure (P_C) to 120 MPa, pore fluid pressure (P_P) to 40 MPa (pore fluid of either water or argon), and temperature to 450^{o}C (2) loading the core at an axial displacement rate of 4 μm/s to assess the effect of this loading stage (all samples loaded to sliding except C1, which tested the experimental setup and C3 which characterised the evolution in permeability without slide). Five experiments also involved a stage (1i) during which the sample was held at elevated temperature and pressure in the presence of fluid (either water or argon) (C3-C7, Table 1); and four of these five experiments involved (1ii) reducing the temperature to 150^{o}C halfway through the hold time (C3, C4, C6 & C7, Table. 5.1). It is noted that sliding on C2 was done while raising the pressure and temperature conditions, in order to assess the immediate effect of these variables (see Table 5.1). The aim of each experiment was as follows:

1. C1 tested the experimental setup.
2. C2 was loaded during setting the experimental conditions to characterise the behaviour of the saw-cut fault under rising hydrothermal conditions.
3. C3 characterised the evolution of permeability in a hydrothermally altered sample without slide.

4. C4 characterised the slip behaviour of a hydrothermally altered sample following a reduction in temperature (150ºC).
5. C5 characterised the slip behaviour of a sample at maintained hydrothermal conditions (450ºC).
6. C6 and C7 characterised the slip behaviour of a sample in the presence of argon in identical pressure and temperature conditions to C4.

Table 5.1 Summary of experiments performed in this study on slip on bare-interface calcite faults.

Ref	Healing temp, T_h +/-5 (ºC)	Deformation temp, T_d +/-5 (ºC)	Slide time (hr)	Effective stress σ_{eff} (P_C-P_P) (MPa)	Saturation fluid	Experiment type
C1	450	-	0-2	80	None	Test
C2	-	0-450	0-2	80	Water	Slide
C3	450	150	4-8	80	Water	Hold-repeated load
C4	450	150	4-5	80	Water	Hold-slide
C5	450	450	4-5	80	Water	Hold-slide
C6	450	150	4-5	80	Argon	Hold-slide
C7	450	150	4-5	80	Argon	Hold-slide

The experiments were conducted at conditions relevant for the depth range of both shallow and deep SSEs (i.e., temperatures below 200ºC for SSEs, and 350-450ºC for deep SSEs, approximately; see Saffer and Wallace (2015)). The axial deformation rate (4 μm/s) is set to ensure that the experiment could be fully completed within a single working day (to ensure that the experiment was always monitored, as is required in this setup due to the high temperatures reached). Permeability was measured periodically, using the oscillation technique (see section 2.2), in order to track the evolution of permeability during loading and subsequent slip (Kranz et al., 1990). In order to study the microstructures produced during the initial concentration of stress during loading i.e., the nucleation phase, rather than subsequent instabilities, the

experiments were only run until the initial phase of slip-weakening or stress drop has been produced. In the case of the samples which underwent stick-slip type behaviour (C2, C5-C7), this was the very first, large stress drop. In the case of the sample that underwent long-duration slip-weakening, this was estimated from degree of the stress drop in the stick-slip cases, to ensure that subsequent instabilities did not occur. After this time, the experiment was stopped, and the sample retrieved (apart from experiment C2, which did not utilise a hold time; see Table 5.1). At the end of each experiment, the samples remained held within their copper jackets, so the final textures were preserved. They were preserved in Epoxy resin immediately after the sample was retrieved from the apparatus. Following hardening of the resin (~24 hrs later) the samples were vertically cut to intersect the fault zone and thin sectioned. Microscopic analysis was carried out on each sample to assess any microstructural changes.

5.3 Results

The results from experiments C2, C4, C5 and C7 are described below. C1 was a pilot experiment to test the experimental setup, and C3 was not slid, but was instead testing the permeability oscillation method and permeability evolution pre-slip.

5.3.1 Stress-strain

Fig. 5.1 shows the comparative data between the different experiments to illustrate the effect of hold time and different pore fluid (water/argon) upon sample strength and displacement. All samples initially showed a similar linear relationship between the coefficient of friction, μ, and displacement. The initial value of the peak value of μ, μ_{pk}, of sample C2, in water saturated conditions, was 0.45, which was followed by a stick-slip type drop to 0.31. However, the strength of C2 continued to increase following incremental stick-slip type drops, as the pressure and temperature conditions rose to σ_{eff} = 80 MPa and T = 450°C. The subsequent value of μ_{pk} was 0.57, followed by 0.62, then 0.63. Following a total experiment duration of 4 hrs in the presence of water, with an induced temperature drop to 150°C halfway through the experiment (C4), the value of μ_{pk} was 49% greater than exhibited by C2, at 0.77. In the presence of water, with maintained temperature throughout the duration of the experiment (450°C), μ_{pk} was 0.73 (C5) which was followed by a stick-slip type drop and then a further mediated stress drop (Fig 5.1). Furthermore, following an initially similar relationship between strength and displacement as the other samples, C5 took on a notably shallow trend between μ and shear displacement (Fig. 5.1) beyond a displacement of ~0.25 mm, indicating ductility at this elevated temperature, undergoing 0.28 mm greater displacement before fault slip. After a hold

period in the presence of argon at 150°C, μ_{pk} was 0.70 (C7) and was followed by a stick-slip type stress drop (see original paper by Byerlee (1978) for a detailed explanation on classic force-displacement curves).

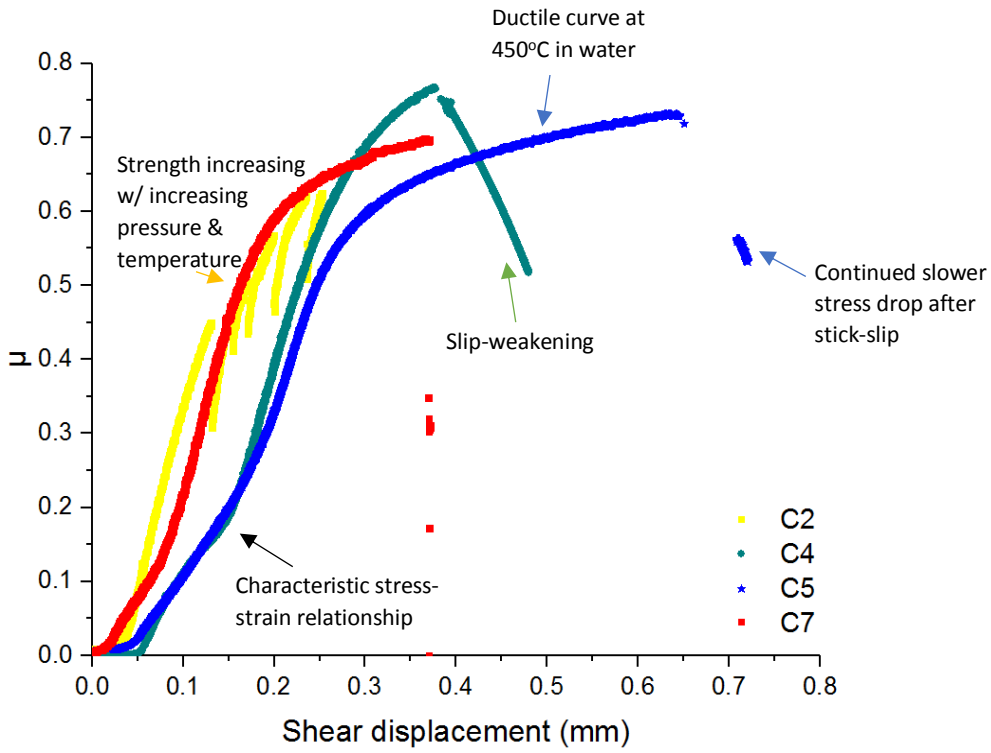


Figure 5.1 Comparative stress-strain data between C2, C4, C5 and C7.

5.3.2 Permeability

Permeability was measured at each stage throughout the experiments (Fig. 5.2) using the oscillation method described in section 2.2. Fluid was oscillated from the top of the sample, into the drill hold intercepting the fault surface, along the fault and its response measured at the base. Thus, the permeability measurement is taken to be the bulk permeability of the fault zone, with minimal contribution from the bulk of the sample. No permeability data could be obtained for the argon-saturated experiments (C6/C7); the permeability of the fault zone must have been either too high or too small to utilise the oscillation technique (see section 2.2).

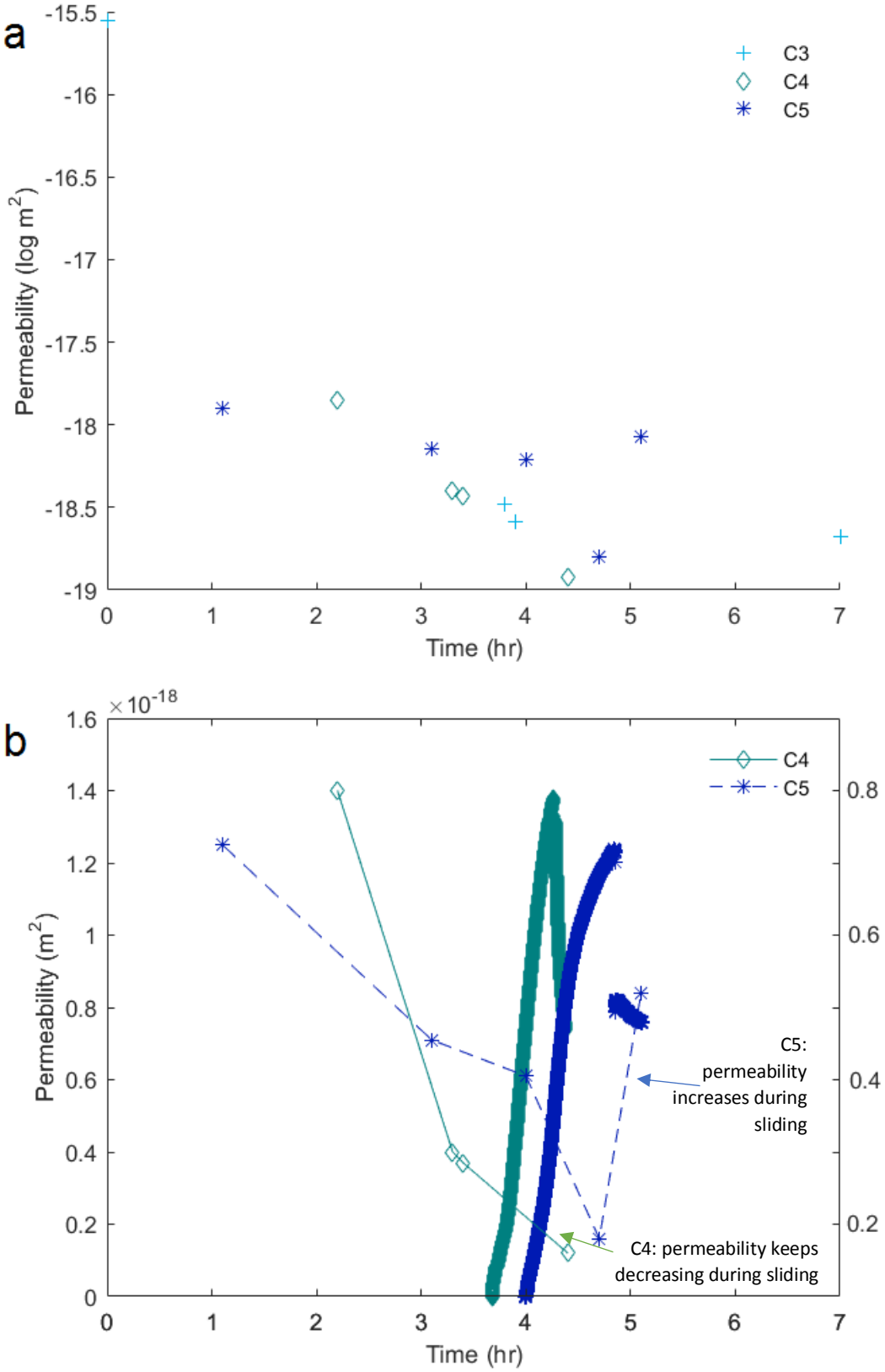


Figure 5.2 Permeability vs time graphs during deformation of bare-interface calcite faults (a) The variation in permeability throughout the hydrothermally altered experiments over time. (b) The relationship between sample loading, sliding and permeability over time.

Over a period of 3.8 hours, from room temperature to achieving hydrothermal conditions (450°C), the permeability of C3 dropped by three orders of magnitude from its starting value, from 2.8×10^{-16} m^2 to 3.3×10^{-19} m^2 (Fig. 5.2a). After 4 hours of hold (with loading, but no sliding), C3's permeability continued to decrease, but levelled out to a stable 2.5 +/-0.4×10^{-19} m^2, i.e., the permeability reduction rate is fast in the initial stages of the hold period, and decelerates in the later stages. These values obtained are reasonable for experimental fault zone permeability (see Tenthorey et al. (2003)). All hydrothermally altered samples (C1-C5) show that the permeability continued to decrease during loading (Fig. 5.2b). When the temperature was reduced to 150°C halfway through the experiment (C4), permeability did not recover when the fault slipped (Fig. 5.2b). However, when 450°C was maintained throughout the experiment (C5), the permeability recovered by 81% of its pre-sliding value upon fault slip and by 27% of its pre-loading value (Fig. 5.2b).

5.3.3 Duration of stress drop

The drop in μ following μ_{pk}, for both the hydrothermally (water) and thermally (argon) altered experiments that slid at 150°C (C4 and C7 respectively), was 0.28 and 0.34, respectively (Fig. 5.3). The drop in μ following μ_{pk} for the hydrothermally (water) altered experiment that was slid at 450°C (C5) was 0.21. However, the duration of this initial weakening period was notably different between different experiments (Fig. 4.3). For both the thermally altered fault (C7) and the hydrothermally altered fault (C5) with no change in hydrothermal conditions, i.e., kept at 450°C, the stress drop duration was in the order of ~1 sec (Fig. 5.3b). However, for a hydrothermally altered fault with an associated temperature drop to 150°C halfway through the experiment time (C4), the associated stress drop following peak shear stress took place over 351.6 sec (Fig. 5.3a).

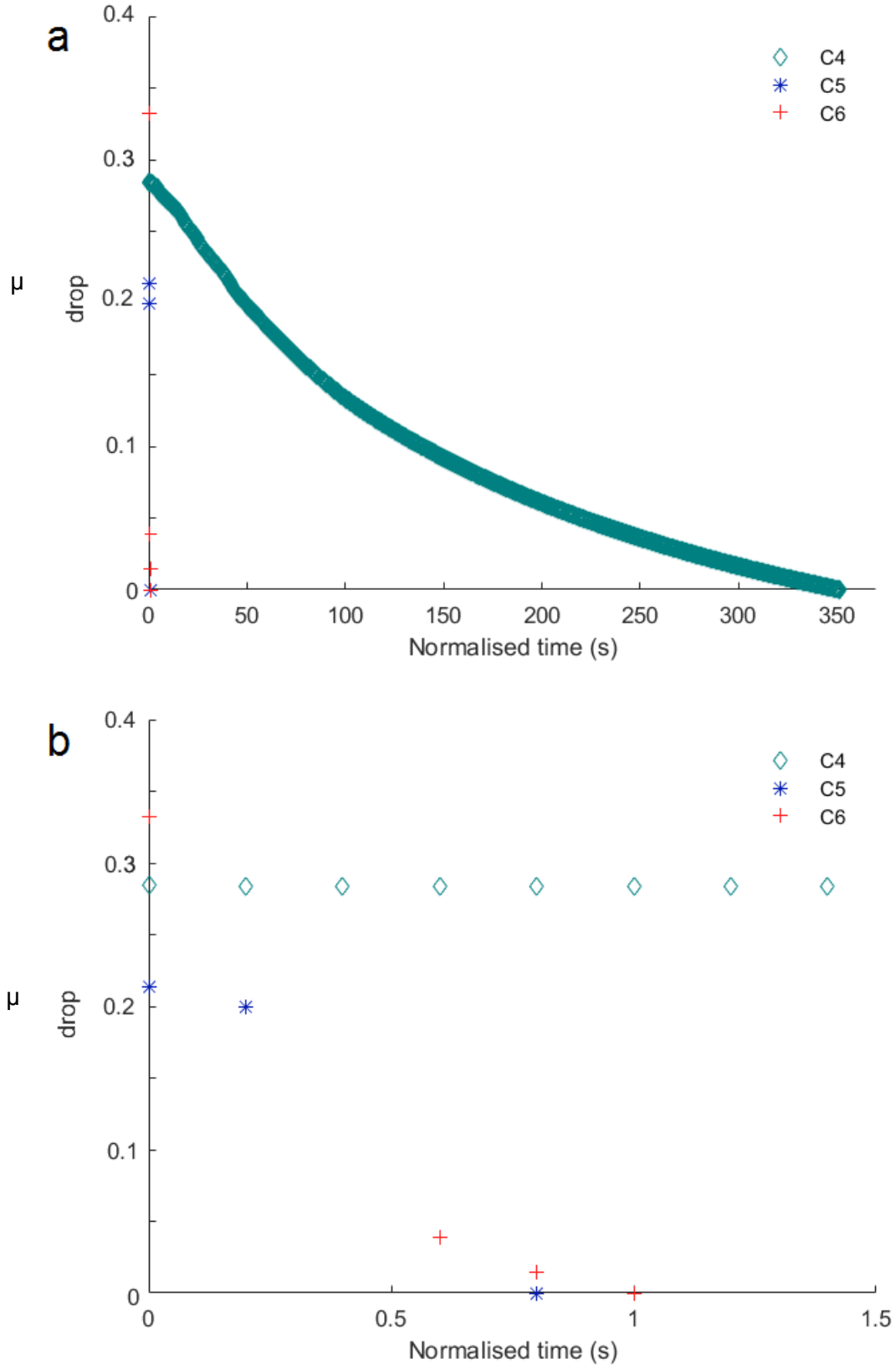


Figure 5.3 Comparative data of the duration and degree of stress drop following peak stress between C4, C5 and C6.

5.3.4 Microstructures

The resulting textures following deformation are hereafter illustrated and described (Fig. 5.4 & 5.5).

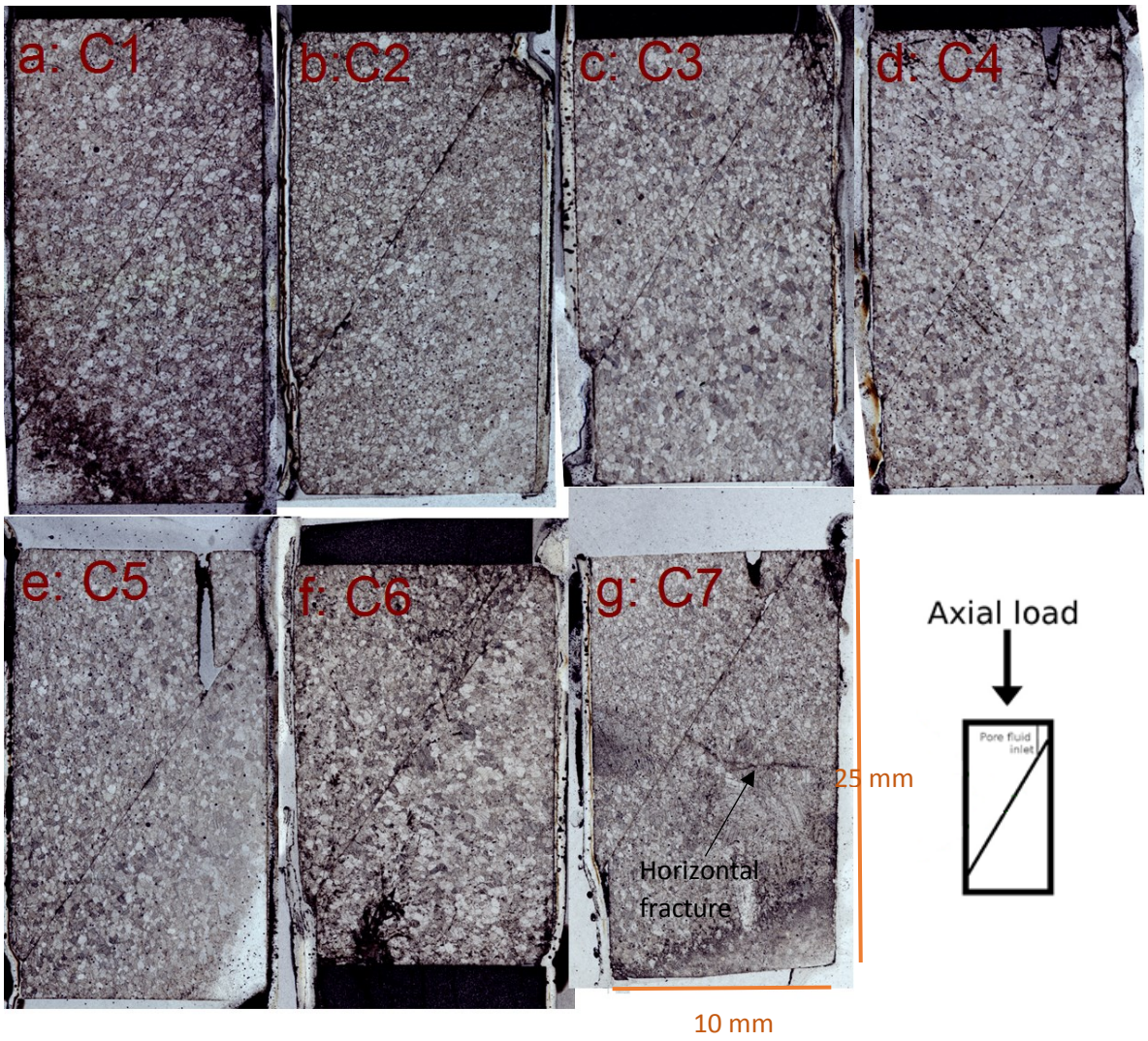


Figure 5.4 Scanned thin sections of all deformed Carrara marble samples (C1-C7).

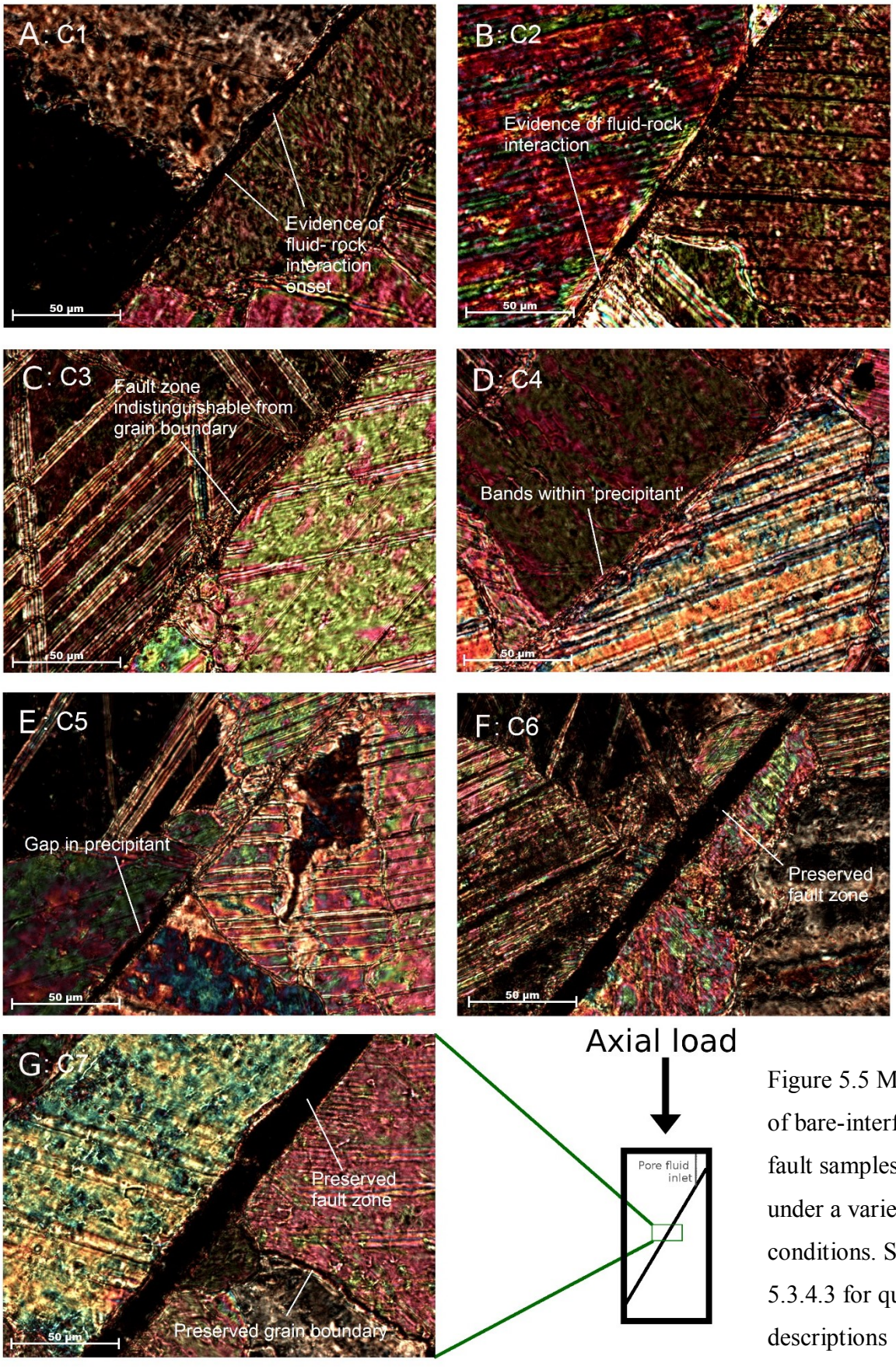


Figure 5.5 Micrographs of bare-interface calcite fault samples deformed under a variety of conditions. See 5.3.4.1-5.3.4.3 for qualitative descriptions

5.3.4.1 Microstructures in argon saturated samples

Alteration of the host rock appears to depend on whether argon or water is the pore fluid (see Fig 5.4 & 5.5). Only samples deformed in argon (C6 &C7) showed cracks and fractures developed in the host rock (Fig. 5.4f, g). Notably, in C7, there are horizontal extension microfractures (~500 μm long) propagating from the fault plane, sub-parallel to the applied normal stress (Fig. 5.4g). This could be tensile cracking formed when unloading the sample, post shear dilation, or thermally-activated cracking (Kim and Kemeny, 2009; Pollet and Burns, 1977; Zhang and He, 2013). Such cracks are not seen in any of the hydrothermally altered samples (e.g., Fig. 5.5a-e, C1-C5).

Following deformation in the presence of argon (C6 & C7), the fault zone is clearly preserved (Fig. 5.5f-g). The final fault zone width is ~10-15 μm wide. Minor, long wavelength asperities (< 2 μm high) can be seen along the fault plane surfaces, and the grain boundaries are still distinct (Fig. 5.5g).

5.3.4.2 Microstructures in low-temperature, water saturated samples

Textures produced in the fault zone also depend not only on whether argon or water was the pore fluid, but also on the precise conditions throughout the experiments (Fig. 5.5). Evidence of precipitant/cement is present along the fault planes of C2. (Fig. 5.5b). In samples where the temperature was reduced to 150^{o}C halfway through the experiment (C3 & C4, Fig. 5c, d), the fault zone is almost indistinguishable from a grain boundary, which is a significant change in fault topology. A precipitant/cement runs between the fault contacts and along all grain boundaries. These fault zones are compacted to 4-5 μm wide. The precipitant/host rock contact is only barely distinguishable. The textures within this precipitant/cement phase within the fault zone permit discrimination of which sample underwent sliding between C3 and C4; elongated bands can just be seen within the precipitant in C4, indicating some 'stretching' of this phase (Fig. 5.5d). The original rock texture is preserved, aside from twinning in the host rock crystals and the precipitant/cement along the grain contacts.

5.3.4.3 Microstructures in high-temperature, water saturated samples

The sample kept at constant hydrothermal conditions at 450^{o}C (C5, Fig. 5e) has well defined fault contacts interspersed with sections of precipitant/cement. The width of the fault zone varies with the amount of the precipitant phase; the fault zone width is up to 7 μm where the fault zone is well defined (e.g., C5, Fig. 5.5e), and there is limited evidence of precipitation

(although there is still evidence of a thin film along the fault contact). The fault zone width is only 4 μm wide in parts infilled with this phase. There are small wavelength asperities along the fault contact of ~2 μm high. The fault zone is still well defined overall; there is no apparent damage zone, but a clear distinction between the fault and the surrounding host crystals (C5, Fig. 5.5e). The grain contacts show evidence of this precipitant/cement, although the faults boundaries are still well defined.

5.4 Discussion

The experimental results presented here affirm a complex relationship between carbonate fault zone properties and fluids, demonstrating both end member and competing effects. The results show that hydrothermal processes in a fault zone can result in an alteration of fault strength, a change in fault zone topology, and an initial phase of long-duration slip-weakening.

5.4.1 Cohesion processes

There is a change in peak shear strength between samples depending on experimental conditions (Fig. 5.1). This is due to a change in cohesive strength within each sample (for all experiments), but especially for the hydrothermally (water) altered samples (Fig. 5.1, C4). It is proposed that mechanical strengthening for all experiments is achieved by means of compaction, whereby the contacts at the fault zone interface and at grain contacts are densified (Tenthorey et al., 2003). In the presence of an inert fluid (e.g., argon), compaction due to increased axial displacement and thermally-activated compaction are the only means of 'healing' (as opposed to chemical processes (Marone, 1997; Yasuhara et al., 2005)). This leads to the frictional behaviour purely depending on the friction between the contacts, which depends on how 'rough' the contacts are (Harbord et al., 2017), which, in this case, enables standard stick-slip type behaviour (C7, Fig. 5.1). However, in the presence of a reactive fluid (e.g., water), initial mechanical compaction is accompanied by water-assisted processes. As there were no temperature gradients imposed across the samples, and the only source of carbonate was from the host rock (no input supersaturated fluid or pre-existing gouge material), the mechanism to produce the compacted, cemented fault zone (C4, Fig. 5.5d) is likely to be intergranular pressure solution (IPS) (Rutter, 1983). In the presence of water and stress, high normal stress gradients around grain boundaries must have permitted the pore fluids to become saturated in calcite from contact with the surrounding rock, and the chemical potential and pressure gradient allowing the calcite-rich fluid to infill the fault zone. The compaction associated with, and mechanism of, IPS can be seen in the associated microstructures (Fig. 5.5)

i.e., the fault zone compacted to grain boundary width, and the presence of precipitant/cement within the fault zone and along the grain boundaries. The lack of fractures in the host rock of the hydrothermally altered samples (C1-C5, Fig. 5.4) may have also been due to the increased cohesion due to IPS, which bonded the host rock as well as the fault zone and effectively made the bulk samples less brittle. Water-assisted compaction processes in carbonates decrease permeability and increases the intergranular contact area (Croize et al., 2013), which is evident within the fault zone; see C1-C5, Fig. 5.5). These results are consistent with previous studies, which have shown that hydrothermal reactions may give rise to fault strengthening far above what may be expected (Dieterich, 1972; Nakatani and Scholz, 2004; Niemeijer et al., 2008). Initial drops in permeability in samples C3, C4, and C5 (Fig. 5.2) are attributed to compaction during initial loading and temperature rise. When the temperature was kept at 450°C (C5) for the entire hold time, the permeability reduction rate slowed through time (Fig. 5.2), representative of the reduction in the rate of compaction. The permeability reduction rate increased again when the rock was subsequently loaded (due to further compaction). However, when μ_{pk} was reached, the permeability rapidly increased (Fig. 5.2), indicating a breach in the fault zone, which can be seen within the fault zone; see Fig. 5.5e. Conversely, the permeability reduction rate remained high when the temperature is subsequently reduced to 150°C during hold (Fig. 5.2), possibly due to the effect of IPS effectively 'sealing' the fault zone. Upon reloading and the breach of peak stress, the permeability reduction rate decreases, possibly indicative of small bonds stretching with the increasing load dominating over further compaction (which can be seen in the form of production of bands in the fault zone (Fig. 5.5d), or little more compaction is able to take place. The permeability continued to decrease even during sliding (Fig. 5.2), indicating that the fault zone did not 'break', as can be seen in Fig. 5.5d. In the presence of argon rather than water, purely thermal treatment and mechanical compaction of the fault zone increased the sample strength, but to a lesser degree (see Fig. 5.1). C6 and C7 show wide, well preserved fault zones (Fig. 5.5f, g), indicating the permeability was too high in the thermally altered experiment to be measured by the oscillation method (see Fig. 5.2 for permeability data and section 2.2 for methods). Thus, the pore fluid pressure exerted by inert argon must have predominantly acted to keep the fault zone open, rather than inducing any changes in rheology.

5.4.2 The role of temperature

The stress-strain relationships (Fig. 5.1) and microstructures (Fig. 5.5) shed some light as to the key difference in processes occurring at different temperatures. When the temperature is

raised alongside deformation (C2), the sample becomes stronger after each slide (Fig. 5.1), indicating that temperature and pressure-dependent strengthening mechanisms are at play. Following hold-time and at reduced temperature (at 150ºC: C4, Fig. 5.5d), an infilled fault zone is produced, which seemingly distributes strain effectively, as shown by long-duration slip-weakening (Fig. 5.1). Thermally-activated (water-assisted) compaction mechanisms at much higher temperatures may have led to a partially-cemented, brittle fault zone (at 450ºC: C5, Fig. 5.5e). A partially infilled fault zone can also be seen in C2 (Fig. 5.5b), which also exhibited stick-slip type behaviour, but likely did not have sufficient time for IPS to become established (no hold time; see Table 5.1). However, in the case of C5, It is difficult to deduce whether the fault zone is only partially cemented (possibility due to reduced IPS given the inverse relationship of calcite solubility with temperature, allowing excess pore fluid pressure to build up within the gaps and hence enable stress drop at lower values of μ), or whether the gaps in the precipitant are a result of the brittle behaviour of the fault zone during initial stress drop, where rupture has propagated and the precipitant/cement has been broken and the original pieces lost in sample preservation.. A 'break' in the precipitant is indicated by the recovering permeability following sliding (Fig. 5.2). As indicated by the lower gradient relationship between μ and strain than is exhibited at lower temperatures and the lower strength of C5 compared to C4 (Fig. 5.1), 450ºC may represents a transition to more ductile behaviour (previous experiments on Solnhofen limestone indicate a brittle-ductile transition (σ_{eff} = 100 MPa) at > 500ºC (Evans et al., 1990), although it is slightly more porous than Carrara marble and thus may delocalise stress, making 450ºC a reasonable temperature for transition to ductile deformation in my samples). Furthermore, following the initial stress drop, stable sliding appears to occur (C5, Fig. 5.1). Thus, there appears to be competition between ductile and brittle behaviours at 450ºC. Notably, stick-slip behaviour that broke the precipitant seal may have produced some granular material within the fault zone, which could have enabled some granular flow and thus stable sliding subsequent to this initial stress drop, although this warrants further investigation.

At reduced temperatures (150ºC, C4), the fault zone is infilled by precipitant/cement. This has resulted in a stronger fault zone (μ_{pk} = 0.77, Fig. 5.1), likely due to the increase in grain contact area and the development of cohesive bonds, not just in the fault zone, but throughout the sample. Given the resulting long duration stress drop following $\mu_{pk,}$ and the continued decrease in permeability even during slip, it is likely that the cement is not fully lithified at this lower temperature; otherwise, brittle behaviour would most likely have been enabled, i.e., fracturing

of a lithified cement (Marone and Saffer, 2007). Thus, it is likely that there is interplay between the results of IPS: compaction and cohesion achieved through precipitation within the fault zone, lubrication, the production of a saturated film which is able to support or distribute some shear stress (Rutter, 1983), as well as possibly crystal plasticity (which have been shown to act at lower temperatures < 150^{o}C (Verberne et al., 2014; Verberne et al., 2013)), as well as purely thermally-activated compaction mechanisms. These processes have led to a major change in fault zone rheology and topology (the production of a fault zone which is indistinguishable from a grain boundary) and ultimately distribute strain rather than localising it.

5.4.3 Mechanisms mediating slip

IPS and thermally-activated compaction mechanisms may be crucial in explaining whether a fault will experience long-duration slip-weakening or transition straight to unstable stick-slip behaviours. The experiments undertaken in the presence of argon (C6, C7) are demonstrative of pure frictional behaviour of the fault zone (Fig. 5.1), i.e., given the lack of any chemical processes occurring, the behaviour is purely based on the friction between the fault contacts at the experimental conditions (see Table 5.1). In the presence of water, however, the fault zone is altered via IPS which alters the rheology, topology, and hence the mechanical behaviour on the fault. Given the dramatic stress drop over an extended period associated with lower temperature and in the presence of fluid, I conclude that IPS and thermally-activated compaction could be important factors in nucleating and controlling different fault slip behaviours. The competition between purely thermal compaction, which would lead to a brittle stick-slip type fault zone, and mechanisms activated in the presence of a reactive fluid and host rock, notably precipitation of a ductile matrix, may ultimately enable the fault zone to act almost like a strong gel that distributes stress and strain effectively throughout (by means of self-organisation to accommodate the applied stress and strain (Cates et al., 1998)). This is supported by the fact that permeability did not recover even during slip, and the precipitant in the fault zone is not breached (C4, Fig. 5.2 & 5.3). I did not continue the experiments to the point of instability, in order to characterise the textures produced in the first phase of stress concentration (i.e., the slip-weakening phase/first dress drop), rather than subsequent motion. However, it is possible that this phase of slip-weakening may indicate that slow-slip type behaviours may be incumbent. Rather than slip-weakening enabling slow earthquakes, as previously suggested (Ikari et al., 2013a), I suggest that a slip-weakening phase may indicate the 'condition' of the fault zone (Chambon et al., 2002) and thus is representative of the possible subsequent frictional behaviour. As slip-weakening is an instability in itself (friction

decreasing from a peak value to a residual value with increasing slip across the frictional interface (Rubino et al., 2017)), it should be related to the subsequent frictional behaviour of the fault zone. Recent work has indeed indicated that the dynamic coefficient of friction and the slip-weakening distance depend on the dynamics of the process (Rubino et al., 2017). Subsequent to this work, further research should examine the subsequent instabilities induced following a slip-weakening phase. This could ascertain whether the characteristics of the subsequent instabilities have any relationship to the characteristics of the slip-weakening phase, e.g., duration, amplitude, etc., under specific conditions.

The alterations in strength and permeability, the changes in fault zone topology, i.e., the infill of precipitant/cement, and the production of comparatively long-duration slip-weakening behaviour, may have important implications for earthquake nucleation processes in carbonates. Influx of fluids and heating could initiate numerous coupled mechanical-chemical processes. Cohesion mechanisms due to the presence of fluids of pore fluids leading to cementation, decreasing the fault zone permeability (sealing) and increasing the cohesive strength of the fault zone (healing) would mean that a greater shear stress would have to build to breach the fault, thus increasing the earthquake recurrence interval. Furthermore, if conditions are right, slow-slip type behaviour could be enabled, thus negating the seismic risk. Further work is needed to gain more information on the evolution of fault properties, with a focus on fault zone topology and fluid-flow to understand the influence of water-assisted processes. The role of gouge, either sediment introduced into a fault zone, or produced due to fault slip or fracturing processes, also warrants further investigation.

5.5 Conclusions

Hydrothermal reactions in a carbonate fault zone may result in strength alteration of the fault zone, as well as distinct changes to the fault zone topology. Microstructural analysis indicates that hydrothermal reactions result in the production of a precipitant and compaction of the fault zone. The rapid permeability decrease (three orders of magnitude) at the earliest stages of hydrothermal treatment indicates that mechanical and chemical healing and sealing mechanisms occur from the onset. Without a pre-existing gouge layer or input of a supersaturated fluid, the mechanism of mineral transportation by diffusion from the host rock is clearly important, a mechanism that is common in reactive rocks such as carbonates and may enable different slip behaviours on faults.

Chapter VI: Slow-slip events on limestone faults enabled by temperature-activated and fluid-dependent flow, cementation and compaction

The full spectrum of fault slip behaviour ranges from aseismic 'fault creep' to 'slow-slip', in which a fault slips over weeks to months, to seismic stick-slip, which is associated with earthquakes. Despite the high societal and economic importance, the physical conditions that pre-dispose a fault to slip in these different ways are still poorly understood, especially since such enigmatic behaviours are known to occur over a range of temperatures (12-230^{o}C), depths, and geological settings. To investigate the possible role of fluid-dependent temperature-activated processes, triaxial rock deformation experiments were undertaken on gouge-filled faults at different temperatures (30-300^{o}C) followed by crystallography and microscopic (XRD and SEM) analysis. The results suggest that, within saturated carbonate-rich fault zones, these different behaviours can be attributed to the competition between granular flow and compaction of the gouge. The SEM analyses show decreasing porosity, the production of nanograins and incremental grain aggregation associated with a transition from creep to slow oscillatory behaviour to stick-slip with increasing temperature. These changes in slip behaviour can be attributed to thermally-driven processes in the presence of fluids and could have significant implications for understanding the generation mechanisms of slow-slip events (SSEs).

6.1 Introduction

Seismological and geodetic observations have revealed a number of slip behaviours on faults, including creep, slow-slip, and stick-slip (Ide et al., 2007; Linde et al., 1996; Peng and Gomberg, 2010). Stick-slip type fault slip is associated with destructive earthquakes, whereas slow-slip and creep behaviours go unnoticed by the general population, and are only detectable by geodetic methods. Twenty years ago, it was believed that the earthquake cycle followed an uneven two-step pattern of rapid sliding followed by slow reloading. However, following the discovery of SSEs (the first discovered slow-slip event was on the San Andreas Fault in 1996 (Linde et al., 1996)) it became clear that the physical mechanisms behind fault slip are not completely understood. SSEs are transient slip events that involve displacement on a fault that occurs over hours to weeks to months, rather than seconds (Linde et al., 1996; Saffer and Wallace, 2015). Constraining the conditions that enable a fault to slow-slip rather than stick-

slip has important implications for understanding earthquake processes. Initially, fluid-assisted deformation processes at elevated temperatures were suggested to account for the seismic-aseismic transition (Blanpied et al., 1995); however the discovery of SSEs at various subduction margins that do not share a common temperature window have led to the role of temperature in controlling the style of fault slip behaviour being largely discounted (McCaffrey et al., 2008; Saffer and Wallace, 2015). Other hypotheses put forward to explain the variations in fault slip behaviours focus on the role of fluid pressure (Kodaira et al., 2004; Saffer and Wallace, 2015), slip-weakening (Ikari et al., 2013a), and fault roughness (Harbord et al., 2017), all of which can tip the force balance in the criterion for slip instability:

$$K < K_C = -(a-b)\,\sigma'_N / D_C \tag{6.1}$$

whereby the elastic stiffness of the loading system K (stress/length) must be smaller than a critical stiffness K_C defined by the properties of the fault, where σ'_N is the effective normal stress, and D_C is a critical slip distance over which fault strength evolves (Scholz, 2002).

The parameter $a-b$ is defined by the experimentally measured change in steady-state friction in response to a change in sliding velocity from V_0 to V (see Chapter I for further details):

$$(a-b) = \frac{\Delta\mu}{\ln(\frac{V}{V_0})} \tag{6.2}$$

Carbonate terrains have been host to destructive earthquakes, notably in the Italian Apennines, where devastating earthquakes propagated along limestone faults in 2009 (Anzidei et al., 2009; Chiaraluce, 2012) and 2016 (Gentili et al., 2017). Regions where carbonate rocks/sediments exist have also been host to SSEs, notably the Costa Rica margin (Kimura et al., 1997), and again in the carbonate-rich Italian Apennines (Amoruso et al., 2002; Borghi et al., 2016; Crescentini et al., 1999). Calcite is a particularly interesting mineral, for a number of reasons: as calcite is highly reactive at ambient conditions (atmospheric pressure, room temperature) with even slightly acidic fluids, flaws and fractures can be easily exploited. Thus, carbonate-bearing faults are important pathways for fluid distribution in the brittle upper crust (Collettini et al., 2014; Delle Piane et al., 2017; Gratier and Gamond, 1990; Sibson, 1996; Tesei et al., 2013). In addition, the solubility of calcite in water varies inversely with temperature (and only slightly with pressure), which is opposite to that of the majority of common subsurface minerals (Stumm and Morgan, 1981). Research on the frictional behaviour of carbonates has increased dramatically within the last few years, following original works in the 1970's and earlier (Mogi, 1966, 1972, 1974; Paterson, 1958). The more recent experimental work has shown that calcite-

dominated rock i.e.., limestone, transitions from velocity-strengthening (aseismic) at temperatures below 80ºC, to velocity-weakening behaviour (seismic) at temperatures above 80ºC (Verberne et al., 2014; Verberne et al., 2013; Verberne et al., 2010). It has been suggested that this may be due to enhanced crystal plasticity at asperity contacts, although crystal plasticity alone cannot explain the aseismic-seismic transition (Verberne, 2015), and generally acts at higher temperatures (> 546ºC; see Tjioe and Borja (2015)). Other research has shown that variable slip velocities (Collettini et al., 2014; Tesei et al., 2014; Ruina, 1983) have a significant influence on the transition from velocity-strengthening to velocity-weakening behaviour, as do interstitial fluid conditions, and system stiffness (Byerlee and Brace, 1968; Leeman et al., 2016; Ruina, 1983; Scuderi et al., 2016). The Niemeijer-Spiers model (Niemeijer and Spiers, 2007) predicts that, at least in phyllosilicate mixtures, unstable velocity-weakening behaviour is due to the combination of granular flow and intergranular pressure solution (IPS) with increasing temperature; granular flow leads to dilation of the gouge layer and as temperature increases, the activation of IPS leads to compaction of the gouge layer. The influence of solution processes generally has been shown to be of importance for changes in fault rheology, possibly due to the reprecipitation of dissolved material resulting from IPS rather than the process of IPS itself (Angevine et al., 1982; Bos, 2000). It is suspected to be of importance in the manifestation of SSEs (Saffer and Marone, 2003), or at least for a transition to unstable slip (Marone and Saffer, 2007; Trütner et al., 2015).

In this work, I aim to further investigate fluid- and temperature-assisted processes, and the textures they produce, which may be important in enabling SSEs in carbonate dominated regimes.

6.2 Data and Methods

I performed saw-cut sliding experiments in a servo-controlled, triaxial testing machine at the China Earthquake Administration (CEA), and subsequent microscopic and chemical analyses (Scanning Electron Microscopy (SEM) and X-Ray Diffraction (XRD)). Water-saturated powder (4:1 ratio) representing fault gouge/incoming sediment was sandwiched between fault blocks (oriented 35º to the central axis) and placed within the pressure vessel (see Fig. 2.3). To ensure that pore fluid reached the gouge between the saw-cuts, a drill hole was made from the top of the sample to intercept the gouge layer (see Fig 2.3). The experiment pressure and temperature conditions were set, following which the sample was held to establish equilibrium at the set conditions (3 hr hold). Axial pressure was then applied using a servo-controlled

hydraulic ram. The maximum displacement is limited by the displacement available in the apparatus (4 mm).

The experiments were carried out at a confining pressure (P_C) of 150 MPa, pore fluid pressure (P_P) of 100 MPa and temperature conditions ranged from 30°C to 300°C. This 50 MPa effective stress (P_C–P_P) is equivalent to ~5 km depth, appropriate for the shallow region where shallow SSEs occur (Saffer and Wallace, 2015). Given the large range of temperatures at which SSEs have been observed (Saffer and Wallace, 2015), this range is replicated in the laboratory, in order to explore the effect that a sole variation in temperature (without changing any other parameters) can have on slip behaviour. Given the reliance of solution processes in carbonates on temperature (Stumm and Morgan, 1981), and previous suggestions that temperature may play a role in controlling fault slip behaviour (Blanpied et al., 1995), I hypothesise that fluid-assisted temperature-dependent processes may enable an aseismic-seismic transition in carbonates.

Velocity steps, i.e., changing the rate of displacement, were also employed. A shear displacement rate of 0.244 μm/s was applied during initial loading, subsequently altered to 1.22 μm/s and 0.0488 μm/s in progressive steps (apart from when the maximum displacement permitted by the apparatus had already been reached, or the copper jacket broke). Velocity stepping enabled an assessment of velocity-strengthening/velocity-weakening behaviour; calculating the *a-b* value (see Chapter I & Equation 6.2) characterises the change in strength following velocity stepping. > 0 = velocity-strengthening behaviour (stable), < 0 = velocity-weakening behaviour (unstable). Ranges of *a-b* values are provided for experiments where multiple velocity steps were achieved; this was not achieved in some experiments where the copper jacket broke, or maximum displacement was reached. The parameter *a-b* is calculated assuming that softening or hardening trends are independent of the rate sensitivity of frictional strength. The slip hardening trend is the overall upward trend of the dataset, indicating overall strengthening over time; a negative value indicates slip softening, i.e., lessening strength over time. The displacements rates of 0.244 μm/s, 1.22 μm/s, and 0.0488 μm/s were chosen because they are easily accommodated by the experimental setup, they are not too slow that the experiment will take more than ~12 hrs, nor too fast that jacket rupture is likely. The ratio between these displacement rates is 5, making calculations simple. Furthermore, many previous works use these displacement rates so any comparison necessary is simple (He et al., 2013; He et al., 2007; Verberne et al., 2010). $\Delta\mu$ was calculated by subtracting μ_f, the value of μ following a period of slip-weakening/ first stress drop from the coefficient of friction of peak

strength, μ_{pk}. This value indicates the change in strength following the initiation of slip on the fault.

Most experiments (see Table 6.1) utilised limestone fault blocks and limestone gouge. Additional experiments included (i) utilising gabbro as the host rock; (ii) no pore fluid, and (iii) chert (or limestone/chert mix) as the fault gouge. These were undertaken at different temperatures to characterise the sole importance of carbonate as the host rock/gouge and the role of reactive fluids. Sample numbering is as follows; 'L' samples = limestone hosted and limestone gouge, 'G' = gabbro hosted and limestone gouge, 'C' = 100% chert gouge, 'LC' = 50% limestone and 50% chert gouge; see Table 6.1. The number following the letter indicates the temperature at which the experiment was undertaken at, e.g., L300 = limestone hosted, limestone gouge, deformed at 300ºC. A subsequent number indicates a change in confining pressure conditions and a subsequent 'd' means dry, e.g., L70_50d = limestone hosted, limestone gouge, deformed at 70ºC at P_C = 50MPa with no pore fluid. A subsequent number with no 'd' indicates a change in temperature conditions, e.g., L70_160_70 = limestone hosted, limestone gouge, deformed at 70ºC, then 160ºC, then 70ºC.

Following deformation, the samples were preserved in LR white resin after they had dried for 24 hrs. The samples were then cut in half lengthways using a low-speed diamond saw to expose the fault zone, at which point XRD and SEM analyses were undertaken (see section 2.2 for further details).

6.3 Results

6.3.1 Mechanical results

6.3.1.1 Limestone samples

Typical elastic loading is observed in all experiments undertaken on limestone host rock and gouge (L30-L300), preceding characteristically different slip behaviours (Fig. 6.1). The friction coefficient vs. shear displacement (Fig. 6.1) for limestone host/limestone gouge experiments show an overall transition from stable sliding type behaviour to quasi-static oscillations, with increasing temperature.

L30 demonstrated stable sliding behaviour, i.e., no change in stress with increased displacement following reaching peak stress (μ_{pk}; Fig. 6.1). From 50-130ºC (L50-L130), oscillations occur immediately after a phase of decreased stress with increasing displacement (i.e., a period of slip-weakening; friction decreasing from a peak value to a residual value with

increasing slip across the frictional interface (Rubino et al., 2017)). These oscillations persist at all displacement rates. At 30ºC, two small magnitude, very slow stress drops occur at the end of the experiment; ~150 sec each at a shear displacement rate of 0.0488 μm/s, see Fig. 6.1. Oscillatory behaviour in L50 became apparent following a long but low-magnitude period of slip-weakening but was not clear following a velocity step change to 1.22 μm/s. Oscillatory behaviour in L60 was clear at the lower displacement rates, but sporadic at a shear displacement rate of 1.22 μm/s. L70 exhibited clear oscillatory behaviour at all displacement rates but was less apparent in the second 1.22 μm/s velocity step. This was also the case for L80, L100, and L130. All these experiments exhibited a period of slip-weakening preceding slow oscillatory behaviour; overall the duration and magnitude (Fig. 6.3c) of slip-weakening and the duration of the subsequent slow oscillations inversely scale with temperature (Table 6.1, Fig. 6.7), whereas the magnitude of the slip-weakening, and the magnitude of the subsequent slow oscillations scale with temperature (Table 6.1, Fig. 6.7). The duration from peak to trough of these oscillations (i.e., the stress drop duration) lasted half a minute at 50ºC, decaying to ~7 sec by 130ºC at a shear displacement rate of 0.244 μm/s, but is relatively independent of displacement rate. The duration of the slip-weakening phase also decreases overall, from ~45 min at 50ºC to ~4 min at 130ºC. The peak coefficient of friction increases overall with increasing displacement during these experiments (L50-L130), showing an overall slip hardening trend (Fig. 6.1, Table 6.1). The average amplitude of the oscillations at a displacement rate of 0.244 μm/s are reported in Table 6.1. All experiments where $T < 130$ºC exhibited an overall slip hardening trend (Fig. 6.3d). The rate of slip hardening and the a-b value (Fig. 6.3a) decrease with increasing temperature overall. A transition from velocity-strengthening behaviour (stable, a-$b > 0$) to velocity-weakening behaviour (unstable, a-$b < 0$) starts at ~160ºC (Fig. 6.3a). Aside from L100, the peak strengths (μ_{pk}) of these medium-temperature samples (50-130ºC) exhibiting slow oscillatory behaviour were the lowest of all the experiments (Table 6.1 & Fig. 6.3b).

At 160ºC, the sample exhibits first velocity-strengthening behaviour, which changes to velocity-weakening beyond the first velocity-step. At this temperature, the duration of stress drop in the oscillations lasts ~3 sec. Above 160ºC (L220 & L300), all values of a-b are negative and μ_{pk} is much greater (by +0.872 +/-0.014) (Fig. 6.1 & 6.3). The magnitude of the oscillations beyond peak stress drop inversely scale with displacement rate, as is also the case at lower temperatures, but are of greater magnitude overall (Table 6.1).

6.3.1.2 Additional experiments: gabbro host, chert gouge, dry samples and changing conditions during the experiment

Parameters obtained from additional experiments, where a number of variables were changed, including host rock type, gouge content, presence of pore fluid and multiple temperatures during the same experiment are also listed in Table 6.1, and the mechanical data from these experiments are shown in Fig. 6.2.

The experiments utilising gabbro as the host rock showed stable sliding behaviour at 70ºC (G70), followed immediately by stick-slip velocity-weakening behaviour at 100ºC (G100), with no intermediate stage. The dry experiment undertaken at P_C = 50 MPa (L70_50d) demonstrated overall velocity-strengthening behaviour, but exhibited random stress drops and exhibited limited characteristic, predictable behaviour up to ~2.75 mm displacement (which contrasts with the experiments undertaken in the presence of fluids, which showed constant oscillatory behaviour, duration and amplitude dependent on the temperature at which they were deformed). In addition, L70_50d underwent a slip softening trend overall (Table 6.1 & Fig. 6.3). It also exhibited shorter duration oscillations than its fluid counterpart, L70 (Table 6.1 & Fig. 6.2). The value of μ_{pk} obtained from this experiment is comparable to previous studies undertaken in the absence of pore fluid (Shimamoto and Logan, 1981; Verberne et al., 2014; Verberne et al., 2013). The dry experiment undertaken at P_C = 150 MPa (L70_150d) showed stick-slip type oscillations but showed a notably different trend to the rest of the experiments (Fig. 6.2).

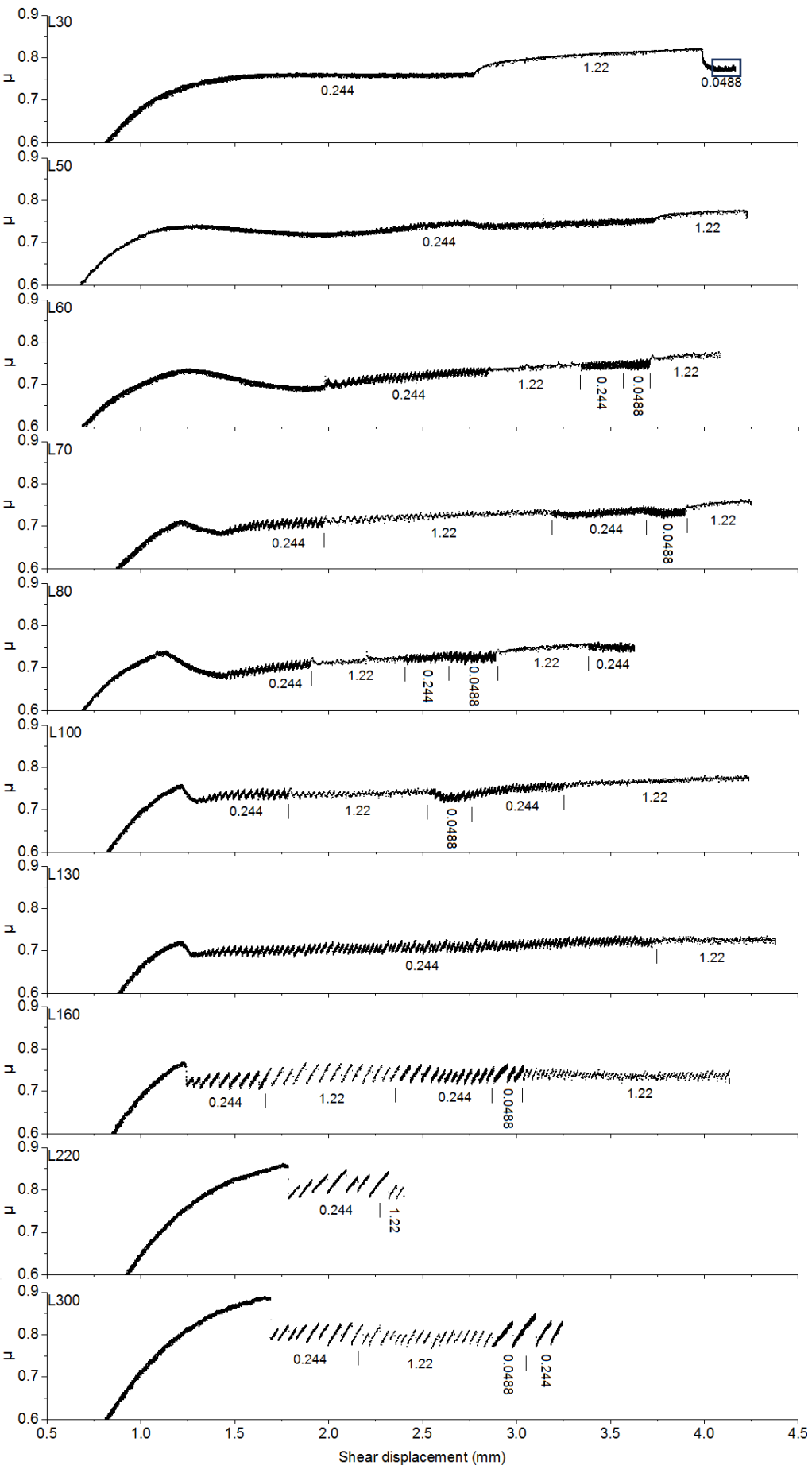
Chert gouge samples hosted by limestone were notably stronger and transitioned to velocity-weakening behaviour at lower temperatures than their limestone counterparts, although medium-duration oscillations were still apparent (see Table 6.1 and Fig. 6.1). At 70ºC (C70), during the first velocity step, the sample demonstrated velocity-weakening behaviour (Fig. 6.1) but was followed by velocity-strengthening behaviour (Table 6.1). At 100ºC (SC100), where the gouge was made up of 50% chert and 50% limestone, only velocity-weakening behaviour was observed. At 160ºC, using a pure chert gouge (C160), only velocity-weakening, stick-slip type behaviour was exhibited.

The experiment that utilised multiple temperatures (70ºC, followed by 160ºC, followed by 70ºC; L70_160_70) was characteristic of the behaviours exhibited by L70 and L160 initially, although on the third stage (the second 70ºC stage) the gouge was exhibiting velocity-weakening behaviour, and shorter duration instabilities than during the first 70ºC stage.

The range of frictional coefficients obtained in my experiments are comparable to those found in previous works (Barton, 1976; Verberne et al., 2014; Verberne et al., 2013).

Table 6.1 Experiments performed at the China Earthquake Administration on gouge-filled faults and key parameters obtained

Exp	Sample description	T (°C)	σ_{eff}	Pore fluid Y/N	Hold time (hr)	Duration of weakening phase (sec)	Magnitude of weakening phase	Duration of oscillation stress drop (sec)	Magnitude of oscillations 0.244μm	μ_{pk}	$\Delta\mu$ (μ_{pk}-μ_f)	Average slip hardening rate (mm^{-1})	Average *a-b*	*a-b values in subsequent steps*
L30	Limestone host, limestone gouge	30	50	Y	2	-	-	-	-	0.763	-	0.016	0.010	0.0099 0.011
L50	Limestone host, limestone gouge	50	50	Y	2	2730	0.0191	33+/-4	0.0123 +/-0.001	0.738	0.02	0.024	0.0079	0.0079
L60	Limestone host, limestone gouge	60	50	Y	2	2490	0.0405	31+/- 6	0.0189 +/-0.001	0.732	0.042	0.036	0.0025	0.0018 0.0027 0.0018 0.0038
L70	Limestone host, limestone gouge	70	50	Y	2	810	0.0296	18 +/- 5	0.0216 +/-0.002	0.711	0.028	0.021	0.0030	0.0020 0.0032 0.0038 0.0029
L80	Limestone host, limestone gouge	80	50	Y	2	1212	0.0490	18 +/- 5	0.0185 +/-0.001	0.736	0.055	0.034	0.0023	0.0029 0.0033 0.0029 0.0014 0.001
L100	Limestone host, limestone gouge	100	50	Y	2	316	0.0384	8 +/-2	0.0219 +/-0.001	0.756	0.036	0.014	0.0025	0.0011 0.0029 0.0024 0.0037
L130	Limestone host, limestone gouge	130	50	Y	2	230	0.0365	7+/-2	0.0220 +/-0.002	0.721	0.027	0.009	0.0022	0.0022
L160	Limestone host, limestone gouge	160	50	Y	2	7	0.0504	3 +/-1	0.0356 +/-0.004	0.765	0.05	-0.001	-3.11 E-05	0.0032 -0.0001 -0.0013 -0.0020
L220	Limestone host, limestone gouge	220	50	Y	2	2	0.0779	1+/-1	0.0400 +/-0.007	0.858	0.077	-0.008	-0.0077	-0.0077
L300	Limestone host, limestone gouge	300	50	Y	2	2	0.0941	1+/-1	0.0349 +/-0.009	0.886	0.096	-0.008	-0.0042	-0.0044 -0.0034 -0.0050
G70	Gabbro host, limestone gouge	70	50	Y	2	-	-	-	-	0.704	-	0.035	0.0067	0.0065 0.0070
G100	Gabbro host, limestone gouge	100	50	Y	2	97	0.0454	5+/-1	0.0320 +/-0.003	0.747	0.704	0.005	-0.0026	-0.0034 -0.0015 -0.0032
L70_ 50d	Limestone host, limestone gouge	70	50	N	2	-	-	7+/-2	0.0081 +/-0.002	0.739	-	-0.024	0.0048	0.0042 0.0090 0.0043 0.0016
L70_ 150d	Limestone host, limestone gouge	70	150	N	2	-	-	9+/-2	0.0093 +/-0.001	-	-	-	-	
C70	Limestone host, chert gouge	70	50	Y	2	1050	0.0244	12+/-3	0.0111 +/-0.0006	0.791	0.024	0.012	-0.0006	-0.0017 0.0004
LC100	Limestone host, 50/50 chert/limestone gouge	100	50	Y	2	385	0.0211	7 +/-2	0.0244 +/-0.001	0.771	0.016	0.013	-0.0026	-0.0040 -0.0040 -0.0016 -0.0012 -0.0025
C160	Limestone host, chert gouge	160	50	Y	2	-	-	2 +/-1	0.0377 +/-0.002	0.794	-	-0.008	-0.0022	-0.0029 -0.0011 -0.0069 -0.0021 0.0017
L70_ 160 _70	Limestone host, limestone gouge	70-160-70	50	Y	0	70: 330	70: 0.0528	70: 10+/-2 160: 4+/-2 70: 6+/-2	70: 0.010 +/-0.002 160: 0.0333 +/-0.003 70: 0.0174 +/-0.003	0.695	-	0.031 0.014 0.015	0.0023 -0.0019 -0.0014	



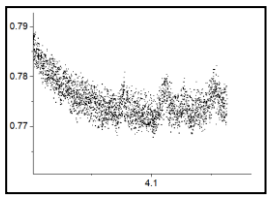


Figure 6.1 Coefficient of friction-shear displacement plots illustrating the characteristic mechanical behaviour at each temperature for limestone samples. I have zoomed in on the instabilities which become apparent at the end of L30. Refer to Table 6.1 for experimental conditions.

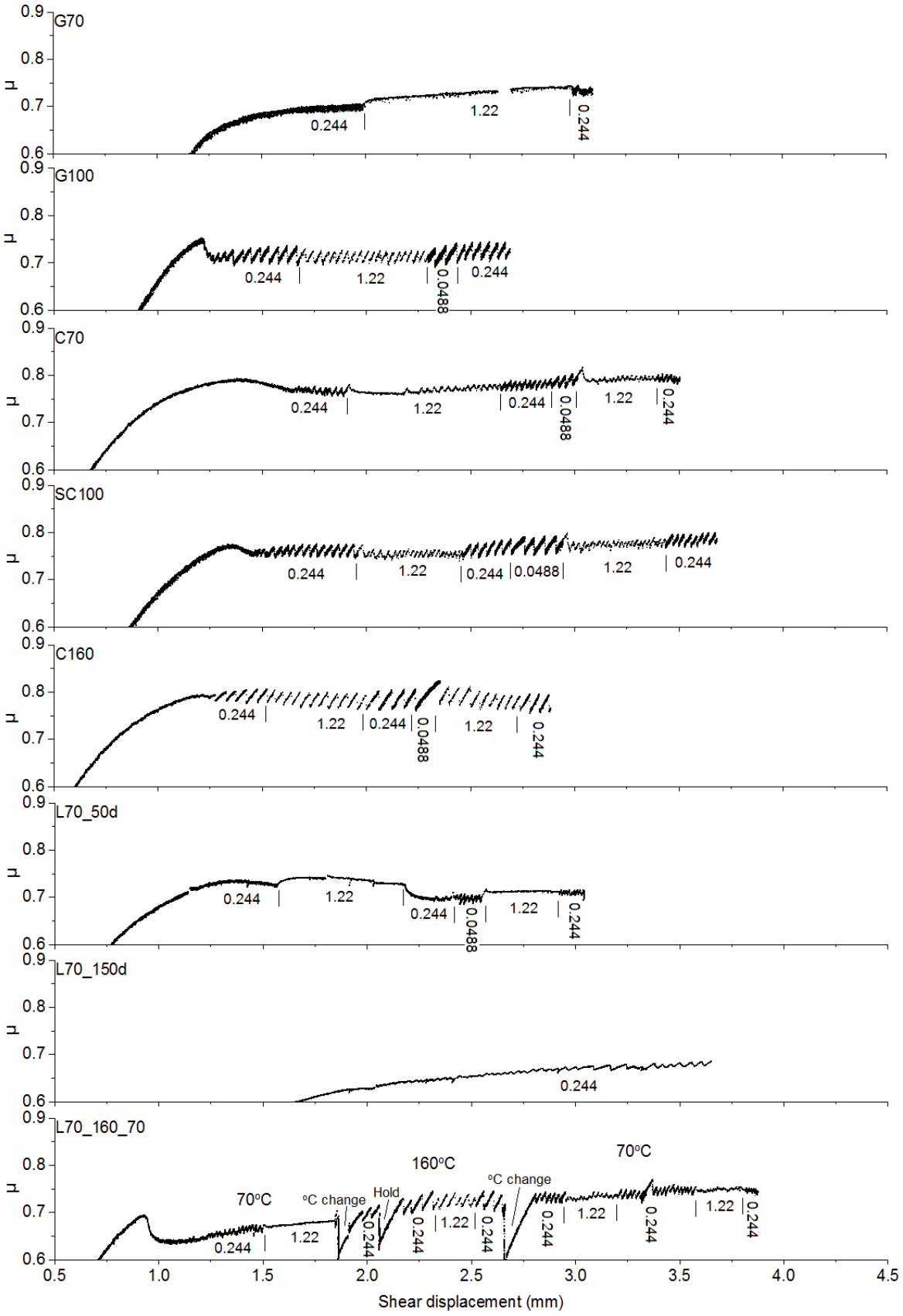


Figure 6.2 Experiments utilising gabbro host rock, chert gouge, no pore fluid pressure and multiple temperature steps. Refer to Table 6.1 for experimental conditions.

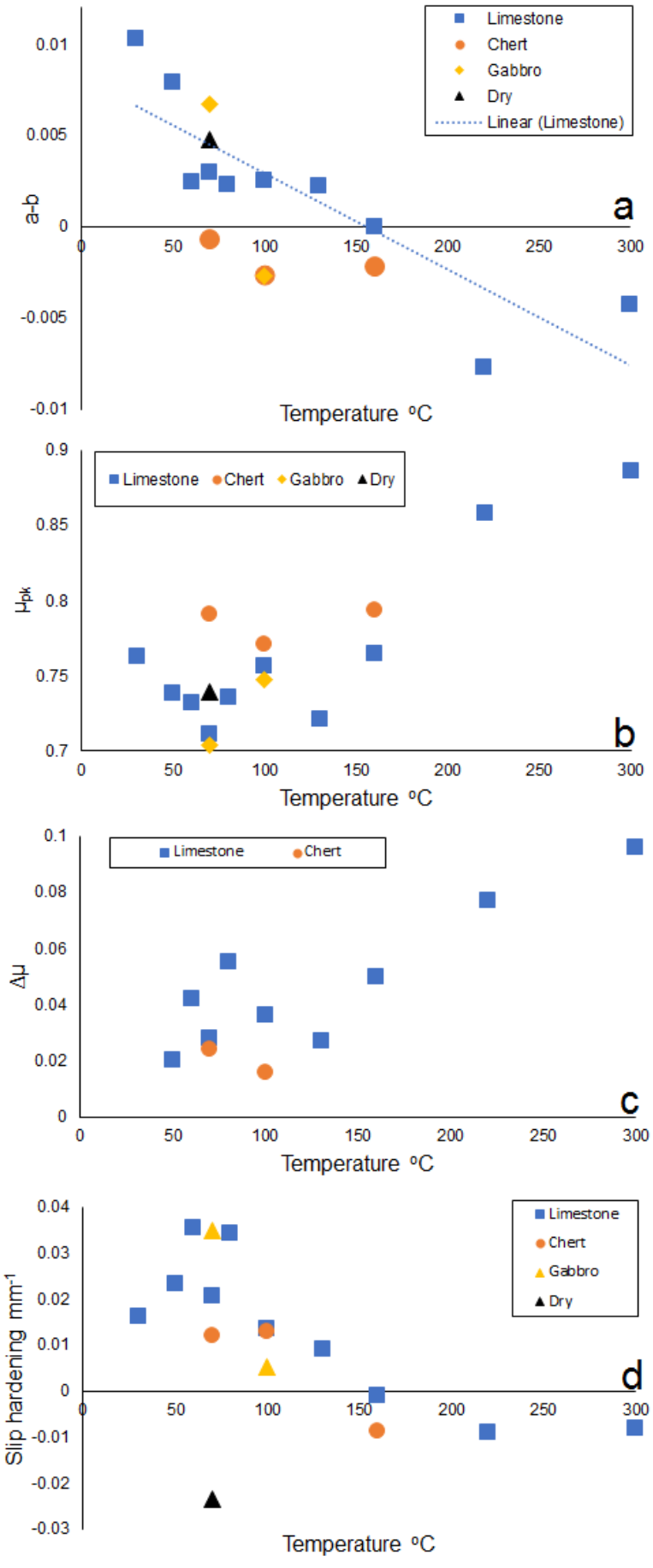


Figure 6.3 Variation of the (a) *a-b* parameter, (b) μ_{pk} and (c) μ_{pk}- μ_f with temperature. *N.B.* No gabbro, dry, stable sliding samples are shown on (c); this is because these experiments did not exhibit an initial stress drop/ G100 exhibited stick-slip behaviour during the slip-weakening phase

L = limestone samples; G = gabbro hosted samples; d = dry samples; C = chert gouge samples (pure and mix, see Table 6.1).

6.3.2 Microstructural results

All deformed samples showed boundary (B) and R_1 type shears within the gouge. The R_1 type shears are defined bands of reduced grain size distributed through the gouge matrix (Fig. 6.4).

There are notable differences between the resulting gouges deformed at different temperatures. At 30ºC (Fig. 6.4a-c), the bulk limestone gouge still appears relatively granular and porous (as it was at the beginning of the experiment), and the shear bands are pervasive throughout the gouge (Fig. 6.4a). The grains decrease in size from several μm at the outer margins of the shear bands (Fig. 6.4b) to < 1 μm in the shear band core (Fig. 6.4c). There is a mixture of coarser, angular grains and more rounded grains in the bulk gouge, but within the shear band core, the grains appear more rounded (Fig. 6.4b). High-resolution inspection using the In-lens detector (Fig. 6.4c) shows that the grains within the shear band core appear sintered/cemented, aggregated and are < 300 nm diameter. There is a distinct loss of structure within the shear band and it is distinctly less porous than the bulk gouge.

With increased temperature, the bulk gouge appears far more lithified, with decreased porosity (Fig. 6.4d). The gouge zone is wider, at 760 μm width, a 27% increase on the gouge zone width at 30ºC (Fig. 6.4a, d). The R_1 type shears are more chaotic, i.e., branching and deviating in different directions (Fig. 6.4e). Any free grains are ~1 μm in size, but these are only distinguishable in the shear band (Fig. 6.4e). At high resolution, the grains adjacent to the shear bands show evidence of truncation, grain overgrowth and indentation, are semi-fused together, and have nanograins on their surface (Fig. 6.4f). Above 200ºC, the gouge has changed into a more compact aggregate (Fig. 6.4g). The shear bands formed are rather well-defined clean fractures, of ~7 μm width which are connected to the boundary shears (the R_1 type shears deflect and flatten towards the gouge-rock interface; Fig. 6.4g). There is grain size reduction adjacent to the main fracture (grains ~0.1-1 μm; Fig. 6.4h) and numerous transgranular and intragranular cracks, which are not seen in samples deformed at lower temperatures (Fig. 6.4i). These cracked grains host numerous nanograins upon their surface of < 100 nm in diameter (Fig. 6.4i). There are smaller, horizontal fractures present, which may be caused by post-shear dilation. The sense of motion indicated by all shear bands is the same across all experiments and consistent with the direction of compression, indicating that this is a direct result of the experiments, as opposed to subsequent unloading.

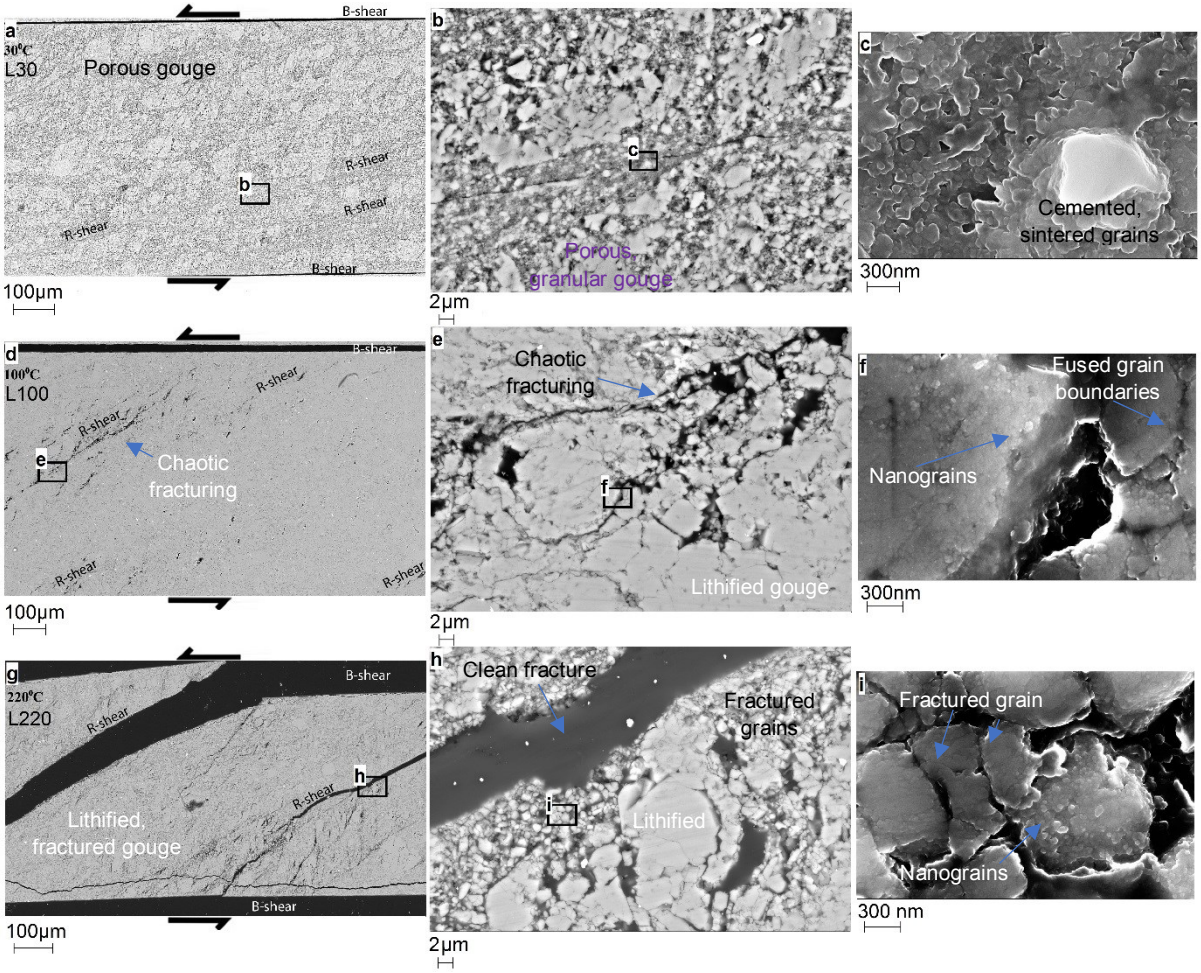


Figure 6.4 SEM photographs of deformed limestone gouge. (a), (d) and (g) are backscatter diffraction image of limestone gouge deformed at 30°C (L30), 100°C (L100) and 220°C (L220) respectively. The box indicates the area zoomed in for images (b), (e) and (h) which are backscatter diffraction image of limestone gouge deformed at 30°C (L30), 100°C (L100) and 220°C (L220) respectively at higher resolution. The box indicates the area zoomed in for images (c), (f) and (i), which are images of the limestone gouge deformed at 30°C (L30), 100°C (L100) and 220°C (L220) respectively at even higher resolution and with the use of the In-Lens detector.

Given the distinct change in mechanical behaviour (Fig. 6.1) and microstructure (Fig. 6.4) in gouges deformed between 30°C and 100°C, additional FIB-SEM into the sample and subsequent FEG-TEM was undertaken on the gouges deformed between these temperatures to get a 3D impression of the gouge adjacent to the shear bands.

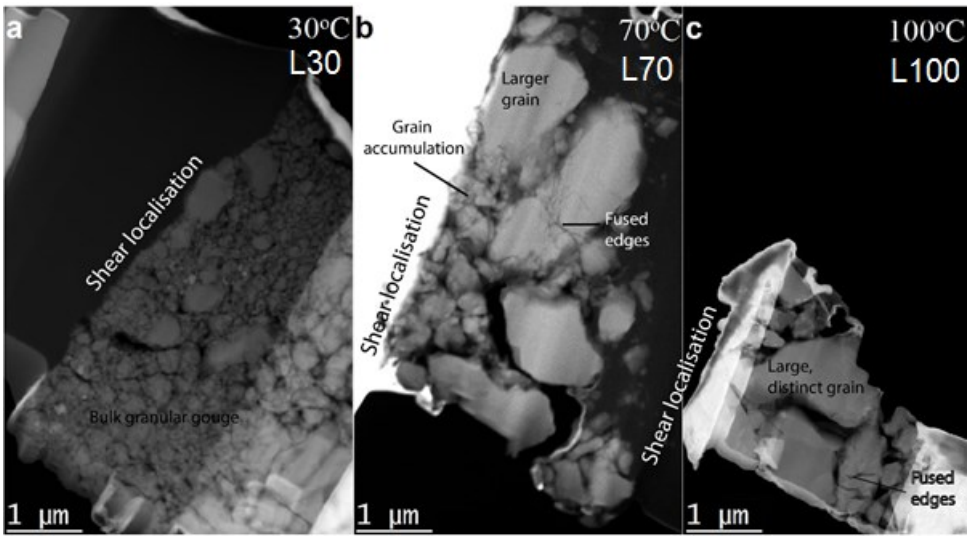


Figure 6.5 FEG-TEM performed on limestone samples deformed between 30°C-100°C. (a) Limestone gouge deformed at 30°C (L30). (b) Limestone gouge deformed at 70°C (L70). (c) Limestone gouge deformed at 100°C (L100). The edge of the gouge is the limit of the shear band.

As per Fig 6.4a, Fig 6.5a shows that the bulk gouge deformed at 30°C is still relatively granular. However, at 70°C (6.5b), there is a mix of smaller grains (100 nm scale) and larger grains (~1 µm scale) fused at the edges, and notably medium sized grain (50 nm) with defined edges, but which appear to be made up of an accumulation of smaller grains on closer inspection. By 100°C (Fig. 6.5c), the grains appear larger and more distinct from one another, although there is still evidence of fused grain boundaries.

6.3.3 XRD results

There are only minor differences in the X-Ray diffractograms following deformation at different temperatures (Fig. 6.6). The main calcite peak (Fig 6.6) is > 8000 counts following deformation at 30°C (L30) and at 220°C (L220), whereas at 70°C and 130°C the main calcite peak is ~7000 counts. Overall, however, the XRD results indicate that the crystallography remains the same; the structure of the calcium carbonate remains consistently crystalline.

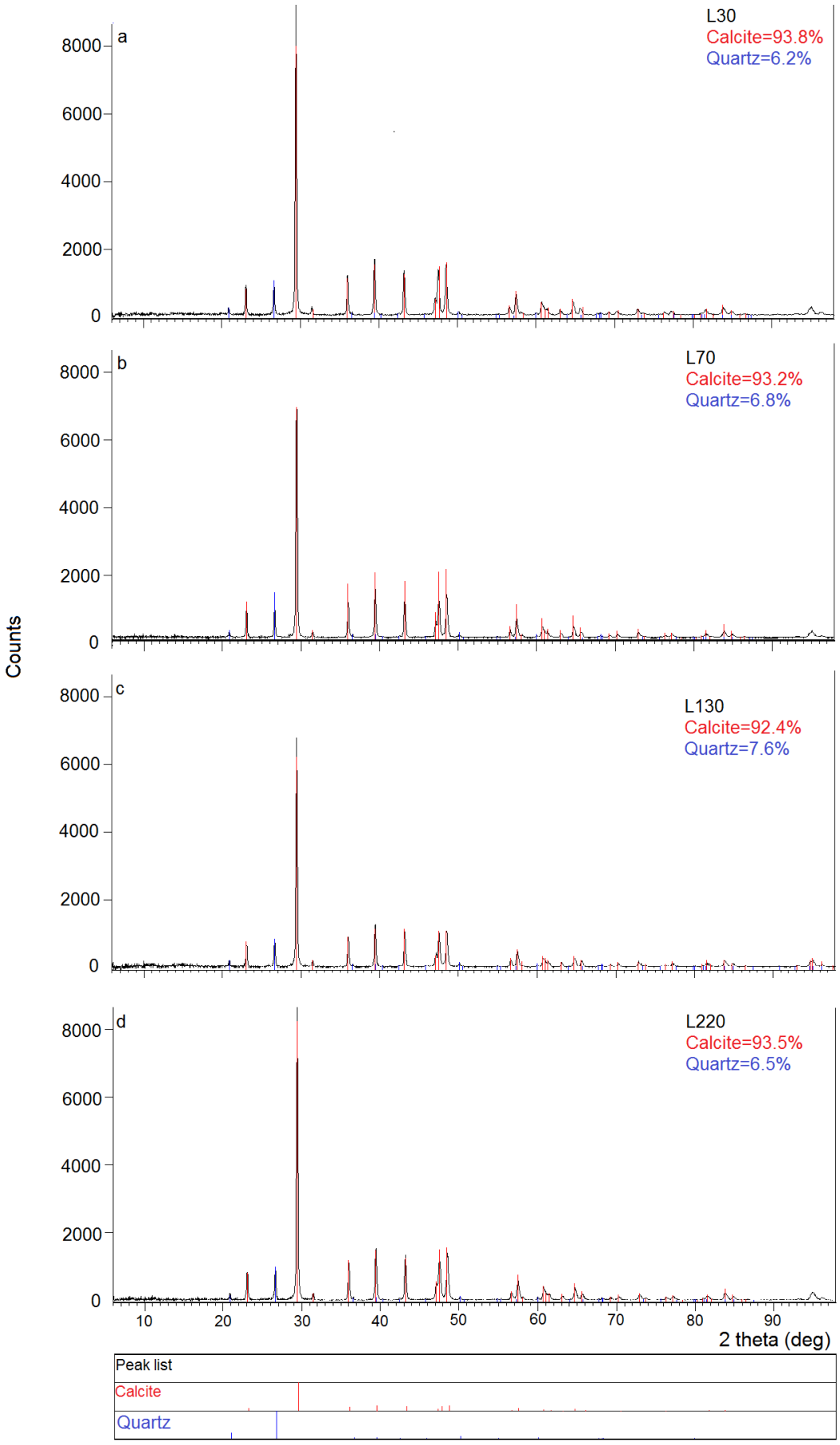


Figure 6.6 XRD spectra from gouges deformed at 30ºC, 70ºC, 130ºC and 220ºC.

6.4 Discussion

6.4.1 Overall trends in mechanical behaviour

The experiments undertaken in limestone samples show a change from velocity-strengthening to velocity-weakening behaviour, from ~160ºC (Fig. 6.1). Up to 130ºC, all samples show an overall slip hardening trend (Fig. 6.1, 6.3c and Table 6.1). Seemingly conflicting with the velocity-strengthening behaviour, slow oscillatory behaviour was also observed up to 130ºC (see Fig. 6.3a). The samples that exhibit slow oscillatory behaviour, also have lower values of μ_{pk} (see Fig. 6.3b).

The overall progressive change from velocity-weakening to velocity-strengthening behaviour shows that there must be a change in the deformation mechanism controlling slip. The temperature dependence exhibited indicates that there is likely to be a thermally-activated or thermally-controlled process defining these progressive characteristics in mechanical behaviour (Blanpied et al., 1991; Blanpied et al., 1995; Mitchell et al., 2013). Furthermore, the evolution of velocity-strengthening to velocity-weakening during L160 (Fig. 6.1) with increased displacement suggests microstructural evolution during slip itself. Small deviations from the main trends between samples exhibiting similar behaviour (see Fig. 6.3) are likely due to slight heterogeneities in sample composition (see Fig. 6.6. for relative calcite/quartz composition of the respective fault gouges) or grain size within the fault gouge.

6.4.2 Mechanisms of deformation

SEM (Fig. 6.4 & 6.5) has permitted high-resolution analysis of the textures in the gouge subsequent to deformation. This allows me to attempt to uncover possible grain-scale mechanisms operative within the gouge which may be responsible for strength alterations, the transition to velocity-weakening behaviour with increasing temperature and the slow oscillations.

6.4.2.1 Room temperature

Subsequent to deformation, L30 remains a granular gouge (Fig. 6.4a, 6.5a). The strain is localised in R_1 type shears within the gouge, where there is extreme grain size reduction and sintered/cemented grains. The presence of angular grains in the bulk of the gouge (Fig. 6.4b) and the sintered/cemented grains within the shear bands (Fig. 6.4c) suggest the operation of two processes at this low temperature respectively; (i) dilatational granular flow of gouge (Chen et al., 2015; den Hartog et al., 2014; Niemeijer and Spiers, 2007; Verberne et al., 2013)

and (ii) intergranular pressure solution (IPS) (Rutter, 1983), which ultimately would act to counteract each other. IPS would operate upon the grains in the highly stressed shear bands (Fig. 6.4c). The bulk control is likely due to granular flow, which can be inferred from the stable sliding behaviour throughout the majority of the experiment observed (Fig. 6.1), and the bulk porous, angular, granular gouge still apparent after deformation (Fig. 6.4a, b & 6.5a) which typically exhibits stable sliding behaviour (Frye, 2002; Marone and Saffer, 2007). However, slower, diffusive processes may become more important with time, as increased strain increases intergranular contact areas, thus increasing intergranular fluid-assisted processes such as pressure solution; see Lehner (1995). At higher displacements as shear bands develop, velocity-weakening behaviour can start to become apparent in crushed rock and granular fault gouge (Beeler et al., 1996; Mair and Marone, 1999). At least initially, any compaction creep effects will be negligible, or are suppressed by dominant granular flow, in which case the strength and the value of *a-b* is entirely controlled by grain boundary friction (den Hartog and Spiers, 2013; Ikari et al., 2011). However, as slow oscillations are exhibited at the very end of the experiment (see Fig. 6.1a), this could indicate the IPS is becoming a more significant mechanism with increasing slip and time. This could be illustrative of the re-precipitation of the dissolved material, providing relatively cemented boundaries, which distribute strain more locally, enabling oscillations (6.1a). These slow oscillations in the laboratory may be equivalent of SSEs in the field.

6.4.2.2 Mid-range (50-130°C) temperatures

When the sample is dry at 70°C, P_C = 50 MPa, relatively stable sliding is observed, albeit exhibiting random stress drops, progressing to oscillatory behaviour with time at a displacement rate of 0.0488 μm^{-1}; see Fig. 6.2. This suggests that, with increasing compaction due to increased temperature, and under dry conditions, granular flow is dominant initially but yields slightly to solid-state diffusive mass transfer. However, in the presence of water, continuous slow oscillations are exhibited at all strain rates, from the end of L30, up to L130 (Fig. 6.1). This could be attributed to the inverse relationship of calcite solubility with temperature (Stumm and Morgan, 1981), permitting IPS to play an important role up to mid-range (~130°C) temperatures. The duration of the slip-weakening phase and the subsequent oscillations appear to vary with an inverse power-law with temperature (Fig. 6.7), in the same manner that the solubility of calcite varies (Stumm and Morgan, 1981). As previously calculated for temperature range 80-100°C, the decrease in solubility of calcite in water will tend to offset the positive effect of temperature on the coefficient of diffusion in fluids

(Verberne, 2015). Sub-optimal IPS at these mid-range temperatures, where the solubility is low may enables semi-cemented grain boundaries, i.e., cohesion achieved through cementation (Gratier et al., 2013). Looking at the transition in microstructures between L30 and L100 (Fig 6.5), I note that L70 (Fig. 6.5b) exhibits elements of both L30 and L100; a relatively granular gouge, yet many of these smaller grains are clustered into what is yet to become a larger grain, showing grain growth mechanisms at play, yet still a bulk gouge which could enable granular flow. The R_1 type shears of L100 are chaotic microcracks (Fig. 6.4e). There are smaller, angular grains present in the shear band (Fig. 6.4e) but also larger grains weakly fused with other grains at their edges and nanospheres on the surface of these grains (Fig. 6.4f). Notably, the μ_{pk} of samples deformed within the temperature range 50-130ºC are lower than that of L30 (see Table 6.1 and Fig. 6.3), which suggests that the fusing is relatively weak. Furthermore, the XRD analysis (Fig 6.6) shows that in these mid-range temperatures, the calcite peak counts are lower than at 30ºC or 220ºC, which may suggest that reprecipitation has not yet resulted in pure, strong crystalline material. These weakly-fused features, and the associated mechanical behaviour (Fig. 6.1), demonstrate that granular flow is no longer the dominant mechanism. The chaotic microcracks, i.e., branching and deviating direction (Fig. 6.4d,e), are typical of a 'semi-brittle' regime (Evans et al., 1990), and indicate that there may have been competition between deformation mechanisms, one attempting to distribute and the other attempting to localise shear (Burlini and Bruhn, 2005; Evans et al., 1990; Nicolas et al., 2016; Wei and Anand, 2008). At lower temperatures, granular flow dominates over slow diffusive processes, which enables the critical state flow observed in L30 (Fig. 6.1a). As the temperature increases, compaction creep by diffusive mass transfer will compete with the dilation associated with granular flow. This is described in detail by the Niemeijer-Spiers model (Niemeijer and Spiers, 2007); the transition to velocity-weakening behaviour is ultimately caused by the enhanced compaction rate, which leads to porosity reduction and bulk increased grain contact area (Bos and Spiers, 2002; Niemeijer and Spiers, 2006), becoming greater than the dilatational granular flow rate. The presence of fluid could also permit intergranular lubrication/films of adsorbed water, which are dependent upon the grain surface electrokinetic potential, and complexly depends upon the presence of impurities (Cicerone et al., 1992) (my samples contained 6.2-7.6% quartz, see Fig. 6.6) as well as on pressure and temperature (Rodríguez and Araujo, 2006). It is possible that this thin solvent film could support some shear stress (Rutter, 1983) and alter the manner of strain distribution. Unfortunately, samples have to be preserved dry so that the resin may cement the textures formed, and thus some evidence of the role of fluids is lost.

In the 50-130ºC temperature range, however, I infer that predominantly competition between granular flow and compaction and cohesion via IPS has led to the chaotic shear bands observed (Fig. 6.4e), the presence of some compacted, new grains, yet also adjacent uncemented gouge and semi-cemented grain boundaries (Fig. 6.5b). This competition may lead to intrinsic weakness, which also explains why μ_{pk} is lower in these mid-range temperatures (50-130ºC). As slip and time increase during the experiment, compaction mechanisms may begin to dominate as they become established, which may explain the overall slip hardening trends below 130ºC. As per L30, the value of *a-b* may be entirely controlled by grain boundary friction (den Hartog and Spiers, 2013; Ikari et al., 2011) i.e., the semi-cemented fused grain boundaries observed at 70ºC (Fig. 6.5b) and 100ºC (Fig. 6.4f), which are essentially sub-optimal reprecipitation of a weak, ductile matrix which distribute strain effectively and permits slow oscillatory behaviours.

6.4.2.2 High (> 160ºC) temperatures

Above 160ºC, thermally-activated mechanisms that act to compact and lithify the gouge should be dominant, as the solubility of calcite has dropped considerably with increased temperature, and temperature-dependent compaction mechanisms which are not active at lower temperatures take over (Lockner and Beeler, 2002). Without any intergranular lubrication/adsorption of water at higher temperatures, contact of grains may lead to full, lithified bonding. This leads to larger slip (Rabinowicz and Tanner, 1966). XRD analysis (Fig. 6.6d) also shows higher calcite peak counts than at mid-range temperatures. This suggests recrystallisation at higher (> 160ºC) temperatures.

L160 itself appears to represent a 'threshold lithification state', with oscillations on the order of seconds (see Table 6.1) and being notably stronger than samples deformed at < 160ºC (see Table 6.1, Fig. 6.1 & 6.3). Above 160ºC, the samples become velocity-weakening, and start to behave like brittle solids (Marone and Saffer, 2007), resulting in large, defined fractures, grain size reduction, and fractured grains at the shear band margins (see Fig. 6.4g-i). This is due to cataclasis, which involves the brittle fragmentation of newly formed grains with rotation of grain fragments, with grains being crushed and reorganised where the strain localises (Engelder, 1974). Fractures can be seen in L220 across the gouge layer (Fig. 6.4g), and. at μm scale, individual grains have fractured (Fig. 6.4i). Notably in L220, there are a large number of nanograins on the surface of μm scale fractured grains (see Fig. 6.4i). The fracturing and abrasion at parent grain surfaces could have led to the detachment of ~nm sized fragments from

the parent grains (Yang et al., 2010). These are also visible in L100 (Fig. 6.4f), but to a lesser degree, possibly indicating only the start of fracturing and abrasion at this temperature. It is also possible that the nanograins are the product of precipitation, whereby healing is due to cementation. The mechanism of their formation ultimately remains uncertain, as does the role these nanograins may play, and thus warrants further investigation.

6.4.4 Possible contributing mechanisms to different slip behaviours

Crystal plasticity, a strongly thermally-activated mechanism, has been shown to operate at mid-range temperatures (~80ºC) in calcite (Verberne et al., 2013). However, pure crystal plastic flow is a velocity-strengthening mechanism. Therefore, it must be assumed that the relative contributions of this mechanism must decrease when other mechanisms become more dominant at higher temperatures; however, it may compete with other mechanisms at mid-range temperatures (50-130ºC) thus contributing to the slow oscillatory behaviour observed.

Previous works have used hydrostatic conditions to study aseismic-seismic transitions in carbonates (Verberne et al., 2010), whereas I performed my experiments closer to the lithostatic conditions associated with shallow SSEs (Audet et al., 2009; Kodaira et al., 2004; Shelly et al., 2006). Given that in the field, excess pore fluid pressure is associated with SSEs, it is possible that it is important for inducing the long duration events observed (Fig. 6.1), coupled with the competition between granular flow and compaction mechanisms. The initial porosity reduction associated with compaction may indirectly result in weakening of the rock by generating excess pore fluid pressures locally, notably within the chaotic microcracks (produced at 100ºC; see Fig. 6.4d, e) where porosity remains. Excess pore fluid pressures could also be a result of fluid pressure distribution perturbations in the gouge during localised slip, or thermal pressurisation (which counteracts the role of dilatancy (Segall et al., 2010)). Excess fluid pressures, in an already highly pressured regime (at P_P= 100 MPa, see Table 6.1), may tend to lithostatic locally within the shear zones. Unfortunately, direct measurement of pressures within the shear bands is not possible in these experiments. However, the fact that limestone samples hosted by gabbro do not undergo slow oscillatory behaviour indicates that interaction between the host rock and the gouge may be of importance, possibly because dilatation cannot occur effectively, or gouge is not able to diffuse into gabbro host rock through IPS. Chert gouge samples, however, do undergo medium duration oscillations (~6 sec less at 70ºC than their limestone counterparts), but show velocity-weakening behaviour throughout. This is possibly because the solubility of quartz increases with temperature, and thus has a different relative importance at this stage,

thus changing the relationship with bulk strength and porosity alterations (the sample is notably stronger; see Table 6.1 & Fig. 6.3). These additional experiments indicate that higher pore fluid pressures in the shear bands cannot be solely responsible for slow oscillatory behaviours. Elevated pore fluid pressure should compete with compaction mechanisms (seeking to keep the fault zone open). Thus, I suggest that the relationship between granular flow and water-assisted compaction mechanisms of IPS, intergranular lubrication combined with crystal plasticity and locally high pore fluid pressures, may lead to these slow oscillations. Notably in calcite, the offset in the role of IPS and crystal plasticity, as one decreases with temperature and the other pertains to velocity-strengthening behaviour (also considering that the crystal formation of calcite is a function of the saturation constant (Kazmierczak et al., 1982), may be the key in combination with elevated pore fluid pressures locally. Additional experimentation, possibly combining lithostatic pore fluid pressures with a number of host/gouge mixes, is required to produce a full model.

It has further been suggested that the chemical effects of pressurised water and the mechanical effect of any local pore fluid perturbations during slip could have significant implications on the physical meaning of rate-and-state friction parameters (Verberne, 2015). Indeed, my results show velocity-strengthening behaviour (a positive value of a-b) in the presence of (slow) instabilities, which is counter-intuitive. Further work is required to investigate the role of high pore fluid pressure, although currently it is not possible to measure perturbations on such a local scale. More studies which demonstrate instabilities in a velocity-strengthening regime (slow or otherwise) are required in order to understand whether rate-and-state friction parameters are still relevant in this context.

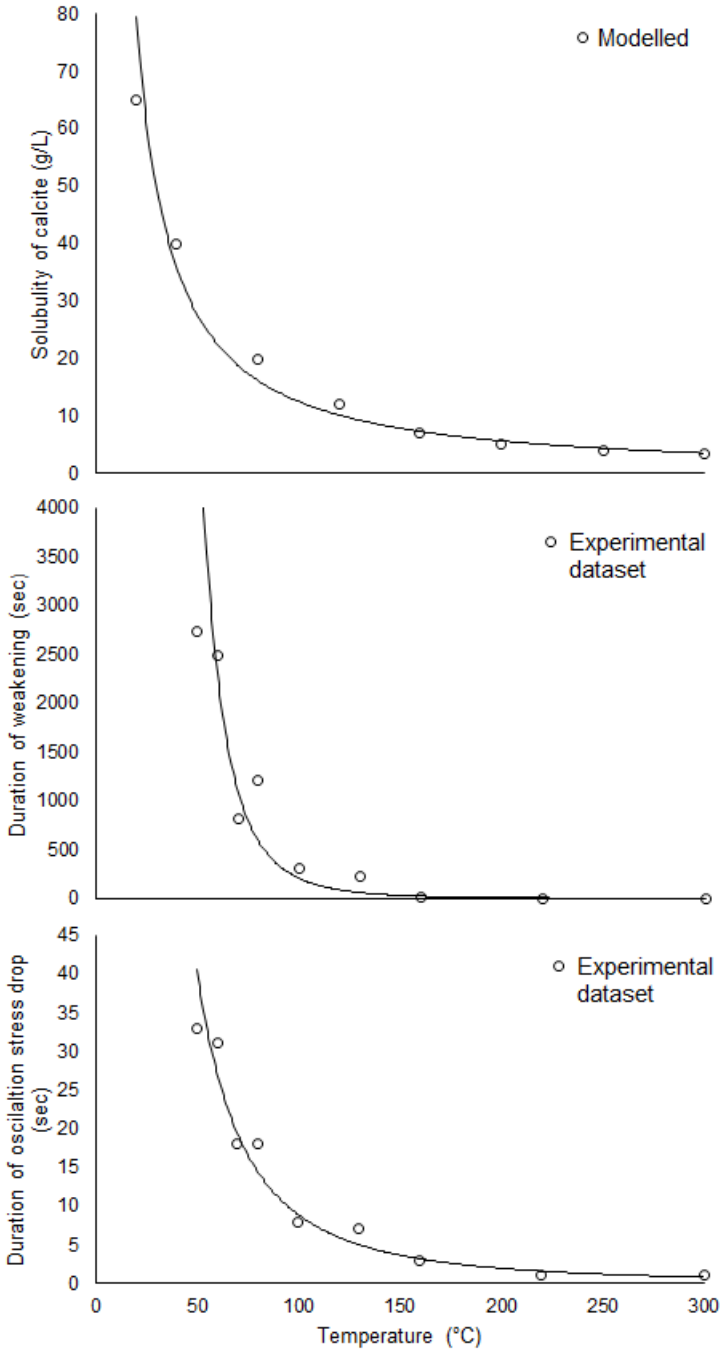


Figure 6.7 The solubility of calcite, the duration of the slip-weakening phases and the duration of the stress drops of the subsequent oscillations all have an inverse power relationship with temperature

6.5 Implications

Velocity-weakening behaviour can lead to unstable seismogenic slip with significant stress drops in limestone, i.e., earthquakes of significant magnitude (Bullock et al., 2014; Chiaraluce, 2012; Nielsen, 2017). SSEs have also occurred in carbonate hosted regimes (Amoruso et al., 2002; Borghi et al., 2016; Crescentini et al., 1999). It is therefore important to consider what could permit SSEs in some circumstances, yet unstable seismogenic slip in others.

The behaviour of limestone samples at temperatures < 160ºC indicates relatively stable, or at least slow, oscillatory behaviour, suggesting relatively stable sliding behaviour in the very uppermost crust, i.e., at 30-160°C. By contrast, the velocity-weakening that was exhibited at temperatures > 160ºC indicates the possibility of large seismic hazard if fault motion occurs at depths associated with these higher temperatures. Above 220ºC, the stress drops are especially large and thus faults within carbonate platforms may be prone to unstable, stick-slip type motions at depths >~6 km, depending on the local geotherm and pressure.

A transition depth, driven by changes in the thermal and hydrologic environment, may represent a window in which SSEs could occur. I have indicated that a combination of mechanisms associated with the presence of fluids and increasing temperature may be relevant to induce slow, smaller magnitude events, especially in carbonate-dominated regimes. The temperature range at which I see especially slow oscillations (~30 sec long, 30-60ºC) corresponds approximately with the temperature range (up to ~60 °C) that SSEs have been detected at, at the Costa Rica margin (Dixon et al., 2014), where the incoming sediment is composed of pelagic carbonates (Kimura et al., 1997; Saffer and McKiernan, 2005) and there is a high convergence rate (Vannucchi et al., 2003). This may permit high carbonate fluxes and high pore fluid pressures, making my proposed mechanism a possible candidate for SSEs here. However, SSEs occur in a variety of lithologies, geological settings, and temperatures (Ito et al., 2013; Kitajima and Saffer, 2014; Matsuzawa et al., 2015; Ujiie et al., 2013). Further experimental work, which explores the role of pressure, especially locally high pore fluid pressure, and combinations of different types of host rock and gouge relevant for slow-slip event sources should be undertaken. The possibility that the rate-and-state friction parameters may not be relevant for slow-slip type behaviours should also be investigated.

6.6 Conclusions

My experimental results show that increasing temperature within saturated, gouge-filled, limestone faults is accompanied by transitional slip behaviours. The SEM analysis indicates that high porosity 'immature' sediments accommodate pervasive shear by dilatational granular flow and exhibit velocity-strengthening, aseismic behaviour, but (water- and temperature-assisted) compaction and cementation mechanisms take precedence with increased temperature, leading to localised shear, hence velocity-weakening, seismic-type behaviour. I believe that a complex relationship exists between water and temperature assisted cementation and compaction mechanisms, which ultimately lead to sub-optimal reprecipitation, intergranular lubrication, and the ability for the gouge to dilate, enabling slow oscillations (possibly alongside crystal plasticity and locally elevated pore fluid pressures). I believe that these slow oscillations are comparable to SSEs in the field. These results may also have implications for the use of the *a-b* parameter to indicate stable/unstable behaviour, as the samples were exhibiting 'instabilities' well within the velocity-strengthening regime.

Chapter VII: Discussion

This thesis has described a multi-disciplinary study aimed at determining the properties and role of carbonate cementation in fault zones. Through field and microstructural observations of natural and experimental faults, I have attempted to understand and explain the physical processes which lead to the formation of these cements, and their subsequent influence upon fault zone properties, primarily strength, permeability, and response to shear. Detailed discussions and conclusions have been presented within each chapter. This chapter aims to bring together the main discussion points, link together the individual chapters, and discuss the implications of the main findings for shallow crustal carbonate fault zones. I will also attempt to answer the fundamental questions I posed in Chapter I. Finally, I will highlight the limitations of this work, and outline potential further work that could be done to build on these results.

7.1 Summary of main findings

In Chapter III, I presented data that constrain precipitation temperatures within the Zuccale Fault core. I suggested that intense foliation initiated by pluton emplacement, and intensified by shearing, combined with overpressured hydrothermal fluids within a thin layer of strata and the presence of weak minerals, may have reduced the coefficient of friction. This excessive reduction in friction, compared to the surrounding rock, may have enabled motion along the non-optimally oriented fault. In Chapter IV, I showed that the Psatha Fault underwent early faulting in the phreatic zone, followed by uplift and further deformation across the water table, followed by further uplift without additional deformation. I subsequently showed that the features produced by fracturing and precipitation i.e., veins within the Psatha Fault host rock, can have an influence over future fracture propagation, but macroscale processes will ultimately dominate over microscale heterogeneities. The relative importance of granular flow vs. cohesive processes in a newly formed fault was also discussed. In Chapter V, I showed that hydrothermal reactions can alter the strength, permeability, and slip behaviour of a calcite fault. This illustrated the importance of both temperature and pore fluid type in controlling a fault's physical properties. Chapter VI illustrated the key role that temperature may have on fault slip behaviour in a limestone gouge: with increased temperature, a transition from granular flow to cataclasis due to water-assisted compaction processes induces transitional slip behaviour.

7.2 To what extent do pre-existing textures inform upon the history of a fault?

My study has shown that pre-existing textures inform upon the history of a fault fairly well, at least on a local scale. However, a study focussed only on deformation-fluid-flow features, without taking into account local and regional structures, may lead to incorrect conclusions regarding the history of a fault. Regional and fault-scale structural data are needed to understand possible mechanisms for fluid influx, fluid source, temperature fluctuations, etc. Conversely, detailed analysis of deformation-fluid-flow features can challenge previously made assumptions, which have been inferred solely from structural analyses. Combined with existing structural data, the study of deformation-fluid-flow features can help provide details on the deformation history and evolution of a fault.

Work on the Zuccale Fault (Chapter III) and the Psatha Fault (Chapter IV) support the idea that detailed studies of existing deformation-fluid-flow features within fault zones can help to provide substantial information about how the fault zone may have evolved to its present state. In a retrospective manner, the textures produced in experiments (Chapter V, VI) ultimately define the conditions to which the samples were subjected. Both methods help to quantify the properties and role of pre-existing structures and fluid-rock interactions in fault zones.

The geochemical signatures from the cements within the Psatha Fault zone (Fig.4.1.8) tell us that deformation occurred both above and below the water table. Precipitation within the fault zone was ultimately permitted by the fluid pathways enhanced due to deformation (Bussolotto et al., 2015). The range of features themselves on the fault included a range of breccias, indicating that cataclasis was the dominant mechanism of deformation. The study of the deformation-fluid-flow features on the Psatha Fault has indicated uplift through time, supporting local structural evidence as well as structural evidence from other faults in the region (Roberts and Stewart 1994). This was achieved through the use of microscopy and isotope analysis of the various cements present in the fault zone (Fig. 4.1.7 & 4.1.8).

The study of the carbonate-rich Zuccale Fault core, through a combination of microscopy (Fig. 3.7) and isotope analyses (Table 3.1, Fig. 3.9 & 3.10), has indicated that hot fluids were trapped within a thin (~25 cm) region of strata in the fault core, ultimately permitting slip at a sub-Byerlee angle. This interpretation supports structural evidence regarding pluton emplacement (Smith et al., 2011a). Although previous studies have inferred a similar mechanism (Collettini and Holdsworth, 2004; Smith et al., 2011a), this present work provides the first quantitative

details on the temperature of the fluids which infiltrated the fault zone, giving more substantial evidence on the possible source of the fluids. However, without existing structural analysis from across the island supporting pluton emplacement (Smith et al., 2011a), geochemical analysis alone would only have indicated a role of deeper, hot fluids in a more general sense.

Veins within both the Psatha (Fig. 4.1.6) and Zuccale (Fig. 3.4) fault zones could have been attributed to hydrofracturing from purely structural analyses. However, the use of microscopy (Fig. 3.7, Fig. 4.1.7) and isotope analyses (Fig. 3.9, 3.10, Table 3.1, Fig. 4.1.8) on the calcite crystals have indicated that they are the result of more recent meteoric fluids circulating in, and precipitating within, open fractures. Although not presented in the main body of this thesis, but available in Appendix A, I have further demonstrated how geochemical analysis can help to indicate different mechanisms of precipitation and thus point to a different geological history.

In a similar manner, the textures produced in experimental fault zones are characteristic of the fault slip behaviour they exhibit (Chapters V-VI). So conversely, if these textures were observed in the field, I could infer the conditions to which the fault may have been exposed, and the slip behaviour that may have been exhibited. The transition of fault slip behaviours seen in the hydrothermal frictional experiments testing the role of temperature, fluids and presence of gouge upon frictional behaviour and the aseismic-seismic transition (Chapter VI) are linked to a granular, porous gouge with pervasive shear bands (aseismic, low temperature), a more lithified gouge with larger semi-fused grains present and more chaotic shear bands (quasi-static oscillations, mid-range temperature), and a lithified gouge with well-defined clean fractures and grain size reduction next to these fractures (stick-slip, high temperature); see Fig. 6.4 and 6.5. In a similar manner, the textures produced in the experiments presented in Chapter V, aimed at testing the chemical and mechanical effects of fluids preceding purely frictional behaviour on bare-interface calcite faults (undertaken at MIT, Fig. 5.5), were coupled with the behaviour they exhibited. In the presence of argon, only stick-slip behaviour was observed, and there was no change in fault zone topology or texture (Fig. 5.5f & g). When stick-slip behaviour was observed in the presence of water, fracturing was evident within the fault zone (Chapter V, Fig. 5.5e). When long duration slip-weakening was observed, deformation bands were evident. The experiments carried out on the heavily veined Psatha Fault host rock (Chapter IV Part II) provided information on how fractures may propagate on a microscale and a macroscale and enabled me to infer a model of how the textures may evolve in the future (if the fault is still active). The tests also clarified that the Psatha Fault host rock fails in a brittle manner in conditions relevant for its approximate exhumation depth.

7.3 Can heterogeneities produced by fluid-rock interactions permit fault motion at a sub/non-optimal orientation?

Heterogeneities produced by fluid-rock interactions can permit fault motion at a sub/non-optimal orientation in some cases, depending upon the strength contrast between the host rock and the pre-existing weakness.

Two chapters within this thesis (Chapter III and Chapter IV) discuss the possible mechanisms that may permit fault motion at a less than optimal orientation. Rock deformation experiments on the altered Psatha Fault rock (Chapter IV Part II) indicate that future fracture propagation can focus along pre-existing optimally-oriented untwinned veins, if (i) there is a distinct contrast with the strength of the surrounding host rock, (ii) the veins are oriented in such a way that provides an ideal, continuous fracture propagation path, and (iii) they are in the optimal orientation according to the stress field (as per standard Andersonian rock mechanical theory). If the vein is *slightly* sub-optimally oriented to the optimal fracture propagation pathway (by ~10^{o}), then a fracture may divert to propagate within an untwinned vein. If the untwinned vein is non-optimally oriented (> 30^{o} from optimal propagation direction, see Fig. 1.5) then it will simply be cross-cut (e.g., Fig. 4.2.5b). These modes are in accordance with the JPW model (see Chapter I). Fractures forced to propagate through overprinted, multiply deformed regions results in complex fracture patterns (Fig. 4.2.5d). This work indicates that non-optimally oriented carbonate infills should be cross-cut rather than becoming reactivated.

However, the Zuccale Fault core is at a non-optimal angle (~15^{o}), and structural evidence suggests that it was active at this low angle (see Chapter III, Collettini and Holdsworth, 2004; Smith et al., 2007). This suggests that there must be other mechanisms at play to enable stress to concentrate within such a non-optimally oriented fault, rather than forming a new, optimally oriented fault. In the case of the Zuccale Fault, I have suggested that a combination of capped hydrothermal fluids concentrated within a thin layer of strata (the higher temperature preferentially yielding ductile-type flow, thermal softening and the generation of fluid overpressures) along with intense, aligned foliation initiated by pluton emplacement, grain-size sensitive deformation, and the presence of weak minerals, could enable slip at lower stresses and thus may permit slip on a non-optimally oriented fault as opposed to creating a new optimally aligned (cross-cutting) fracture (see Chapter III). I suggest that the cross-cutting optimally oriented faults across the Zuccale Fault core occur when the influence of hydrothermal fluids decreases, allowing cataclastic processes to dominate, resulting in cross-

cutting optimally oriented faults across the pre-existing core (also alluded to by Collettini and Holdsworth (2004) and Smith et al. (2011a)). Overall, I suggest that the strength and frictional properties between the surrounding rock and an LANF must be distinctly different to permit slip. Although the untwinned veins within the Psatha Fault rock (Chapter IV) are weaker than the host and thus would enable fracture propagation along them in an ideal scenario, they are not *sufficiently* weak to deflect fracture propagation to non-optimal angles. In the case of the Zuccale Fault (Chapter III), the combination of hot, overpressured fluids, intense foliation, and weak minerals provides a coefficient of friction so low that, in this case, it is easier to reactivate the non-optimally oriented fault than to cross-cut this intense weakness. An example of this has been demonstrated in the work of Ambrose et al., (2014), whereby fracture propagation along highly foliated shales was enabled at angles as low as ~15^{o}. My work invites further studies on the role of foliation, weak minerals, and trapped hot fluids in a fault zone.

7.4 To what scale are heterogeneities produced by fluid-rock interactions important?

Heterogeneities produced by fluid-rock interactions are important all scales (nano to basin). However, the effect they have on rock physical properties depends on the extent to which relatively small-scale interactions contrast the optimal macroscale behaviour.

The four main chapters (III-VI) in this thesis all indicate that fluid-rock interactions are important at their relative scale.

The fluid-rock interactions that dominated the Zuccale Fault (Chapter III) core took place from grain scale (weak minerals) to fault scale (concentration of fluids), which permitted slip on a non-optimally oriented fault. This indicates that heterogeneities produced by fluid-rock interactions can influence one another in a positive feedback system.

The Psatha Fault (Chapter IV Part I) hosts various breccias, gouges, and veins across the extent of the outcrop (Fig. 4.1.5 & 4.1.6) indicating significant fluid-rock interactions during the fault zone evolution. The subsequent rock deformation experiments on the altered Psatha Fault rock (Chapter IV Part II) showed that at a local scale, fractures could be deflected by existing fluid-rock interaction features such as veins if they were in a sub-optimal orientation (Fig. 4.2.4a); however, ultimately all the small-scale fractures linked up together to produce an optimally oriented fault which was of typical Andersonian orientation (Fig. 4.2.3). Where the small-scale fractures formed however, this was reliant upon smaller scale features such as veins, and thus may have a strong influence upon the roughness of the fault; this in turn may have influenced the subsequent fault slip behaviour; see Chapter IV Part II. Notably, the way in which the

smaller-scale fractures oriented themselves within, merged with, or cross-cut the pre-existing crystals in the host rock (Fig. 4.2.8), is similar to what has been seen on a basin scale (Phillips et al., 2016), indicating that these relationships (i) are scalable, and (ii) that smaller-scale interactions, determined by pre-existing structures, may have an influence on much larger-scale processes. It has been suggested that ultimately, tiny mineral grains could drive plate tectonics (Bercovici and Ricard, 2014).

The additional experiments undertaken on bare-interface calcite faults (Chapter V) and carbonate-gouge-filled faults (Chapter VI) produced characteristic textures (Fig. 5.5, 6.4, 6.5) depending on the conditions under which they were deformed. From the work done on the Psatha Fault (Chapter IV Part II), it is reasonable to extrapolate that the smaller scale heterogeneities produced within the fault zones during these experiments (from shear bands, to fractures, and their associated permeability contrasts) could subsequently influence the evolution of these fault zones, if they were used in further experiments. Notably, when the temperature was changed throughout the experiment L70_160_70 (Chapter VI), although each stage was dominated by the behaviour relevant for that temperature (i.e., slow oscillations at 70°C, stick-slip behaviour at 160°C, transitioning back to slow oscillations at 70°C) the subsequent oscillations at the second 70°C stage were shorter, and the sample was stronger than it was during the first 70°C step (Fig. 6.2). This indicates that the microstructures produced in the previous higher temperature regime had an effect on the subsequent behaviour.

7.5 What is the relative importance of fault system parameters on fault zone characteristics?

Very important. Fault characteristics change due to fluid-rock interactions, which change the fault's strength, permeability, and ultimately its slip behaviour. The interaction between numerous parameters are important for resolving which mechanism ultimately controls changes in strength, permeability, and slip behaviour: (i) temperature; (ii) fault contact roughness; (iii) the presence of granular material in the fault zone; (iv) host rock lithology; (v) fault gouge lithology; (vi) presence of fluid; (vii) fluid type.

7.5.1 Fault slip behaviour

In this work, I have illustrated that numerous parameters, in combination with the presence of fluid, can affect fault zone characteristics. The key finding is the effect of rising hydrothermal conditions on fault slip behaviour. This was most clearly illustrated in the work presented in Chapter VI, which presented hydrothermal frictional experiments, studying the effect of

temperature, the presence of gouge and fluid on frictional behaviour and the aseismic-aseismic transition. Under rising hydrothermal conditions, a clear transition was illustrated from aseismic velocity-strengthening granular flow, to quasi-static oscillations (attributed to competition between dilatant granular flow and (temperature- and fluid-dependent) cohesive and compaction processes at mid-range temperatures), to stick-slip velocity-weakening behaviour, where thermally-activated compaction dominated at higher temperatures (Fig. 6.1). A similar transition was seen in bare-interface calcite fault samples with no gouge present (Chapter V): at mid-range temperatures (150ºC), long duration slip-weakening was observed (Fig. 5.1), whereas at much higher temperatures (450ºC) stick-slip behaviour was observed, although the relationship between stress and strain was much more 'plastic', indicating a transition to ductile flow at this higher temperature. Notably, long-duration slip-weakening at 150ºC (experiment C4, Fig. 5.1) was achieved following a reduction in temperature from 450ºC, illustrating that even if a fault has been subjected to different conditions, it operates with respect to the behaviour defined by the present conditions (as also shown in experiment L70_160_70, Fig 6.2, as mentioned in section 7.4). However, as stick-slip behaviour was still exhibited in carbonates at 450ºC, this slightly contradicts my interpretation that such higher temperatures would help promote ductile flow in the Zuccale Fault core (Chapter III). However, given that this temperature may show a transition point to preferentially permitting ductile flow, in combination with other factors such as intense foliation, weak minerals, and locally high pore fluid pressure, this may enable slower, more controlled slip, as opposed to stick-slip type behaviour. Locally high pore fluid pressures may play an important role as a contribution to slow oscillatory behaviour, as alluded to in Chapter VI, as well as permitting slip on a non-optimally oriented fault (Chapter III). Unfortunately, the experimental setups did not permit me to determine whether high pore fluid pressures occur on a very local scale. Furthermore, samples must be preserved dry, and thus some evidence of the role of fluids is lost. Where slow oscillations occur in the field, however, they generally occur in areas of locally high pore fluid pressure (Kodaira et al., 2004; Saffer and Wallace, 2015). At this stage, I infer that high pore fluid pressure is of importance in combination with other fluid-assisted processes, due to the fact that enigmatic events such as slow oscillations and non-optimal fault activation only appear to occur in the presence of fluids (Kodaira et al., 2004; Saffer and Wallace, 2015; Smith et al., 2007).

Additional experiments enabled me to discriminate between the dominant mechanism that was altering fault slip. The effect of the host rock and gouge lithology were tested at the CEA

(Chapter VI). There were no quasi-static oscillations when the host rock was gabbro rather than limestone; the sample went from exhibiting stable sliding straight to stick-slip over the identical temperature range where quasi-static oscillations had been exhibited in experiments with a limestone host (Fig. 6.1). This indicates that the interaction between the host rock and gouge is important, possibly as it allows dilatancy to compete with the cohesive processes starting to dominate within the gouge. In a similar manner, when limestone was the host rock and pure chert or a chert mix was utilised as the gouge (Fig. 6.2), the samples transitioned to velocity-weakening behaviour at lower temperatures than their limestone counterparts, although medium-duration oscillations were still apparent. This may be due to the different solubility of quartz at mid-range temperatures in comparison to carbonate, or again the ability to the gouge to interact with and/or dilate against/into a host rock of a different lithology. The theory behind this concept was modelled by Segall et al. (2010), whereby quasi-static oscillations are enabled only when the dilatancy efficiency is above a critical value.

The presence of gouge was an important factor in changing the slip behaviour of the fault zone. Whether granular material was input, as is the case of the experiments undertaken on limestone gouge under hydrothermal conditions (see Chapter VI), or created during fracture formation, as is the case of the experiments on the altered Psatha Fault host rock, (see Chapter IV Part II), its presence enabled granular flow to accommodate pervasive shear and permitted stable sliding type behaviour. In the case of the Psatha Fault host rock, even though the experiment was undertaken at 200ºC, granular material within the fault zone was newly created due to fracturing. Therefore, this material had not been subjected to cohesive processes, so granular flow may have been permitted at this higher temperature. Of course, following hold time in saturated conditions, stick-slip behaviour was eventually exhibited (see Fig. 4.2.6c). Fault roughness may also have contributed to the stable sliding behaviour exhibited (Fig. 4.2.6a) following formation of the main fracture within the Psatha Fault host rock (Fig. 4.2.3), in combination with the formation of granular material and subsequently, the 'smoothing' of the fault following further deformation may also have contributed to the stick-slip type behaviour after two days hold (Fig. 4.2.6c), in combination with any cohesive processes active during the hold. The impact of fault roughness upon fault slip behaviour (rougher faults favouring stable sliding and smoother faults favouring stick-slip type behaviour) is discussed in Harbord et al. (2017).

7.5.2 Fault zone permeability

In Chapter V, I illustrated how deformation at a different temperature, and in the presence of reactive fluids, can significantly alter the permeability of a fault zone. Ultimately, this was due to the change in the fault topology and rheology following alteration. In the presence of an inert fluid, the fault zone remains open (Fig. 5.5g) and the sample remains extremely permeable – in fact, too permeable to be measured by the oscillation method (see Chapter V). However, with water as the pore fluid rather than argon, permeability was measurable, and was found to drop by three orders of magnitude during the initial hold period. At lower temperatures (150ºC), permeability did not recover upon sliding, whereas at 450ºC, the permeability recovered to 81% of its pre-sliding value. This is attributed to the rheological properties imparted by the treatment at the different temperatures, in the presence of water. At 150ºC (C4), the fault zone is compacted, and fully saturated with a carbonate-rich precipitant. Water-assisted compaction processes have increased intergranular contact area throughout the sample, and most notably within the fault zone (Fig. 5.5d). At 450ºC (C5), permeability rapidly increases during the initial stress drop, indicating a breach in the fault zone, which is also seen in micrograph (Fig. 5.5e). Overall, this indicates that a relatively ductile fault zone (C4) does not breach and permit flow, thus retaining low permeability, but a brittle fault zone (C5) will breach and become more permeable, as would be expected (Hausegger et al., 2010). This shows how temperature and the influence of fluids are extremely important parameters in controlling rheological properties, which ultimately alter the permeability of the fault zone during deformation.

Unfortunately, permeability data are not available for the other experiments, as the other experimental setups (conducted at UoP and CEA, see Chapter IV Part II & VI) are not designed to measure permeability. I would anticipate that in the case of the Experiment 2 undertaken on the altered Psatha Fault host rock (Chapter IV Part II), permeability would be too low to measure by the oscillation technique at the start of the experiment (see Brace et al. (1968) for methods to measure permeability in very low permeability rocks). Following fracture formation permeability would increase drastically (e.g., as per Lamur et al. (2017)). It is likely, however, that the permeability created by fracture formation would be too high to be measured by the oscillation technique. On day 2, where slip-weakening was exhibited, the permeability should be able to be measured by the oscillation technique, but would be low following cohesion and compaction processes in the presence of fluid over the 24 hr hold period, and would decrease further with increased strain rather than increasing rapidly during slip (in a

similar way to C4, Fig. 5.2; see also Xue et al. (2013), Gratier (2011), Kaproth (2013)). However, on day 3, where the cohesive resistance has decreased to zero and small stick-slip type oscillations are exhibited, I would expect the permeability to be higher, and increase further as the stick-slip type behaviour continues with increased strain. An increase in permeability following the production of brittle shears has been seen in other experiments, e.g., Leclère et al. (2016). In the case of the hydrothermal frictional experiments which studied the effect of temperature, presence of gouge and fluids upon frictional behaviour and the aseismic-seismic transition (Chapter VI), I would expect a similar trend. During hold, I would expect a decrease in permeability (as is seen in other hold-slide type experiments, e.g., Im et al. (2018), Kato et al. (2003)). During load, permeability would decrease further, as the sample is compacted further (as is frequently shown when loading samples; e.g., Karner et al. (1997), Rutter and Hackston (2017), Kato et al. (2003)). Where stable sliding behaviour is exhibited, as per L30 (see Fig. 6.1), I would expect permeability to recover slightly as flow is permitted between the grains as they roll, but to level out; modest permeability recovery following stable sliding was observed by Crawford et al. (2008).

However, slip could also result in the fault aperture reducing, leading to a further reduction in permeability, as is observed by Zhong et al. (2016). Where stick-slip behaviour is exhibited (S160, S220, S300), I would expect permeability to rapidly increase, as was the case for C5 at 450ºC (Fig. 5.2), correlating with the formation of fractures within the lithified gouge. Where slip-weakening behaviour is exhibited, I would expect permeability to decrease further following hold, as was seen in C4 (Chapter V, as is also exhibited by experiments by Leclère et al. (2016)). Subsequent to slip-weakening, if slow oscillatory behaviour is exhibited (S50-S130), I would expect a slight increase in permeability due to the production of chaotic shear bands accommodating strain which may permit flow (permeability has been shown to recover during slow-slip, e.g., Wu et al. (2017), Guglielmi et al. (2017)) but not to the extent of the permeability increase exhibited by stick-slip samples. Permeability data are also not available during deformation within the Zuccale Fault core (Chapter III). I have assumed that the presence of an impermeable seal is important to trap the hot fluids within the foliated strata, thus permitting slip at a non-optimal angle, and thus I would assume that permeability would be persistently low, as noted by Collettini et al. (2006), but would drop further during periods of loading and overpressure (Clemenzi et al., 2015), as demonstrated by the experiments on bare-interface calcite faults in Chapter V.

7.5.3 Fault strength

This work indicates that strength can be altered dramatically as a consequence of changing certain parameters. Predominantly, I have focussed on how temperature and the presence of fluids can alter fault strength.

The strength of the altered Psatha Fault host rock (Chapter IV Part II) was quantified in terms of the applied axial stress, rather than in terms of μ (Fig. 4.2.2 & 4.2.6). This is because a new fracture was formed, and although it is of optimal orientation (~30°), it is not a clean-cut plane, thus the value of axial stress in MPa is a more accurate representation of its strength as opposed to shear or μ. (Hackston (2013) presented data in terms of axial stress following the production of new fractures). However, for the purposes of comparison, I have calculated the strengths of the samples in terms of μ.

Table 7.1 Comparison table of values of μ of fault surfaces from experiments carried out in this study. Values are given where available; when creep was exhibited, $\mu_f = \mu_{pk}$, and some experiments were not continued after the initial stress drop following μ_{pk}.

Institution	Experimental conditions	Peak coefficient of friction, μ_{pk}	Coefficient of friction, μ_f, (immediately after peak stress drop)
UoP	Day 1: Triaxial, Fluid = water, P_P = 10 MPa, P_C = 25 MPa, T = 200°C, Hold time = 0 hrs, newly formed fault in veined limestone		0.88
UoP	Day 2: Triaxial, Fluid = water, P_P = 10 MPa, P_C = 25 MPa, T = 200°C, Hold time = 24hrs, newly formed fault in veined limestone	0.91	-
UoP	Day 3: Triaxial, Fluid = water, P_P = 10 MPa, P_C = 25MPa, T = 200°C, Hold time = 24 hrs, newly formed fault in veined limestone	0.87	0.85
MIT	C4: Triaxial, Fluid = water, P_P = 40 MPa, P_C = 120MPa, Hold time = 4 hrs, T = 450°C reduced to 150°C after 2 hrs, input fault @ 30° in Carrara marble	0.77	-

MIT	C5: Triaxial, Fluid = water, P_P = 40 MPa, P_C = 120 MPa, Hold time = 4 hrs, T = 450°C, input fault @ 30° in Carrara marble	0.73	-
MIT	C7: Triaxial, Fluid = argon, P_P = 40 MPa, P_C = 120 MPa, Hold time = 4hrs, T = 450°C reduced to 150°C after 2 hrs, input fault @ 30° in Carrara marble	0.70	-
CEA	L30: Triaxial, Fluid = water, P_P = 50 MPa, P_C = 150 MPa, Hold time = 3 hrs, T = 30°C, input fault @ 30° in limestone with limestone gouge	0.76	-
CEA	L50: Triaxial, Fluid = water, P_P = 50 MPa, P_C =150 MPa, Hold time = 3 hrs, T = 50°C, input fault @ 30° in limestone with limestone gouge	0.74	-
CEA	L60: Triaxial, Fluid = water, P_P = 50 MPa, P_C = 150 MPa, Hold time = 3 hrs, T = 60°C, input fault @ 30° in limestone with limestone gouge	0.74	0.70
CEA	L70: Triaxial, Fluid = water, P_P = 50 MPa, P_C = 150 MPa, Hold time = 3 hrs, T = 70°C, input fault @ 30° in limestone with limestone gouge	0.72	0.69
CEA	L80: Triaxial, Fluid = water, P_P = 50 MPa, P_C = 150 MPa, Hold time = 3 hrs, T = 80°C, input fault @ 30° in limestone with limestone gouge	0.74	0.69
CEA	L100: Triaxial, Fluid = water, P_P = 50 MPa, P_C = 150 MPa, Hold time = 3 hrs, T = 100°C, input fault @ 30° in limestone with limestone gouge	0.76	0.74
CEA	L130: Triaxial, Fluid = water, P_P = 50 MPa, P_C = 150 MPa, Hold time = 3 hrs, T = 130°C, input fault @ 30° in limestone with limestone gouge	0.73	0.70
CEA	L160: Triaxial, Fluid = water, P_P = 50 MPa, P_C = 150 MPa, Hold time= 3hrs, T=160°C, input fault @ 30° in limestone with limestone gouge	0.77	0.73

CEA	L220: Triaxial, Fluid = water, P_P = 50 MPa, P_C = 150 MPa, Hold time = 3 hrs, T = 220°C, input fault @ 30° in limestone with limestone gouge	0.86	0.80
CEA	L300: Triaxial, Fluid = water, P_P = 50 MPa, P_C = 150 MPa, Hold time = 3 hrs, T = 300°C, input fault @ 30° in limestone with limestone gouge	0.89	0.80
CEA	G70: Triaxial, Fluid = water, P_P = 50 MPa, P_C = 150 MPa, Hold time = 3 hrs, T = 70°C, input fault @ 30° in gabbro with limestone gouge	0.70	-
CEA	G100: Triaxial, Fluid = water, P_P = 50 MPa, P_C = 150 MPa, Hold time = 3 hrs, T = 100°C, input fault @ 30° in gabbro with limestone gouge	0.75	0.71
CEA	L70_50d: Triaxial, Fluid = none, P_P = 0 MPa, P_C = 50 MPa, Hold time = 3 hrs, T = 70°C, input fault @ 30° in limestone with limestone gouge	0.74	-
CEA	C70: Triaxial, Fluid = none, P_P = 0 MPa, P_C = 50 MPa, Hold time= 3 hrs, T = 70°C, input fault @ 30° in limestone with chert gouge	0.79	0.77
CEA	LC100: Triaxial, Fluid = none, P_P = 0 MPa, P_C = 50 MPa, Hold time= 3hrs, T =100°C, input fault @ 30° in limestone with limestone/chert gouge	0.77	0.76
CEA	C160: Triaxial, Fluid = none, P_P = 0 MPa, P_C = 50 MPa, Hold time = 3 hrs, T = 160°C, input fault @ 30° in limestone with chert gouge	0.79	0.79

By comparing the strength of the samples, I can make several inferences about the processes that have led to the changes in strength.

It appears that high temperature is key to producing the strongest samples. This is likely due to temperature-dependent compaction. The hydrothermal frictional experiments testing the role of temperature, fluids and presence of gouge upon frictional behaviour and the aseismic-seismic transition (Chapter VI) showed that samples deformed at temperatures > 200°C were

distinctly stronger (μ_f and μ_{pk} both ≥ 0.80; see Fig. 6.1 & Table 6.1) than those deformed at lower temperatures. In the experiments testing the influence of pre-existing structures within the Psatha Fault host rock (Chapter IV Part II) which were deformed at 200ºC, these samples had a $\mu_{pk} > 0.85$. However, the value of μ_{pk} for the Psatha samples (Table 7.1) was determined for a very rough surface, as the fault was not saw-cut but rather created in the experiment. This likely led to a higher coefficient of friction, due to interlocking contacts on the fault surface when pressure was applied (Wang and Scholz, 1994). Notably, however, a temperature too high, which approaches a threshold for ductile rather than brittle behaviour, leads to a decrease in strength, as is shown by bare-interface calcite sample C7 (450ºC, Chapter V).

The role of fluid-rock interactions is also crucial in altering the fault strength. However, the effect is notably different depending on whether the fault is saw-cut, or whether there is gouge present, which further illustrates the important role of the make-up and evolution of the fault. When there is no gouge present (the bare-interface calcite faults in Chapter V), fluid-rock interactions at a mid-range temperature act to compact and heal the fault (Fig. 5.5d) and cause an increase in strength, as illustrated by C4 (Fig. 5.1). This also appears to be the case when the fault contact is not dominated by gouge, in the case of the Psatha Fault samples, where fluid-rock interactions between the fault surfaces at elevated temperature led to an increase in strength ($\mu_{pk} = 0.91$; see Table 7.1). Although some granular material would have been produced in the creation of the fault, there predominantly still would be contact between the two fault surfaces. However, when gouge is the dominant component of the fault zone (Chapter VI), the competition between different mechanisms at mid-range temperatures (dilatant granular flow and cohesive and compaction mechanisms (IPS, temperature-enhanced compaction), as well as possibly intergranular lubrication, crystal plasticity, and locally elevated pore fluid pressure) within the gouge lead to an overall reduction in strength of the fault zone (Fig. 6.3b). However, at lower temperatures (~30ºC), dilatant granular flow can be important in maintaining strength if the gouge can dilate into the host rock; G70 illustrates that, if the gouge cannot dilate into the host rock (because gabbro is impermeable and non-reactive in the timescale (see the importance of dilatancy efficiency in Segall et al. (2010))), then the fault zone is weaker (Fig. 6.2). Finally, if a pore fluid pressure exists, but fluid-rock interactions are not possible (due to the fluid being inert, in the case of the bare-interface calcite fault samples saturated in argon, C6 and C7, Chapter V) then the overall effect of the presence of the fluid is purely mechanical and weakening (Fig. 5.1).

7.6 How important are chemical effects of fluid-rock interactions compared to mechanical effects?

Debatably the chemical effects of fluid-rock interactions are as important as mechanical effects, and potentially even more so in certain special circumstances. My results have alluded to the mechanical importance of locally elevated pore fluid pressure, but also the importance of precipitation. Thermally-activated compaction processes are also very important. Notably, chemical effects are more susceptible to temperature.

This work, in regard to both the field studies (the Zuccale Fault, Chapter III and the Psatha Fault, Chapter IV Part I) and the experimental studies (Psatha Fault host rock deformation, Chapter IV Part II, bare-interface calcite fault experiments at MIT, Chapter V, and hydrothermal frictional gouge experiments at CEA, Chapter VI) shows the exceptionally important effects that fluid-rock interactions have on fault properties. In many cases, the characteristics subsequently displayed (strength, slip behaviour) can be attributed to a combination of chemical and mechanical effects.

In the case of the Zuccale Fault, Chapter III, the mechanical effects of localised high pore fluid pressure and intense foliation worked in combination with the chemical effects of dissolution processes and hydrothermally produced minerals to enable slip on a fault oriented at < 15°. It is unlikely that solely mechanical mechanisms would have enabled slip at such a low angle (Clemenzi et al., 2015), as also demonstrated by Experiment 1 on the Psatha Fault host rock (see Chapter IV Part II) but rather, in a positive feedback system with chemical effects. However, the relative contributions are not quantified. Further experiments to test these parameters individually and in combination should be carried out, as detailed in Chapter III and discussed later in this chapter (section 7.8).

My experimental work on the Psatha Fault host rock indicated that features produced by chemical interactions (Chapter IV Part I) can alter subsequent fracture propagation (Chapter IV Part II). Veins produced by precipitation within fractures (a chemical process) can deflect fracture propagation (a mechanical process) and provide an optimal, continuous fracture propagation path (Fig. 4.2.5a). Furthermore, without subsequent precipitation in fractured rock, a fault would become more permeable, weaker and simply break down over multiple deformation cycles. The chemical processes leading to 'fault rock recycling' (Wibberley and Shipton, 2010) i.e., this healing and sealing of fractures is an essential part of the deformation cycle. Initially, pre-existing features such as veins may affect subsequent fracture propagation

on a local scale, but eventually, as indicated by the Psatha Fault host rock experiments, Chapter IV Part II), twinned crystals may eventually be of equivalent strength to the original rock and thus the deformation cycle on a local scale effectively starts again (Fig. 4.2.7). This is strong evidence of the interplay between mechanical processes and features produced by chemical interactions.

The experiments undertaken on bare-interface calcite faults at MIT (Chapter V) distinctly illustrate the mechanical influence of a fluid, as opposed to the chemical influence. When argon was used as the pore fluid, the pore fluid acted solely to keep the fault zone open (Fig. 5.5f, g), reduce the effective stress and weaken the rock (Fig. 5.1). However, when water was used as the pore fluid under the same conditions, precipitation occurred in the fault zone, reducing the fault zone to the width of a grain boundary (Fig. 5.5d) and enabling long-duration slip-weakening (Fig 5.1). The fault zone was also stronger, due to the cohesive and compaction processes enabled. This distinct contrast between experiments utilising an inert fluid and distilled water at the same conditions illustrates how chemical interactions within a fault zone can provoke major changes in the rock physics properties (see also Faulkner and Rutter (2000)). In a similar manner, I undertook a dry experiment on limestone fault gouge at CEA (Chapter VI) at 70^{o}C as a comparison to the water-saturated limestone gouge experiment at 70^{o}C. The behaviour was distinctly chaotic in comparison (L70_50d Fig. 6.9) and the oscillations were shorter in duration. Notably, in this experimental setup I could not utilise an inert fluid in place of water for the pore fluid, as I for the bare-interface calcite fault experiments at MIT (Chapter V), so the results are not directly comparable. However, it again illustrates the difference in the mechanical behaviour induced when a reactive fluid is present compared to when one is not. I have further inferred that granular flow dominates at low temperature (~30^{o}C) in the hydrothermal frictional experiments on gouge at CEA (Chapter VI), a mechanical process, and that thermal compaction dominates at high temperatures (> 160^{o}C). However, it is the influence of fluids at mid-range temperature (50-130^{o}C) which may enable slow oscillatory behaviour in a velocity-strengthening regime; via both chemical (pressure solution) and mechanical (lubrication, locally enhanced pore fluid pressures) mechanisms.

7.7 What is the relevance of the mechanisms exhibited in rock deformation experiments to the field?

This work has shed light on the mechanisms that may be important for enigmatic slip events such as SSEs and slip on LANFs.

Based on my observations, it appears that the structural evolution and dominant deformation mechanism operating in a fault zone in the upper crust may vary significantly, as a function of depth and lithological heterogeneities in the protolith. Some heterogeneities may be unrelated to, or indirectly related, to deformation, but may go on to influence subsequent fault slip and fluid-flow, which in turn will influence the fault zone evolution and architecture. This work has relevance for understanding fault zone evolution, which has implications for (i) understanding the longevity of carbonate reservoirs, (ii) assessing carbon sequestration potential, (iii) understanding how cementation may alter earthquake nucleation processes in tectonically-active limestone terrains, and (iv) understanding the multi-scale character of carbonate faults.

The experimental work described in this thesis has investigated the role of fluid type, temperature and bare-interface/gouge-filled fault behaviours with subsequent microstructural analyses to constrain the deformation mechanisms operating during fault slip. The results show that the dominant deformation mechanisms operating within a fault zone vary, depending on conditions such as temperature, fault rock composition, gouge composition, the presence of fluid and its composition, and deformation rate. These factors will control fault slip stability, and the subsequent structures within the fault zone, which in turn can affect the frictional behaviour of the fault as the fault evolves. The Psatha Fault host rock (Chapter IV Part II), bare-interface calcite fault (Chapter V) and hydrothermal frictional gouge (Chapter VI) experiments on gouge all comprise important stages of fault zone evolution. The tests on the Psatha Fault involve the formation of a new fault, the immediate role of granular material produced, subsequent cohesion and smoothing of asperities. The bare-interface calcite fault slip experiments undertaken at MIT (Chapter V) are representative of a discrete slip surface or a relatively smooth fault that is subjected to hydrothermal alteration, or the purely mechanical effects of fluids. The hydrothermal frictional experiments on gouge undertaken at the CEA may represent the role of sediment influx into a subduction zone, or the role of granular material on a relatively smooth fault at different depths in the crust. A combination of these experiments,

or a longer duration experiment, could further test how a carbonate fault evolves. This is discussed more in section 7.8.

The most significant finding in this work is how temperature and fluids may alter the slip behaviour of faults. Previously, temperature had been dismissed as having a significant role in the production of SSEs, due to the different temperature regimes in which they occur (McCaffrey et al., 2008; Saffer and Wallace, 2015). However, I suggest that temperature may not only be exceptionally important, but that it acts in combination with, or against, other variables, which in turn alters its effectiveness. In carbonates, raising the temperature produces a transition from stable sliding to slow-slip to stick-slip (Fig. 6.1). However, the presence of a reactive fluid is essential to enable this transition effectively (see Chapter V), as is the ability for the precipitant/sediment to dilate (see Chapter VI). The fault roughness may also influence this transition (see Harbord et al., 2017).

Another important finding relevant to the field involves the way that pre-existing textures may influence further fracture propagation or fault reactivation. The tests on the Psatha Fault host rock (Chapter IV Part II) indicate that at a microscale, further fracturing is influenced by existing textures, but at the macroscale, misaligned or deviated fractures will still align to produce an optimally oriented fracture (Fig. 4.2.3). This work also indicates that if it is easier, pre-existing weaknesses will be cross-cut to produce an optimally oriented fracture. However, work on the Zuccale Fault (Chapter III) has indicated that if the conditions are such that a non-optimally aligned plane of weakness is easier to activate, then slip will occur at a non-optimal angle. My work has suggested that this may be due to a combination of mechanical and chemical factors (hot fluids, weak minerals, dissolution processes, foliation, and localised pore fluid pressure). This work has implications for other LANFs worldwide, as well as fault reactivation.

Ultimately, the coupled approach of fault zone characterisation followed by rock deformation experiments demonstrates the complex interactions of fault zone architecture and diagenetic healing and sealing processes in controlling future slip and fault zone evolution of shallow crustal carbonate fault zones.

7.8 Unresolved issues and suggested further work

Chapter III detailed results on the temperatures reached in the Zuccale Fault zone. The fine-grained weak material combined with the evidence of high temperature in a thin layer of strata (from the clumped isotope results, Table 3.1) suggests influx of high temperature fluids, which led to a concentrated high pore fluid pressure and ductile flow. However, the error associated with the high temperature data is large (see Table 3.1). Therefore, a great number of clumped isotope analyses (~30 per sample, including replicates) would need to be carried out to substantially reduce this error. This was not possible in this study, due to the substantial additional funding that would have been required. However, the orientation of the Zuccale Fault remains a conundrum in Earth science, and thus warrants more investigation.

The role of pressure on the frictional behaviour of faults also warrants further investigation. Even though intergranular pressure solution (IPS) in carbonates is more more dependent on temperature than on pressure (Stumm and Morgan, 1981), given that temperature and pressure both change with depth, the role of pressure should be investigated to shed more light on mechanisms involving slow-slip behaviours in subduction zones, as an increase solely in temperature has proved to yield a transition from stable sliding to stick-slip type behaviour. Alterations in both confining pressure and pore fluid pressure need to be investigated. In my experiments on hydrothermally altered gouges (Chapter VI), I observed that cohesive and compaction processes competed with, and ultimately dominated over, granular flow from medium to high temperatures (50-300ºC). Conversely, granular flow and fault roughness dominated over the role of fluids at high temperature (200ºC) upon the newly formed fault in the Psatha Fault host rock under low pore fluid pressure (Chapter IV Part II). By utilising a pre-existing smooth fault with no pre-existing gouge (Chapter V) at approximately hydrostatic pressure, a transition from long duration slip-weakening to stick-slip occurred with increasing temperature. However, when a higher confining pressure was used in the absence of pore fluid, the fault was distinctly stronger, showed stick-slip type oscillations but overall distinctly different behaviour to the rest of the experiments (see L70_150d, Fig. 6.2). It is not clear to what degree pressure may have been a factor in these different experiments, or in the case of the Psatha samples, whether the greater roughness of the fault enabled stable sliding following the formation of the fault (Fig. 4.2.6a). The manner in which roughness of faults may alter fault slip behaviour has been investigated (Harbord et al., 2017), and was found that smooth faults tend to favour velocity-weakening type behaviour, and rough faults velocity-strengthening behaviour. Alongside the work of Scuderi et al. (2016), Leeman et al. (2016) and Verberne et

al. (2014), I suggest that experimental studies which alter a number of variables side by side (including pressure and fault roughness) could provide greater insight into which mechanism dominates under which conditions.

My experiments have illuminated certain parts of the life cycle of a fault. Further work could investigate a more complete fault zone 'life cycle': a fault is produced, is subsequently smoothed during further deformation, and the ground-up material produced during the initial fault formation either enables granular flow continuously, likely at low temperatures, or cohesive processes cement this granular material, enabling stick-slip, likely at higher temperatures (as suggested by my experiments; see Chapter IV Part II, V & VI). An 'ultimate' experiment would include a suite of experiments at different temperatures and pressures, relevant for different depths in the crust in a true-triaxial set-up to investigate the relative importance of different parameters. This may provide a more realistic picture as to the factors that govern slip behaviour down-dip subduction zones.

Chapter VIII: Conclusions

This thesis examines the properties and role of carbonate cementation within fault zones. Detailed conclusions are given at the end of individual chapters. Here, I provide some overarching conclusions arising from this work:

1. The constraints on the temperature of the precipitating fluids (~451^{o}C) within the Zuccale Fault zone indicates a role of hot fluids. The $\delta^{13}C$ values indicates that these fluids originated from the Porto Azzurro pluton. Such hot fluids may have enable a positive feedback system of dissolution processes, the introduction of particularly weak minerals and possibly fluid overpressures. These processes may have weakened the plane enough in comparison to the surrounding rock to permit slip at a very low (~15^{o}) angle.

2. By establishing cross-cutting relationships between veins, degree of twinning and $\delta^{18}O$ and $\delta^{13}C$ content of calcite veins and cements from distinct breccias on the Psatha Fault, I have constrained the faults' uplift history. My interpretation of progressive uplift interspersed with deformation agrees with the regional history inferred from previous studies of neighbouring faults.

3. Uniaxial deformation experiments on heavily-veined Psatha host rock indicates that new fractures will propagate within optimally oriented non-cohesive structures e.g. recently precipitated veins, rather than heavily twinned, cohesive material.

4. Non-reactive fluids have a purely mechanical effect on fault zone properties i.e. increased pore pressure and hence a weakening effect upon a fault zone. Reactive fluids, such as water, can induce major changes of a carbonate faults' topology, altering strength, permeability and slip behaviour.

5. Dilation of a carbonate gouge competing with (fluid and temperature activated) compaction processes can lead to slow-slip type behaviours. When dilation dominates at lower temperature (~30^{o}C), velocity-strengthening aseismic creep is enabled, but when compaction processes dominate at higher temperature (>160^{o}C), velocity weakening stick-stick type behaviour is enabled.

References

Affek, H.P., 2012. Clumped isotope paleothermometry: principles, applications, and challenges. The Paleontological Society Papers, v. 18, p.101-114.

Ambrose, J., Zimmerman, R. W., & Suarez-Rivera, R. (2014, August). Failure of shales under triaxial compressive stress, i*n* 48th US Rock Mechanics/Geomechanics Symposium. American Rock Mechanics Association.

Amitrano, D., and Schmittbuhl, J., 2002, Fracture roughness and gouge distribution of a granite shear band: Journal of Geophysical Research: Solid Earth, v. 107, no. B12, 2375.

Amoruso, A., Crescentini, L., Morelli, A., and Scarpa, R., 2002, Slow rupture of an aseismic fault in a seismogenic region of Central Italy: Geophysical Research Letters, v. 29, no. 24, pp.72-1.

Anderson, E. M., 1905, The dynamics of faulting: Transactions of the Edinburgh Geological Society, v. 8, no. 3, p. 387-402.

Ando, M., 1979, The Hawaii earthquake of November 29, 1975: Low dip angle faulting due to forceful injection of magma: Journal of Geophysical Research: Solid Earth, v. 84, no. B13, p. 7616-7626.

Angevine, C., Turcotte, D., and Furnish, M., 1982, Pressure solution lithification as a mechanism for the stick-slip behavior of faults: Tectonics, v. 1, no. 2, p. 151-160.

Anzidei, M., Boschi, E., Cannelli, V., Devoti, R., Esposito, A., Galvani, A., Melini, D., Pietrantonio, G., Riguzzi, F., and Sepe, V., 2009, Coseismic deformation of the destructive April 6, 2009 L'Aquila earthquake (central Italy) from GPS data: Geophysical Research Letters, v. 36, no. 17.

Archie, G. E., 1950, Introduction to petrophysics of reservoir rocks: AAPG Bulletin, v. 34, no. 5, p. 943-961.

Argiriou, A. A., and Lykoudis, S., 2006, Isotopic composition of precipitation in Greece: Journal of Hydrology, v. 327, no. 3-4, p. 486-495.

Atkinson, B. K., 1984, Subcritical crack growth in geological materials: Journal of Geophysical Research: Solid Earth, v. 89, no. B6, p. 4077-4114.

Audet, P., Bostock, M. G., Christensen, N. I., and Peacock, S. M., 2009, Seismic evidence for overpressured subducted oceanic crust and megathrust fault sealing: Nature, v. 457, no. 7225, p. 76-78.

Axen, G. J., 1992, Pore fluid pressure, stress increase, and fault weakening in low-angle normal faulting: Journal of Geophysical Research: Solid Earth, v. 97, no. B6, p. 8979-8991.

Axen, G. J., and Karner, G., 2004, Mechanics of LANFs: Rheology and Deformation of the Lithosphere at Continental Margins, Colombia University Press, p. 46-91.

Aydin, A., 1978, Small faults formed as deformation bands in sandstone: Pure and Applied Geophysics, v. 116, no. 4-5, p. 913-930.

Barchi, M., Landuzzi, A., Minelli, G., and Pialli, G., 2001, Outer Northern Apennines, Anatomy of an orogen: the Apennines and Adjacent Mediterranean Basins, Springer, p. 215-253.

Barchi, M. R., 2002, Lithological and structural controls on the seismogenesis of the Umbria region: observations from seismic reflection profiles: Bollettino della Società geologica italiana, v. 121, no. 1, p. 855-864.

Barton, N., The shear strength of rock and rock joints, *in* Proceedings International Journal of Rock Mechanics and Mining Sciences & Geomechanics abstracts 1976, Volume 13, Elsevier, p. 255-279.

Bauer, H., Grasemann, B., and Decker, K., Microstructural investigations of principal slip zones in carbonates, examples from shallow crustal strike-slip faults in the Northern Calcareous Alps (Austria), *in* Proceedings EGU General Assembly Conference Abstracts2014, v. 16, p. 12164.

Beeler, N., Simpson, R., Hickman, S., and Lockner, D., 2000, Pore fluid pressure, apparent friction, and Coulomb failure: Journal of Geophysical Research: Solid Earth, v. 105, no. B11, p. 25533-25542.

Beeler, N., Tullis, T., Blanpied, M., and Weeks, J., 1996, Frictional behavior of large displacement experimental faults: Journal of Geophysical Research: Solid Earth, v. 101, no. B4, p. 8697-8715.

Beeler, N., Tullis, T., and Weeks, J., 1994, The roles of time and displacement in the evolution effect in rock friction: Geophysical Research Letters, v. 21, no. 18, p. 1987-1990.

Behnsen, J., and Faulkner, D. R., 2012, The effect of mineralogy and effective normal stress on frictional strength of sheet silicates: Journal of Structural Geology, v. 42, p. 49-61.

Bell, R., McNeill, L., Bull, J., Henstock, T., Collier, R. L., and Leeder, M., 2009, Fault architecture, basin structure and evolution of the Gulf of Corinth Rift, central Greece: Basin Research, v. 21, no. 6, p. 824-855.

Bell, R. E., McNeill, L. C., Henstock, T. J., and Bull, J. M., 2011, Comparing extension on multiple time and depth scales in the Corinth Rift, Central Greece: Geophysical Journal International, v. 186, no. 2, p. 463-470.

Bell, R., Sutherland, R., Barker, D.H., Henrys, S., Bannister, S., Wallace, L. and Beavan, J., 2010. Seismic reflection character of the Hikurangi subduction interface, New Zealand, in the region of repeated Gisborne slow slip events: Geophysical Journal International, 180, no. 1, p.34-48.

Bercovici, D., and Ricard, Y., 2014, Plate tectonics, damage and inheritance: Nature, v. 508, no. 7497, p. 513-516.

Billi, A., 2005, Grain size distribution and thickness of breccia and gouge zones from thin (< 1m) strike-slip fault cores in limestone: Journal of Structural Geology, v. 27, no. 10, p. 1823-1837.

Billiris, H., Paradissis, D., Veis, G., England, P., Featherstone, W., Parsons, B., Cross, P., Rands, P., Rayson, M., and Sellers, P., 1991, Geodetic determination of tectonic deformation in central Greece from 1900 to 1988: Nature, v. 350, no. 6314, p. 124-129.

Bird, P., Cartwright, J., and Davies, T., 2015, Basement reactivation in the development of rift basins: an example of reactivated Caledonide structures in the West Orkney Basin: Journal of the Geological Society, v. 172, no. 1, p. 77-85.

Bladon, A. J., Clarke, S. M., and Burley, S. D., 2015, Complex rift geometries resulting from inheritance of pre-existing structures: Insights and regional implications from the Barmer Basin rift: Journal of Structural Geology, v. 71, p. 136-154.

Blanpied, M., Lockner, D., and Byerlee, J., 1991, Fault stability inferred from granite sliding experiments at hydrothermal conditions: Geophysical Research Letters, v. 18, no. 4, p. 609-612.

Blanpied, M., Marone, C., Lockner, D., Byerlee, J., and King, D., 1998, Quantitative measure of the variation in fault rheology due to fluid-rock interactions: Journal of Geophysical Research: Solid Earth, v. 103, no. B5, p. 9691-9712.

Blanpied, M. L., Lockner, D. A., and Byerlee, J. D., 1992, An earthquake mechanism based on rapid sealing of faults: Nature, v. 358, no. 6387, p. 574-576.

Blanpied, M. L., Lockner, D. A., and Byerlee, J. D., 1995, Frictional slip of granite at hydrothermal conditions: Journal of Geophysical Research: Solid Earth, v. 100, no. B7, p. 13045-13064.

Blenkinsop, T. G., 1991, Cataclasis and processes of particle size reduction: Pure and Applied Geophysics, v. 136, no. 1, p. 59-86.

Blenkinsop, T. G., and Rutter, E., 1986, Cataclastic deformation of quartzite in the Moine thrust zone: Journal of Structural Geology, v. 8, no. 6, p. 669-681.

Boncio, P., and Lavecchia, G., 2000, A structural model for active extension in Central Italy: Journal of Geodynamics, v. 29, no. 3-5, p. 233-244.

Borghi, A., Aoudia, A., Javed, F., and Barzaghi, R., 2016, Precursory slow-slip loaded the 2009 L'Aquila earthquake sequence: Geophysical Journal International, v. 205, no. 2, p. 776-784.

Bortolotti, V., Fazzuoli, M., Pandeli, E., Principi, G., Babbini, A., and Corti, S., 2007, Geology of central and eastern Elba Island, Italy: Ofioliti, v. 26, no. 2a, p. 97-150.

Bos, B., 2000, Faults, fluids and friction: effect of pressure solution and phyllosilicates on fault slip behaviour, with implications for crustal rheology, Faculteit Aardwetenschappen. [PhD thesis]

Bos, B., and Spiers, C. J., 2002, Frictional-viscous flow of phyllosilicate-bearing fault rock: Microphysical model and implications for crustal strength profiles: Journal of Geophysical Research: Solid Earth, v. 107, no. B2, p. 1-13.

Bouillin, J.-P., Bouchez, J.-L., Lespinasse, P., and Pecher, A., 1993, Granite emplacement in an extensional setting: an AMS study of the magmatic structures of Monte Capanne (Elba, Italy): Earth and Planetary Science Letters, v. 118, no. 1-4, p. 263-279.

Brace, W., 1972, Laboratory studies of stick-slip and their application to earthquakes: Tectonophysics, v. 14, no. 3, p. 189-200.

Brace, W., and Byerlee, J., 1966, Stick-slip as a mechanism for earthquakes: Science, v. 153, no. 3739, p. 990-992.

Brace, W., and Kohlstedt, D., 1980, Limits on lithospheric stress imposed by laboratory experiments: Journal of Geophysical Research: Solid Earth, v. 85, no. B11, p. 6248-6252.

Brace, W. F., Walsh, J., and Frangos, W., 1968, Permeability of granite under high pressure: Journal of Geophysical research, v. 73, no. 6, p. 2225-2236.

Brantut, N., Heap, M., Meredith, P., and Baud, P., 2013, Time-dependent cracking and brittle creep in crustal rocks: A review: Journal of Structural Geology, v. 52, p. 17-43.

Brasier, A. T., 2007, Palaeoenvironmental reconstructions from Quaternary tufas and calcretes, central Greece: University of East Anglia. [PhD thesis]

Budd, D. A., Frost III, E. L., Huntington, K. W., and Allwardt, P. F., 2013, Syndepositional deformation features in high-relief carbonate platforms: long-lived conduits for diagenetic fluids: Journal of Sedimentary Research, v. 83, no. 1, p. 12-36.

Bullock, R. J., De Paola, N., Holdsworth, R. E., and Trabucho-Alexandre, J., 2014, Lithological controls on the deformation mechanisms operating within carbonate-hosted faults during the seismic cycle: Journal of Structural Geology, v. 58, p. 22-42.

Burlini, L., and Bruhn, D., 2005, High-strain zones: laboratory perspectives on strain softening during ductile deformation: Geological Society, London, Special Publications, v. 245, no. 1, p. 1-24.

Bussolotto, M., Benedicto, A., Moen-Maurel, L., and Invernizzi, C., 2015, Fault deformation mechanisms and fault rocks in micritic limestones: Examples from Corinth rift normal faults: Journal of Structural Geology, v. 77, p. 191-212.

Byerlee, J., 1978, Friction of rocks, Rock friction and earthquake prediction, Springer, p. 615-626.

Byerlee, J. D., 1966, The frictional characteristics of Westerly granite: Massachusetts Institute of Technology. [PhD thesis]

Byerlee, J. D., 1967, Frictional characteristics of granite under high confining pressure: Journal of Geophysical Research, v. 72, no. 14, p. 3639-3648.

Byerlee, J. D., 1993, Model for episodic flow of high-pressure water in fault zones before earthquakes: Geology, v. 21, no. 4, p. 303-306.

Byerlee, J. D., and Brace, W., 1968, Stick slip, stable sliding, and earthquakes—effect of rock type, pressure, strain rate, and stiffness: Journal of Geophysical Research, v. 73, no. 18, p. 6031-6037.

Caine, J. S., Evans, J. P., and Forster, C. B., 1996, Fault zone architecture and permeability structure: Geology, v. 24, no. 11, p. 1025-1028.

Carreras, J., 2001, Zooming on Northern Cap de Creus shear zones: Journal of Structural Geology, v. 23, no. 9, p. 1457-1486.

Cates, M. E., Wittmer, J. P., Bouchaud, J.-P., and Claudin, P., 1998, Jamming, Force Chains, and Fragile Matter: Physical Review Letters, v. 81, no. 9, p.1841.

Chambon, G., Schmittbuhl, J., and Corfdir, A., 2002, Laboratory gouge friction: Seismic-like slip-weakening and secondary rate-and state-effects: Geophysical Research Letters, v. 29, no. 10, p. 4-1-4-4

Chen, J., 2015, Compositional, mechanical and transport properties of carbonate fault rocks and the seismic cycle in limestone terrains: A case study of surface exposures on the Longmenshan Fault, Sichuan, China, UU Dept. of Earth Sciences. [PhD thesis]

Chen, J., Verberne, B. A., and Spiers, C. J., 2015, Interseismic re-strengthening and stabilization of carbonate faults by 'non-Dieterich' healing under hydrothermal conditions: Earth and Planetary Science Letters, v. 423, p. 1-12.

Chen, W.-P., Yu, C.-Q., Tseng, T.-L., Yang, Z., Wang, C.-y., Ning, J., and Leonard, T., 2013, Moho, seismogenesis, and rheology of the lithosphere: Tectonophysics, v. 609, p. 491-503.

Chester, F., and Higgs, N., 1992, Multimechanism friction constitutive model for ultrafine quartz gouge at hypocentral conditions: Journal of Geophysical Research: Solid Earth (1978–2012), v. 97, no. B2, p. 1859-1870.

Chiaraluce, L., 2012, Unravelling the complexity of Apenninic extensional fault systems: A review of the 2009 L'Aquila earthquake (Central Apennines, Italy): Journal of Structural Geology, v. 42, p. 2-18.

Chiaraluce, L., Chiarabba, C., Collettini, C., Piccinini, D., and Cocco, M., 2007, Architecture and mechanics of an active low-angle normal fault: Alto Tiberina fault, northern Apennines, Italy: Journal of Geophysical Research: Solid Earth, v. 112, no. B10.

Chiodini, G., and Cioni, R., 1989, Gas geobarometry for hydrothermal systems and its application to some Italian geothermal areas: Applied geochemistry, v. 4, no. 5, p. 465-472.

Choi, J.-H., Edwards, P., Ko, K., and Kim, Y.-S., 2016, Definition and classification of fault damage zones: A review and a new methodological approach: Earth-Science Reviews, v. 152, p. 70-87.

Ciaccio, M. G., Pondrelli, S., and Frepoli, A., 2006, Earthquake fault-plane solutions and patterns of seismicity within the Umbria Region, Italy, Annals of Geophysics, v. 49, n. 4/5.

Cicerone, D. S., Regazzoni, A. E., and Blesa, M. A., 1992, Electrokinetic properties of the calcite/water interface in the presence of magnesium and organic matter: Journal of Colloid and Interface Science, v. 154, no. 2, p. 423-433.

Clark, I. D., and Fritz, P., 1997, Environmental isotopes in hydrogeology, CRC Press.

Clément, C., Sachpazi, M., Charvis, P., Graindorge, D., Laigle, M., Hirn, A., and Zafiropoulos, G., 2004, Reflection–refraction seismics in the Gulf of Corinth: hints at deep structure and control of the deep marine basin: Tectonophysics, v. 391, no. 1, p. 97-108.

Clemenzi, L., Storti, F., Balsamo, F., Molli, G., Ellam, R., Muchez, P., and Swennen, R., 2015, Fluid pressure cycles, variations in permeability, and weakening mechanisms along LANFs: The Tellaro detachment, Italy: GSA Bulletin, v. 127, no. 11-12, p. 1689-1710.

Collettini, C., and Barchi, M. R., 2002, A low-angle normal fault in the Umbria region (Central Italy): a mechanical model for the related microseismicity: Tectonophysics, v. 359, no. 1-2, p. 97-115.

Collettini, C., Carpenter, B., Viti, C., Cruciani, F., Mollo, S., Tesei, T., Trippetta, F., Valoroso, L., and Chiaraluce, L., 2014, Fault structure and slip localization in carbonate-bearing normal faults: An example from the Northern Apennines of Italy: Journal of Structural Geology, v. 67, p. 154-166.

Collettini, C., De Paola, N., and Goulty, N., 2006, Switches in the minimum compressive stress direction induced by overpressure beneath a low-permeability fault zone: Terra Nova, v. 18, no. 3, p. 224-231.

Collettini, C., and Holdsworth, R., 2004, Fault zone weakening and character of slip along LANFs: insights from the Zuccale fault, Elba, Italy: Journal of the Geological Society, v. 161, no. 6, p. 1039-1051.

Collettini, C., Niemeijer, A., Viti, C., and Marone, C., 2009, Fault zone fabric and fault weakness: Nature, v. 462, no. 7275, p. 907.

Collier, R. E., Pantosti, D., D'addezio, G., De Martini, P. M., Masana, E., and Sakellariou, D., 1998, Paleoseismicity of the 1981 Corinth earthquake fault: Seismic contribution to extensional strain in central Greece and implications for seismic hazard: Journal of Geophysical Research: Solid Earth, v. 103, no. B12, p. 30001-30019.

Conybeare, D., and Shaw, H., 2000, Fracturing, overpressure release and carbonate cementation in the Everest Complex, North Sea: Clay Minerals, v. 35, no. 1, p. 135-149.

Crawford, B., Faulkner, D., and Rutter, E., 2008, Strength, porosity, and permeability development during hydrostatic and shear loading of synthetic quartz-clay fault gouge: Journal of Geophysical Research: Solid Earth, v. 113, no. B3.

Crescentini, L., Amoruso, A., and Scarpa, R., 1999, Constraints on slow earthquake dynamics from a swarm in central Italy: Science, v. 286, no. 5447, p. 2132-2134.

Crittenden, M. D., Coney, P. J., Davis, G. H., and Davis, G. H., 1980, Cordilleran metamorphic core complexes, Geological Society of America.

Croize, D., Renard, F., and Gratier, J.-P., 2013, Compaction and porosity reduction in carbonates: A review of observations, theory, and experiments, Advances in Geophysics, Elsevier, v.54, p. 181-238.

Cruden, A., and McCaffrey, K., 2001, Growth of plutons by floor subsidence: implications for rates of emplacement, intrusion spacing and melt-extraction mechanisms: Physics and Chemistry of the Earth, Part A: Solid Earth and Geodesy, v. 26, no. 4-5, p. 303-315.

Cullity, B., and Stock, S., 1956, The directions of diffracted beams: Elements of X-ray diffraction, Addison-Wesley Publishing Co., USA, p. 78-103.

Daly, M., Chorowicz, J., and Fairhead, J., 1989, Rift basin evolution in Africa: the influence of reactivated steep basement shear zones: Geological Society, London, Special Publications, v. 44, no. 1, p. 309-334.

Daniel, J., and Jolivet, L., 1995, Interaction of detachments and granitic plutons during extension in the Tyrrhenian Sea (Elba island): Bull. Soc. Geol. Fr, v. 166, p. 341-354.

de Graaf, S., Reijmer, J. J., Bertotti, G. V., Bezerra, F. H., Cazarin, C. L., Bisdom, K., and Vonhof, H. B., 2017, Fracturing and calcite cementation controlling fluid-flow in the shallow-water carbonates of the Jandaíra Formation, Brazil: Marine and Petroleum Geology, v. 80, p. 382-393.

De Paola, N., Agosta, F., Balsamo, F., Bullock, R., Dempsey, E., Faoro, I., Holdsworth, R., and Storti, F., 2011, Natural Slip Surfaces in Fault Cores of Seismogenic Carbonate Faults, *in* Proceedings AGU Fall Meeting Abstracts, v. 1, p. 2464.

De Paola, N., Mirabella, F., Barchi, M., and Burchielli, F., 2006, Early orogenic normal faults and their reactivation during thrust belt evolution: the Gubbio Fault case study, Umbria-Marche Apennines (Italy): Journal of Structural Geology, v. 28, no. 11, p. 1948-1957.

Delle Piane, C., Clennell, M. B., Keller, J. V., Giwelli, A., and Luzin, V., 2017, Carbonate hosted fault rocks: A review of structural and microstructural characteristic with implications for seismicity in the upper crust: Journal of Structural Geology, v. 103, p. 1-184

den Hartog, S. A., Saffer, D. M., and Spiers, C. J., 2014, The roles of quartz and water in controlling unstable slip in phyllosilicate-rich megathrust fault gouges: Earth, Planets and Space, v. 66, no. 1, p. 78.

den Hartog, S. A., and Spiers, C. J., 2013, Influence of subduction zone conditions and gouge composition on frictional slip stability of megathrust faults: Tectonophysics, v. 600, p. 75-90.

Di Toro, G., Goldsby, D. L., and Tullis, T. E., 2004, Friction falls towards zero in quartz rock as slip velocity approaches seismic rates: Nature, v. 427, no. 6973, p. 436.

Dieterich, J. H., 1972, Time-dependent friction in rocks: Journal of Geophysical Research, v. 77, no. 20, p. 3690-3697.

Dieterich, J. H., 1978, Time-dependent friction and the mechanics of stick-slip: pure and applied geophysics, v. 116, no. 4-5, p. 790-806.

Dieterich, J. H., 1979, Modeling of rock friction: 1. Experimental results and constitutive equations: Journal of Geophysical Research: Solid Earth, v. 84, no. B5, p. 2161-2168.

Dini, A., Innocenti, F., Rocchi, S., Tonarini, S., and Westerman, D., 2002, The magmatic evolution of the late Miocene laccolith–pluton–dyke granitic complex of Elba Island, Italy: Geological Magazine, v. 139, no. 3, p. 257-279.

Dixon, T. H., Jiang, Y., Malservisi, R., McCaffrey, R., Voss, N., Protti, M., and Gonzalez, V., 2014, Earthquake and tsunami forecasts: Relation of SSEs to subsequent earthquake rupture: Proceedings of the National Academy of Sciences, v. 111, no. 48, p. 17039-17044.

Doglioni, C., 1991, A proposal for the kinematic modelling of W-dipping subductions-possible applications to the Tyrrhenian-Apennines system: Terra Nova, v. 3, no. 4, p. 423-434.

Duffy, O., Brocklehurst, S., Gawthorpe, R., Leeder, M., and Finch, E., 2015, Controls on landscape and drainage evolution in regions of distributed normal faulting: Perachora Peninsula, Corinth Rift, Central Greece: Basin Research, v. 27, no. 4, p. 473-494.

Egeberg, P. K., and Saigal, G. C., 1991, North Sea chalk diagenesis: cementation of chalks and healing of fractures: Chemical geology, v. 92, no. 4, p. 339-354.

Eichhubl, P., Davatzes, N. C., and Becker, S. P., 2009, Structural and diagenetic control of fluid migration and cementation along the Moab fault, Utah: AAPG bulletin, v. 93, no. 5, p. 653-681.

Eiler, J. M., 2007, 'Clumped-isotope' geochemistry—The study of naturally-occurring, multiply-substituted isotopologues: Earth and Planetary Science Letters, v. 262, no. 3, p. 309-327.

Ellis, A. C., 2014, The effect of hydrothermally generated talc upon fault strength: University of Manchester. [PhD thesis]

Elter, P., Giglia, G., Tongiorgi, M., and Trevisan, L., Tensional and compressional areas in recent (Tortonian to present) evolution of Northern Apennines, *in* Proceedings Transactions-American Geophysical Union, 1975, Volume 56, p. 166-166.

Engelder, J. T., 1974, Cataclasis and the generation of fault gouge: Geological Society of America Bulletin, v. 85, no. 10, p. 1515-1522.

Evans, B., Fredrich, J. T., and Wong, T. F., 1990, The Brittle-Ductile Transition in Rocks: Recent experimental and theoretical progres, Geophys. Monogr. Ser, v. 56, p. 1-20.

Evans, J. P., and Chester, F. M., 1995, Fluid-rock interaction in faults of the San Andreas system: Inferences from San Gabriel fault rock geochemistry and microstructures: Journal of Geophysical Research: Solid Earth, v. 100, no. B7, p. 13007-13020.

Everall, T. J., and Sanislav, I. V., 2018, The influence of pre-existing deformation and alteration textures on rock strength, failure modes and shear strength parameters: Geosciences, v. 8, no. 4, p. 124.

Fagereng, Å., Remitti, F., and Sibson, R. H., 2010, Shear veins observed within anisotropic fabric at high angles to the maximum compressive stress: Nature Geoscience, v. 3, no. 7, p. 482.

Fang, Z., and Dunham, E. M., 2013, Additional shear resistance from fault roughness and stress levels on geometrically complex faults: Journal of Geophysical Research: Solid Earth, v. 118, no. 7, p. 3642-3654.

Faulkner, D., Jackson, C., Lunn, R., Schlische, R., Shipton, Z., Wibberley, C., and Withjack, M., 2010, A review of recent developments concerning the structure, mechanics and fluid-flow properties of fault zones: Journal of Structural Geology, v. 32, no. 11, p. 1557-1575.

Faulkner, D., Lewis, A., and Rutter, E., 2003, On the internal structure and mechanics of large strike-slip fault zones: field observations of the Carboneras fault in southeastern Spain: Tectonophysics, v. 367, no. 3-4, p. 235-251.

Faulkner, D., and Rutter, E., 2000, Comparisons of water and argon permeability in natural clay-bearing fault gouge under high pressure at 20°C: Journal of Geophysical Research: Solid Earth, v. 105, no. B7, p. 16415-16426.

Faulkner, D. R., and Rutter, E. H., 2001, Can the maintenance of overpressured fluids in large strike-slip fault zones explain their apparent weakness? Geology, v. 29, no. 6, p. 503-506.

Fazio, M., 2017, Dynamic laboratory simulations of fluid-rock coupling with application to volcano seismicity and unrest: University of Portsmouth. [PhD thesis]

Fondriest, M., 2014, Structure and mechanical properties of seismogenic fault zones in carbonates. [Ph.D. thesis]

Ford, D. C., and Williams, P. W., 1989, Karst geomorphology and hydrology, Unwin Hyman London.

Fossen, H., 2010, Structural geology, Cambridge University Press.

Frank, W. B., Rousset, B., Lasserre, C., and Campillo, M., 2018, Revealing the cluster of slow transients behind a large slow-slip event: Science Advances, v. 4, no. 5, p. 661.

Fredrich, J., and Evans, B., Strength recovery along simulated faults by solution transfer, *in* Proceedings 33rd US Rock Mech. Symp. 1992, p. 121-130.

Frezzotti, M. L., Tecce, F., and Casagli, A., 2012, Raman spectroscopy for fluid inclusion analysis: Journal of Geochemical Exploration, v. 112, p. 1-20.

Friedman, I., O'Neil, J., and Cebula, G., 1982, Two new carbonate stable-isotope Standards: Geostandards Newsletter, v. 6, no. 1, p. 11-12.

Friedman, I., and O'Neil, J. R., 1977, Compilation of stable isotope fractionation factors of geochemical interest, USGPO.

Frostick, L. E., and Steel, R. J., 1993, Tectonic Controls and Signatures in Sedimentary Successions. Int. Assoc. Sedimentol. Spec. Publ., 20:111-128.

Frye, K. M., 2002, A laboratory study of the friction behavior of granular materials: Massachusetts Institute of Technology. [PhD thesis]

Frye, K. M., and Marone, C., 2002, Effect of humidity on granular friction at room temperature: Journal of Geophysical Research: Solid Earth, v. 107, no. B11, p. 11-13.

Gagnevin, D., Daly, J., and Poli, G., 2004, Petrographic, geochemical and isotopic constraints on magma dynamics and mixing in the Miocene Monte Capanne monzogranite (Elba Island, Italy): Lithos, v. 78, no. 1, p. 157-195.

Garfagnoli, F., Menna, F., Pandeli, E., and Principi, G., 2005, The porto azzurro unit (Mt. Calamita promontory, south-eastern Elba island, Tuscany): stratigraphic, tectonic and metamorphic evolution: Bollettino della Società Geologica Italiana, v. 3, p. 119-138.

Gehne, S., and Benson, P. M., 2017, Permeability and permeability anisotropy in Crab Orchard sandstone: Experimental insights into spatio-temporal effects: Tectonophysics, v. 712, p. 589-599.

Gentili, S., Di Giovambattista, R., and Peresan, A., 2017, Seismic quiescence preceding the 2016 central Italy earthquakes: Physics of the Earth and Planetary Interiors, v. 272, p. 27-33.

Ghisetti, F., and Vezzani, L., 2005, Inherited structural controls on normal fault architecture in the Gulf of Corinth (Greece): Tectonics, v. 24, no. 4.

Ghosh, P., Adkins, J., Affek, H., Balta, B., Guo, W., Schauble, E. A., Schrag, D., and Eiler, J. M., 2006, 13C–18O bonds in carbonate minerals: a new kind of paleothermometer: Geochimica et Cosmochimica Acta, v. 70, no. 6, p. 1439-1456.

Giger, S. B., Cox, S. F., and Tenthorey, E., 2008, Slip localization and fault weakening as a consequence of fault gouge strengthening—Insights from laboratory experiments: Earth and Planetary Science Letters, v. 276, no. 1, p. 73-84.

Gobo, K., Ghinassi, M., Nemec, W., and Sjursen, E., 2014, Development of an incised valley-fill at an evolving rift margin: Pleistocene eustasy and tectonics on the southern side of the Gulf of Corinth, Greece: Sedimentology, v. 61, no. 4, p. 1086-1119.

Goddard, J. V., and Evans, J. P., 1995, Chemical changes and fluid-rock interaction in faults of crystalline thrust sheets, northwestern Wyoming, USA: Journal of Structural Geology, v. 17, no. 4, p. 533-547.

Goldstein, J. I., Newbury, D. E., Michael, J. R., Ritchie, N. W., Scott, J. H. J., and Joy, D. C., 2017, Scanning electron microscopy and X-ray microanalysis, Springer.

Götze, J., 2012, Application of cathodoluminescence microscopy and spectroscopy in geosciences: Microscopy and Microanalysis, v. 18, no. 6, p. 1270-1284.

Gratier, J.-P., 2011, Fault permeability and strength evolution related to fracturing and healing episodic processes (years to millennia): the role of pressure solution: Oil & Gas Science and Technology–Revue d'IFP Energies nouvelles, v. 66, no. 3, p. 491-506.

Gratier, J.-P., Dysthe, D. K., and Renard, F., 2013, The role of pressure solution creep in the ductility of the Earth's upper crust: Advances in Geophysics, v. 54, p. 47-179.

Gratier, J., and Gamond, J., 1990, Transition between seismic and aseismic deformation in the upper crust: Geological Society, London, Special Publications, v. 54, no. 1, p. 461-473.

Gribble, C. D., 1993, Optical mineralogy: principles and practice, CRC Press.

Grover Jr, G., and Read, J., 1983, Paleoaquifer and deep burial related cements defined by regional cathodoluminescent patterns, Middle Ordovician carbonates, Virginia: AAPG Bulletin, v. 67, no. 8, p. 1275-1303.

Guglielmi, Y., Nussbaum, C., Birkholzer, J., De Barros, L., and Cappa, F., 2017, Permeability evolution associated to creep and episodic slow-slip of a fault affecting clay formations: Results from the FS fault activation experiment in Mt Terri (Switzerland), *in* Proceedings AGU Fall Meeting Abstracts.

Hackston, A. J., 2013, Activation of Faulting Under Controlled Stress Conditions: University of Manchester. [PhD thesis]

Haessler, H., Gaulon, R., Rivera, L., Console, R., Frogneux, M., Gasparini, G., Martel, L., Patau, G., Siciliano, M., and Cisternas, A., 1988, The Perugia (Italy) earthquake of 29, April 1984: a microearthquake survey: Bulletin of the Seismological Society of America, v. 78, no. 6, p. 1948-1964.

Haines, S., Marone, C., and Saffer, D., 2010, Frictional properties of low-angle normal fault gouges and implications for low-angle normal fault slip, *in* Proceedings AGU Fall Meeting Abstracts, v.1, p.6.

Han, R., Shimamoto, T., Hirose, T., Ree, J.-H., and Ando, J.-i., 2007, Ultralow friction of carbonate faults caused by thermal decomposition: Science, v. 316, no. 5826, p. 878-881.

Harbord, C. W., Nielsen, S. B., De Paola, N., and Holdsworth, R. E., 2017, Earthquake nucleation on rough faults: Geology, v. 45, no. 10, p. 931-934.

Harker, R. S., 1971, Some aspects of fluid inclusion geothermometry with particular reference to British fluorites: Geology. p.93-94

Hatano, T., 2007, Power-law friction in closely packed granular materials: Physical Review E, v. 75, no. 6.

Hausegger, S., Kurz, W., Rabitsch, R., Kiechl, E., and Brosch, F.-J., 2010, Analysis of the internal structure of a carbonate damage zone: Implications for the mechanisms of fault breccia formation and fluid-flow: Journal of Structural Geology, v. 32, no. 9, p. 1349-1362.

Hayman, N. W., Knott, J. R., Cowan, D. S., Nemser, E., and Sarna-Wojcicki, A. M., 2003, Quaternary low-angle slip on detachment faults in Death Valley, California: Geology, v. 31, no. 4, p. 343-346.

He, C., Luo, L., Hao, Q. M., and Zhou, Y., 2013, Velocity-weakening behavior of plagioclase and pyroxene gouges and stabilizing effect of small amounts of quartz under hydrothermal conditions: Journal of Geophysical Research: Solid Earth, v. 118, no. 7, p. 3408-3430.

He, C., Wang, Z., and Yao, W., 2007, Frictional sliding of gabbro gouge under hydrothermal conditions: Tectonophysics, v. 445, no. 3, p. 353-362.

He, C., Yao, W., Wang, Z., and Zhou, Y., 2006, Strength and stability of frictional sliding of gabbro gouge at elevated temperatures: Tectonophysics, v. 427, no. 1, p. 217-229.

Hickman, S., Sibson, R., and Bruhn, R., 1995, Introduction to special section: Mechanical involvement of fluids in faulting: Journal of Geophysical Research: Solid Earth (1978–2012), v. 100, no. B7, p. 12831-12840.

Hirose, T., and Bystricky, M., 2007, Extreme dynamic weakening of faults during dehydration by coseismic shear heating: Geophysical Research Letters, v. 34, no. 14.

Holdsworth, R. E., and Turner, J. P., 2002, Extensional Tectonics: Regional-scale Processes, Geological Society of London.

Horn, H., and Deere, D., 1962, Frictional characteristics of minerals: Geotechnique, v. 12, no. 4, p. 319-335.

Hubbert, M., and Rubey, W. W., 1959, Role of fluid pressure in mechanics of overthrust faulting: I. Mechanics of fluid-filled porous solids and its application to overthrust faulting: Geological Society of America Bulletin, v. 70, no. 2, p. 115-166.

Hyndman, R., Yamano, M., and Oleskevich, D., 1997, The seismogenic zone of subduction thrust faults: Island Arc, v. 6, no. 3, p. 244-260.

Ide, S., Beroza, G. C., Shelly, D. R., and Uchide, T., 2007, A scaling law for slow earthquakes: Nature, v. 447, no. 7140, p. 76-79.

Ikari, M. J., Marone, C., and Saffer, D. M., 2011, On the relation between fault strength and frictional stability: Geology, v. 39, no. 1, p. 83-86.

Ikari, M. J., Marone, C., Saffer, D. M., and Kopf, A. J., 2013a, Slip-weakening as a mechanism for slow earthquakes: Nature Geoscience, v. 6, no. 6, p. 468-472.

Ikari, M. J., Niemeijer, A. R., and Marone, C., 2015, Experimental investigation of incipient shear failure in foliated rock: Journal of Structural Geology, v. 77, p. 82-91.

Ikari, M. J., Niemeijer, A. R., Spiers, C. J., Kopf, A. J., and Saffer, D. M., 2013b, Experimental evidence linking slip instability with seafloor lithology and topography at the Costa Rica convergent margin: Geology, v. 41, no. 8, p. 891-894.

Im, K., Elsworth, D., and Fang, Y., 2018, The influence of preslip sealing on the permeability evolution of fractures and faults: Geophysical Research Letters, v. 45, no. 1, p. 166-175.

Ioannou, S., Götze, J., Weiershäuser, L., Zubowski, S., and Spooner, E., 2004, Cathodoluminescence characteristics of Archean volcanogenic massive sulfide related quartz: Noranda, Ben Nevis and Matagami districts, Abitibi Subprovince, Canada: Geochemistry, Geophysics, Geosystems, v. 5, no. 2.

Ito, Y., Hino, R., Kido, M., Fujimoto, H., Osada, Y., Inazu, D., Ohta, Y., Iinuma, T., Ohzono, M., and Miura, S., 2013, Episodic SSEs in the Japan subduction zone before the 2011 Tohoku-Oki earthquake: Tectonophysics, v. 600, p. 14-26.

Jackson, J., Gagnepain, J., Houseman, G., King, G., Papadimitriou, P., Soufleris, C., and Virieux, J., 1982, Seismicity, normal faulting, and the geomorphological development of the Gulf of Corinth (Greece): the Corinth earthquakes of February and March 1981: Earth and Planetary Science Letters, v. 57, no. 2, p. 377-397.

Jackson, J. A., 2012, Carbonate Cementation in Sandstones of the Plover Formation, North West Shelf, WA: Queensland University of Technology.

Jaeger, J.C., 1960. Shear failure of anisotropic rock. Geol. Mag. v. 97, p.65-72.

Jaeger, J. C., Cook, N. G., and Zimmerman, R., 2009, Fundamentals of rock mechanics, John Wiley & Sons.

John, B. E., and Foster, D. A., 1993, Structural and thermal constraints on the initiation angle of detachment faulting in the southern Basin and Range: The Chemehuevi Mountains case study: Geological Society of America Bulletin, v. 105, no. 8, p. 1091-1108.

John, C., Jourdan, A., Kluge, T., Dale, A., Davis, S., and Vandeginste, V., 2012, Clumped isotopes applied to carbonate diagenesis and high temperature systems, *in* Proceedings AGU Fall Meeting Abstracts, v. 1, p. 08.

Jolivet, L., Lecomte, E., Huet, B., Denèle, Y., Lacombe, O., Labrousse, L., Le Pourhiet, L., and Mehl, C., 2010, The north cycladic detachment system: Earth and Planetary Science Letters, v. 289, no. 1-2, p. 87-104.

Jones, L. M., Wang, B., Xu, S., and Fitch, T. J., 1982, The foreshock sequence of the February 4, 1975, Haicheng earthquake (M = 7.3): Journal of Geophysical Research: Solid Earth, v. 87, no. B6, p. 4575-4584.

Kanagawa, K., Cox, S. F., and Zhang, S., 2000, Effects of dissolution-precipitation processes on the strength and mechanical behavior of quartz gouge at high-temperature hydrothermal conditions: Journal of Geophysical Research: Solid Earth (1978–2012), v. 105, no. B5, p. 11115-11126.

Kaproth, B. M., 2013, The evolution of fault strength, permeability, and acoustic properties in experimental studies from fault initiation through the seismic cycle. Pennsylvania State University. [PhD thesis]

Karato, S., 2012, Deformation of earth materials: an introduction to the rheology of solid earth, Cambridge University Press.

Karner, S. L., Marone, C., and Evans, B., 1997, Laboratory study of fault healing and lithification in simulated fault gouge under hydrothermal conditions: Tectonophysics, v. 277, no. 1, p. 41-55.

Kato, A., Sakaguchi, A., Yoshida, S., Mochizuki, H., and Kaneda, Y., 2003, Permeability measurements and precipitation sealing of basalt in an ancient exhumed subduction-zone fault: Bulletin of Earthquake Research Institute, v. 78, p. 83-89.

Kato, N., Yamamoto, K., Yamamoto, H., and Hirasawa, T., 1992, Strain-rate effect on frictional strength and the slip nucleation process: Tectonophysics, v. 211, no. 1-4, p. 269-282.

Kazmierczak, T., Tomson, M., and Nancollas, G., 1982, Crystal growth of calcium carbonate. A controlled composition kinetic study: The Journal of Physical Chemistry, v. 86, no. 1, p. 103-107.

Kele, S., Breitenbach, S. F. M., Capezzuoli, E., Meckler, A. N., Ziegler, M., Millan, I. M., et al, 2015. Temperature dependence of oxygen- and clumped isotope fractionation in carbonates: A study of travertines and tufas in the 6-95 degrees C temperature range: Geochimica et Cosmochimica Acta, no. 168, p. 172–192.

Keller, J., and Coward, M., 1996, The structure and evolution of the Northern Tyrrhenian Sea: Geological Magazine, v. 133, no. 1, p. 1-16.

Keller, J., Minelli, G., and Pialli, G., 1994, Anatomy of late orogenic extension: the Northern Apennines case: Tectonophysics, v. 238, no. 1-4, p. 275-294.

Keller, J., and Pialli, G., 1990, Tectonics of the Island of Elba; a reappraisal: Bollettino della Societa Geologica Italiana, v. 109, no. 2, p. 413-425.

Kim, K., and Kemeny, J., 2009, Effect of thermal shock and rapid unloading on mechanical rock properties, *in* Proceedings 43rd US Rock Mechanics Symposium, American Rock Mechanics Association.

Kim, S.-T., Mucci, A., and Taylor, B. E., 2007, Phosphoric acid fractionation factors for calcite and aragonite between 25 and 75 C: revisited: Chemical Geology, v. 246, no. 3-4, p. 135-146.

Kimura, G., Silver, E., Blum, P., and Others, A., 1997, Proceedings of the Ocean Drilling Program, Vol. 170, Initial Reports, Costa Rica Accretionary Wedge, Ocean Drilling Program.

Kirkpatrick, J., Bezerra, F., Shipton, Z., Do Nascimento, A., Pytharouli, S., Lunn, R., and Soden, A., 2013, Scale-dependent influence of pre-existing basement shear zones on rift faulting: a case study from NE Brazil: Journal of the Geological Society, v. 170, no. 2, p. 237-247.

Kitajima, H., and Saffer, D. M., 2012, Elevated pore fluid pressure and anomalously low stress in regions of low frequency earthquakes along the Nankai Trough subduction megathrust: Geophysical Research Letters, v. 39, no. 23.

Kitajima, H., and Saffer, D. M., 2014, Consolidation state of incoming sediments to the Nankai Trough subduction zone: Implications for sediment deformation and properties: Geochemistry, Geophysics, Geosystems, v. 15, no. 7, p. 2821-2839.

Knipe, R., Fisher, Q., Jones, G., Clennell, M., Farmer, A., Harrison, A., Kidd, B., McAllister, E., Porter, J., and White, E., 1997, Fault seal analysis: successful methodologies,

application and future directions: Norwegian Petroleum Society Special Publications, v. 7, p. 15-38.

Knipe, R., Larsen, R., Brekke, B., Larsen, B., and Talleraas, E., 1992, Faulting processes and fault seal: Structural and tectonic modelling and its application to petroleum geology, p. 325-342.

Kodaira, S., Iidaka, T., Kato, A., Park, J.-O., Iwasaki, T., and Kaneda, Y., 2004, High pore fluid pressure may cause silent slip in the Nankai Trough: Science, v. 304, no. 5675, p. 1295-1298.

Kranz, R., Saltzman, J., and Blacic, J., Hydraulic diffusivity measurements on laboratory rock samples using an oscillating pore fluid pressure method, *in* Proceedings International Journal of Rock Mechanics and Mining Sciences & Geomechanics Abstracts1990, Volume 27, Elsevier, p. 345-352.

Kurz, W., Rabitsch, R., and Hausegger, S., 2007, Formation of fault breccias and cataclastic shear zones within layered carbonates: examples from the Eastern Alps, *in* Proceedings Geophysical Research Abstracts, v. 9, p. 2722.

Kurzawski, R. M., Stipp, M., Niemeijer, A. R., Spiers, C. J., and Behrmann, J. H., 2016, Earthquake nucleation in weak subducted carbonates: Nature Geoscience. v. 9, no. 9, p. 717–722.

Labaume, P., Sheppard, S. M., and Moretti, I., 2001, Fluid-flow in cataclastic thrust fault zones in sandstones, Sub-Andean Zone, southern Bolivia: Tectonophysics, v. 340, no. 3, p. 141-172.

Lamur, A., Kendrick, J., Eggertsson, G., Wall, R., Ashworth, J., and Lavallée, Y., 2017, The permeability of fractured rocks in pressurised volcanic and geothermal systems: Scientific Reports, v. 7, no. 1, p. 6173.

Langford, R., and Clinton, C., 2004, In situ lift-out using a FIB-SEM system: Micron, v. 35, no. 7, p. 607-611.

Lazar, B., and Holland, H. D., 1988, The analysis of fluid inclusions in halite: Geochimica et Cosmochimica Acta, v. 52, no. 2, p. 485-490.

Lea, D.W., 2014, Elemental and Isotopic Proxies of Past Ocean Temperatures. In: Holland H.D. and Turekian K.K. (eds.) Treatise on Geochemistry, Second Edition, v. 8, p. 373-397.

Leclère, H., Faulkner, D., Wheeler, J., and Mariani, E., 2016, Permeability control on transient slip-weakening during gypsum dehydration: Implications for earthquakes in subduction zones: Earth and Planetary Science Letters, v. 442, p. 1-12.

Lee, H. P., Olson, J. E., Holder, J., Gale, J. F., and Myers, R. D., 2015, The interaction of propagating opening mode fractures with preexisting discontinuities in shale: Journal of Geophysical Research: Solid Earth, v. 120, no. 1, p. 169-181.

Lee, Y.-J., Morse, J. W., and Wiltschko, D. V., 1996, An experimentally verified model for calcite precipitation in veins: Chemical Geology, v. 130, no. 3, p. 203-215.

Leeder, M., Collier, R., Abdul Aziz, L., Trout, M., Ferentinos, G., Papatheodorou, G., and Lyberis, E., 2002, Tectono-sedimentary processes along an active marine/lacustrine half-graben margin: Alkyonides Gulf, E. Gulf of Corinth, Greece: Basin Research, v. 14, no. 1, p. 25-41.

Leeder, M., Portman, C., Andrews, J., Collier, R. L., Finch, E., Gawthorpe, R., McNeill, L., Perez-Arlucea, M., and Rowe, P., 2005, Normal faulting and crustal deformation, Alkyonides Gulf and Perachora peninsula, eastern Gulf of Corinth rift, Greece: Journal of the Geological Society, v. 162, no. 3, p. 549-561.

Leeder, M., Seger, M., and Stark, C., 1991a, Sedimentation and tectonic geomorphology adjacent to major active and inactive normal faults, southern Greece: Journal of the Geological Society, v. 148, no. 2, p. 331-343.

Leeder, M., Seger, M., and Stark, C., 1991b, Sedimentology and tectonic geomorphology adjacent to active and inactive normal faults in the Megara basin and Alkyonides Gulf, Central Greece: Journal of the Geological Society, London, v. 148, p. 331-343.

Leeman, J., Saffer, D., Scuderi, M., and Marone, C., 2016, Laboratory observations of slow earthquakes and the spectrum of tectonic fault slip modes: Nature Communications, v. 7, 11104.

Lehner, F. K., 1995, A model for intergranular pressure solution in open systems: Tectonophysics, v. 245, no. 3, p. 153-170.

Linde, A. T., Gladwint, M. T., Johnston, M. J., Gwythert, R. L., and Bilham, R. G., 1996, A slow earthquake sequence on the San Andreas fault: Nature, v. 383, p. 5.

Liotta, M., Bellissimo, S., Favara, R., and Valenza, M., 2008, Isotopic composition of single rain events in the central Mediterranean: Journal of Geophysical Research: Atmospheres, v. 113, no. D16.

Lister, G. S., and Baldwin, S. L., 1993, Plutonism and the origin of metamorphic core complexes: Geology, v. 21, no. 7, p. 607-610.

Lister, G. S., and Davis, G. A., 1989, The origin of metamorphic core complexes and detachment faults formed during Tertiary continental extension in the northern Colorado River region, USA: Journal of Structural Geology, v. 11, no. 1-2, p. 65-94.

Lockner, D., Byerlee, J., Kuksenko, V., Ponomarev, A., and Sidorin, A., 1991, Quasi-static fault growth and shear fracture energy in granite: Nature, v. 350, no. 6313, p. 39-42.

Lockner, D. A., and Beeler, N. M., 2002, Rock failure and earthquakes: International Geophysics Series, v. 81, no. A, p. 505-538.

Losh, S., 1997, Stable isotope and modeling studies of fluid-rock interaction associated with the Snake Range and Mormon Peak detachment faults, Nevada: Geological Society of America Bulletin, v. 109, no. 3, p. 300-323.

Main, I. G., and Meredith, P. G., 1991, Stress corrosion constitutive laws as a possible mechanism of intermediate-term and short-term seismic quiescence: Geophysical journal international, v. 107, no. 2, p. 363-372.

Maineri, C., Benvenuti, M., Costagliola, P., Dini, A., Lattanzi, P., Ruggieri, G., and Villa, I. M., 2003, Sericitic alteration at the La Crocetta deposit (Elba Island, Italy): interplay between magmatism, tectonics and hydrothermal activity: Mineralium Deposita, v. 38, no. 1, p. 67-86.

Mair, K., and Marone, C., 1999, Friction of simulated fault gouge for a wide range of velocities and normal stresses: Journal of Geophysical Research: Solid Earth, v. 104, no. B12, p. 28899-28914.

Mancktelow, N. S., and Pennacchioni, G., 2005, The control of precursor brittle fracture and fluid–rock interaction on the development of single and paired ductile shear zones: Journal of Structural Geology, v. 27, no. 4, p. 645-661.

Marone, C., 1997, On the rate of frictional healing and the constitutive law for time-and slip-dependent friction: International Journal of Rock Mechanics and Mining Sciences, v. 34, no. 3-4, p. 181-187.

Marone, C., 1998, The effect of loading rate on static friction and the rate of fault healing during the earthquake cycle: Nature, v. 391, no. 6662, p. 69.

Marone, C., Raleigh, C. B., and Scholz, C., 1990, Frictional behavior and constitutive modeling of simulated fault gouge: Journal of Geophysical Research: Solid Earth, v. 95, no. B5, p. 7007-7025.

Marone, C., and Saffer, D. M., 2007, Fault friction and the upper transition from seismic to aseismic faulting: The Seismogenic Zone of Subduction Thrust Faults, p. 346-369.

Marone, C., and Scholz, C., 1988, The depth of seismic faulting and the upper transition from stable to unstable slip regimes: Geophysical Research Letters, v. 15, no. 6, p. 621-624.

Marquer, D., and Burkhard, M., 1992, Fluid circulation, progressive deformation and mass-transfer processes in the upper crust: the example of basement-cover relationships in

the External Crystalline Massifs, Switzerland: Journal of Structural Geology, v. 14, no. 8, p. 1047-1057.

Marshall, D. J., and Mariano, A. N., 1988, Cathodoluminescence of geological materials, Taylor & Francis.

Matsuzawa, T., Asano, Y., and Obara, K., 2015, Very low frequency earthquakes off the Pacific coast of Tohoku, Japan: Geophysical Research Letters, v. 42, no. 11, p. 4318-4325.

McCaffrey, R., Wallace, L. M., and Beavan, J., 2008, Slow-slip and frictional transition at low temperature at the Hikurangi subduction zone: Nature Geoscience, v. 1, no. 5, p. 316-320.

McCaig, A. M., Wayne, D. M., Marshall, J. D., Banks, D., and Henderson, I., 1995, Isotopic and fluid inclusion studies of fluid movement along the Gavarnie Thrust, central Pyrenees; reaction fronts in carbonate mylonites: American Journal of Science, v. 295, no. 3, p. 309-343.

McKenzie, D., 1972, Active tectonics of the Mediterranean region: Geophysical Journal of the Royal Astronomical Society, v. 30, no. 2, p. 109-185.

Melosh, B. L., Rowe, C. D., Gerbi, C., Bate, C. E., and Shulman, D., 2016, The spin zone: Transient mid-crust permeability caused by coseismic brecciation: Journal of Structural Geology, v. 87, p. 47-63.

Michie, E., Haines, T., Healy, D., Neilson, J., Timms, N., and Wibberley, C., 2014, Influence of carbonate facies on fault zone architecture: Journal of Structural Geology, v. 65, p. 82-99.

Miller, S. A., Collettini, C., Chiaraluce, L., Cocco, M., Barchi, M., and Kaus, B. J., 2004, Aftershocks driven by a high-pressure CO2 source at depth: Nature, v. 427, no. 6976, p. 724.

Minissale, A., 2004, Origin, transport and discharge of CO2 in central Italy: Earth-Science Reviews, v. 66, no. 1-2, p. 89-141.

Minissale, A., Magro, G., Martinelli, G., Vaselli, O., and Tassi, G., 2000, Fluid geochemical transect in the Northern Apennines (central-northern Italy): fluid genesis and migration and tectonic implications: Tectonophysics, v. 319, no. 3, p. 199-222.

Mirabella, F., Boccali, V., and Barchi, M., 2005, Segmentation and interaction of normal faults within the Colfiorito fault system (central Italy): Geological Society, London, Special Publications, v. 243, no. 1, p. 25-36.

Mirabella, F., Ciaccio, M., Barchi, M., and Merlini, S., 2004, The Gubbio normal fault (Central Italy): geometry, displacement distribution and tectonic evolution: Journal of Structural Geology, v. 26, no. 12, p. 2233-2249.

Mitchell, E., Fialko, Y., and Brown, K., 2013, Temperature dependence of frictional healing of Westerly granite: Experimental observations and numerical simulations: Geochemistry, Geophysics, Geosystems, v. 14, no. 3, p. 567-582.

Mitchell, T., Renner, J., and Sibson, R., 2011, Experimental fault reactivation on favourably and unfavourably oriented faults, *in* Proceedings AGU Fall Meeting Abstracts.

Mogi, K., 1966, Pressure dependence of rock strength and transition from brittle to ductile flow: Bull. Earthq. Res. Inst., Univ. Tokyo, v. 44, p. 215-232.

Mogi, K., 1972, Fracture and flow of rocks, Developments in Geotectonics, Volume 4, Elsevier, p. 541-568.

Mogi, K., 1974, On the pressure dependence of strength of rocks and the Coulomb fracture criterion: Tectonophysics, v. 21, no. 3, p. 273-285.

Moore, D. E., and Lockner, D. A., 2004, Crystallographic controls on the frictional behavior of dry and water-saturated sheet structure minerals: Journal of Geophysical Research: Solid Earth, v. 109, no. B3.

Moore, D. E., and Lockner, D. A., 2008, Talc friction in the temperature range 25–400 C: Relevance for fault-zone weakening: Tectonophysics, v. 449, no. 1-4, p. 120-132.

Moretti, I., Sakellariou, D., Lykousis, V., and Micarelli, L., 2003, The Gulf of Corinth: an active half graben?: Journal of Geodynamics, v. 36, no. 1, p. 323-340.

Morewood, N., and Roberts, G., 2002, Surface observations of active normal fault propagation: implications for growth: Journal of the Geological Society, v. 159, no. 3, p. 263-272.

Morrow, C., Moore, D. E., and Lockner, D., 2000, The effect of mineral bond strength and adsorbed water on fault gouge frictional strength: Geophysical Research Letters, v. 27, no. 6, p. 815-818.

Musumeci, G., Mazzarini, F., and Cruden, A., 2015, The Zuccale Fault, Elba Island, Italy: a new perspective from fault architecture: Tectonics, v. 34, no. 6, p. 1195-1218.

Nakata, R., Hino, H., Kuwatani, T., Yoshioka, S., Okada, M., and Hori, T., 2017, Discontinuous boundaries of SSEs beneath the Bungo Channel, southwest Japan: Scientific reports, v. 7, no. 1, p. 6129.

Nakatani, M., and Scholz, C. H., 2004, Frictional healing of quartz gouge under hydrothermal conditions: 1. Experimental evidence for solution transfer healing mechanism: Journal of Geophysical Research: Solid Earth (1978–2012), v. 109, no. B7.

Nicolas, A., Fortin, J., Regnet, J., Dimanov, A., and Guéguen, Y., 2016, Brittle and semi-brittle behaviours of a carbonate rock: influence of water and temperature: Geophysical Journal International, v. 206, no. 1, p. 438-456.

Nielsen, S., 2017, From slow to fast faulting: recent challenges in earthquake fault mechanics, Phil. Trans. R. Soc. A, v. 375.

Niemeijer, A., Marone, C., and Elsworth, D., 2008, Healing of simulated fault gouges aided by pressure solution: Results from rock analogue experiments: Journal of Geophysical Research: Solid Earth, v. 113, no. B4.

Niemeijer, A., and Spiers, C., 2006, Velocity dependence of strength and healing behaviour in simulated phyllosilicate-bearing fault gouge: Tectonophysics, v. 427, no. 1-4, p. 231-253.

Niemeijer, A., and Spiers, C., 2007, A microphysical model for strong velocity weakening in phyllosilicate-bearing fault gouges: Journal of Geophysical Research: Solid Earth, v. 112, no. B10.

Numelin, T., Marone, C., and Kirby, E., 2007, Frictional properties of natural fault gouge from a low-angle normal fault, Panamint Valley, California: Tectonics, v. 26, no. 2.

Nur, A., and Byerlee, J. D., 1971, An exact effective stress law for elastic deformation of rock with fluids: Journal of Geophysical Research, v. 76, no. 26, p. 6414-6419.

Oliver, N., 1996, Review and classification of structural controls on fluid-flow during regional metamorphism: Journal of Metamorphic Geology, v. 14, no. 4, p. 477-492.

Olsen, M. P., Scholz, C. H., and Léger, A., 1998, Healing and sealing of a simulated fault gouge under hydrothermal conditions: Implications for fault healing: Journal of Geophysical Research: Solid Earth, v. 103, no. B4, p. 7421-7430.

Parry, W., 1998, Fault-fluid compositions from fluid-inclusion observations and solubilities of fracture-sealing minerals: Tectonophysics, v. 290, no. 1, p. 1-26.

Parsons, T., and Thompson, G. A., 1993, Does magmatism influence low-angle normal faulting?: Geology, v. 21, no. 3, p. 247-250.

Pascucci, V., Merlini, S., and Martini, I. P., 1999, Seismic stratigraphy of the Miocene-Pleistocene sedimentary basins of the Northern Tyrrhenian Sea and western Tuscany (Italy): Basin Research, v. 11, no. 4, p. 337-356.

Paterson, M., 1958, Experimental deformation and faulting in Wombeyan marble: Geological Society of America Bulletin, v. 69, no. 4, p. 465-476.

Paterson, M. S., and Wong, T.-f., 2005, Experimental rock deformation-the brittle field, Springer.

Paton, D. A., and Underhill, J. R., 2004, Role of crustal anisotropy in modifying the structural and sedimentological evolution of extensional basins: the Gamtoos Basin, South Africa: Basin Research, v. 16, no. 3, p. 339-359.

Peccerillo, A., and Panza, G., 1999, Upper mantle domains beneath central-southern Italy: petrological, geochemical and geophysical constraints: Pure and Applied Geophysics, v. 156, no. 3, p. 421-443.

Peng, Z., and Gomberg, J., 2010, An integrated perspective of the continuum between earthquakes and slow-slip phenomena: Nature Geoscience, v. 3, no. 9, p. 599-607.

Phillips, T. B., Jackson, C. A., Bell, R. E., Duffy, O. B., and Fossen, H., 2016, Reactivation of intrabasement structures during rifting: A case study from offshore southern Norway: Journal of Structural Geology, v. 91, p. 54-73.

Pik, R., and Marty, B., 2009, Helium isotopic signature of modern and fossil fluids associated with the Corinth rift fault zone (Greece): implication for fault connectivity in the lower crust: Chemical Geology, v. 266, no. 1-2, p. 67-75.

Pili, E., Poitrasson, F., and Gratier, J.-P., 2002, Carbon–oxygen isotope and trace element constraints on how fluids percolate faulted limestones from the San Andreas Fault system: partitioning of fluid sources and pathways: Chemical Geology, v. 190, no. 1, p. 231-250.

Pollet, J., and Burns, S., 1977, Thermally activated crack propagation—theory: International Journal of Fracture, v. 13, no. 5, p. 667-679.

Poppe, L., Paskevich, V., Hathaway, J., and Blackwood, D., 2001, A laboratory manual for X-ray powder diffraction: US Geological Survey Open-File Report, v. 1, no. 041, p. 1-88.

Prezbindowski, D. R., 1985, Burial cementation—is it important? A case study, Stuart City Trend, south central Texas, SEPM, v. 36, p. 241-264.

Price, N. J., 1966, Fault and joint development: in brittle and semi-brittle rock, Pergamon, London.

Price, N. J., and Cosgrove, J. W., 1990, Analysis of geological structures, Cambridge University Press.

Proffett Jr, J. M., 1977, Cenozoic geology of the Yerington district, Nevada, and implications for the nature and origin of Basin and Range faulting: Geological Society of America Bulletin, v. 88, no. 2, p. 247-266.

Rabinowicz, E., and Tanner, R., 1966, Friction and wear of materials: Journal of Applied Mechanics, v. 33, p. 479.

Renard, F., Bernard, D., Thibault, X., and Boller, E., 2004, Synchrotron 3D microtomography of halite aggregates during experimental pressure solution creep and evolution of the permeability: Geophysical Research Letters, v. 31, no. 7.

Rietbrock, A., Tiberi, C., Scherbaum, F., and Lyon-Caen, H., 1996, Seismic slip on a low angle normal fault in the Gulf of Corinth: Evidence from high-resolution cluster analysis of microearthquakes: Geophysical Research Letters, v. 23, no. 14, p. 1817-1820.

Roberts, G. P., and Ganas, A., 2000, Fault-slip directions in central and southern Greece measured from striated and corrugated fault planes: Comparison with focal mechanism and geodetic data: Journal of Geophysical Research: Solid Earth, v. 105, no. B10, p. 23443-23462.

Roberts, G. P., and Gawthorpe, R. L., 1995, Strike variation in deformation and diagenesis along segmented normal faults: an example from the eastern Gulf of Corinth, Greece: Geological Society, London, Special Publications, v. 80, no. 1, p. 57-74.

Roberts, S., and Jackson, J., 1991, Active normal faulting in central Greece: an overview: Geological Society, London, Special Publications, v. 56, no. 1, p. 125-142.

Rodríguez, K., and Araujo, M., 2006, Temperature and pressure effects on zeta potential values of reservoir minerals: Journal of colloid and interface science, v. 300, no. 2, p. 788-794.

Rosenbaum, J., and Sheppard, S., 1986, An isotopic study of siderites, dolomites and ankerites at high temperatures: Geochimica et cosmochimica acta, v. 50, no. 6, p. 1147-1150.

Rossetti, F., Tecce, F., Billi, A., and Brilli, M., 2007, Patterns of fluid-flow in the contact aureole of the Late Miocene Monte Capanne pluton (Elba Island, Italy): the role of structures and rheology: Contributions to Mineralogy and Petrology, v. 153, no. 6, p. 743-760.

Rowe, K., and Rutter, E., 1990, Palaeostress estimation using calcite twinning: experimental calibration and application to nature: Journal of Structural Geology, v. 12, no. 1, p. 1-17.

Royden, L., Patacca, E., and Scandone, P., 1987, Segmentation and configuration of subducted lithosphere in Italy: An important control on thrust-belt and foredeep-basin evolution: Geology, v. 15, no. 8, p. 714-717.

Rubino, V., Rosakis, A., and Lapusta, N., 2017, Understanding dynamic friction through spontaneously evolving laboratory earthquakes: Nature Communications, v. 8, p. 15991.

Ruina, A., 1983, Slip instability and state variable friction laws: Journal of Geophysical Research: Solid Earth, v. 88, no. B12, p. 10359-10370.

Rutter, E., 1976, A Discussion on natural strain and geological structure-The kinetics of rock deformation by pressure solution: Phil. Trans. R. Soc. Lond. A, v. 283, no. 1312, p. 203-219.

Rutter, E., 1983, Pressure solution in nature, theory and experiment: Journal of the Geological Society, v. 140, no. 5, p. 725-740.

Rutter, E., 1986, On the nomenclature of mode of failure transitions in rocks: Tectonophysics, v. 122, no. 3-4, p. 381-387.

Rutter, E., and Hackston, A., 2017, On the effective stress law for rock-on-rock frictional sliding, and fault slip triggered by means of fluid injection: Phil. Trans. R. Soc. A, v. 375, no. 2103.

Rutter, E., Llana-Funez, S., and Brodie, K., 2009, Dehydration and deformation of intact cylinders of serpentinite: Journal of Structural Geology, v. 31, no. 1, p. 29-43.

Saffer, D. M., Frye, K. M., Marone, C., and Mair, K., 2001, Laboratory results indicating complex and potentially unstable frictional behavior of smectite clay: Geophysical Research Letters, v. 28, no. 12, p. 2297-2300.

Saffer, D. M., and Marone, C., 2003, Comparison of smectite-and illite-rich gouge frictional properties: application to the updip limit of the seismogenic zone along subduction megathrusts: Earth and Planetary Science Letters, v. 215, no. 1, p. 219-235.

Saffer, D. M., and McKiernan, A. W., 2005, Permeability of underthrust sediments at the Costa Rican subduction zone: Scale dependence and implications for dewatering: Geophysical Research Letters, v. 32, no. 2.

Saffer, D. M., Silver, E. A., Fisher, A. T., Tobin, H., and Moran, K., 2000, Inferred pore fluid pressures at the Costa Rica subduction zone: implications for dewatering processes: Earth and Planetary Science Letters, v. 177, no. 3, p. 193-207.

Saffer, D. M., and Wallace, L. M., 2015, The frictional, hydrologic, metamorphic and thermal habitat of shallow slow earthquakes: Nature Geoscience, v. 8, p. 594–600.

Samson, I., Anderson, A., and Marshall, D. D., 2003, Fluid inclusions: analysis and interpretation, Mineralogical Association of Canada.

Savage, S. B., 1984, The mechanics of rapid granular flows, Advances in applied mechanics, Volume 24, Elsevier, p. 289-366.

Schleicher, A., Van der Pluijm, B., and Warr, L., 2010, Nanocoatings of clay and creep of the San Andreas fault at Parkfield, California: Geology, v. 38, no. 7, p. 667-670.

Schleicher, A., Van der Pluijm, B., and Warr, L., 2012, Chlorite-smectite clay minerals and fault behavior: New evidence from the San Andreas Fault Observatory at Depth (SAFOD) core: Lithosphere, v. 4, no. 3, p. 209-220.

Scholle, P. A., and Ulmer-Scholle, D. S., 2003, A Color Guide to the Petrography of Carbonate Rocks: Grains, Textures, Porosity, Diagenesis, AAPG Memoir 77, AAPG.

Scholz, C., 1988, The brittle-plastic transition and the depth of seismic faulting: Geologische Rundschau, v. 77, no. 1, p. 319-328.

Scholz, C. H., 1998, Earthquakes and friction laws: Nature, v. 391, no. 6662, p. 37-42.

Scholz, C. H., 2002, The mechanics of earthquakes and faulting, Cambridge University Press.

Scholz, C. H., Sykes, L. R., and Aggarwal, Y. P., 1973, Earthquake prediction: a physical basis: Science, v. 181, no. 4102, p. 803-810.

Schön, J. H., 2015, Physical properties of rocks: Fundamentals and principles of petrophysics, Elsevier.

Scrocca, D., Carminati, E., and Doglioni, C., 2005, Deep structure of the southern Apennines, Italy: Thin-skinned or thick-skinned?: Tectonics, v. 24, no. 3.

Scuderi, M., Marone, C., Tinti, E., Di Stefano, G., and Collettini, C., 2016, Precursory changes in seismic velocity for the spectrum of earthquake failure modes: Nature Geoscience, v. 9, p. 695–700.

Segall, P., Rubin, A. M., Bradley, A. M., and Rice, J. R., 2010, Dilatant strengthening as a mechanism for SSEs: Journal of Geophysical Research: Solid Earth, v. 115, no. B12.

Serri, G., Innocenti, F., and Manetti, P., 1993, Geochemical and petrological evidence of the subduction of delaminated Adriatic continental lithosphere in the genesis of the Neogene-Quaternary magmatism of central Italy: Tectonophysics, v. 223, no. 1-2, p. 117-147.

Shaw, R. P., 2005, Understanding the micro to macro behaviour of rock-fluid systems, Geological Society of London.

Shelly, D. R., Beroza, G. C., Ide, S., and Nakamula, S., 2006, Low-frequency earthquakes in Shikoku, Japan, and their relationship to episodic tremor and slip: Nature, v. 442, no. 7099, p. 188.

Shimamoto, T., 1986, Transition between frictional slip and ductile flow for halite shear zones at room temperature: Science, v. 231, no. 4739, p. 711-714.

Shimamoto, T., and Logan, J. M., 1981, Effects of simulated fault gouge on the sliding behavior of Tennessee sandstone: nonclay gouges: Journal of Geophysical Research: Solid Earth, v. 86, no. B4, p. 2902-2914.

Shimamoto, T., and Logan, J. M., 1984, Laboratory friction experiments and natural earthquakes: an argument for long-term tests: Tectonophysics, v. 109, no. 3, p. 165-175.

Sibson, R., 1977, Fault rocks and fault mechanisms: Journal of the Geological Society, v. 133, no. 3, p. 191-213.

Sibson, R., 1981, Fluid-flow accompanying faulting: field evidence and models: Earthquake prediction, p. 593-603.

Sibson, R., 1985, A note on fault reactivation: Journal of Structural Geology, v. 7, no. 6, p. 751-754.

Sibson, R., 1986a, Brecciation processes in fault zones: inferences from earthquake rupturing: Pure and Applied Geophysics, v. 124, no. 1-2, p. 159-175.

Sibson, R., 1986b, Earthquakes and rock deformation in crustal fault zones: Annual Review of Earth and Planetary Sciences, v. 14, no. 1, p. 149-175.

Sibson, R., 1992, Implications of fault-valve behaviour for rupture nucleation and recurrence: Tectonophysics, v. 211, no. 1, p. 283-293.

Sibson, R., 1994, Crustal stress, faulting and fluid-flow: Geological Society, London, Special Publications, v. 78, no. 1, p. 69-84.

Sibson, R., 1996, Structural permeability of fluid-driven fault-fracture meshes: Journal of Structural Geology, v. 18, no. 8, p. 1031-1042.

Sibson, R., 2000, Fluid involvement in normal faulting: Journal of Geodynamics, v. 29, no. 3, p. 469-499.

Sibson, R., 2002, Geology of the crustal earthquake source: International Geophysics Series, v. 81, no. A, p. 455-474.

Sibson, R., 2003, Thickness of the seismic slip zone: Bulletin of the Seismological Society of America, v. 93, no. 3, p. 1169-1178.

Sibson, R., Moore, J. M. M., and Rankin, A., 1975, Seismic pumping—a hydrothermal fluid transport mechanism: Journal of the Geological Society, v. 131, no. 6, p. 653-659.

Smith, D. L., and Evans, B., 1984, Diffusional crack healing in quartz: Journal of Geophysical Research: Solid Earth (1978–2012), v. 89, no. B6, p. 4125-4135.

Smith, S., Collettini, C., and Holdsworth, R., 2008, Recognizing the seismic cycle along ancient faults: CO2-induced fluidization of breccias in the footwall of a sealing low-angle normal fault: Journal of Structural Geology, v. 30, no. 8, p. 1034-1046.

Smith, S., Holdsworth, R., and Collettini, C., 2011a, Interactions between LANFs and plutonism in the upper crust: Insights from the Island of Elba, Italy: Geological Society of America Bulletin, v. 123, no. 1-2, p. 329-346.

Smith, S., Holdsworth, R., Collettini, C., and Imber, J., 2007, Using footwall structures to constrain the evolution of LANFs: Journal of the Geological Society, v. 164, no. 6, p. 1187-1191.

Smith, S., Holdsworth, R., Collettini, C., and Pearce, M., 2011b, The microstructural character and mechanical significance of fault rocks associated with a continental low-angle normal fault: the Zuccale Fault, Elba Island, Italy: Geological Society, London, Special Publications, v. 359, no. 1, p. 97-113.

Sornette, D., 1999, Earthquakes: from chemical alteration to mechanical rupture: Physics Reports, v. 313, no. 5, p. 237-292.

Stahl, W. J., 1977, Carbon and nitrogen isotopes in hydrocarbon research and exploration: Chemical Geology, v. 20, p. 121-149.

Stesky, R., 1978, Rock friction-effect of confining pressure, temperature, and pore fluid pressure: pure and applied geophysics, v. 116, no. 4-5, p. 690-704.

Stesky, R., Brace, W., Riley, D., and Robin, P.-Y., 1974, Friction in faulted rock at high temperature and pressure: Tectonophysics, v. 23, no. 1-2, p. 177-203.

Storti, F., Billi, A., and Salvini, F., 2003, Particle size distributions in natural carbonate fault rocks: insights for non-self-similar cataclasis: Earth and Planetary Science Letters, v. 206, no. 1, p. 173-186.

Streit, J. E., and Hillis, R. R., 2004, Estimating fault stability and sustainable fluid pressures for underground storage of CO 2 in porous rock: Energy, v. 29, no. 9, p. 1445-1456.

Stuart, W. D., 1974, Diffusionless dilatancy model for earthquake precursors: Geophysical Research Letters, v. 1, no. 6, p. 261-264.

Stumm, W., and Morgan, J. J., 1981, Aquatic chemistry: an introduction emphasizing chemical equilibria in natural waters, John Wiley.

Sulem, J., and Famin, V., 2009, Thermal decomposition of carbonates in fault zones: Slip-weakening and temperature-limiting effects: Journal of Geophysical Research: Solid Earth, v. 114, no. B3.

Tămaş, C. l. G., and Milėsi, J. P., 2002, Hydrovolcanic breccia pipe structures-General features and genetic criteria. I. Phreatomagmatic breccias: Studia UBB Geologia, v. 47, no. 1, p. 127-147.

Taylor, B., Weiss, J. R., Goodliffe, A. M., Sachpazi, M., Laigle, M., and Hirn, A., 2011, The structures, stratigraphy and evolution of the Gulf of Corinth rift, Greece: Geophysical Journal International, v. 185, no. 3, p. 1189-1219.

Taylor, H. P., and Turi, B., 1976, High-18 O igneous rocks from the Tuscan magmatic province, Italy: Contributions to Mineralogy and Petrology, v. 55, no. 1, p. 33-54.

Taymaz, T., Yilmaz, Y., and Dilek, Y., 2007, The geodynamics of the Aegean and Anatolia: introduction: Geological Society, London, Special Publications, v. 291, no. 1, p. 1-16.

Tenthorey, E., Cox, S. F., and Todd, H. F., 2003, Evolution of strength recovery and permeability during fluid–rock reaction in experimental fault zones: Earth and Planetary Science Letters, v. 206, no. 1, p. 161-172.

Tesei, T., Collettini, C., Barchi, M. R., Carpenter, B. M., and Di Stefano, G., 2014, Heterogeneous strength and fault zone complexity of carbonate-bearing thrusts with possible implications for seismicity: Earth and Planetary Science Letters, v. 408, p. 307-318.

Tesei, T., Collettini, C., Viti, C., and Barchi, M. R., 2013, Fault architecture and deformation mechanisms in exhumed analogues of seismogenic carbonate-bearing thrusts: Journal of Structural Geology, v. 55, p. 167-181.

Tjioe, M., and Borja, R. I., 2015, On the pore-scale mechanisms leading to brittle and ductile deformation behavior of crystalline rocks: International Journal for Numerical and Analytical Methods in Geomechanics, v. 39, no. 11, p. 1165-1187.

Trütner, S., Hüpers, A., Ikari, M. J., Yamaguchi, A., and Kopf, A. J., 2015, Lithification facilitates frictional instability in argillaceous subduction zone sediments: Tectonophysics, v. 665, p. 177-185.

Tse, S. T., and Rice, J. R., 1986, Crustal earthquake instability in relation to the depth variation of frictional slip properties: Journal of Geophysical Research: Solid Earth, v. 91, no. B9, p. 9452-9472.

Tucker, M. E., and Wright, V. P., 1990, Diagenetic processes, products and environments: Carbonate sedimentology, p. 314-364.

Ujiie, K., Tanaka, H., Saito, T., Tsutsumi, A., Mori, J. J., Kameda, J., Brodsky, E. E., Chester, F. M., Eguchi, N., and Toczko, S., 2013, Low coseismic shear stress on the Tohoku-Oki megathrust determined from laboratory experiments: Science, v. 342, no. 6163, p. 1211-1214.

Vannucchi, P., Ranero, C. R., Galeotti, S., Straub, S. M., Scholl, D. W., and McDougall-Ried, K., 2003, Fast rates of subduction erosion along the Costa Rica Pacific margin:

Implications for nonsteady rates of crustal recycling at subduction zones: Journal of Geophysical Research: Solid Earth (1978–2012), v. 108, no. B11.

Verberne, B., Spiers, C., Niemeijer, A., De Bresser, J., De Winter, D., and Plümper, O., 2014, Frictional properties and microstructure of calcite-rich fault gouges sheared at sub-seismic sliding velocities: Pure and Applied Geophysics, v. 171, no. 10, p. 2617-2640.

Verberne, B. A., 2015, Strength, stability, and microstructure of simulated calcite faults sheared under laboratory conditions spanning the brittle-plastic transition, UU Dept. of Earth Sciences. [PhD thesis]

Verberne, B. A., de Bresser, J. H., Niemeijer, A. R., Spiers, C. J., de Winter, D. M., and Plümper, O., 2013, Nanocrystalline slip zones in calcite fault gouge show intense crystallographic preferred orientation: Crystal plasticity at sub-seismic slip rates at 18–150 C: Geology, v. 41, no. 8, p. 863-866.

Verberne, B. A., He, C., and Spiers, C. J., 2010, Frictional properties of sedimentary rocks and natural fault gouge from the Longmen Shan fault zone, Sichuan, China: Bulletin of the Seismological Society of America, v. 100, no. 5B, p. 2767-2790.

Virgo, S., Abe, S., and Urai, J. L., 2013, Extension fracture propagation in rocks with veins: Insight into the crack-seal process using Discrete Element Method modeling: Journal of Geophysical Research: Solid Earth, v. 118, no. 10, p. 5236-5251.

Voorn, M., Exner, U., Barnhoorn, A., Baud, P., and Reuschlé, T., 2015, Porosity, permeability and 3D fracture network characterisation of dolomite reservoir rock samples: Journal of Petroleum Science and Engineering, v. 127, p. 270-285.

Wang, W., and Scholz, C. H., 1994, Wear processes during frictional sliding of rock: A theoretical and experimental study: Journal of Geophysical Research: Solid Earth, v. 99, no. B4, p. 6789-6799.

Warren, B. E., 1969, X-ray Diffraction, Courier Corporation.

Wei, Y., and Anand, L., 2008, On micro-cracking, inelastic dilatancy, and the brittle-ductile transition in compact rocks: A micro-mechanical study: International Journal of Solids and Structures, v. 45, no. 10, p. 2785-2798.

Wernicke, B., 1995, Low-angle normal faults and seismicity: A review: Journal of Geophysical Research: Solid Earth, v. 100, no. B10, p. 20159-20174.

Wernicke, B., and Axen, G. J., 1988, On the role of isostasy in the evolution of normal fault systems: Geology, v. 16, no. 9, p. 848-851.

Westaway, R., 1999, The mechanical feasibility of low-angle normal faulting: Tectonophysics, v. 308, no. 4, p. 407-443.

Westerman, D., Dini, A., Innocenti, F., and Rocchi, S., 2004, Rise and fall of a nested Christmas-tree laccolith complex, Elba Island, Italy: Geological Society, London, Special Publications, v. 234, no. 1, p. 195-213.

Weyl, P. K., 1959, Pressure solution and the force of crystallization: a phenomenological theory: Journal of Geophysical Research, v. 64, no. 11, p. 2001-2025.

Whipp, P., Jackson, C. A. L., Gawthorpe, R., Dreyer, T., and Quinn, D., 2014, Normal fault array evolution above a reactivated rift fabric; a subsurface example from the northern Horda Platform, Norwegian North Sea: Basin Research, v. 26, no. 4, p. 523-549.

Wibberley, C. A., and Shipton, Z. K., 2010, Fault zones: A complex issue: Journal of Structural Geology, v. 32, no. 11, p. 1554-1556.

Wintsch, R., Christoffersen, R., and Kronenberg, A., 1995, Fluid-rock reaction weakening of fault zones: Journal of Geophysical Research: Solid Earth, v. 100, no. B7, p. 13021-13032.

Woodcock, N., Dickson, J., and Tarasewicz, J., 2007, Transient permeability and reseal hardening in fault zones: evidence from dilation breccia textures: Geological Society, London, Special Publications, v. 270, no. 1, p. 43-53.

Woodcock, N., and Mort, K., 2008, Classification of fault breccias and related fault rocks: Geological Magazine, v. 145, no. 3, p. 435-440.

Woodcock, N., Omma, J., and Dickson, J., 2006, Chaotic breccia along the Dent Fault, NW England: implosion or collapse of a fault void?: Journal of the Geological Society, v. 163, no. 3, p. 431-446.

Wu, W., Reece, J. S., Gensterblum, Y., and Zoback, M. D., 2017, Permeability evolution of slowly slipping faults in shale reservoirs: Geophysical Research Letters, v. 44, no. 22.

Xue, L., Li, H.-B., Brodsky, E. E., Xu, Z.-Q., Kano, Y., Wang, H., Mori, J. J., Si, J.-L., Pei, J.-L., and Zhang, W., 2013, Continuous permeability measurements record healing inside the Wenchuan earthquake fault zone: Science, v. 340, no. 6140, p. 1555-1559.

Yang, D., Cizek, P., Hodgson, P., and Wen, C., 2010, Microstructure evolution and nanograin formation during shear localization in cold-rolled titanium: Acta Materialia, v. 58, no. 13, p. 4536-4548.

Yasuhara, H., Marone, C., and Elsworth, D., 2005, Fault zone restrengthening and frictional healing: The role of pressure solution: Journal of Geophysical Research: Solid Earth, v. 110, no. B6.

Zhang, L., and He, C., 2013, Frictional properties of natural gouges from Longmenshan fault zone ruptured during the Wenchuan Mw7. 9 earthquake: Tectonophysics, v. 594, p. 149-164.

Zhang, L., He, C., Liu, Y., and Lin, J., 2017, Frictional properties of the South China Sea oceanic basalt and implications for strength of the Manila subduction seismogenic zone: Marine Geology, v. 394, p. 16-29.

Zhong, Z., Elsworth, D., and Hu, Y., 2016, Evolution of strength and permeability in stressed fractures with fluid–rock interactions: Pure and Applied Geophysics, v. 173, no. 2, p. 525-536.

Appendix A: Climate indications from carbonate-cemented tubes

Carbonate precipitation can be induced by many different processes, from fault motion to microbiological activity. The textures and geochemical signatures of resulting cements can indicate the original carbonate precipitation trigger, or later processes of recrystallisation/replacement. Carbonate-cemented tubes, found southwest of El Médano, Tenerife, have been previously interpreted as sand injection structures related to earthquake activity. A detailed study of the carbonate cements, including field characterisation, conventional and cathodoluminescence microscopy and stable isotope analyses, constrains the tubes' formation mechanism. The cement textures are characteristic of plant concretions. Furthermore, there are two distinct sizes of carbonate-cemented tubes; large, protruding structures and small bifurcations. The $\delta^{18}O$ and $\delta^{13}C$ values range from -1.6‰ to 0.4‰ V-PDB and -5.4‰ to 0.3‰ respectively in the larger tubes' cement, and -4.6‰ to -2.4‰ and -6.8‰ to -4.9‰ respectively in the smaller tubes' cement. The clear groupings of these isotopic signatures indicate a coupled phytocast (stem cast)- rhizolith (root cast) development mechanism. The presence of these structures and the correct interpretation of their cements' isotopic signatures can be used to infer seasonal climate variations during the Holocene.

A.1 Introduction

Carbonate cements are prevalent in a variety of environments, from hydrocarbon basins to supratidal flats (Harris et al., 1985; Morad, 2009). As precipitation of calcium carbonate can be brought about by numerous factors, i.e., changes in *pH*, changes in the ion concentrate of the solution, changes in temperature (Stumm and Morgan, 1981; Larsen and Chilingarian, 1982), a study of carbonate cements can give valuable information on the migration and chemical evolution of fluids (Thornburg and Suess, 1990), reflective of the hydrologic conditions and the structural controls of cementation at the time of precipitation. Stable oxygen and carbon isotopes analysis can be used to constrain the fluid and carbon sources involved in the cementation process (Hoefs, 2008) and help to discriminate the mechanism of precipitation. Cement textures fingerprint the original cementation mechanism characteristics. In addition, growth patterns and information within crystals can be decoded, revealing the physicochemical conditions of their formation (García-Ruiz and Otálora, 2015). This information can then be utilised to infer the overarching factors controlling cementation, such as climate and tectonics (Tanner, 2010). Indeed, where other indicators are lacking (e.g., lack of widespread calcretes for groundwater analogues (Parker and Sellwood, 1994)) or are easily misconstrued (e.g.,

distinguishing lacustrine deposits from their marine counterparts (Burke and Gerhard, 2000), or fault breccia from karstic breccia), constraining the mechanism of carbonate cementation can help to constrain the formative geological processes. However, it is often challenging to discriminate between different mechanisms of carbonate cementation (e.g., Loope, 2013; Sarkar et al., 2014).

Carbonate-cemented tubes are identified southwest of El Médano, Tenerife, protruding from the beach sands. Ignimbrite interaction with wet sands (Carracedo and Day, 2002; Martin and Nemeth, 2004) and liquefaction related sand injection, induced by overpressured impermeable overlying strata (González de Vallejo et al., 2005) were suggested for their formation, the latter of which is communicated on information boards in the area. Most recently, a 'biogenic origin' has been proposed (Kröchert et al., 2008). In this study, carbon and oxygen stable isotopes and textural analyses are applied to determine the precipitation conditions and identify the fluid and carbon source, which can define the mechanism, and environment, of precipitation. My study suggests a coupled phytocast (plant stem casts)-rhizolith (root casts) formation, which sheds light on the seasonal climatic conditions when they formed.

A.2 Geological setting

Tenerife lies in the Canary archipelago between 28 ^{o}N and 29 ^{o}N and 16 ^{o}W and 17 ^{o}W (Fig. A.1a). The climate is Mediterranean: hot, dry summers with wet, milder winters (Sperling et al. 2004). Tenerife's development is characterised by the growth of three main shield volcanoes, with an eruption history spanning the last 12 Ma (Carracedo and Day, 2002; Guillou et al., 2004). The Canary Islands are considered to be a typical example of a hotspot evolutionary track (Schmincke, 1976, 1982; Carracedo, 1994).

On the southeast corner of Tenerife lies the town of El Médano (Fig. A.1b & A.2a)). The area is a renowned wind surfing resort, thanks to the trade winds which have swept the coastline since the Holocene (Coudé-Gaussen and Rognon, 1993). Southwest of the town of El Médano, in the shadow between Montaña Roja and Montaña Bocinegro on Tenerife's south coast, lies a 200 m^2 dune plain with carbonate-cemented tubes (Fig. A.2) protruding from the sands, identified by Hausen et al. (1956) as delta deposits. At the northern edge of the plain is an outcrop (SO1; Fig. A.2a) which displays several lithologic units of the area (Fig. A.3). At the base of the exposed strata are > 3.0 m thick pumice rich ignimbrite deposits (Carracedo and Day, 2002). Above the ignimbrite is a paleosol, i.e., a compacted soil, of maximum thickness 1.7 m, containing sulphuric clasts of varying angularity, gastropods and embedded scoria. The

paleosol is overlain by sands partially cemented by carbonate (Kröchert et al., 2008), which contain cross-bedding, boring-like holes, and reach a maximum thickness of 2.5m along the outcrop. The sands are dated to 10.081 ± 0.993 ka, as calculated by thermoluminescence dating techniques (González de Vallejo et al., 2005). A thin layer (mm-scale) white calcareous crust, distributed between the structures on the top of the sandstone layer and eroded in places, has been dated by the same methods to 3.490 ±0.473 ka (González de Vallejo et al., 2005).

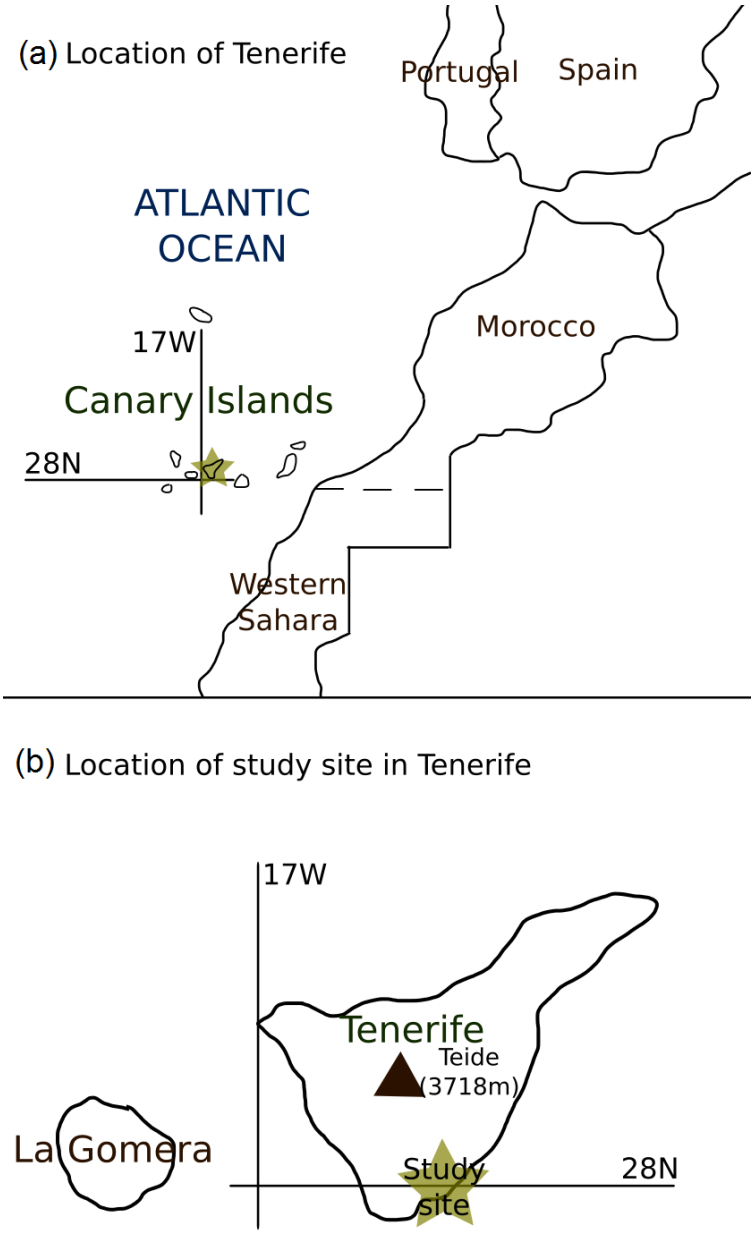


Figure A.1 (a) Geographical map indicating the location of Tenerife. (b) Study site in Tenerife.

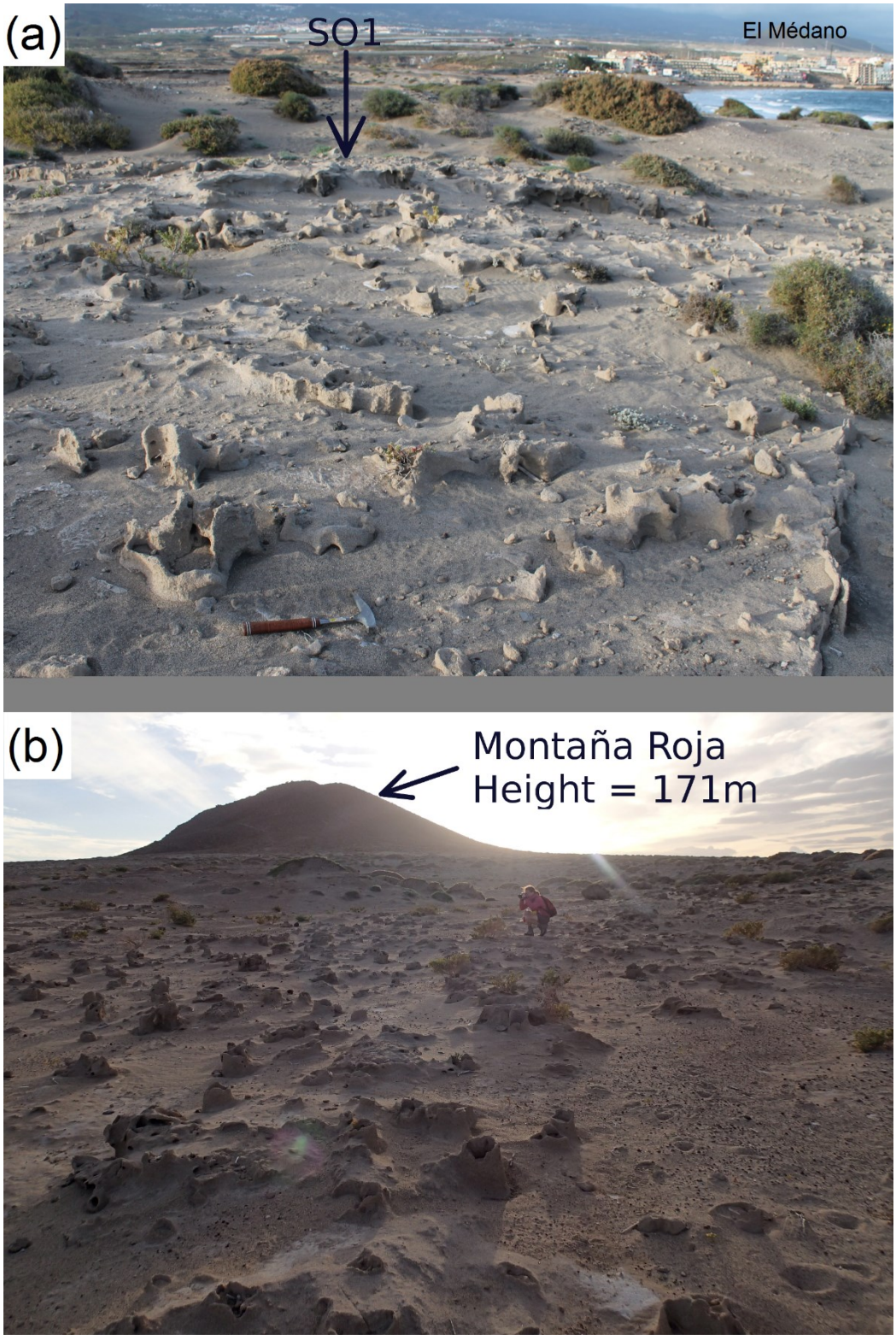


Figure A.2 Carbonate-cemented tubes in study site. (a) Carbonate-cemented tubes position in relation to outcrop SO1 and the town of El Médano; (b) Carbonate-cemented tubes position in relation to Montaña Roja.

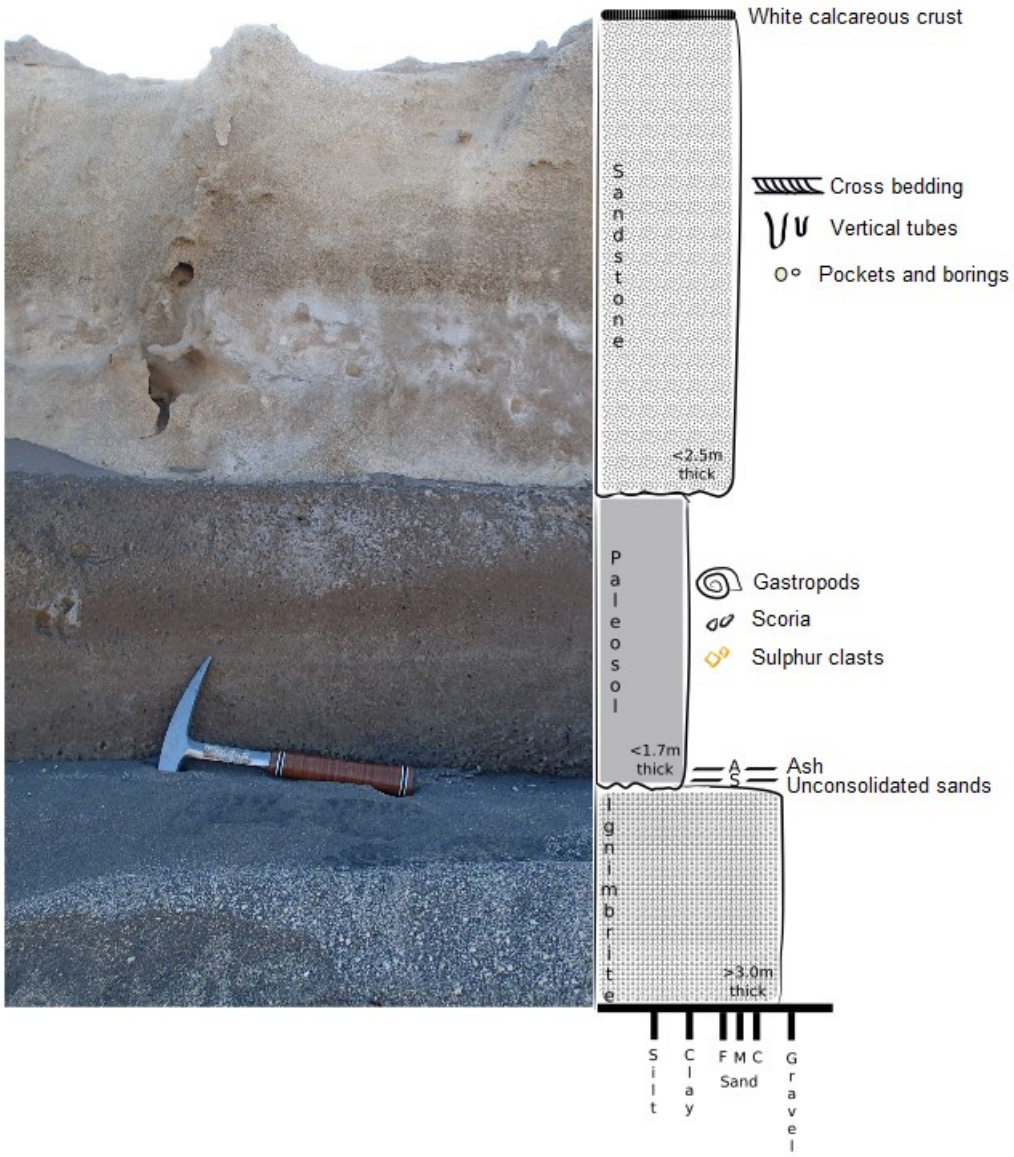


Figure A.3 Lithology of the stratigraphic interval hosting the studied sandstone at outcrop SO1

A.3 Methods

A combination of fieldwork, microscopy (optical and cathodoluminescence (CL)), and stable carbon and oxygen isotope analyses are employed to understand the formation of these carbonate-cemented tubes and hence gain insight into the environment of precipitation during the Holocene. This combination of techniques provides constraints on the diagenetic sequence and the relative timing of cement precipitation, in order to identify the formation mechanism of the carbonate-cemented tubes.

The structures were first characterized by descriptions in the field, their distribution noted, and structures and textures captured in photographs and sample collections. Samples collected in the field (at ~10 m intervals) were used for further microscopic and geochemical analyses.

Microscopic analysis of the host rock and the carbonate-cemented tubes is carried out for identification of mineralogy and distinction between cement generations. A CITL mk5 cold cathodoluminescence stage mounted on a Nikon 50i microscope with a Nikon digital camera is used for both transmitted light and CL microscopy.

Stable carbon and oxygen isotope analysis was carried out on the carbonate cements that lithified the carbonate-cemented tubes. Where possible, individual cement rings within individual tubes were sampled (where individual cement rings are > 1 mm thick so as to avoid mixing). A fresh surface was uncovered at either end of the tubes by sawing both ends. A high-speed drill, fitted with a 0.5 mm drill bit, was used to powder samples of the carbonate cement. Aliquots of 100 μg of the drilled carbonate samples, were reacted with phosphoric acid at a temperature of 100^{o}C using a Gasbench II connected to a ThermoFisher Delta V Plus mass spectrometer. All values are reported in per mil relative to V-PDB. Reproducibility and accuracy was monitored by replicate analysis of laboratory standards calibrated by assigning $\delta^{13}C$ values of +1.95‰ to NBS19 and -46.6‰ to LSVEC and $\delta^{18}O$ values of -2.20‰ to NBS19 and -23.2‰ to NBS18 (Friedman et al., 1982). Standard deviation of the standards was 0.06‰ and 0.05‰ for $\delta^{18}O$ and $\delta^{13}C$ respectively.

The stable oxygen isotopic composition in a cement depends on both the stable oxygen isotopic composition of the fluid and the temperature at which it formed (Friedman and O'Neil, 1977b). A carbonate cement that formed at higher temperature has a more depleted $\delta^{18}O$ signature than a cement formed at lower temperature, assuming they formed from a fluid with the same $\delta^{18}O$ composition. In addition, different types of fluids also have different $\delta^{18}O$ signatures; seawater and brines are the most enriched in $\delta^{18}O$, whereas meteoric fluids have more depleted signatures (Lloyd, 1966; Hoefs, 2008). The carbon isotopic value can be derived from an inorganic source, or an organic one where kinetic fractionation plays an important role (Worden and Smalley, 1996; Hoefs, 2008). Organisms preferentially use lighter isotopic species due to ‘energy costs’, thus ending up with significant fractionation between the substrate and the biological product, resulting in a less depleted isotopic signature (Hollander and McKenzie, 1991; Labaume et al., 2001; Hoefs, 2008).

A.4 Results

I identified two distinct morphologies of carbonate-cemented tubes; (i) taller (average ~15 cm high), wider tubes of > 5 cm diameter (average ~10 cm) (hereby referred to as 'larger tubes'), the majority of which were standalone with an outward tapering umbrella/apron at the base (Fig. A.4a), although some were connected to other vertical tubes via cemented bases (Fig. 4b); and (ii) smaller tubes of < 5 cm diameter (average 1 cm) which extended from the base of the larger tubes, bifurcating at various orientations (15-75^{o}) to the bedding (Fig. A.4c), passing through the sands and into the paleosol below (Fig. A.4d). 25% of the tubes were the former, larger tubes with the remaining 75% comprising these small bifurcating tubes. Some of the larger tubes were infilled with carbonate cement (Fig. A.4e), some had a thin (< 1 mm) cement coating in their internal rim (Fig. A.4f), whilst others had no cement coating visible (Fig. A.4g). The small tubes had varying degrees of cement infill; some had a ~3 mm thick rim coating the inside of the tube (Fig. A.4h) whilst others were completely infilled with carbonate cement (Fig. A.4i). Within some of the small tubes there are individual cement rings of ~1 mm. Each cement is hereafter referred to as follows; the cement between the sand grains in the larger structures is 'large tube host rock cement' = LTHC, the cement infilling the large tubes (e.g., Fig. A.4e) is 'large tube internal cement' = LTIC, the cement that is that is between the sand grains in the smaller tubes is 'small tube host rock cement' = STHC, and the cement infilling the small tubes is 'small tube internal cement' = STIC (e.g., Fig. A.4i). In addition, there were linear cemented features that are standalone or intersected by a tube (Fig. A.4j), and there was also a white calcareous crust interspersed through the carbonate-cemented tubes (Fig. A.4k). Living plants could be found stabilising the sands surrounding the tubes on the uncemented dunes (Fig. A.4l).

The overall distribution, orientation and size of the carbonate-cemented tubes showed no distinct pattern across the main site from outcrop SO1, although they were generally grouped into dense groups of tubes of ~5 m^2. The linear cemented features (Fig. A.4j) also displayed no preferred orientation.

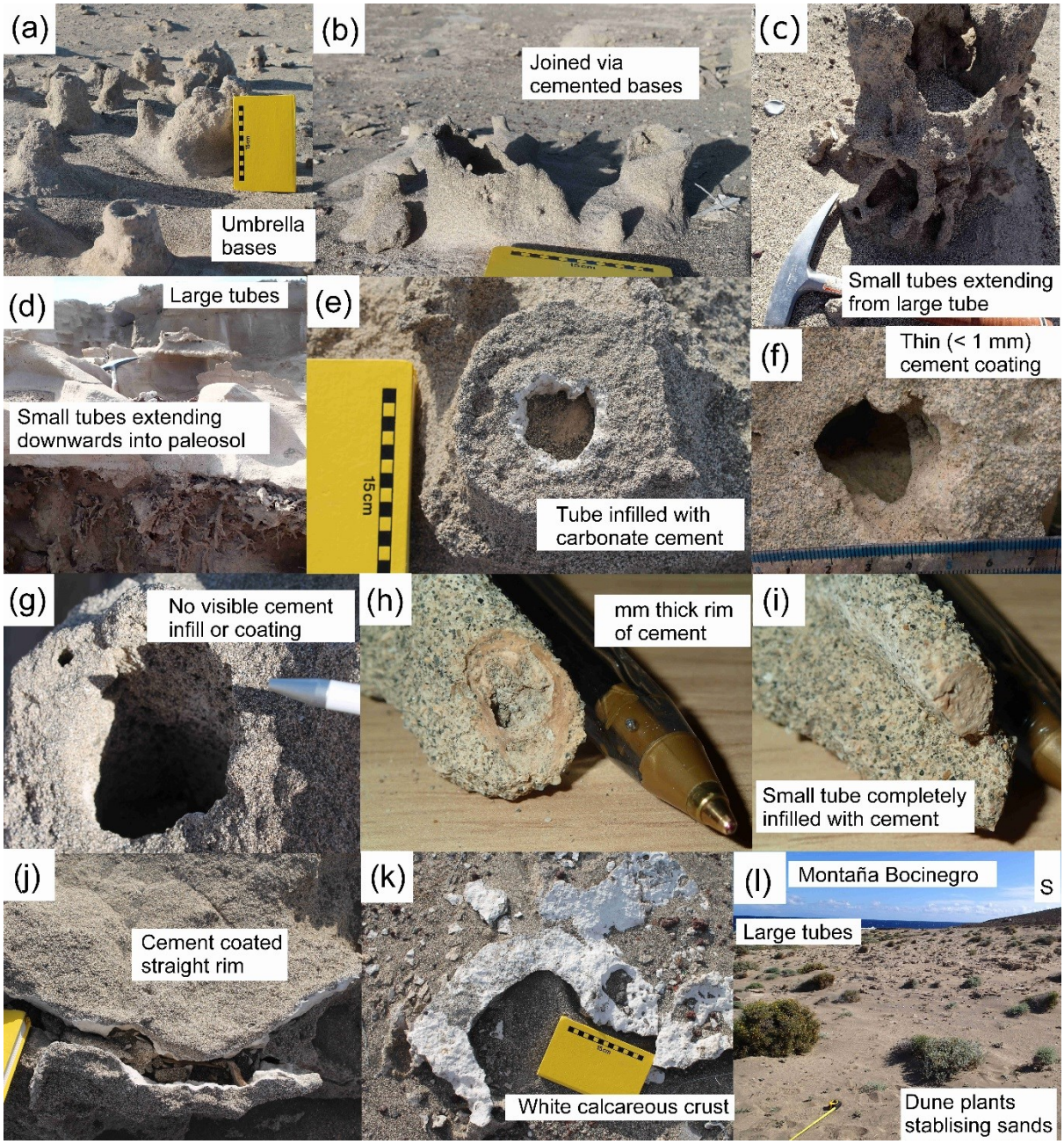


Figure A.4. Range of features on the site. (a) Large cemented-tubes with apron/umbrella bases; (b) Multiple structures cemented along the large tubes' bases (c) Large tube with branches/small tubes extending from the base; (d) Small tubes extending downward through the sandstone into the paleosol; (e) Large tube infilled with cement; (f) Large tube with < 1 mm internal coating of cement; (g) Large tube with no visible infill or coating of cement; (h) Small tube partially filled with cement; (i) Small tube fully cemented; (j) Linear cemented features as seen throughout the site; (k) White calcareous crust interspersed throughout the site; (l) Plants stabilising the dune sands.

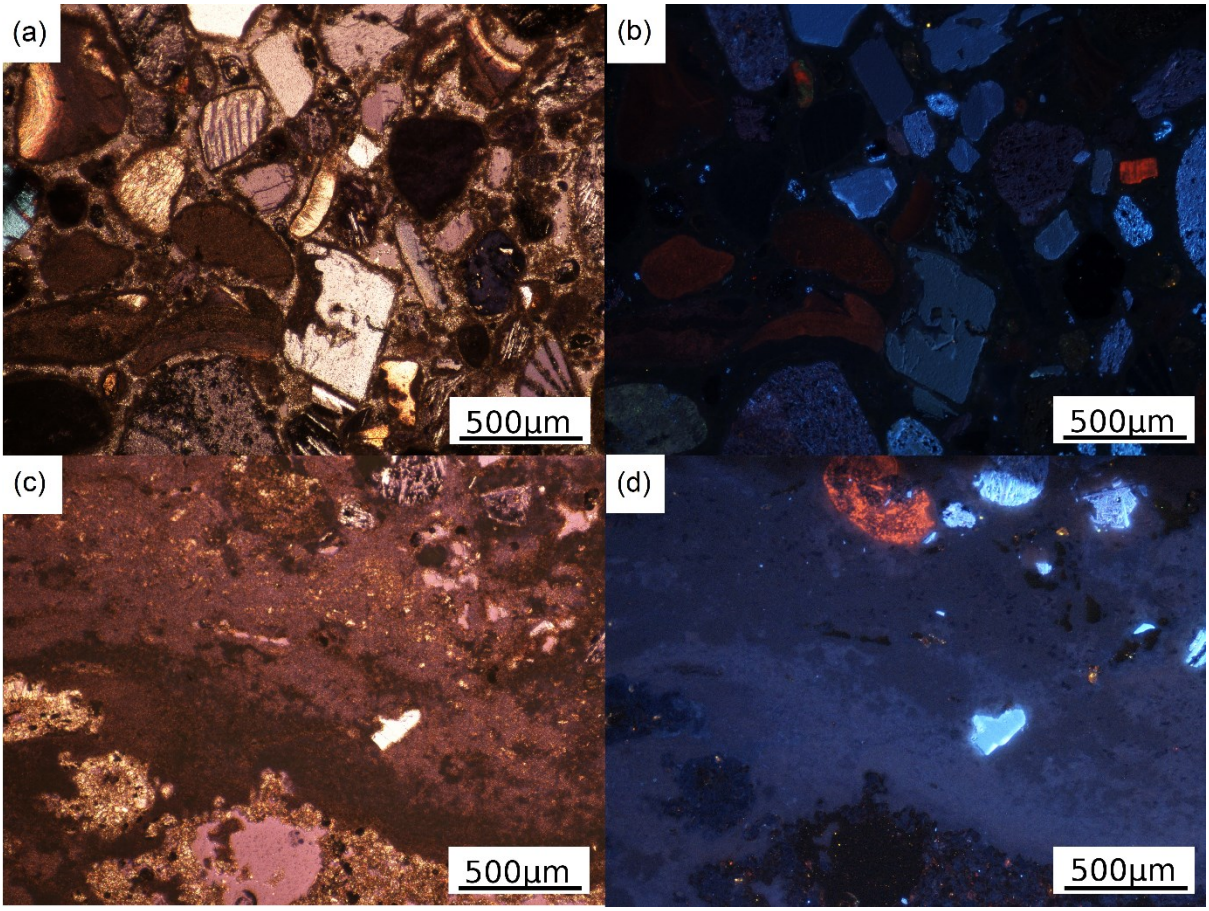


Figure A.5. Optical (a, c) and cathodoluminescence (b, d) microscopy images of sandstone and cements. a-b: Sand composition of large and small structure host rock; c-d: Example of STIC.

The sands hosting all tubes are fine to medium grained (125-500 µm) and moderately sorted. They are quartz dominated, with some pyroclasts of feldspar and olivine, and interspersed with calcite grains, calcified filaments and volcanic rock fragments (Fig. A.5a). Whole and fragmented gastropods are also found within the sands and in the cemented tubes. The sands which host the tubes are cemented by a sparry-calcite cement. The dominant quartz has a dark blue/green dull luminescence under cold cathodoluminescence, whereas the carbonate clasts are mainly non-luminescent or dark orange (Fig. A.5b). The STIC is characterised by brown 'mottled' fabrics (irregular patchy arrangements) (Fig. A.5c) and is non-luminescent (Fig. A.5d). There is also some void filling sparite. The cement zones are well preserved and there is no pitting.

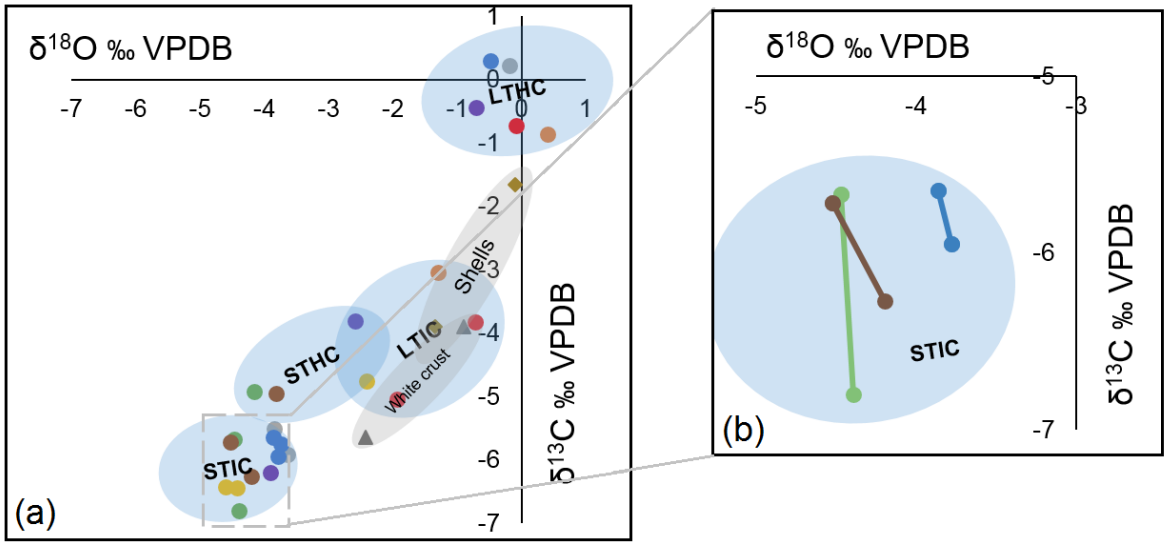


Figure A.6 Isotopic variation in $\delta^{18}O$ and $\delta^{13}C$ values for the carbonate-cemented tubes. a) Overall trend of isotopic signatures. The same colour indicates that they came from parts of the same structure i.e., LTHC, LTIC, STHC and STIC all from one overall structure, if all parts are discernible and available. Shell values = ♦; White calcareous crust =▲. b) Isotopic variation within internal cement rings from the same feature. Only three small tubes sampled had > 1 mm clear individual rings. The additional values in STIC in part (a) are from two small tube internal cements, bifurcating from the same large structure.

The $\delta^{18}O$ values of the cements range from -4.6‰ to 0.4‰ V-PDB and $\delta^{13}C$ values from -6.8‰ to -0.3‰ V-PDB (Fig. A.6). There are four major groupings of $\delta^{18}O$ and $\delta^{13}C$ values (Fig. A.6); STIC (Fig. A.4h,i) has the most depleted $\delta^{18}O$ and $\delta^{13}C$ signatures, whereas LTHC (Fig. A.4a, b, c) has the most enriched. The isotopic values for LTIC (Fig A.4e,f) and the white calcareous crust (Fig. A.4k) lie approximately within the same range; the $\delta^{18}O$ signature ranges from -2.6‰ to -0.7‰ in LTIC and from -2.4‰ to -0.9‰ in the white calcareous crust, and the $\delta^{13}C$ signatures range from -5.0‰ to -3.0‰ and -5.6‰ to -3.9‰ respectively. Individual cement rings within STIC vary in $\delta^{13}C$ by +/-1.1‰ around -5.7‰. The $\delta^{13}C$ values of gastropod shells found within the sands were -3.9‰ and -1.7‰.

A.5 Discussion

Studies using solely morphological interpretations are not able to discriminate between different mechanisms of carbonate precipitation in this location. Sand injection as the mechanism for the formation of these tubes has been dismissed based on the lack of a permeable and impermeable layer within the sands (Kröchert et al., 2008). Interaction of ignimbrites with wet beach sands is rejected, because the ignimbrite deposits underlying the sands are older. However, the lack of specific strata does not discard seismic or volcanic activity; a more impermeable layer, or ignimbrites associated with a more recent eruption (younger than the underlying ignimbrite), could have been eroded since the tubes' formation.

Only through textural and geochemical analysis of the cements am I able to prove or disprove a seismic or volcanic related origin and constrain the formation mechanism of these carbonate-cemented tubes. There is no evidence of altered crystal size, shape or orientation which would occur if sediments were subjected to heat/stress (Jaroslow et al., 1996), nor is there evidence of altered grain orientation or internal laminae indicative of viscous laminar flow (Dott Jr, 1966). Furthermore, fabrics typical of seismic events e.g., pressure solution and ductile fabrics (Moore et al., 2007) are not observed. The observed isotopic signatures reject any influence from rocks from depth or hot fluids (Friedman and O'Neil, 1977a); isotopic values associated with injection sandstones produced in multiple sequences are usually highly scattered due to fluid mixing and multiple carbon sources (e.g., $\delta^{13}C$ = -20 +/-20‰ V-PDB (Jonk et al., 2005)). My isotopic signatures fell within a narrow range; $\delta^{18}O$ signatures from -4.6‰ to 0.4‰ and $\delta^{13}C$ from -6.8‰ to 0.3‰ across all samples. Within this range, the isotopic signatures are grouped into clusters depending on the part of the tube the cement was sampled from.

There are a number of indicators that suggest that these carbonate-cemented tubes are plant-derived. The cloudy mottled brown fabrics in my samples, notably in STIC (Fig. A.2c, d), are typical of organic material, which are commonly associated with rhizocretions and calcrete (Horbury and Qing, 2004). Calcrete, a hardened carbonate layer formed on calcareous materials associated with climate fluctuations in semi-arid climates, is structurally similar (Purvis and Wright, 1991; Alonso-Zarza, 1999) to the white calcareous crust found amongst my carbonate-cemented tubes. The infilling of cement within many structures could be that described by Calvet et al. (1975), which is produced following the death and decay of a plant. The non-luminescence of the cement, which indicates low manganese and low iron carbonate, is also typical of rhizocretions (Klappa, 1980). Carbonate rims are also commonly associated

with calcrete and rhizoliths (Wright and Tucker, 1991), which are structurally similar to the linear cemented features found across the site (Fig. A.4j). The interpretation that these carbonate-cemented tubes are plant-derived agrees with some interpretations made by Kröchert et al. (2008), who argues that the carbonate-cemented tubes are large rhizoliths.

A number of studies have described the formation and preservation of pedogenic plant cast carbonates and calcrete (Calvet et al., 1975; Klappa, 1980; Mount and Cohen, 1984; Purvis and Wright, 1991; Wright and Tucker, 1991; Horbury and Qing, 2004; Liutkus et al., 2005; Alonso-Zarza et al., 2008). However, a number of lines of evidence indicate that the large tubes are not pedogenic features. The size of the large tubes, ~10 cm diameter, found in my site is notably different from other studies from semi-arid regions, which are typically 10 to 100 mm diameter scale (e.g., Loope, 1988; Rodrıguez-Aranda and Calvo, 1998; Owen et al., 2008; Tanner and Lucas, 2017), bar those described by Alonso-Zarza et al. (2008), Liutkus et al. (2005) and Matteucci et al. (2007). Such large carbonate-cemented tubes have previously been attributed to cement rims forming around roots and leaving behind a cast c. 30 times the diameter of the root (Alonso-Zarza et al., 2008). Even with a moderate diversity of flora, most plants are excluded from being a plant mould host as few (< 2%) are saline tolerant (Glenn et al., 1999). Thus, assuming that the same plant type is responsible for the casts over the relatively short time scale of formation during the Holocene, there is no mechanism which could cause similar sized and structured roots to produce such comparatively large vertical tubes (Fig. A.1a, b, e-g), whilst others in the immediate vicinity produce much smaller bifurcations (Fig. A.1h, i). Furthermore, the outer diameter of a root cast should reach a maximum just beyond the rhizosphere (the narrow region of soil directly influenced by the roots (Klappa, 1980)). Roots of dune dwelling plants, such as St. John's Wort (Hypericum perforatum), which are found on the El Médano beaches today, are typically mm-scale (Zobayed and Saxena, 2003) and thus the root casts of such dune plant are limited to a couple of cm in diameter (e.g., Rodrıguez-Aranda and Calvo, 1998; Turner and Makhlouf, 2005; Cramer and Hawkins, 2009).

The stable isotope results shed light on the reason for the two distinct size groupings of carbonate-cemented tubes. From ~12 ka to modern times, the Canary Islands rain typically had a $\delta^{18}O_{fluid}$ value of ~-3.5‰ to -2.5‰ V-SMOW and the average temperature was 20ºC (Yanes et al., 2011). Calcium carbonate precipitated from this meteoric fluid at 20ºC would have a $\delta^{18}O_{cc}$ signature between -4.5‰ and -3.5‰ V-PDB (Friedman and O'Neil, 1977a), which spans the $\delta^{18}O$ range of STIC. As roots predominantly uptake meteoric groundwaters, cementation within roots could explain these isotopic signatures. However, LTHC is much more enriched

in $\delta^{18}O$ and $\delta^{13}C$; it is unlikely that this enrichment was caused by recrystallisation, as the cement zones are well preserved and there is no pitting. Notably, both LTHC and LTIC are more enriched in $\delta^{18}O$ and $\delta^{13}C$ than STHC and STIC. Physical mixing of different phases in the samples, i.e., cement and calcite grains within the host rock, is rejected because (i) great care was taken to only sample cement, (ii) the isotopic signature of gastropod shells found within the sands is more depleted than that of LTHC, and (iii) LTIC, an internal, pure cement is more enriched in $\delta^{18}O$ and $\delta^{13}C$ than STHC, a host cement. If a pure cement displays more enriched signatures, enrichment of the large tube cements cannot be explained by physical mixing. These isotopic clusters suggest a slightly different formation mechanism between the small and large tubes, or different precipitation conditions. Liutkus (2009) identified larger vertical tubes as 'phytocretions' or 'phytocasts' (Liutkus and Wright (2008)), calcium carbonate plant casts that formed around saline tolerant plant stems, which mimic rhizocretions in their outward morphology. I suggest that the large tubes (Fig. A.1d) are these 'phytocasts' and the small bifurcating tubes (Fig. A.1e, f) are root casts, 'rhizoliths'. Both indicate fluctuating water tables and seasonally drier periods.

The formation mechanism suggested is similar to that of paludal tufa (Pedley, 1990; Liutkus, 2009). The distinct features of phytocasts including an umbrella/apron type cemented base and a consistent tube diameter rather than tapering like rhizoliths. Liutkus (2009) indicate that the presence of this cemented apron base shows that the stem of the plant is encrusted down to the surface of the sands. I suggest a mechanism (schematically summarised in Fig. A.7) which encompasses coupled phytocast-rhizolith formation, which has not been detailed previously:

(i) Saline tolerant plants colonise dune sands in response to continual tidal activity in the surf zone of a warm, humid environment. These can survive in a wide range of environmental conditions, preferring sandy soils and damp dunes, and can store reserves in their roots to compensate during harsh times (Ahuja et al., 2010). Such saline-tolerant dune plants anchor the sands and are subject to tidal overwash by marine waters.

(ii) Calcite-rich aeolian sands elevate the carbonate content around the plants as the plants stabilise the sands, as is the case in Lanzarote where the calcium is supplied by the aeolian dust coming from the Sahara and Sahel (Huerta et al., 2015).

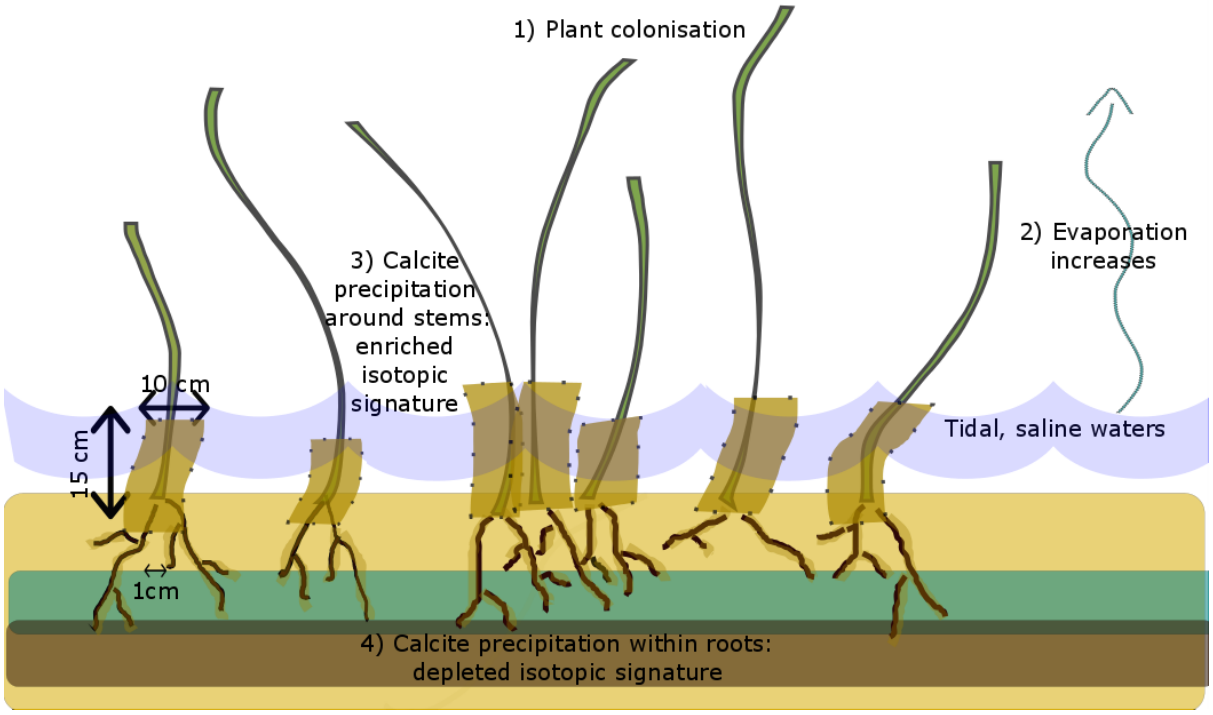


Figure A.7. Schematic illustration of coupled formation of phytocast – rhizolith structures.

(iii) Later in the growing season, increasing evaporation/evapotranspiration leads to a decrease in pCO_2 (Pedley, 1990). As plants remove CO_2 from the water, the *pH* of the system also increases. Carbonate precipitation is favoured under these high salinity and alkalinity conditions.

(iv) Precipitation of carbonate in the sands around the plant stem in the surf zone forms a hard-cylindrical rim. This cylindrical rim acts as a casing around the plant and preserves the root traces. In most large tubes, the initial stage of calcite precipitation is closest to the plant stem i.e., the innermost cement. However, where there is a tube that is completely infilled with cement, the tube has been infilled after the plant has decayed. Equilibration of dissolved inorganic carbon (DIC) with atmospheric CO_2 (~-8‰) enriches the $\delta^{13}C$ signature in LTHC, up to ~1‰ (Emrich et al., 1970), and the $\delta^{18}O$ signature is enriched through the input of tidal, marine water.

(v) The newly formed hard, but still porous, rim provides a sheltered environment for further calcification within other parts of the plant (Wright and Tucker, 1991), which takes place in the meteoric vadose zone beneath the surface. Plant-respired

CO_2 and DIC represent the dominant carbon input for the STIC, with little atmospheric exchange, and thus this cement is more depleted in $\delta^{13}C$. More depleted $\delta^{18}O$ signatures in STHC and STIC represent the uptake of predominantly meteoric water from the vadose zone. LTIC has a coupled influence from saline and meteoric water, due to tidal overwash but also uptake of meteoric groundwater within the stem. This coupled precipitation around and within the stem and the roots produces a large vertical tube with associated small bifurcations (Fig. A.1c).

Calcium carbonate can precipitate extremely fast (~1.6 mm within one growing season). Thus, the presence of calcium carbonate rims or infill pertains to a certain point in time, indicating seasonal surface conditions and ambient surface water conditions (Liutkus, 2009). Small variations between $\delta^{13}C$ values of internal cement rings within the same feature (Fig. A.3b) may indicate several growing seasons and hence varying seasonal signatures between growing seasons, indicative of changes in water-use efficiency (sometimes by less than 1‰ (Ehleringer et al., 1992)); or alternatively, may be related to changes in relative abundances of organic versus inorganic carbon uptake. The calcrete, which precipitates in conjunction with enhanced water evaporation at the surface, may be temporally controlled in relation to the life and death of the plant, but it is likely that the fluids and carbon source are associated with multiple rather than specific parts of the plant. In the case of my isotope results, it is possible that the calcrete which shows more depleted isotopic values has had more input from meteoric fluids and plant-respired CO_2 and DIC, although this is not well constrained.

The stable isotope results recorded by this specific carbonate provide critical information that can be used to define environmental parameters. Rather than recording soil moisture values (as with pedogenic carbonates (Cerling, 1984)), the ambient surface water conditions are recorded, and these are sensitive to evaporation and precipitation ratios and the temperature and $\delta^{18}O$ of the water from which the cement precipitates. It is important to discriminate between phytocasts and rhizoliths because if solely the soil CO_2 diffusion-equilibrium model is used to interpret the isotopic signatures, incorrect palaeoclimate interpretations may be made (Liutkus, 2009), such as changing fluid composition and/or temperature over time. These tubes are a useful indicator of past seasonal climates and for validating a tidal overwash influence. However, it is important to note that the geochemical information derived from these carbonates are only illustrative of a seasonal point in time and do not record a complete signal. Nonetheless, with limited palaeoclimatic data in the Canaries over the last 5 Ka (De Nascimento et al., 2009), these tubes indicate a seasonal climate during the Holocene. In

addition, these large carbonate-cemented tubes are not unique to Tenerife but are found in other parts of the Canary Islands (Gran Canaria; Alonso-Zarza et al. (2008)), as well as in the USA (Liutkus and Wright, 2008; Liutkus, 2009) and Somalia (Matteucci et al., 2007) where the seasonal difference in climate is notable. When dating methods and isotopic studies become much more accurate in space and time, such analyses of phytocast and rhizolith cements could be exceptionally useful in interpreting seasonal variations which cannot be obtained by other means.

The present-day position of these tubes outside the influence of tidal overwash also indicates sea level change or tectonic uplift. Previous studies have indicated uplift of southern Tenerife during the Holocene (Carracedo et al., 2007; Kröchert, 2009). Fossil shells in beach deposits uplifted by 7.5-9 m were 14C-dated at a Holocene age of 2460±35 BP (Buchner et al., 2015). Hence, the existence of the tubes signifies a period when dune plants were subject to tidal overwash, but high enough that meteoric groundwater has a dominant influence.

A.6 Conclusions

In this work I used a combination of field characterisation, microscopic analysis and isotopic studies to constrain the formation mechanism of carbonate-cemented tubes in El Médano, Tenerife. I propose that these structures are phytocasts and associated rhizoliths, which form in response to a seasonally varying climate in a region subject to tidal overwash. I note that it is important to discriminate between the isotopic signatures associated with the cements of phytocasts and rhizoliths, otherwise incorrect palaeoclimate interpretations may be made. As there are a number of regions worldwide which exhibit these large carbonate-cemented tubes, these structures, in conjunction with advances in the accuracy of dating methods, may permit important insights into paleoclimate.

References

Ahuja, I., de Vos, R. C., Bones, A. M., and Hall, R. D., 2010, Plant molecular stress responses face climate change: Trends in Plant Science, v. 15, no. 12, p. 664-674.

Alonso-Zarza, A. M., 1999, Initial stages of laminar calcrete formation by roots: examples from the Neogene of central Spain: Sedimentary Geology, v. 126, no. 1, p. 177-191.

Alonso-Zarza, A. M., Genise, J., Cabrera, M., Mangas, J., Martín-Pérez, A., Valdeolmillos, A., and Dorado-Valiño, M., 2008, Megarhizoliths in Pleistocene aeolian deposits from

Gran Canaria (Spain): ichnological and palaeoenvironmental significance: Palaeogeography, Palaeoclimatology, Palaeoecology, v. 265, no. 1, p. 39-51.

Buchner, E., Kröchert, J., and Schmieder, M., 2015, An updated and refined Holocene uplift history of southern Tenerife (Canary Islands) and the possible consequences for future volcanic activity: Geological Magazine, v. 152, no. 06, p. 1137-1144.

Burke, R., and Gerhard, L., 2000, Aragonite cementation and related sedimentary structures in Quaternary lacustrine deposits, Great Salt Lake, Utah.: The Geology of Antelope Island, Davis County, Utah, no. 1, p. 99.

Calvet, F., Pomar, L., and Esteban, M., 1975, Las rizocreciones del Pleistoceno de Mallorca Inst. Invest. Geol. Univ. Barcelona, v. 30, p. 35-60.

Carracedo, J., 1994, The Canary Islands: an example of structural control on the growth of large oceanic-island volcanoes: Journal of Volcanology and Geothermal Research, v. 60, no. 3, p. 225-241.

Carracedo, J. C., Badiola, E. R., Guillou, H., Paterne, M., Scaillet, S., Torrado, F. P., Paris, R., Fra-Paleo, U., and Hansen, A., 2007, Eruptive and structural history of Teide Volcano and rift zones of Tenerife, Canary Islands: Geological Society of America Bulletin, v. 119, no. 9-10, p. 1027-1051.

Carracedo, J. C., and Day, S., 2002, Canary Islands, Dunedin Academic Press Ltd.

Cerling, T. E., 1984, The stable isotopic composition of modern soil carbonate and its relationship to climate: Earth and Planetary science letters, v. 71, no. 2, p. 229-240.

Coudé-Gaussen, G., and Rognon, P., 1993, Contrasting origin and character of Pleistocene and Holocene dust falls on the Canary Islands and southern Morocco: genetic and climatic significance: Geological Society, London, Special Publications, v. 72, no. 1, p. 277-291.

Cramer, M., and Hawkins, H.-J., 2009, A physiological mechanism for the formation of root casts: Palaeogeography, Palaeoclimatology, Palaeoecology, v. 274, no. 3, p. 125-133.

De Nascimento, L., Willis, K. J., Fernández-Palacios, J. M., Criado, C., and Whittaker, R. J., 2009, The long-term ecology of the lost forests of La Laguna, Tenerife (Canary Islands): Journal of Biogeography, v. 36, no. 3, p. 499-514.

Dott Jr, R. H., 1966, Cohesion and Flow Phenomena in Clastic Intrusions: AAPG Bulletin, v. 50, no. 3, p. 610-611.

Ehleringer, J., Phillips, S., and Comstock, J., 1992, Seasonal variation in the carbon isotopic composition of desert plants: Functional Ecology, p. 396-404.

Friedman, I., O'Neil, J., and Cebula, G., 1982, Two New Carbonate Stable-Isotope Standards: Geostandards Newsletter, v. 6, no. 1, p. 11-12.

Friedman, I., and O'Neil, J. R., 1977a, Compilation of stable isotope fractionation factors of geochemical interest, *in* Fleisher, M., ed., Data of Geochemistry, Volume 440: Washington, United States Government Printing Office.

Friedman, I., and O'Neil, J. R., 1977b, Compilation of stable isotope fractionation factors of geochemical interest, USGPO.

García-Ruiz, J. M., and Otálora, F., 2015, Handbook of Crystal Growth (Second Edition).

Glenn, E. P., Brown, J. J., and Blumwald, E., 1999, Salt tolerance and crop potential of halophytes: Critical reviews in plant sciences, v. 18, no. 2, p. 227-255.

González de Vallejo, L. I., Tsigé, M., and Cabrera, L., 2005, Paleoliquefaction features on Tenerife (Canary Islands) in Holocene sand deposits: Engineering geology, v. 76, no. 3, p. 179-190.

Guillou, H., Carracedo, J. C., Paris, R., and Torrado, F. J. P., 2004, Implications for the early shield-stage evolution of Tenerife from K/Ar ages and magnetic stratigraphy: Earth and Planetary Science Letters, v. 222, no. 2, p. 599-614.

Harris, P. M., Kendall, C. G. S. C., and Lerche, I., 1985, Carbonate cementation—a brief review, Carbonate cementation – a brief review. In: Schneidermann, N. & Harris, P.M. (eds) Carbonate Cements. Society of Economic Paleontologists and Mineralogists, Special Publications, v. 36, p. 79–95.

Hausen, H., Mikkola, T., Wessman, C., and Wiik, H., 1956, Contributions to the geology of Tenerife (Canary Islands), Societas Scientiarum Fennica.

Hoefs, J., 2008, Stable isotope geochemistry, Springer Science & Business Media.

Hollander, D. J., and McKenzie, J. A., 1991, CO2 control on carbon-isotope fractionation during aqueous photosynthesis: A paleo-pCO2 barometer: Geology, v. 19, no. 9, p. 929-932.

Horbury, A. D., and Qing, H., 2004, 'Pseudobreccias' revealed as calcrete mottling and bioturbation in the Late Dinantian of the southern Lake District, UK: Sedimentology, v. 51, no. 1, p. 19-38.

Huerta, P., Rodríguez-Berriguete, Á., Martín-García, R., Martín-Pérez, A., Fernández, Á. L. I., and Alonso-Zarza, A. M., 2015, The role of climate and aeolian dust input in calcrete formation in volcanic islands (Lanzarote and Fuerteventura, Spain): Palaeogeography, Palaeoclimatology, Palaeoecology, v. 417, p. 66-79.

Jaroslow, G., Hirth, G., and Dick, H., 1996, Abyssal peridotite mylonites: implications for grain-size sensitive flow and strain localization in the oceanic lithosphere: Tectonophysics, v. 256, no. 1, p. 17-37.

Jonk, R., Hurst, A., Duranti, D., Parnell, J., Mazzini, A., and Fallick, A., 2005, Origin and timing of sand injection, petroleum migration, and diagenesis in Tertiary reservoirs, south Viking Graben, North Sea: AAPG bulletin, v. 89, no. 3, p. 329-357.

Klappa, C. F., 1980, Rhizoliths in terrestrial carbonates: classification, recognition, genesis and significance: Sedimentology, v. 27, no. 6, p. 613-629.

Kröchert, J., 2009, Volcanic evolution of Southern Tenerife (Canary Islands) during the Pleistocene and Holocene: Universität Stuttgart. [PhD thesis].

Kröchert, J., Buchner, E., and de Vallejo, L. I. G., 2008, Conspicuous sediment structures in fossil beach deposits (southern Tenerife, Canary Islands, Spain): paleoliquefaction features versus biogenic origin: Marine Geophysical Researches, v. 29, no. 3, p. 177-184.

Labaume, P., Sheppard, S. M., and Moretti, I., 2001, Fluid-flow in cataclastic thrust fault zones in sandstones, Sub-Andean Zone, southern Bolivia: Tectonophysics, v. 340, no. 3, p. 141-172.

Larsen, G., and Chilingarian, G. V., 1982, Diagenesis in sediments and sedimentary rocks, Newnes.

Liutkus, C. M., 2009, Using Petrography and Geochemistry to Determine the Origin and Formation Mechanism of Calcitic Plant Molds; Rhizolith or Tufa?: Journal of Sedimentary Research, v. 79, no. 12, p. 906-917.

Liutkus, C. M., and Wright, J. D., 2008, The influence of hydrology and climate on the isotope geochemistry of playa carbonates: a study from Pilot Valley, NV, USA: Sedimentology, v. 55, no. 4, p. 965-978.

Liutkus, C. M., Wright, J. D., Ashley, G. M., and Sikes, N. E., 2005, Paleoenvironmental interpretation of lake-margin deposits using δ13C and δ18O results from early Pleistocene carbonate rhizoliths, Olduvai Gorge, Tanzania: Geology, v. 33, no. 5, p. 377-380.

Lloyd, R., 1966, Oxygen isotope enrichment of seawater by evaporation: Geochimica Et Cosmochimica Acta, v. 30, p. 801-814.

Loope, D. B., 1988, Rhizoliths in ancient eolianites: Sedimentary Geology, v. 56, no. 1-4, p. 301-314.

Loope, D. B., 2013, Confusing seismites in Eolian sandstones with trace fossils, *in* Proceedings 2013 GSA Annual Meeting in Denver.

Martin, U., and Nemeth, K., 2004, Sedimentary interaction between pyroclastic flow deposits of the Poris Member from the Las Canadas and monogenetic volcanic fields in a beach setting near Montana Roja scoria cone, Tenerife Sur, Spain: Occasional Papers of the Geological Institute of Hungary, v. 203, p. 74.

Matteucci, R., Belluomini, G., and Manfra, L., 2007, Late Holocene environmental change in the coastal southern Somalia inferred from Achatina and rhizoliths: Journal of African Earth Sciences, v. 49, no. 3, p. 79-89.

Moore, J. C., Rowe, C., and Meneghini, F., 2007, How Accretionary Prisms Elucidate Seismogenesis in Subduction Zones: The Seismogenic Zone of Subduction Thrust Faults, p. 288.

Morad, S., 2009, Carbonate Cementation in Sandstones: Distribution Patterns and Geochemical Evolution (Special Publication 26 of the IAS), John Wiley & Sons.

Mount, J. F., and Cohen, A. S., 1984, Petrology and geochemistry of rhizoliths from Plio-Pleistocene fluvial and marginal lacustrine deposits, east Lake Turkana, Kenya: Journal of Sedimentary Research, v. 54, no. 1.

Owen, R. A., Owen, R. B., Renaut, R. W., Scott, J. J., Jones, B., and Ashley, G. M., 2008, Mineralogy and origin of rhizoliths on the margins of saline, alkaline Lake Bogoria, Kenya Rift Valley: Sedimentary Geology, v. 203, no. 1, p. 143-163.

Parker, A., and Sellwood, B. W., 1994, Quantitative diagenesis: recent developments and applications to reservoir geology, Springer.

Pedley, H., 1990, Classification and environmental models of cool freshwater tufas: Sedimentary Geology, v. 68, no. 1, p. 143-154.

Purvis, K., and Wright, V., 1991, Calcretes related to phreatophytic vegetation from the Middle Triassic Otter Sandstone of south west England: Sedimentology, v. 38, no. 3, p. 539-551.

Rodrıguez-Aranda, J., and Calvo, J., 1998, Trace fossils and rhizoliths as a tool for sedimentological and palaeoenvironmental analysis of ancient continental evaporite successions: Palaeogeography, Palaeoclimatology, Palaeoecology, v. 140, no. 1, p. 383-399.

Sarkar, S., Choudhuri, A., Banerjee, S., Van Loon, A., and Bose, P. K., 2014, Seismic and non-seismic soft-sediment deformation structures in the Proterozoic Bhander Limestone, central India: Geologos, v. 20, no. 2, p. 89-103.

Schmincke, H.-U., 1976, The geology of the Canary Islands, Biogeography and ecology in the Canary Islands, Springer, p. 67-184.

Schmincke, H.-U., 1982, Volcanic and chemical evolution of the Canary Islands, Geology of the Northwest African continental margin, Springer, p. 273-306.

Sperling, F. N., Washington, R., and Whittaker, R. J., 2004, Future climate change of the subtropical North Atlantic: implications for the cloud forests of tenerife: Climatic Change, v. 65, no. 1-2, p. 103-123.

Stumm, W., and Morgan, J. J., 1981, Aquatic chemistry: an introduction emphasizing chemical equilibria in natural waters, John Wiley.

Tanner, L. H., 2010, Continental carbonates as indicators of paleoclimate: Developments in Sedimentology, v. 62, p. 179-214.

Tanner, L. H., and Lucas, S. G., 2017, Paleosols of the Upper Paleozoic Sangre de Cristo Formation, north-central New Mexico: Record of early Permian palaeoclimate in tropical Pangaea: Journal of Palaeogeography, v. 6, no. 2, p. 144-161

Thornburg, T. M., and Suess, E., 1990, Carbonate cementation of granular and fracture porosity: Implications for the Cenozoic hydrologic development of the Peru continental margin, *in* Proceedings Proc. ODP, Sci. Results, v.112, p. 95-109.

Turner, B. R., and Makhlouf, I., 2005, Quaternary sandstones, northeast Jordan: age, depositional environments and climatic implications: Palaeogeography, Palaeoclimatology, Palaeoecology, v. 229, no. 3, p. 230-250.

Worden, R. H., and Smalley, P. C., 1996, H2S-producing reactions in deep carbonate gas reservoirs: Khuff Formation, Abu Dhabi: Chemical Geology, v. 133, no. 1-4, p. 157-171.

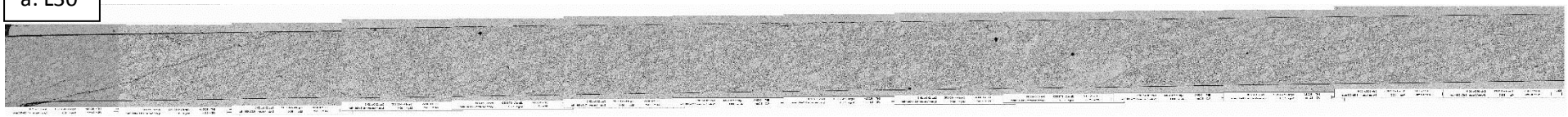
Wright, V. P., and Tucker, M. E., 1991, Calcretes, Blackwell Scientific Publications.

Yanes, Y., Yapp, C. J., Ibáñez, M., Alonso, M. R., De-la-Nuez, J., Quesada, M. L., Castillo, C., and Delgado, A., 2011, Pleistocene–Holocene environmental change in the Canary Archipelago as inferred from the stable isotope composition of land snail shells: Quaternary Research, v. 75, no. 3, p. 658-669.

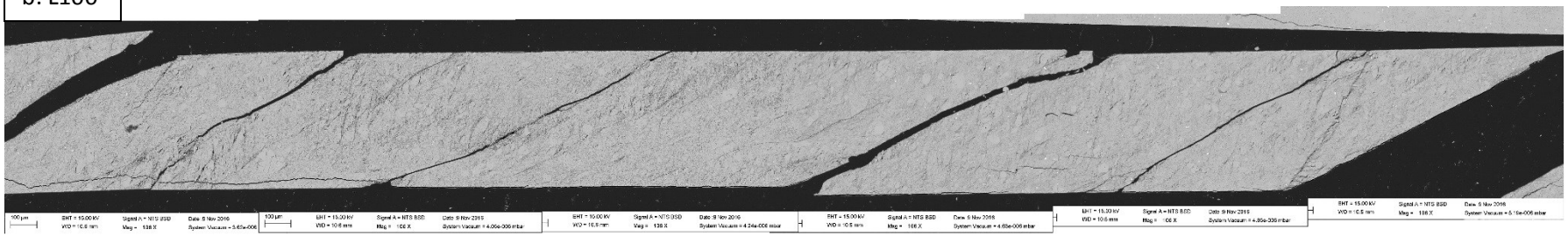
Zobayed, S., and Saxena, P., 2003, In vitro-grown roots: a superior explant for prolific shoot regeneration of St. John's wort (Hypericum perforatum L. cv 'New Stem') in a temporary immersion bioreactor: Plant Science, v. 165, no. 3, p. 463-470.

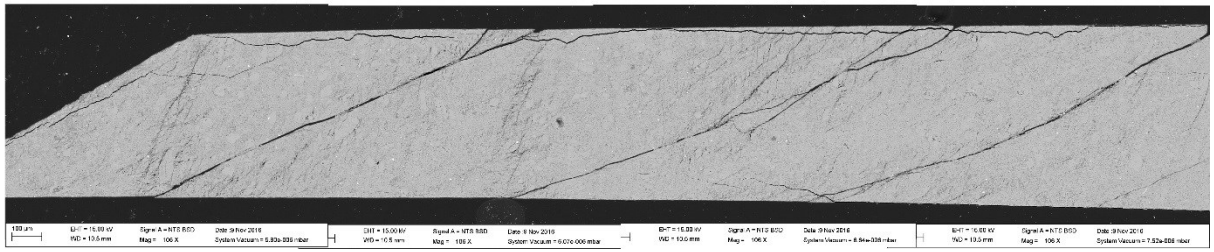
Appendix B: Full images of limestone fault zones (Chapter VI)

a: L30



b: L100





c: L220

